Volume 12 Number 4 2002

ISSN 0961-5539

International Journal of

Numerical Methods for Heat & Fluid Flow

Numerical models for printing and coating flows

Guest Editor: Professor D.T. Gethin

Emerald

www.emeraldinsight.com

International Journal of
Numerical Methods for Heat & Fluid Flow

ISSN 0961-5539

Volume 12
Number 4
2002

Numerical models for printing and coating flows
Guest Editor
Professor D.T. Gethin

Paper format
International Journal of Numerical Methods for Heat & Fluid Flow includes eight issues in traditional paper format. The contents of this issue are detailed below.

Internet Online Publishing
with Archive, Active Reference Linking, Key Readings, Institution-wide Licence, and E-mail Alerting Service and Usage Statistics Access via the Emerald Web site:
http://www.emeraldinsight.com/ft
See p. 331 for full details of subscriber entitlements.

This issue is part of a comprehensive multiple access information service

CONTENTS

CONTENTS
continued

International Journal of Numerical Methods for Heat & Fluid Flow online

An advanced knowledge resource for the entire organization

Access via the Emerald Web site – http://www.emeraldinsight.com/ft

Subscribers to this journal benefit from access to a fully searchable knowledge resource stretching far beyond the current volume and issue. *International Journal of Numerical Methods for Heat & Fluid Flow* online is enhanced with a wealth of features to meet the need for fast, effortless, and instant access to the core body of knowledge. Furthermore, this user-friendly electronic library may be networked throughout the subscribing organization to maximize the use and value of the subscription. This is augmented with advanced search facilities and "choice of access" through a variety of alternative journal gateways.

Emerald online access includes:

Institution-wide Licence

Our liberal licence allows everyone within your institution to access the journals via the Internet, making your subscription more cost-effective. It has been designed to provide a comprehensive, simple system with minimum administration. Access can be granted by IP range or username and password. ATHENS authentication is enabled.

Current Issue + Journal Archive

Internet access via Emerald Fulltext to information as it becomes available online and to material from past volumes. Users can choose to browse the database for relevant articles or search using the powerful search engine provided.

Active Reference Linking

Direct links from the journal article references to abstracts of the most influential articles cited. Where possible, this link is to the full text of the article.

Key Readings

Abstracts of articles, relating to keywords, are selected to provide readers with current awareness of interesting articles from other publications in the field. The abstracts are available online and are updated regularly upon publication of the latest issue.

Usage Statistics

Online Journal Usage Statistics are now available. This feature allows Emerald Administrators to download their usage statistics with regard to their organization's journal usage. Usage Statistics allow you to review the value of electronic dissemination of your journal subscriptions throughout your organization. They can also help determine the future trends for information within your organization. For further information go to http://www.emeraldinsight.com/stats

Emerald Alert

The table of contents e-mail alerting service will e-mail you the contents page of any chosen journal whenever the latest issue becomes available online. For further information please go to http://www.emeraldinsight.com/alerts

Support Resources

A comprehensive range of resources is available online that help users learn how to effectively use online information resources and that helps information professionals market resources to their users. For further information please go to http://www.emeraldinsight.com/support

Choice of Access

Electronic access to this journal is available via a number of channels, enabling end users' libraries to reach the content through their preferred delivery system.

The Emerald Web site – http://www.emeraldinsight.com/ft – is the recommended means of electronic access as it provides fully searchable and high value-added access to the complete content of the journal. Refer to the next section for "how to access" via the Emerald Web site.

Subscribers can also access and search the article content of this journal through the following journal gateway services:
Ebsco Online
http://www.ebsco.com/online
Huber E-Journals
http://e-journals.hanshuber.com/english/
Minerva
http://www.minerva.at/
OCLC Firstsearch "Electronic Collections Online'
http://www.uk.oclc.org/oclc/menu/eco.htm
RoweCom's "Information Quest"
http://www.informationquest.com
SilverPlatter
http://www.silverplatter.com
SwetsBlackwell's "Swetsnet*Navigator*"
http://www.swetsnetnavigator.nl

How to access this journal through Emerald

Organizations must first register for online access (instructions provided at http://www.emeraldinsight.com/register), after which the content is available to everyone within the organization's domain. To access this journal's content, simply log on either from the journal homepage or direct through the Emerald Web site.

Emerald Customer Support Services
For customer service and technical help, contact:
E-mail: support@emeraldinsight.com
Telephone: (44) 1274 785278
Fax: (44) 1274 785204

EDITORIAL ADVISORY BOARD

International Journal of Numerical Methods for Heat & Fluid Flow, Vol. 12 No. 4, 2002, p. 332.

Computational simulation of the printing of Newtonian liquid from a trapezoidal cavity

C.A. Powell, M.D. Savage and J.T. Guthrie

Keywords Lagrangian method, Finite element method, Fluid flow

A Lagrangian finite element algorithm is described for solving two-dimensional, time-dependent free surface fluid flows such as those that occur in industrial printing processes. The algorithm is applied using a problem specific structured meshing strategy, implemented with periodic remeshing to control element distortion. The method is benchmarked on the problem of a stretching filament of viscous liquid, which clearly demonstrates the applicability of the approach to flows involving substantial free surface deformation. The model printing problem of the transfer of Newtonian liquid from an upturned trapezoidal trench (3-D cavity with a large transverse aspect ratio) to a horizontal substrate, which is pulled perpendicularly downwards from the cavity, is solved computationally using the Lagrangian scheme. The idealized 2-D liquid motion is tracked from start-up to the point where a thin sheet forms - connecting the liquid remaining in the cavity to a "sessile" drop on the moving substrate. The effect of varying substrate separation speed is briefly discussed and predictions are made for approximate drop volumes and "limiting" domain lengths.

The application of roughness model to a soft EHL contact

M.F.J. Bohan, T.C. Claypole and D.T. Gethin

Keywords Surface roughness, Fluid flow, Lubrication

The study focuses on the development of a numerical model to explore the impact of surface roughness in soft rolling nip contacts, including representation of a real surface. The solution of the governing equations required the application of a multigridding technique to capture the details of the fluid flow within the roughness wavelengths and a minimum number of fluid nodes per wavelength were established. In the case studies, two extreme roughness profiles were considered, longitudinal and circumferential. The longitudinal roughness had a significant impact on nip pressures and pumping capacity, the latter being determined by the minimum film thickness in the nip. The circumferential roughness was found to have a localised effect on film pressure, but only a very small impact on the film thickness profile. The consequent effect on pumping capacity was small.

Numerical study of transient instabilities in reverse-roller coating flows

M.S. Chandio and M.F. Webster

Keywords Numerical simulation, Finite elements, Free form surfaces

A semi-implicit Taylor-Galerkin/pressure-correction algorithm of a transient finite element form is applied to analyse the flow instabilities that commonly arise during reverse-roller coating. A mathematical model is derived to describe the solvent coating applied to the underside of the sheet, assuming that the lacquer is a Newtonian fluid and considering the flow between application roller and foil. Here, we have investigated the effects of temporal instabilities, caused by adjustment of nip-gap width and foil-position, extending our previous steady-state analysis. Foil shifting is found to have a significant influence upon pressure and lift on the foil, drag on the roller, and free coating profiles. This would result in process instabilities, such as chatter and flow-lines. In contrast, nip-gap adjustment has no influence on the coating finish.

Viscoelastic computations of polymeric wire-coating flows

H. Matallah, P. Townsend and M.F. Webster

Keywords Coatings, Finite elements, Flow

This study considers both a single and multi-mode viscoelastic analysis for wire-coating flows. The numerical simulations utilise a finite element time-stepping technique, a Taylor-Petrov-Galerkin/pressure-correction scheme employing both coupled and decoupled procedures between stress and kinematic fields. An exponential Phan-Thein/Tanner model is used to predict pressure-drop and residual stress for this process.

Rheometrical data fitting is performed for steady shear and pure extensional flows, considering both high and low density polyethylene melts. Simulations are conducted to match experimental pressure-drop/flowrate data for a contraction flow. Then, for a complex industrial wire-coating flow, stress and pressure drop are predicted numerically and quantified. The benefits are extolled of the use of a multi-mode model that can incorporate a wide-range discrete relaxation spectrum to represent flow response in complex settings. Contrast is made between LDPE and HDPE polymers, and dependency on individual relaxation modes is identified in its contribution to overall flow behaviour.

Numerical simulation for viscous free-surface flows for reverse roller-coating

M.S. Chandio and M.F. Webster

Keywords Free form surfaces, Numerical simulation, Finite elements

This article is concerned with the numerical simulation of a reverse roller-coating process, which involves the computation of Newtonian viscous incompressible flows with free-surfaces. A numerical scheme is applied of a transient finite element form, a semi-implicit Taylor-Galerkin/pressurecorrection algorithm. For free-surface prediction, we use kinematic boundary adjustment with a mesh-stretching algorithm. In the present work, an alloy sheet (foil) passes over a large roller and then a smaller applicator roller, which provides the in-feed. In combination, the applicator roller, the foil and the fluid form part of the underside coating mechanism. The aim of this study is to investigate fundamental aspects of the process, to ultimately address typical coating instabilities. These may take the form of chatter and starvation. A uniform coating thickness is the desired objective. A mathematical model is derived to describe the solvent coating applied to the underside of the sheet, assuming that the lacquer is a Newtonian fluid. In particular, the work has concentrated on the flow patterns that result and a parameter sensitivity analysis covering the appropriate operating windows of applied conditions. Effects of independent variation in roll-speed and foil-speed are investigated, to find that maxima in pressure, lift and drag arise at the nip and are influenced in a linear fashion.

Simulation of pressure- and tube-tooling wire-coating flows through distributed computation

A. Baloch, H. Matallah, V. Ngamaramvaranggul and M.F. Webster

Keywords Finite element method, Viscous flows, Parallel computing

This article focuses on the comparative study of annular wire-coating flows with polymer melt materials. Different process designs are considered of pressure- and tube-tooling, complementing earlier studies on individual designs. A novel mass-balance free-surface location technique is proposed. The polymeric materials are represented via shear-thinning, differential viscoelastic constitutive models, taken of exponential Phan-Thien/Tanner form. Simulations are conducted for these industrial problems through distributed parallel computation, using a semi-implicit time-stepping Taylor-Galerkin/pressure-correction algorithm. On typical field results and by comparing short-against full-die pressure-tooling solutions, shear-rates are observed to increase ten fold, while strain rates increase one hundred times. Tube-tooling shear and extension-rates are one quarter of those for pressure-tooling. These findings across design options, have considerable bearing on the appropriateness of choice for the respective process involved. Parallel finite element results are generated on a homogeneous network of Intel-chip workstations, running PVM (Parallel Vitual Machine) protocol over a Solaris operating system. Parallel timings yield practically ideal linear speed-up over the set number of processors.

Numerical modelling of elastohydrodynamic lubrication in soft contacts using non-Newtonian fluids

M.F.J. Bohan, I.J. Fox, T.C. Claypole and D.T. Gethin

Keywords Lubrication, Non-Newtonian fluids

The paper focuses on the solution of a numerical model to explore the sliding and non-Newtonian fluid behaviour in soft

elastohydrodynamic nip contacts. The solution required the coupling of the fluid and elastomer regimes, with the non-Newtonian fluid properties being described using a power law relationship. The analysis showed that the fluid characteristics as defined by the power law relationship led to large differences in the film thickness and flow rate with a movement of the peak pressure within the nip contact. The viscosity coefficient, power law index and sliding ratio were shown to affect the nip performance in a non-linear manner in terms of flow rate and film thickness. This was found to be controlled principally by the level of viscosity defined by the power law equation. The use of a speed differential to control nip pumping capacity was also explored and this was found to be most sensitive at lower entrainment speeds.

Preface

This issue brings together a number of papers under the theme of thin film flows that are generic to printing and a wide range of coating applications. These processes require the deposition of a thin layer of fluid (or polymer) onto a substrate. The simulation of these processes presents a number of numerical challenges. Printing and some coating processes comprise roller pairs in contact, one of which is covered by a soft elastomer that may have a rough textured surface. Also engraved surfaces are frequently used to meter fluid transfer and the mechanism of fluid release from the engraved cell is a complex process. Coatings are applied to thin flexible substrates through a counter rotating roller system that runs in contact with the substrate. Wire coating takes place in a closed die in which a layer of polymer is metered onto the wire substrate to form an insulating surface.

A number of papers are presented covering the issues summarised in the preceding paragraph. The first paper by Powell, Savage and Guthrie describes their current work on filamentation at the point of film splitting, focusing on the behaviour where one surface is engraved. Their model accounts for the tensile stresses in the filament, its profile, adhesion and final detachment.

The second paper is by Bohan, Gethin and Claypole in which they explore the inclusion of a roughness model in rolling soft elastohydrodynamic contacts. In this work the roughness interaction is included directly through the prescription of a local film thickness and the ability of the approach to treat real roughness profiles is demonstrated.

The third and fourth papers are by Chandio and Webster in which they explore numerical techniques to model the reverse roller coating process, including both steady and transient conditions. This presents challenges in the handling the deflection of a thin substrate that deflects laterally in response to the loads generated in the coating nip and in the need to determine automatically the position of the free surface in the nip. The fourth and fifth share the theme of wire coating. The fourth reports the work of Matallah, Townsend and Webster and the fifth the development undertaken by Baloch, Matallah, Ngamaramvaranggul and Webster. These papers focus on the requirement to include complex rheology models to represent the behaviour of the polymer system together with die swell prediction as the product emerges from the coating die.

The sixth paper also explores the benefit of using multiprocessor systems to perform simulation, demonstrating the ability to undertake more complex and demanding simulations efficiently.

The issue is conclude by a paper by Bohan, Fox, Claypole and Gethin in which the authors explore the application of models to represent coating systems supplied by non-Newtonian fluids. The model proposed is capable of accounting for the local shear thinning behaviour that takes place in the plane

International Journal of Numerical Methods for Heat & Fluid Flow, Vol. 12 No. 4, 2001, pp. 336-337.

of the nip junction. The impact on coating performance is demonstrated through a number of case studies.

All of these studies highlight fluid-structure interactions that take place together with the treatment of free surfaces. The issue brings together some of the most recent work addressing these details that are generic to printing and coating applications.

D.T. Gethin

Computational simulation of the printing of Newtonian liquid from a trapezoidal cavity

C.A. Powell, M.D. Savage
Department of Physics and Astronomy, University of Leeds, Leeds, UK
J.T. Guthrie
Department of Colour Chemistry, University of Leeds, Leeds, UK

Keywords *Lagrangian method, Finite element method, Fluid flow*

Abstract *A Lagrangian finite element algorithm is described for solving two-dimensional, time-dependent free surface fluid flows such as those that occur in industrial printing processes. The algorithm is applied using a problem specific structured meshing strategy, implemented with periodic remeshing to control element distortion. The method is benchmarked on the problem of a stretching filament of viscous liquid, which clearly demonstrates the applicability of the approach to flows involving substantial free surface deformation. The model printing problem of the transfer of Newtonian liquid from an upturned trapezoidal trench (3-D cavity with a large transverse aspect ratio) to a horizontal substrate, which is pulled perpendicularly downwards from the cavity, is solved computationally using the Lagrangian scheme. The idealized 2-D liquid motion is tracked from start-up to the point where a thin sheet forms – connecting the liquid remaining in the cavity to a "sessile" drop on the moving substrate. The effect of varying substrate separation speed is briefly discussed and predictions are made for approximate drop volumes and "limiting" domain lengths.*

1. Introduction

In a number of industrial printing processes it is necessary to transfer liquids exhibiting various rheologies from engraved cavities to a substrate in order to create a liquid pattern on the latter. For example, in both the coating and printing industries gravure rolls (rolls engraved with tiny cells/cavities) are used extensively for the deposition of liquid onto a web or other surface prior to drying, for the production of a wide range of products including: cartons, packaging systems, plastic films, metal foils and magazine covers. In gravure printing transfer is direct from tiny cells to a substrate wrapped around a soft backing roll – giving rise to a pattern of discrete liquid dots. In gravure coating, however, the liquid transfer mechanism is indirect; liquid, evacuated from the cells by the action of a passing meniscus (Powell *et al.*, 2000), in turn supplies a small coating "bead" from which a continuous film of uniform

International Journal of Numerical Methods for Heat & Fluid Flow, Vol. 12 No. 4, 2002, pp. 338-355.

DOI 10.1108/09615530210433251

The authors wish to thank the Field Group for supporting the research. C. Powell is funded by EPSRC grant GR/M89249.

thickness is coated to the substrate. Recent experimental studies (eg Benkreira and Patel (Benkreira and Patel, 1993)) have done much to further our understanding of the gravure coating process, whilst 2-D finite element (Powell *et al.*, 2000) and 1-D finite difference (Schwartz *et al.*, 1998) simulations of the meniscus-driven evacuation of liquid from individual gravure cavities have further elucidated the process. To date, however, there has been no corresponding numerical modelling of the gravure printing process to accompany experimental studies (Kunz, 1983; Piette *et al.*, 1997; Bohan *et al.*, 2000).

Other common examples of engraved-cavity based printing processes are pad printing (Collard, 1984), where the relevant transfer of link is from a cavity to a pad (or tampon) that is pressed downwards against the cavity and then lifted perpendicularly away, and screen printing (Guthrie, 1992; Mock, 1999), in which ink is flooded over a screen containing open image areas, and a squeegee is then drawn across the screen – simultaneously pushing the screen against a substrate and forcing ink through the open areas. The particular feature of interest to us in screen printing is the reopening of the gap between screen and substrate and the subsequent stretching of liquid from the screen image areas once the squeegee passes. To date there has been no attempt to computationally simulate liquid transfer in either pad or screen printing.

We note that the problem of drop formation from an orifice, of central importance to an understanding of ink-jet printing, has – in contrast to the engraved-cavity based processes mentioned above – received a great deal of attention both experimental and computational. Indeed, a variety of numerical approaches have been adopted to simulate drop formation including volume-of-fluid (VOF) (Zhang, 1999) and an Eulerian finite element method employing a purpose-designed mesh (Wilkes *et al.*, 1999). These different numerical approaches have their relative strengths and weaknesses. The VOF method, for example, does not exhibit a very high degree of accuracy on small scales due to the use of a fixed mesh, though this is compensated for by the fact that meshing and logic problems are removed – enabling straightforward simulation of complicated free surface behaviour.

In the present work we employ of Lagrangian finite element algorithm to solve the 2-D, time-dependent free surface flows, subject to substantial free surface deformation, that typically occur in cavity-based printing processes. Lagrangian finite element analysis is recognised as a very accurate tool for studying the transient free surface fluid flows that occur in a variety of engineering applications, including: thin film coating (Bach and Hassager, 1985), sloshing flows (Ramaswamy *et al.*, 1986), industrial metal casting (Muttin *et al.*, 2001) and wave breaking (Radovitzky and Ortiz, 1998). The major advantage is the use of a convected computational mesh, which enables simple, yet very accurate, tracking of the free surfaces – provided, of course, that at any time a mesh may be generated that discretises the domain effectively. We

employ a problem specific structured meshing strategy to implement the Lagrangian algorithm, together with periodic remeshing to control element distortion. In the next section the method is outlined, with attention drawn to important features, and then in section 3 the method is benchmarked on the problem of a stretching liquid filament. As a first step to understanding the micro-scale liquid transfer processes occurring in cavity-based printing, we formulate and solve numerically an idealised printing problem in which liquid is transferred from an upturned trapezoidal cavity to a moving substrate.

2. Lagrangian finite element method

2.1 Governing equations

Denoting a typical velocity by U and a typical length scale by d, then the non-dimensional equations of momentum and mass conservation for an incompressible, Newtonian fluid of density ρ, viscosity μ and surface tension τ are written in Eulerian form as:

$$\mathrm{Re}\left(\frac{\partial \underline{u}}{\partial t} + \underline{u}\cdot\nabla\underline{u}\right) = \nabla\cdot\underline{\underline{\sigma}} + \mathrm{St}\hat{\underline{g}}, \tag{1}$$

$$\nabla\cdot\underline{u} = 0. \tag{2}$$

Here $\underline{u}$ denotes the fluid velocity, $\hat{\underline{g}}$ is a unit vector in the direction of gravity (g), $\mathrm{Re} = \rho U d/\mu$ and $\mathrm{St} = \rho g d^2/\mu U$ are the Reynolds and Stokes numbers, and the stress tensor, $\underline{\underline{\sigma}}$, is defined by

$$\underline{\underline{\sigma}} = -p\underline{\underline{I}} + [\nabla\underline{u} + \nabla\underline{u}^T]. \tag{3}$$

We use the Lagrangian description of the flow in which the fluid particle locations, and hence the dependent variables, are functions of some known initial configuration, $\underline{x}_0$ (defined at time t_0), and the time elapsed. Thus

$$\underline{x} = \underline{x}(\underline{x}_0, t_0, t), \quad \underline{u} = \underline{u}(\underline{x}_0, t_0, t), \quad p = p(\underline{x}_0, t_0, t). \tag{4}$$

The major advantage of this description is that the computational mesh is identified with the fluid and hence convected with the flow. For free surface simulations this implies that nodes in the computational discretisation that are located on a free surface stay there as the fluid domain evolves, and these nodes are simply found as part of the overall fluid deformation, $\underline{x} = \underline{x}(\underline{x}_0, t_0, t)$. As a consequence the location of moving free surfaces and the imposition of boundary conditions there are rendered straightforward, whereas if one used the alternative Eulerian description of the fluid it would be necessary to impose an additional "kinematic" condition to solve for the free surface nodes, e.g. ref. Wilkes *et al.*, 1999.

2.2 Boundary conditions

On no-slip boundaries essential velocity conditions are imposed exactly. Natural free surface conditions are imposed in the standard way (Ruschak, 1980) using the familiar normal stress balance:

$$\hat{\underline{n}} \cdot \underline{\underline{\sigma}} = \frac{1}{\mathrm{Ca}} \frac{\mathrm{d}\hat{\underline{t}}}{\mathrm{d}s}, \tag{5}$$

where $\underline{t}$ and $\hat{n}$ are, respectively, unit vectors tangent and normal to the free surface, $\mathrm{Ca} = \bar{\mu} U/\tau$ is the capillary number, and s denotes length along the free surface.

Determination of the correct mathematical treatment for a contact line, which occurs where a free surface meets a solid boundary under dynamic conditions, is the subject of much theoretical research (see Hocking (1994) and Shikhmurzaev (1997) for two fundamentally different perspectives on the problem). In terms of incorporating a contact line into a finite element simulation of flow involving capillary effects, the two key issues that must be resolved are:

(1) the introduction of local tangential slip near the contact line to remove the stress singularity that occurs if the usual no-slip conditions are applied (Dussan, 1976),

(2) the boundary condition at the contact line relating the contact angle to the independent variables and physical parameters.

In addition a degree of local mesh refinement is required to incorporate the modeling and accurately resolve the high velocity gradients. A recent paper (Powell and Savage, 2001) gives the specific numerical details of how this may be accomplished for the particular choice of a "Tanner law" (Greenspan, 1978) boundary condition, relating contact angle to contact line speed. An identical treatment is used for incorporating the moving contact lines in the printing application presented in this work. The only difference here is the choice of a constant dynamic contact angle boundary condition, which is imposed by satisfying the following equation:

$$\hat{\underline{t}}_b \cdot \hat{\underline{t}}_{fs} = \cos \theta_{\mathrm{D}}, \tag{6}$$

where θ_{D} is the prescribed dynamic contact angle, $\hat{t}_b$ is the known tangent to the solid boundary and $\hat{\underline{t}}_{fs}$ is the free surface tangent at the contact line, which may be calculated accurately using the isoparametric element representation. This equation allows the contact line location to be updated as part of the overall numerical solution scheme.

2.3 Finite element implementation

The Lagrangian finite element algorithm used to solve the governing equations, subject to appropriate initial and boundary conditions, has been

described elsewhere (Powell and Savage, 2001), thus here we only given an outline. The fluid domain is discretised using isoparametric triangular V6/P3 elements (Zienkiewicz, 1977; Taylor and Hood, 1973), so the velocity components and pressure are interpolated over an element as:

$$u = \sum_{i=1}^{6} N_i(x,y)\bar{u}_i(t), \quad v = \sum_{i=1}^{6} N_i(x,y)\bar{v}_i(t), \quad p = \sum_{i=1}^{3} L_i(x,y)\bar{p}_i(t), \tag{7}$$

where "–" denotes a nodal value. We apply the Galerkin method to obtain the finite element equations:

$$[M]\begin{pmatrix} \dot{\underline{U}} \\ \dot{\underline{V}} \\ \dot{P} \end{pmatrix} + [C]\begin{pmatrix} \underline{U} \\ \underline{V} \\ \underline{P} \end{pmatrix} = (F), \tag{8}$$

where $\underline{U} = (\bar{u}_1, \ldots, \bar{u}_6), \underline{V} = (\bar{v}_1, \ldots, \bar{v}_6), \underline{P} = (\bar{p}_1, \bar{p}_2, \bar{p}_3)$ and "$\cdot$" denotes the material time derivative D/Dt. The matrix M is the mass, or inertia matrix, C is the diffusion matrix and F contains the gravity and surface tension contributions [1]. For a given set of element coordinates the matrices M, C and F may be evaluated using numerical integration; here all domain integrals are approximated using a 4-point Gaussian scheme and boundary integrals using a 3-point scheme. For time integration we employ a "Θ-scheme":

$$\begin{pmatrix} \underline{U} \\ \underline{V} \\ \underline{P} \end{pmatrix}_{t+\Delta t} = \begin{pmatrix} \underline{U} \\ \underline{V} \\ \underline{P} \end{pmatrix}_{t} + \Delta t \left[\Theta \begin{pmatrix} \dot{\underline{U}} \\ \dot{\underline{V}} \\ \dot{P} \end{pmatrix}_{t+\Delta t} + (1-\Theta) \begin{pmatrix} \dot{\underline{U}} \\ \dot{\underline{V}} \\ \dot{\underline{P}} \end{pmatrix}_{t} \right] \tag{9}$$

Θ is initially given the value 1, corresponding to a simple backward difference approximation, then subsequently Θ takes a value of 1/2 – thus switching to the second-order accurate Crank-Nicolson, or trapezoidal, method. This switching strategy avoids the need for specifying initial conditions on pressure. In a previous study of surface tension dominated flows (Powell and Savage, 2001) it was noted that changing Θ to 1/2 too quickly can introduce significant inaccuracies into the solution, thus in such flows the switching is delayed for several time steps. A value for Δt is found heuristically by testing several different time steps and comparing the solutions.

The iterative solution scheme, used to advance the fluid motion through a time increment Δt and obtain the new fluid domain and velocity and pressure fields, is as follows (see refs Bach and Hassager (1985) and Powell and Savage (2001) for further information):

(1) Make initial estimates of velocities and coordinates at time $t + \Delta t$:

$$\underline{u}^1_{t+\Delta t} = \underline{u}_t, \quad \underline{x}^1_{t+\Delta t} = \begin{cases} \underline{x}_t + \Delta t \underline{u}^1_{t+\Delta t} & \text{tstep} = 1 \\ \underline{x}_t + \frac{\Delta t}{2}(\underline{u}^*_{t+\Delta t} + \underline{u}^1_{t+\Delta t}) & \text{tstep} > 1 \end{cases} \tag{10}$$

where tstep is the number of the current time step and $\underline{u}^*_{t+\Delta t}$ is given by a two step Adams-Bashforth estimate:

$$\underline{u}^*_{t+\Delta t} = \underline{u}_t + \frac{\Delta t}{2}\left[3\frac{D\underline{u}_t}{Dt} - \frac{D\underline{u}_{t-\Delta t}}{Dt}\right]. \tag{11}$$

Then starting with $n = 1$ repeat steps (2)–(4).

(2) Assemble the element equations on configuration $\underline{x}^n_{t+\Delta t}$, impose boundary conditions and solve to find $\underline{u}^{n+1}_{t+\Delta t}$ and $p^{n+1}_{t+\Delta t}$; the large system of linear finite element equations is solved by Gaussian elimination using Hood's frontal method (Hood, 1976).

(3) Find a new configuration from:

$$\underline{x}^{n+1}_{t+\Delta t} = \underline{x}_t + \frac{\Delta t}{2}\left(\underline{u}^{n+1}_{t+\Delta t} + \underline{u}_t\right). \tag{12}$$

(4) Check for convergence by seeing if $\underline{x}^{n+1}_{t+\Delta t} - \underline{x}^n_{t+\Delta t}$ is less than some specified tolerance; if not repeat from step (2).

Steps (1)–(4) are repeated until the preassigned total time is reached, or the simulation reaches steady state.

2.4 Meshing issues

At the end of each time step the amount of mesh deformation is calculated using the following measure (Bach and Hassager, 1985):

$$D_p = \frac{V_p}{\min_n N \; J_n W_n}, \tag{13}$$

where J_n is the determinant of the transformation Jacobian from local to global coordinates at the nth Gauss point in element p, W_n is the Gaussian weight for the nth Gauss point, N is the number of Gauss points and $V_p = \sum_{i=1}^{N} J_i W_i$ is the element area. D_p takes its minimum value of 1.0 when element p is undeformed, but this value grows as the element distorts (becoming infinite if the Jacobian becomes singular). Our numerical algorithm searches through each element of the mesh and checks that D_p is less than some maximum permitted tolerance, if D_p exceeds this limit in one or more elements the decision is made to remesh.

In a previous application of the present Lagrangian scheme to capillary flow involving dynamic contact line motion (Powell and Savage, 2001) the free

surface deformations are not particularly significant and hence the construction of a structured mesh is not difficult and few remeshings are required to prevent element distortion. Printing problems, by contrast, typically involve liquid domains that are subject to severe free surface deformations thus in order to apply the Lagrangian scheme it is necessary to either devise more flexible problem specific structured meshes or resort to a fully automatic unstructured mesh approach. We adopt the former alternative, and so the fluid domain is initially discretised and then periodically remeshed using structured meshes of isoparametric triangular V6/P3 elements.

It is worth noting that a great deal of research has been carried out into the development of unstructured mesh generation and adaptive refinement algorithms, see, for instance, refs Shephard (1988); Joe (1991); Rebay (1993). Significant advances in these fields have undoubtably increased the attractions of Lagrangian finite element analysis to CFD practitioners, since early Lagrangian-based algorithms were carried out on fixed meshes and could not cope with large fluid domain deformations. Indeed, in recent years unstructured meshing algorithms have been incorporated into Lagrangian finite element simulators in studies of metal casting (Muttin *et al.*, 1993) and wave breaking (Radovitzky and Ortiz, 1998). However aspects of any fluid domain meshing procedure invariably remain problem specific, since the design of a computational mesh represents both a physical as well as a geometrical problem. Hence adding mesh refinement for special features such as moving contact lines and sharp boundary corners often requires non-trivial user interaction even for an unstructured algorithm. Furthermore, serious programming issues are encountered when an unstructured mesh is used in conjunction with a highly efficient frontal solution approach such as Hood's method (Hood, 1976) which we employ in this study. The task of renumbering elements and nodes in order to minimize the frontwidth becomes far from straightforward, and the numbering scheme must be recalculated every time the mesh is updated. For these reasons in this work we follow the structured mesh route; details about the mesh structure used for a specific problem are given in the appropriate place.

Once the new mesh is generated accurate mesh-to-mesh transfer is ensured by iteratively solving the old element interpolation equations to locate nodes in the new mesh and then employing the isoparametric mapping (Bach and Villadsen, 1984). When this is completed the simulation may continue through another time increment.

3. Validation and applications

3.1 Stretching viscous filament

We consider a stretching (planar) viscous filament, as illustrated in Figure 1. A quantity of viscous liquid is initially held between two stationary plates, the top plate is then impulsively pulled perpendicularly away from the bottom

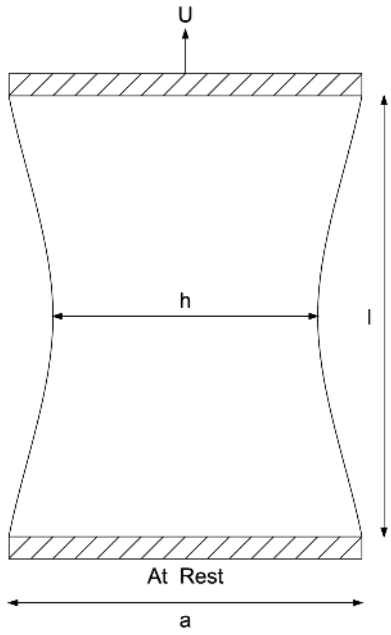

Figure 1.
The stretching of a (planar) viscous fluid filament

plate with a constant velocity U. Perfect adherence is assumed between the liquid and the plates and consequently the filament thins most in its central region. Stretching filament devices are used in experiments to test the extensional properties of polymers, and numerical simulations of viscoelastic fluids often use the stretching filament as a benchmark problem, eg Harlen, (1996). In the present study inertia effects are assumed to be small ($\mathrm{Re} = \rho Ua/\mu$ is given a value of 10^{-2}), furthermore, gravity, which serves to create a top-bottom asymmetry in the filament, and surface tension, which causes an extra squeezing effect in the middle of the filament, are both neglected. On the plates two no-slip velocity boundary conditions are specified, and the free surface normal stress balance reduces to:

$$\hat{\underline{n}} \cdot \underline{\underline{\sigma}} = \underline{0}. \tag{14}$$

For simplicity the fluid filament is assumed to have an initially square shape (with $l/a = 1.0$), Figure 2 shows the initial finite element mesh containing 200 elements. As the simulation proceeds and the filament stretches the number of horizontal element strips is increased automatically during remeshing so that the free surface representation retains a specified level of refinement. Nodes are equally spaced along the free surfaces, resulting in more element strips in the regions of high curvature adjacent to the plates. Figure 3 shows the finite element mesh and the velocity vectors when the aspect ratio is 3.5 and the fluid

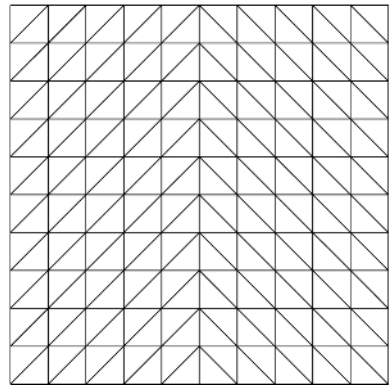

Figure 2.
Initial finite element mesh

has undergone considerable deformation; the simulation can be continued without difficulty until the filament becomes very thin and problems of mesh resolution are eventually encountered. The mesh shown contains 416 elements – more than double the initial number. The calculated change in volume for this simulation is negligible, and the filament is found to be top-bottom symmetric as predicted in the absence of gravity.

The velocity vectors shown in Figure 3(b) are scaled with respect to the speed of the top plate; the fluid motion is essentially unidirectional and the velocities increase linearly with length along the filament.

Figure 4 gives the minimum filament thickness, h_{min}, as a function of time – quantities being non-dimensionalised using a and U as typical scales. Initially h_{min} decreases quite rapidly but the rate of thinning gradually slows. One may obtain a simple analytical expression for the evolving free surface position by assuming that the filament thickness is approximately constant except in the regions very close to the plates (as suggested by Figure 3). In this case we assume h is independent of length along the filament, i.e. $h = h(t)$, then conservation of mass yields the following:

$$h\frac{\partial u}{\partial x} + \frac{\mathrm{d}h}{\mathrm{d}t} = 0, \tag{15}$$

where the velocity u is a function of length along the filament, x, and time. Taking the plate velocities as approximate conditions on u, imposed at some unspecified positions "close to the plates", and taking the initially square domain shape as an initial condition on h, the above equation may be integrated to give

$$h = \frac{1}{1+t}. \tag{16}$$

This expression is also plotted in Figure 4 where happily the agreement for the sheet thinning between the simple analytical (ANAL) and numerical (FEM)

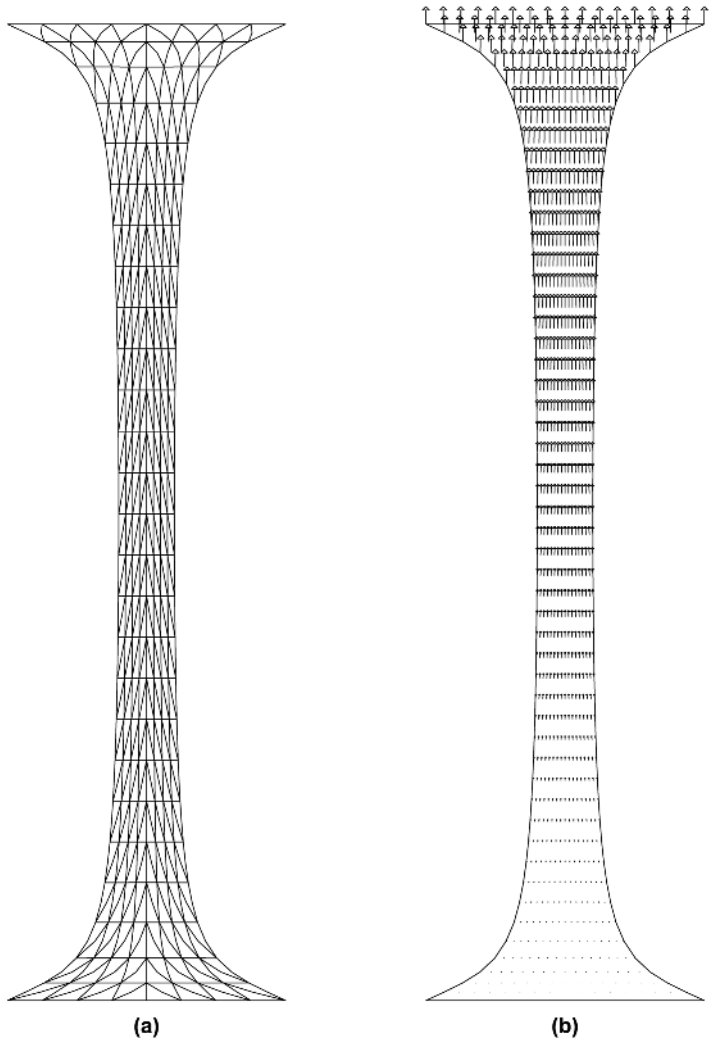

Figure 3.
Result of filament stretching simulation when $l/a = 3.5$: (a) finite element mesh, (b) velocity vectors

curves is pretty close. Of course, the difference between the two curves occurs because the simple analytical model takes no account of the regions of high meniscus curvature at the plates and hence cannot predict the sheet thinning exactly.

3.2 Printing liquid from a trapezoidal cavity

Here the Lagrangian finite element algorithm is employed to simulate the idealized 2-D transfer process, involving a Newtonian fluid pulled from an upturned trapezoidal trench (which may be thought of as a 3-D cavity with a large transverse aspect ratio) by a downwards moving substrate. The

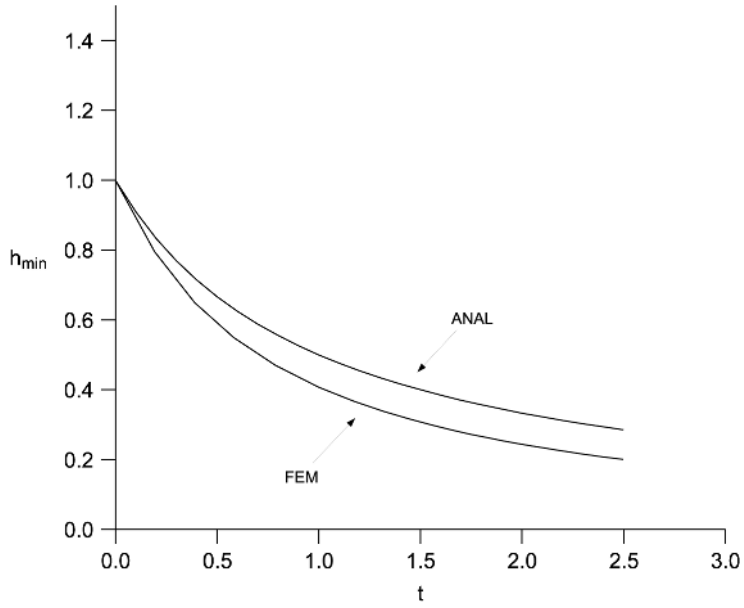

Figure 4.
The minimum filament thickness as a function of time calculated numerically (FEM); also plotted is the approximate analytical expression $h_{\min} = 1/1 + t$ (ANAL)

trapezoidal design is commonly used in printing industries and so has been chosen as a representative cavity for this problem. In our model (see Figure 5) we initially assume the presence beneath the cavity of a liquid layer bounded by two vertical free surfaces to overcome the significant theoretical difficulties that are introduced if the cavity and substrate are initially in contact. The lower surface is impulsively pulled downwards with constant speed U and the liquid is set in motion subject to the following assumptions:

(1) There is perfect adherence between the liquid and the moving surface on which there are two "static" contact lines. In real applications there will possibly be some amount of slippage between liquid and solid at the

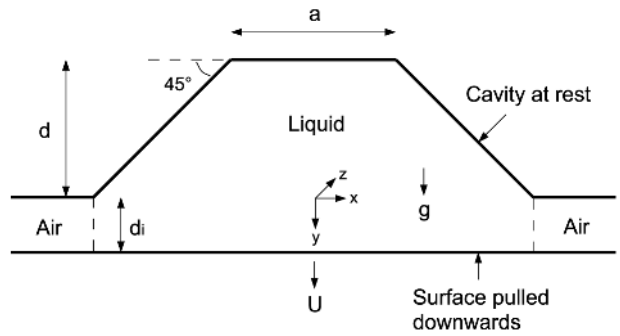

Figure 5.
Cross-section of the trapezoidal trench at $t = 0$.

contact lines, though in practice substrates are suitably prepared so that the printed liquids tend to adhere to them.

(2) Here exists local slip between the liquid and the trapezoidal cavity walls at two dynamic contact lines – the specific modelling of which is discussed below.

(3) Away from the edges of the trench the liquid motion is approximately independent of the transverse coordinate z, up to the time when a thin viscous sheet is formed, connecting liquid remaining in the trench to that on the downward moving surface. The computation is terminated when the minimum sheet thickness falls below a specified tolerance, prior to which it is assumed that the influence of transverse edge effects and the formation of instabilities can both be ignored within the main body of the sheet.

Taking the speed of the lower surface, U, and the cavity depth, d, as typical scales, then for a Newtonian fluid with viscosity μ, density ρ and surface tension τ, non-dimensionalising the problem introduces the following groups: $\mathrm{Re} = \rho U d/\mu$, $\mathrm{Ca} = \mu U/\tau$, and $\mathrm{St} = \rho g d^2/\mu U$. To incorporate the dynamic contact lines we specify:

(1) an explicit linear slip velocity distribution, introducing an unknown slip length, l, which must be estimated;

(2) a constant dynamic contact angle, θ_D (measured through the fluid).

Thus the contact lines are allowed to move along the sloped cavity walls, though they are assumed to re-pin if they reach the bottom corners of the cavity. There are, of course, a variety of possibilities for the dynamic contact line treatment. In the absence of any experimental visualisations of micro-scale cell emptying in printing processes we chose a straightforward constant angle model, though it would not be difficult to refine the modeling in light of experimental input at a later time (see Powell and Savage, (2001) for example).

Figure 6 shows the evolving liquid domain for a sample calculation in which the following parameter values were used: $a/d = 1.0$, $\mathrm{St} = 0.1$, $\mathrm{Ca} = 0.1$, $\mathrm{Re} = 1.0$, $\theta_D = 75°$. In the early stages of the motion the menisci become highly curved and the effect of surface tension appears to dominate. As the liquid domain extends the gravitational acceleration has more of an effect, the liquid being forced downwards out of the cavity and into the sheet. In the later stages of the simulation a thin liquid sheet forms, connecting the fluid that remains in the cavity to a "sessile" drop forming on the moving surface. In this calculation the contact lines do in fact reach the base of the cavity where it is assumed that they re-pin. The simulation is terminated when the minimum sheet thickness falls below 0.1, this is an arbitrary stopping point when it is possible to obtain an estimate of the fraction of the initial liquid in the large sessile drop by calculating the fraction below the minimum sheet (or "neck")

location – though it should be noted that the algorithm may in fact be continued without trouble until the sheet is much thinner. For this sample calculation approximately 93 per cent of the liquid lies below the neck when the simulation is terminated.

Two snapshots of the computational mesh and velocity vectors, taken at times $t = 0.072$ and $t = 2.3$, are shown in Figure 7. The mesh pictures illustrate how a structured strategy using horizontal strips of elements is able to effectively discretise the liquid domain from start-up through to the later stages of the motion. Local mesh refinement is included in the dynamic contact line regions in order to accurately resolve the velocity field. At $t = 2.3$, when the contact lines have re-pinned at the cavity base and the rounded sessile drop is well formed, the mesh shown is constructed by equally spacing the nodes along the free surface. This naturally results in a greater number of element strips in the regions of rapidly changing velocity adjacent to the cavity base and where the sheet opens out into the sessile drop. Furthermore, since each horizontal element strip contains the same number of elements, we achieve a much higher mesh refinement in the thin sheet region. The corresponding velocity plot at $t = 2.3$ shows that gravity is indeed the dominant effect in the later stages of the simulation, with the highest velocities generated as fluid is forced downwards through the neck region and into the drop. We note that simulations are restricted to cases where θ_D is strictly greater than 45°, since the use of horizontal element strips in the discretisation cannot cope with free surfaces that become multi-valued functions of the vertical coordinate, y. Of course, if subsequent visualization experiments point to much smaller values of the contact angle then a modified, more general meshing strategy can be

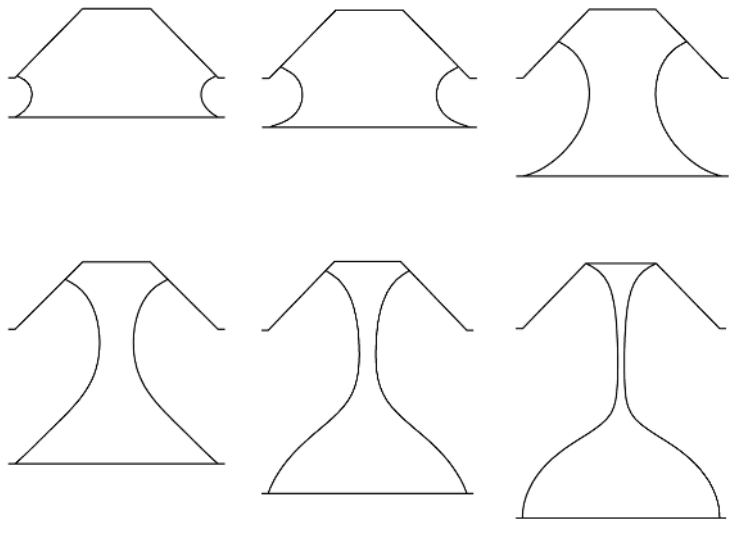

Figure 6.
Result of simulation performed with the following parameters: $a/d = 1.0$, $\theta_D = 75°$, $\mathrm{Re} = 1.0$, $\mathrm{Ca} = 0.1$, $\mathrm{St} = 0.1$; the evolving liquid domain is shown at six different times: $t = 0.072$, 0.215, 0.931, 1.498, 1.868, 2.3

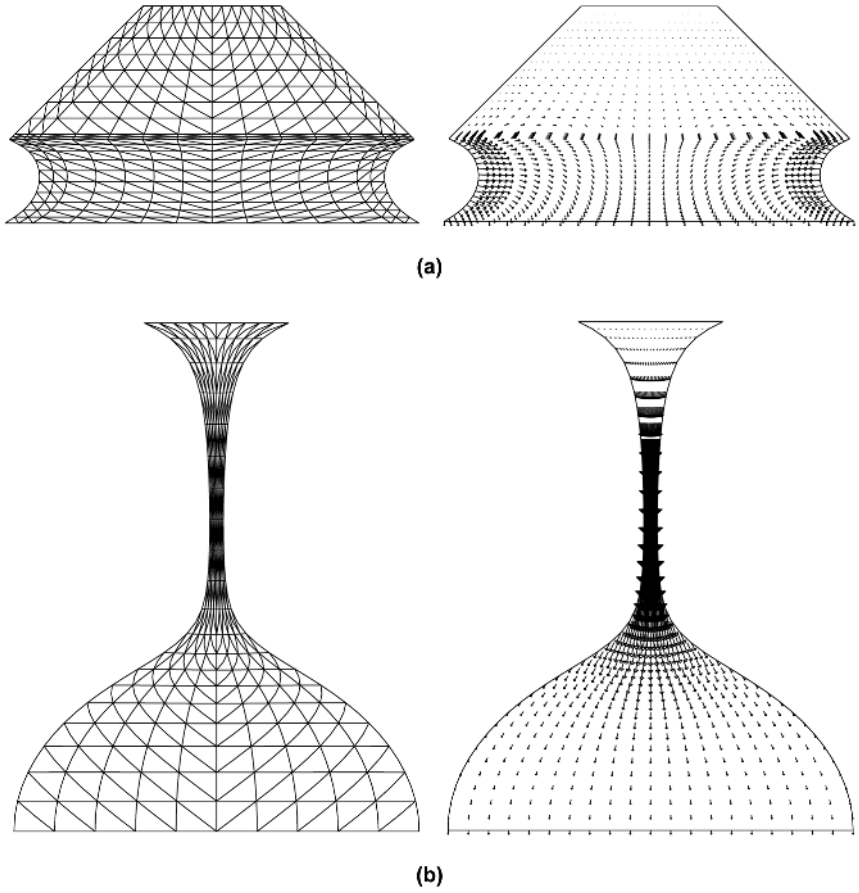

Figure 7.
Computational mesh and velocity vectors shown at times (a) $t = 0.072$ and (b) $t = 2.3$

implemented into the Lagrangian algorithm. Mesh resolution studies have been conducted to determine levels of refinement resulting in mesh independent results; at the point when a simulation is terminated a suitable mesh typically contains around 600 elements.

Figure 8 shows the minimum sheet thickness as a function of time for the same simulation. In the early stages of the liquid motion the rate of domain thinning is large, but this rate gradually slows as the sheet forms and continues to stretch. It is not possible to determine if the thin sheet is close to rupture since there is no large negative gradient on the curve; indeed this suggests that at later times any sheet rupture will be three-dimensional in nature.

To demonstrate the predictive use of our algorithm to industrialists and experimentalists seeking to control their liquid transfer process, the effect of varying the separation speed of the substrate is explored. Denoting a reference

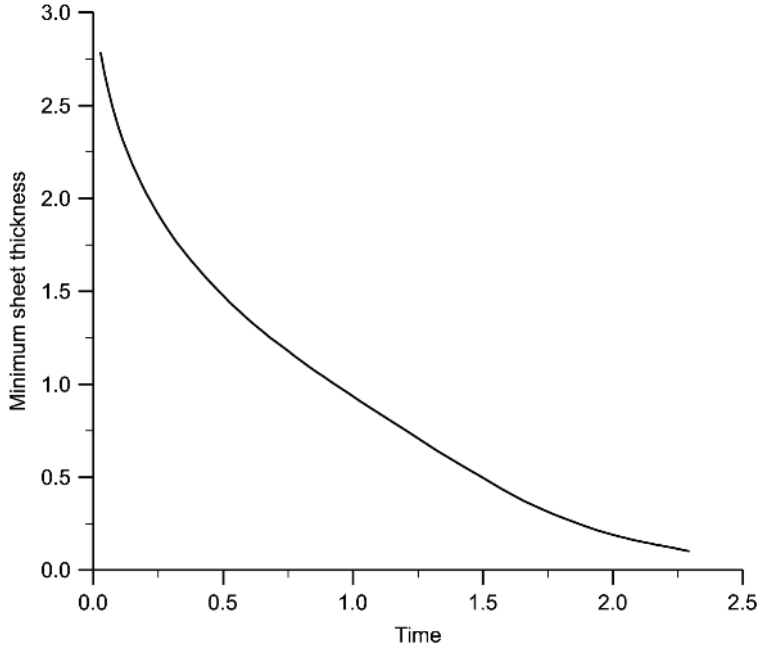

Figure 8.
Minimum sheet thickness versus time for the sample calculation

substrate speed by U^* which gives Reynolds, Stokes and capillary numbers (Re*, St*, Ca*) say, then changing the speed to $U = nU^*$ changes the dimensionless groups to (nRe*, St*/n, nCa^*). Here it is assumed that U^* leads to the following group values: Re* = 1.0, St* = 0.1 and Ca* = 0.1 (with $a/d = 1.0$ and $\theta_D = 75°$), and the effects of halving and doubling the separation speed by taking n equal to 0.5 and 2, respectively, are considered. It is immediately clear from Figure 9(a), which compares liquid domains when the minimum sheet thickness falls below 0.1, that increasing U/U^* from 0.5 to 2.0 leads to:

- a significant lengthening of the "final" fluid domain,
- a longer thin sheet region and
- a corresponding decrease in the fraction of liquid in the sessile drop.

These trends are quantified in Figures 9(b), which plots the final distance from cavity to substrate, and 9(c), which gives the fraction of liquid lying below the neck. The shortest limiting domain length and largest sessile drop fraction (when approximately 94 per cent of the liquid lies below the neck) occur at the lowest separation speed, which is in accord with intuition since the gravity-driven cavity emptying has more time to occur than at a higher substrate speed. This suggests that one may control the approximate sessile drop size to a certain extent by simply varying the substrate speed, but a high speeds the creation of a long thin sheet prior to rupture may be an undesirable side-effect.

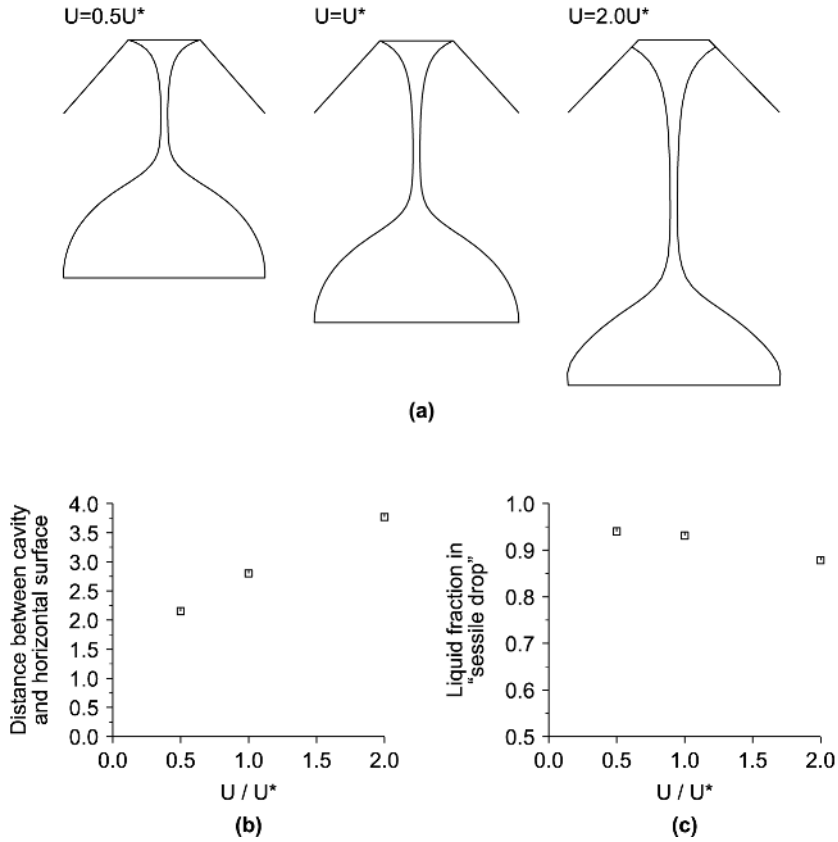

Figure 9.
The effect of U/U^* upon the cavity emptying process (U^* denoting a reference substrate speed – see text): (a) "final" liquid domain profiles, (b) "final" distance from top of cavity to moving substrate, (c) approximate final liquid fraction in "sessile drop"

4. Conclusion

A Lagrangian finite element algorithm for solving time-dependent free surface flows, which uses a structured meshing strategy to allow for large free surface deformations, has been described and successfully applied to both a stretching filament and a model printing problem. We stress that the cavity emptying work presented here constitutes a first step towards simulating and understanding the (fully three-dimensional) micro-scale liquid transfer phenomena occurring in a range of industrial printing processes. Numerous extensions to the present work are underway, including:

- introduction of an asymmetric separation between the cavity and substrate to account for a roll-based printing configuration such as gravure printing
- incorporation of non-Newtonian rheology to model more realistically the types of inks used in printing processes

- consideration of process instabilities that occur due to imperfect cell filling prior to printing.

An experimental program into the micro-scale printing of liquid from engraved cells under different conditions is currently underway at the University of Leeds. It is intended to report some of the experimental results together with complementary numerical simulations in a future publication.

Note

1. Details of the individual contributions to the matrices M, C and F are given in numerous papers, see, for example, ref (Bach and Villadsen, 1984).

References

Bach, P. and Hassager, O. (1985), "An algorithm for the use of the Lagrangian specification in Newtonian fluid mechanics and applications to free-surface flow", *J. Fluid Mech.*, 152, pp. 173-90.

Bach, P. and Villadsen, J. (1984), "Simulation of the vertical flow of a thin, wavy film using a finite-element method", *Int. J. Heat Mass Transfer*, 27 No. 6, pp. 815-27.

Benkreira, H. and Patel, R. (1993), "Direct gravure roll coating", *Chem. Eng. Sci.*, 48, pp. 2329-35.

Bohan, M.F.J., Claypole, T.C. and Gethin, D.T. (2000), "The effect of process parameters on product quality of rotogravure printing", *Proc. Inst. Mech. Eng. Part B.*, 214 No. 3, pp. 205-19.

Collard, G. (1984), "Pad-transfer printing – taking a new look", *Plastics Engineering*, 40 No. 2, pp. 49-50.

Dussan, V.E.B. (1976), "The moving contact line: the slip boundary condition", *J. Fluid Mech.*, 77 No. 4, pp. 665-84.

Greenspan, H.P. (1978), "On the motion of a small viscous droplet that wets a surface", *J. Fluid Mech.*, 84 No. 1, pp. 125-43.

Guthrie, J.T. (1992), "The physical-chemical and philosophical aspects of screen printing processes", *JOCCA-Surface Coatings International*, 75 No. 3, pp. 94-6.

Harlen, O.G. (1996), "Simulation of viscoelastic flows", in, *First European Coating Symposium On The Mechanics Of Thin Film Coatings*, World Scientific, Singapore pp. 366-74.

Hocking, L.M. (1994), "The spreading of drops with intermolecular forces", *Phys. Fluids*, 6, pp. 3224-8.

Hood, P. (1976), "Frontal solution program for unsymmetric matrices", *Int. J. Numer. Meth. Engng.*, 10, pp. 379-99.

Joe, B. (1991), "GEOMPACK – a software package for the generation of meshes using geometric algorithms", *Adv. Eng. Software*, 13 No. 5–6, pp. 325-31.

Kunz, W. (1983), "Interactions between materials involved in gravure printing", *Wochenblatt Fur Papierfabrikation*, 111 No. 6, pp. 1922-2.

Mock, G.N. (1999), "The development of rotary-screen printing", *Textile Chemist and Colorist & American Dyestuff Reporter*, 1 No. 3, pp. 43-9.

Muttin, F., Coupez, T., Bellet, M. and Chenot, J.L. (1993), "Lagrangian finite element analysis of time-dependent viscous free-surface flow using an automatic remeshing technique: application to metal casting flow", *Int. J. Numer. Meth. Engng.*, 36, pp. 2001-15.

Powell, C.A. and Savage, M.D. (2001), "Numerical simulation of transient free surface flow with moving contact lines", *Commun. Numer. Meth. Engng.*, 17, pp. 581-8.

Piette, P., Morin, V. and Maume, J.P. (1997), "Industrial-scale rotogravure printing tests", *Wochenblatt Fur Papierfabrikation*, 125 No. 16, pp. 744.

Powell, C.A., Savage, M.D. and Gaskell, P.H. (2000), "Modelling the meniscus evacuation problem in direct gravure coating", *Trans. Inst. Chem. Eng.*, 78 No. A, pp. 61-7.

Rebay, S. (1993), "Efficient unstructured mesh generation by means of Delaunay triangulation and Bowyer-Watson algorithm", *J. Compute. Phys.*, 105, pp. 125-38.

Ruschak, K.J. (1980), "A method for incorporating free boundaries with surface tension in finite element fluid flow simulators", *Int. J. Numer. Meth. Engng.*, 15, pp. 639-48.

Radovitzky, R. and Ortiz, M. (1998), "Lagrangian finite element analysis of Newtonian fluid flows", *Int. J. Numer. Meth. Engng.*, 43, pp. 607-19.

Ramaswamy, B., Kawahara, M. and Nakayama, T. (1986), "Lagrangian finite element method for the analysis of two-dimensional sloshing problems", *Int. J. Numer. Meth. Fluids*, 6, pp. 659-70.

Shephard, M.S. (1988), "Approaches to the automatic generation and control of finite element meshes", *Appl. Mech. Rev.*, 41 No. 4, pp. 169-85.

Shikhmurzaev, Y.D. (1997), "Moving contact lines in liquid/liquid/solid systems", *J. Fluid Mech.*, 334, pp. 211-49.

Schwartz, L.W., Moussalli, P., Campbell, P. and Eley, R.R. (1998), "Numerical modeling of liquid withdrawal from gravure cavities in coating operations", *Trans. Inst. Chem. Eng.*, 76 No. A, pp. 22-9.

Taylor, C. and Hood, P. (1973), "A numerical solution of the Navier-Stokes equations using the finite element technique", *Computers and Fluids*, 1, pp. 73-100.

Wilkes, E.D., Phillips, S.D. and Basaran, O.A. (1999), "Computational and experimental analysis of dynamics of drop formation", *Phys. Fluids*, 11 No. 12, pp. 3577-98.

Zhang, X. (1999), "Dynamics of drop formation in viscous flows", *Chem. Eng. Sci.*, 54, pp. 1759-74.

Zienkiewicz, O.C. (1977), *The finite element method*, McGraw-Hill.

The application of roughness model to a soft EHL contact

M.F.J. Bohan, T.C. Claypole and D.T. Gethin
Department of Mechanical Engineering, University of Wales, Swansea

Keywords *Surface roughness, Fluid flow, Lubrication*

Abstract *The study focuses on the development of a numerical model to explore the impact of surface roughness in soft rolling nip contacts, including representation of a real surface. The solution of the governing equations required the application of a multigridding technique to capture the details of the fluid flow within the roughness wavelengths and a minimum number of fluid nodes per wavelength were established. In the case studies, two extreme roughness profiles were considered, longitudinal and circumferential. The longitudinal roughness had a significant impact on nip pressures and pumping capacity, the latter being determined by the minimum film thickness in the nip. The circumferential roughness was found to have a localised effect on film pressure, but only a very small impact on the film thickness profile. The consequent effect on pumping capacity was small.*

Nomenclature

a = Hertzian contact width
b_k = body forces within boundary domain
c^i_{lk} = corner factor for the boundary integral equation
E^* = equivalent elastic modulus
g = fundamental solution of Reynolds equation
h = fluid film thickness
L = load
p = fluid pressure
p_k = traction for the boundary integral equation
p^*_{lk} = traction for Kelvin solution
p_n = fluid pressure at point x_n
R = equivalent roller radius
r_a = roughness amplitude
r_f = roughness frequency
r_p = roughness phase
U = mean sum of the roller surface velocities
u = surface indentation
u_k = displacement for the boundary integral equation
u^*_{lk} = displacement for Kelvin solution
v_n = pressure gradient dp/dx at point x_n
x = co-ordinate for film
Γ = boundary surface
δ = Dirac delta function
ζ = point on the boundary
μ = fluid viscosity
ψ = term within the Reynolds equation
Ω = boundary domain

Introduction

The transfer of a fluid to a substrate in a controlled manner is used in many industrial applications. This is often achieved by the use of alternate hard and rubber covered rollers, Figure 1 and these will operate under conditions ranging from pure rolling to pure sliding dependent on the process. In certain instances a simultaneous lateral motion of the rollers is also employed. In many designs, the systems are used with positive engagements, imposing the

International Journal of Numerical Methods for Heat & Fluid Flow, Vol. 12 No. 4, 2002, pp. 356-374.

DOI 10.1108/09615530210433260

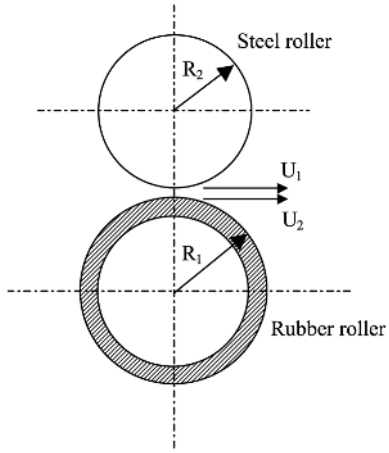

Figure 1.
Schematic of a roller contact

requirement to use a roller covered with a soft rubber and the consequent pressures generated in the nip contact result in significant rubber deformations.

Pressure is generated in the nip by mechanical deformation and hydrodynamic action as the fluid is entrained through the contact. This pressure field developed by this combined action will lead to the deformation of the elastomeric layer and this deformation will affect the film thickness and hence the hydrodynamic pressure component in the nip contact. This contact is referred to as that of Soft Elasto Hydrodynamic Lubrication (Soft EHL) and since the rollers are usually long in comparison with diameter and especially the contact geometry, this effectively forms a line contact.

The emphasis in this paper is concerned with roughness effects in soft EHL contacts, however it is appropriate to review briefly previous work on smooth contacts and this will be dealt with initially. The experimental and numerical analyses of nips have been reported on extensively in the literature. Initial work on dry contacts (Hannah, 1951) has formed the basis of much of this analysis. The methods have been expanded to evaluate boundary conditions (Miller, 1966) and the roller parameters (Meijer, 1968; Jaffar, 1993). The lubrication of layered contacts was first explored in the field of journal bearings (Higgson, 1965–1966) and this was later generalised to contacts with different surfaces in which only small deformations were present (Bennett and Higginson, 1970). The general treatment of large deformation is counterformal contacts is discussed in Hooke and O'Donoghue, 1972. It is assumed that pressure in the nip is dominated by a Hertzian component and separate functions are used to describe the inlet and outlet regions. This was later extended to layered solids (Gupta, 1976), including developments to accommodate a Poissons ratio of 0.5 that is appropriate for rubber and normally introduces a singularity into the

governing elasticity equations. The model was used to explore a wide range of loading conditions.

In many of the preceding works, the linkage between deformation and hydrodynamic action was excluded since the contacts were either dry, or heavily loaded with emphasis on transmissions or rolling element bearing application. The necessity to iterate between the fluid and structural domains was first highlighted in Cudworth, 1979 with specific emphasis on a soft EHL analysis. This has since been developed to evaluate different modes of lubrication dependent on the nip conditions (Hooke, 1986). These have then been further extended to different inlet and process conditions for Newtonian (MacPhee *et al.*, 1992; Bohan *et al.*, 1997) and non-Newtonian fluids (Lim *et al.*, 1996).

All the work reviewed above assumes that the roller surfaces are smooth. One of the first approaches to modelling rough lubricated contacts is set out in Patir and Cheng, 1978 where the authors describe a model where flow coefficients are introduced into the Reynolds equation to capture both isotropic and anisotropic surfaces, idealised using a Gaussian distribution and incorporating anisotropy via a length scale. This approach is particularly applicable in hydrodynamic lubrication, or under circumstances where piezoviscous fluids are not used and the usual pressure term in the Reynolds equation is still significant. Some controversy surrounds the determination of the coefficients that capture the surface geometry, particularly where the film thickness gradients associated with asperities are steep. This has received attention recently in Lunde and Tønder, 1997 in which the authors examine a patch within a bearing film, but use the Reynolds equation to approximate the flow. Subject to the local application of the Reynolds equation, this allowed a calculation of pressure fluctuation details in response to the local asperity profile and the distribution was superimposed on an average pressure generated from the mean film profile.

Surface roughness studies in contacts between hard counter-formal surfaces has focused on nips lubricated by fluids that exhibit a strong piezoviscous behaviour and this has been coupled with elastic deformation of the contact. The consequent high viscosity in the denominator of the pressure term in the Reynolds equation effectively removes this term from the equation. This modelling approach has been explored vigorously recently, mainly in connection with gear and rolling element contacts (Hooke, 1999; Greenwood, 1999). These studies develop models focusing on transport of roughness through the contact, leading to pressure waves and roughness waves of different frequency moving through the contact under circumstances of sliding motion. Under conditions of rolling motion, the original roughness profile is retained and the pressure profile reflects the local film thickness variations.

An up to date review of work in hard elastohydrodynamic lubrication is set out in Dowson and Ehret, 1999 in which the authors have critically examined

key studies chronicling the developments in this area, culminating in work on real surfaces and real lubricants. The present study also addresses this topic, but with specific application to soft elastohydrodynamic contacts in which the deformations are large and the viscosity remains low. Therefore the roughness transport models are not appropriate and the film model will need to account for pressure terms as well as the surface topography.

The purpose of this paper is to evaluate high frequency roughness profiles in a computationally efficient manner. It will to explore the effect of both circumferential and longitudinal roughness profiles on the roller. The applicability of the idealised sinusoidal roughness as an approximation to the real roughness profiles will also be assessed.

Theoretical model background

The overall solution of the soft elastohydrodynamic lubrication problem that is generic to many printing and coating applications is obtained by coupling the solutions from the Reynolds equation with that of the elastic deformation of the roller. Following the review of previous work, this requires a procedure that iterates between the solutions for the structural and fluid domains. Of particular importance to this study is the background theory for solution, with the introduction of roughness characteristics. This will be discussed, followed by its incorporation into the solution procedure.

Reynolds equation

For a Newtonian fluid and a thin film the Reynolds equation may be used to describe the hydrodynamic behaviour in the nip (Dowson, 1962). Provided that the contact width is small in comparison with the roller diameter and the analysis plane is some distance from the roller edge then the Reynolds equation can be written in a one-dimensional form as

$$\frac{d}{dx}\left[\frac{h^3}{12\mu}\frac{dp}{dx}\right] = \left(\frac{u_1 + u_2}{2}\right)\frac{dh}{dx} \tag{1}$$

The assumption of a Newtonian fluid is retained in this work and this is shared with many other publications (MacPhee *et al.*, 1992; Bohan *et al.*, 1997). Some printing inks are non-Newtonian and this can affect the flow characteristics (Lim *et al.*, 1996), however this will be described in a separate investigation. In this solution, the pressure at the inlet and outlet were set to zero together with the pressure gradient, satisfying a well-established Swift-Steiber condition. This was set automatically within the code and it effectively determines the rupture point in the contact to ensure flow continuity. However this condition ignores the possible occurrence of sub-ambient pressures (Lim *et al.*, 1996) that may be treated using an approach balancing viscous and surface tension forces (Carvalho and Scriven, 1997). The choice of the simpler Swift-Steiber condition is justified at this point since this work focuses on the inclusion of roughness

effects, treatment of different film boundary conditions in association with roughness effects will require further detailed attention.

For the purpose of computational efficiency, the Reynolds equation was solved using Green's function with the right hand side of equation (1) replaced by the Dirac delta function $\delta(x-\zeta)$. The solution can be obtained using the following for $g(x,\zeta)$ and its differential, where $h^* = h^3$.

$$g(x,\zeta) = \begin{cases} \int_{\zeta}^{x} \frac{1}{2h^*} dx \ \ for\, \zeta > x \\ -\int_{\zeta}^{x} \frac{1}{2h^*} dx \ \ for\, \zeta < x \end{cases}, \quad \frac{dg(x,\zeta)}{dx} = \begin{cases} \frac{1}{2h^*} \ \ for\, \zeta > x \\ -\frac{1}{2h^*} \ \ for\, \zeta < x \end{cases} \tag{2}$$

Using equation (2) and the Dirac function, the Reynolds equation (1) can be solved providing the following expression for the pressure

$$\begin{aligned} p(\zeta) = {} & [-h^*(x_1)g(x_1,\zeta), h^*(x_2)g(x_2,\zeta)] \begin{bmatrix} v_1 \\ v_2 \end{bmatrix} \\ & + \left[h^*(x_1)\frac{dg}{dx}\Big|_{x=x_1}, -h^*(x_2)\frac{dg}{dx}\Big|_{x=x_2} \right] \begin{bmatrix} p_1 \\ p_2 \end{bmatrix} + \int_{x_1}^{x_2} \psi(x) \cdot g(x,\zeta) dx \end{aligned} \tag{3}$$

Elasticity equations

A number of schemes are available for solving the elasticity equations in the rubber layer. Since deformation is the main focus in this application, this is achieved most economically using a boundary element approach. Assuming the rubber layer on the roller to be linearly elastic due to the relatively small deformation in comparison with its thickness, for a plain strain case, the boundary element integral equation for the solution of the general problem of elastostatics is given below (Brebbia and Dominguez, 1989).

$$c^i_{lk} u^i_k + \int_{\Gamma} p^*_{lk} u_k \, d\Gamma = \int_{\Gamma} u^*_{lk} p_k \, d\Gamma + \int_{\Omega} u^*_{lk} b_k \, d\Omega \tag{4}$$

However, for the problem examined, the body forces are zero, with no thermal or gravitational forces and the equation can be simplified to

$$c^i_{lk} u^i_k + \int_{\Gamma} p^*_{lk} u_k \, d\Gamma = \int_{\Gamma} u^*_{lk} p_k \, d\Gamma \tag{5}$$

This equation can be formulated as a matrix and solved readily for the displacement of the rubber layer. The integrals of the elasticity equation were calculated over the boundary and represented by the sum of integrals over each

of the boundary elements. The element integrals were calculated analytically to ensure computational efficiency. In the model, compatible with the assumption for the film, the elastomer was unwrapped as shown in Figure 2. The lower surface was constrained rigidly to represent adhesion between the steel core and rubber cover and no circumferential movement was allowed at the lateral extremes of the calculation domain.

Film thickness equation

The film thickness is defined by equation (6). The roller roughness is incorporated into this together with the deformation due to the roller loads and a negative value of h_0 represents roller engagement.

$$h(x) = h_0 + \frac{x^2}{2R} + u(x) + r(x) \tag{6}$$

In equation (6), $r(x)$ is the roughness applied to the surface of the roller. This can be defined either as a regular roughness profile or actual measured data can be incorporated as a function of distance through the nip. Within the paper both methods have been employed and their impact investigated. When treated as a function, the roughness profile is given by the equation

$$r(x) = \frac{r_a}{2} \cdot \sin(r_f(x) + r_b) \tag{7}$$

For the actual roughness data a look up table has been generated at the correct nodal intervals based on experimentally measured surfaces and the roughness obtained from an array, given as

$$r(x) = r_m(x) \tag{8}$$

In utilising the approach set out above, it is assumed that the amplitude and wavelength of the roughness is not sufficient to generate localised reverse flows within the asperity zone itself (Lunde and Tønder, 1997). If this occurs, then it can only be dealt with accurately via solution of the Navier Stokes equations and this is computationally prohibitive at this time.

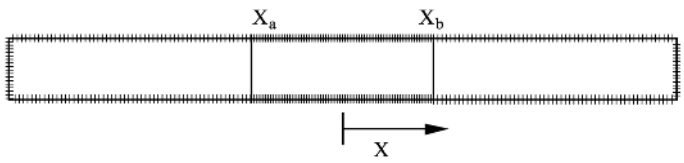

Figure 2.
Schematic discretisation of the boundary

Load

To reflect operation, the rollers are forced into engagement at a pre set level of load. This was embodied in the model and closure of the solution was obtained by the load meeting the following criterion

$$\int_{x_1}^{x_2} p \cdot dx = L \tag{9}$$

Solution procedure

Calculations have been carried out for a rolling nip contact since this is free from the additional complication of roughness and pressure waves travelling through the nip as discussed in Hooke, 1999; Greenwood, 1999. Where sliding is present, coupled with longitudinal roughness, the asperity on the rubber roller surface is likely to be deformed and it will tend to a smoother surface, however this is excluded from the current investigation. However, prior to this investigation, the local deformation of the roughness profile when subjected to a pure pressure loading was analysed using commercial finite element analysis software. The roughness profile was entered as a sinusoidal function based on data obtained from white light interferometry measurements of actual surface roughness profiles from which indications of wavelength and amplitude were derived. Pressure levels were used from experimental data on smooth rollers (Lim *et al.*, 1996) and the material properties of the rubber were determined experimentally. The variables investigated using this system were the mean rubber thickness, pressure, roughness amplitude and the roughness frequency.

In all the models, load was applied to the waveform surface such that the pressure was normal to the rubber surface. For the section considered, the sides of the rubber were constrained in only the X direction allowing for compression, while the base was fixed in both X and Y as they are bonded to a metal core.

Typical displacements computed suggest a change in the profile of 0.5 μm for a roughness depth of 50 μm, the maximum percentage change in the profile height for all the model cases was 1 per cent, essentially capturing the near incompressible rubber property. The analysis shows that for the rubber covering materials and surface profiles used within printing and roller coating applications in which there is a near pure rolling action, the use of a fixed roughness profile is applicable. For further details refer to Bohan *et al.*, 2001.

Compatible with the derivation set out above, within the current approximation an equivalent radius approach was used and the elastomer was unwrapped as shown in Figure 2 where the boundary of the elastomer is subdivided into a number of elements. The equivalent radius approach is appropriate for narrow contact widths and has been shown not to significantly affect the results (Dowson and Higginson, 1959). From the elastomer mesh the fluid domain is applied over the nip contact, $X\mathrm{s}_\mathrm{a}$ to X_b. Since this is sufficiently

remote from the extreme ends of the elastomer, this will eliminate the effect of structural boundary conditions on the simulation of this local fluid structure interaction.

Numerical singularities can occur when a field point ζ_0 is located at a node where the integration takes place. These can be eliminated with the use of corner factors and the techniques are indicated in Brebbia and Dominguez, 1989; Banerjee and Butterfield, 1981.

Consistent with the elastomer mesh, the fluid domain was solved over the nip contact, X_a to X_b. Since this solution strategy accounts for roughness directly by modification of the film thickness profile, the Reynolds equation was solved within the scale of the roughness profile. The interaction with the elastomer was then applied directly via local integration of the pressure field and assigning the resultant force to the adjacent node on the elastomer surface. This may include the data from multiple roughness wavelengths, Figure 3. To achieve an accurate solution, the divisions for the pressure equation solution must be appropriate for the roughness profile wavelength. This effectively leads to a multi grid solution strategy and the sensitivity with respect to this strategy will be explored within the initial numerical studies.

The solution of soft EHL contacts is particularly troublesome due to the large deformation of the elastomer in response to the pressure field and this can lead to large and diverging oscillation (Lim *et al.*, 1996). Following extensive previous development a stable strategy to handle this coupled system has been established as

(1) Assign mesh division and calculate the roughness frequency; recalculate the mesh division if the required nodal sub division is not appropriate.

(2) Set an initial value for the engagement, h_0, from this the Hertzian pressure and the consequent deformation is calculated.

(3) Calculate the film thickness in the nip junction.

(4) Calculate the film pressure.

(5) Recalculate the deformation.

(6) If the deformation has not met the convergence criterion, then repeat from stage (3) with the new deformation.

(7) Once the deformation criterion has been met, examine the load equilibrium. If this is not met then appoint a new value for h_0 and repeat from (2).

The convergence requirement for the analysis was set to be 0.1 per cent on the pressure and indentation, with a minimum number of elements within the roughness wavelength being 36. Overall solution convergence was generally obtained within 500 iterations.

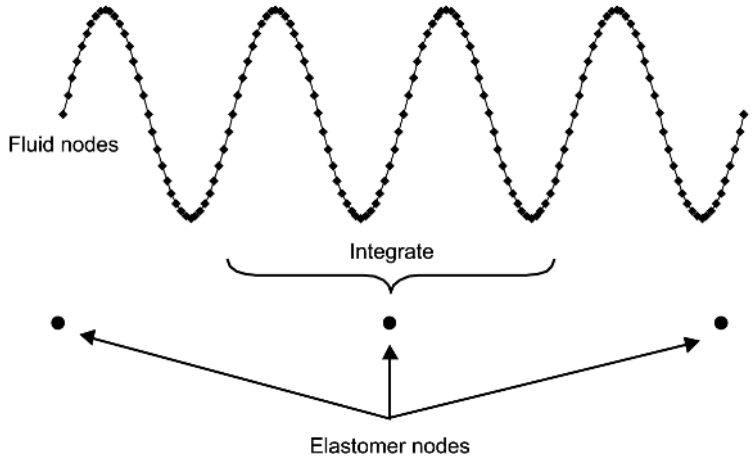

Figure 3.
Discretisation of the fluid regime and connectivity to the elastomer nodes

Sensitivity of surface parameters on the behaviour in the nip

For the purposes of the analysis, a typical industrial printing configuration was chosen and the relevant details are, shown in Table I. They relate to press geometry and the material parameters and guidance on roughness parameters has been derived from measurements. These have been used to show the influence of roller surface roughness on the pressure profile, film thickness and fluid flow rate through the nip. The latter is a main concern in printing and coating application and this is in contrast with hard nip contacts where pressure and film thickness is the focus of attention.

Roughness on the roller surface can be described in extreme circumstances as either longitudinal or circumferential. These are shown in Figure 4 with the longitudinal roughness (a) representing areas of roughness along the roller axis while the circumferential roughness (b) represents the roughness peaks going around the roller. The two types of roughness appear in different applications, dependent on the machine finish applied to the roller. When treating roughness effects directly it is convenient to represent the effect of roughness in both

Table I.
Process parameters used in the sensitivity study

Parameter	Conditions
Load (Nm^{-1})	1750
Roller speed (ms^{-1})	0.25
Fluid viscosity (Pa.s)	3.0
Roller radius (m)	0.045
Rubber layer elastic modulus (Pa)	4.0e+6
Rubber thickness (mm)	8
Rubber roller roughness amplitude (μm)	50
Rubber roller roughness frequency (μm)	50

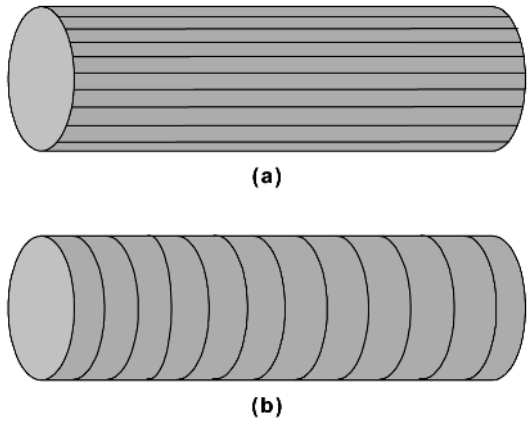

Figure 4.
Schematic of roughness models

directions by combining the solution routines for both the longitudinal or circumferential analysis. A more formal treatment will require a two-dimensional application of the Reynolds equation (Lunde and Tønder, 1997) and when coupled with a deformation analysis, this will again be computationally prohibitive.

Longitudinal roughness

Initially a sensitivity analysis was carried out to evaluate the number of nodes required within each roughness wavelength. The consistency of the results on the pressure, film thickness and flow were evaluated and the results from the flow analysis are shown in Figure 5. The flow was used since this combines both the pressure and film thickness and was the most sensitive parameter with which to optimise the nodal frequency. This work showed that the minimum number of fluid elements within a roughness wavelength should be 36 to obtain a reliable result as well as enforcing local mass conservation. This was used for all subsequent analysis.

The pressure distribution throughout the nip contact shows significant effects for changes in the roughness wavelength, Figure 6, with the effects increasing through the contact. As the wavelength of the roughness increases, noticeable pressure fluctuations are set up in the contact and progressively larger pressure perturbations are predicted. In addition, these increased perturbations lead to some change in the rupture point at the outlet from the contact, particularly at the longer wavelength.

Recent work (Hooke, 1999), primarily on hard narrow contacts, has focussed on relatively long wavelengths, leading to only 5 to 10 complete wavelengths through the contact. The results in Figure 6 show that the profiles obtained under these conditions may not be representative of those found in many

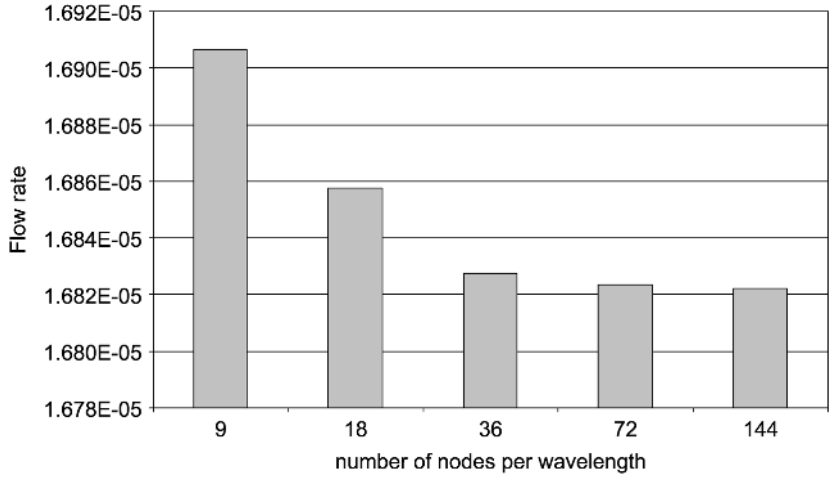

Figure 5.
Multi-griding sensitivity

printing applications where the wavelength of the roughness is much smaller and the contact is significantly wider.

The main purpose of the analysis is to focus on the nip pumping capacity that combines both pressure gradient and film thickness components. Although the roughness profile has an impact on the pressure profile, it may be more appropriate to present averaged (or smoothed) profiles, particularly where the roughness wavelength is short. Thus to aid interpretation of the influence of roughness on the performance through the nip, the pressure and film thickness profiles have had a smoothing function applied. In the analysis,

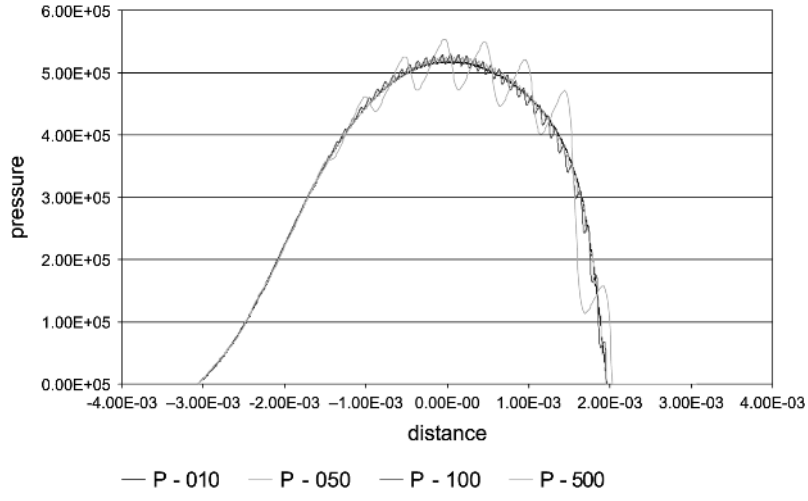

Figure 6.
Pressure distribution for changing wavelength: mean roughness amplitude 50 μm

smoothing combines all the data over a single wavelength and provides an average pressure or film thickness at the mean x co-ordinate of the data that has been analysed.

The roughness amplitude has a large effect on the film thickness profile, Figure 7. The pressure profiles were not modified substantially with only a small increase in maximum pressure, less than 1 per cent. The profiles clearly reflect the constant level of load application demonstrating no marked deviations. In contrast, as the roughness increases the mean film thickness increases, but maintains a consistent form. However, analysis of the actual (non smoothed) film thickness profiles showed that while the mean thickness increases, the minimum gap through the contact decreases. The consequent impact on flow through the nip will be highlighted below.

The impact of changes in the roughness wavelength and phase have also been explored (Bohan *et al.*, 2001). These parameters induce only small changes to both the mean pressure and film thickness profiles, the largest differences are apparent for the maximum pressure encountered in the nip contact. The averaging for the longer wavelengths showed quantization errors due to the length of the cycle compared to the overall nip contact.

The changes of flow rate with the roughness parameters are shown in Figure 8 where clearly roughness amplitude has the most dramatic impact through reduction in flow. This is contrary to what may be expected based on

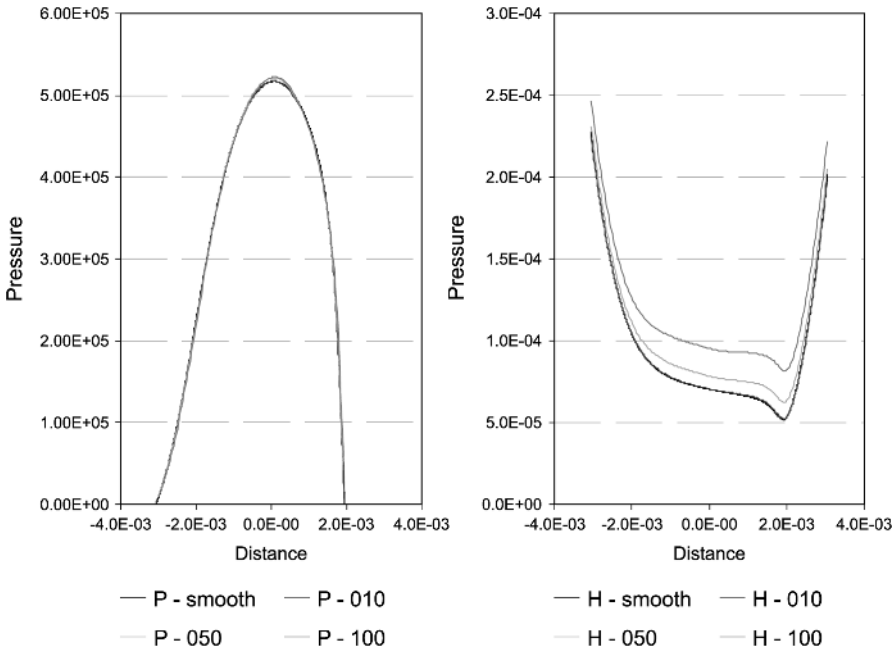

Figure 7.
Pressure and film thickness variations with roughness amplitude

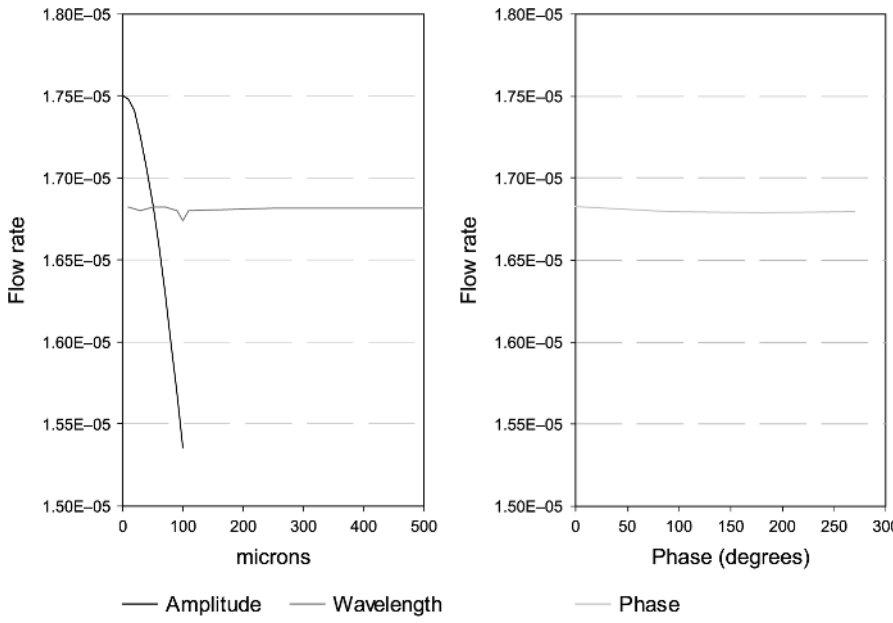

Figure 8.
Flow rate changes with roughness amplitude

the average film thickness that increases with roughness, whereas the minimum film thickness reduces. This confirms that the minimum film thickness determined by the nominal thickness and roughness in the contact determines the pumping capacity. These result compare directly and favourably with the trends for transverse roughness presented in Patir and Cheng, 1978 where the flow factor drops off as the ratio of roughness amplitude to mean film thickness increases. The remaining parameters of wavelength and phase have negligible impact on the pumping capacity within the nip.

Circumferential roughness

Using a direct modelling approach, the treatment of circumferential roughness as shown schematically in Figure 4 is not straight forward. In this work, it has been tackled by dividing the roller into slices through the diameter and solving the governing equations of Soft EHL on the slice. Two extreme scenarios exist, where there is positive clearance in which hydrodynamic deformation is neglected, and where there is complete engagement. Where a clearance gap exists, this infers the neglect of any lateral flow and combining solutions having different minimum film thickness, dependent on the surface profile and slice location. For the loaded condition, the film thickness is determined from the nip analysis modified according to the roughness amplitude. The behaviour has been explored for the case of the sinusoidal profile shown in Figure 9 and the physical parameter settings defined in Table I. For these extreme cases, the

nip width will vary relative to the film thickness, representing flooding for a thin film and starvation in the case of a thick gap. The choice of an appropriate setting is therefore not straightforward and strictly requires a mass balance on the flow entering the nip coupled with its impact on pumping capacity to estimate a formation position. This requires a two dimensional representation of the film that is outside the scope of the present analysis and therefore contact width will need to be estimated as an input variable to the analysis.

Numerical models evaluating the nip performance for a pair of rigid rollers in close contact was carried out. This sensitivity of the system for the roller gap between 1 and 10 microns showed the flow was dominated by the Couette component and minimum film thickness, the gap between the two rollers. The degree of starvation of the contact (prescribed by the contact width) was found to have minimal effects on the flow through the nip.

For the case of engagement, initial calculation was performed for a smooth surface. This gave an engagement (h_0) of 250 μm and this has been used as the datum. Altering this by the roughness amplitude then simulates the surface roughness effect. This necessitates a change in the solution sequence presented above, with the load being the variable altered while the engagement is now fixed.

For a change of 50 μm engagement, the most significant changes occur in the pressure profile and the consequent film width, Figure 10. As the engagement is reduced the contact width reduces and the maximum pressure in the nip also reduces. However, there is much less impact on the final film thickness in the nip, even though the roughness amplitude is 20 per cent of the engagement. There are minor effects such as the point of minimum fluid film thickness moving forward towards the centre of the nip while also increasing, but only by a very small amount.

The results indicate that the circumferential roughness has a much greater impact on the pressure profile than the longitudinal roughness, although this result is likely to be mitigated if a two dimensional film analysis is applied. The most significant result is that the final film thickness profile is not affected significantly by roughness and the pressure profiles retain a similar form.

The impact of the different engagements on flow rate is shown in Figure 11. As expected, as the engagement between the two rollers is increased, the flow rate decreases and conversely. The most important result is that the overall

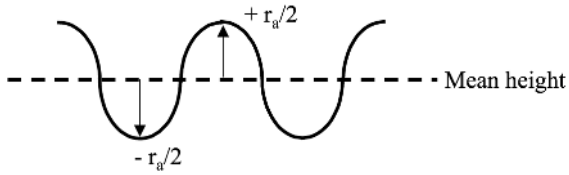

Figure 9.
Schematic of a rough roller surface

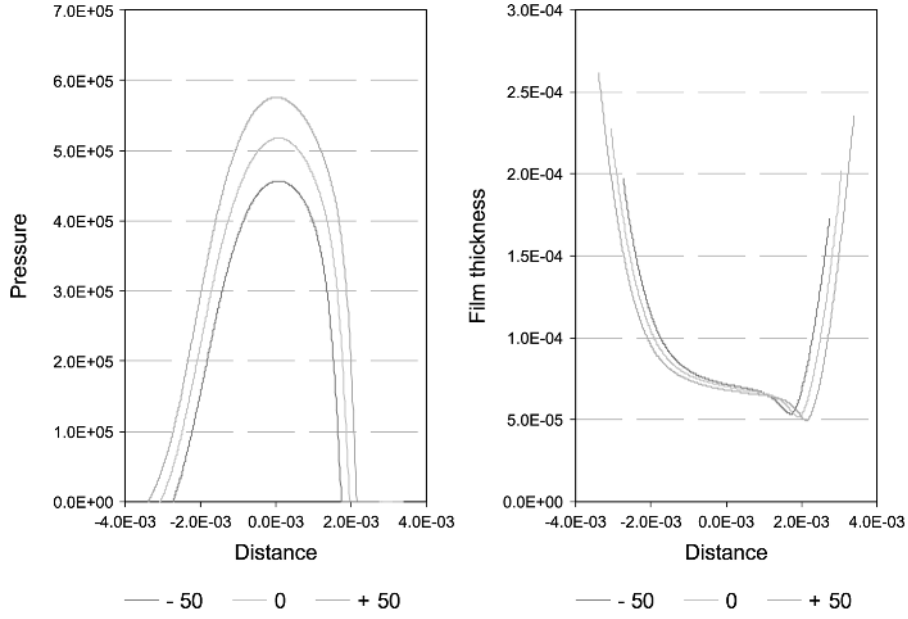

Figure 10.
Pressure and film thickness variations with varying nip gap

impact of circumferential roughness on nip pumping capacity is likely to be small. This is also supported by noting that the ratio of film thickness to roughness is typically 5 for which the effect on flow factor in the film is small (Patir and Cheng, 1978). This is particularly fortuitous since the rubber rollers are generally finish machined by grinding, giving a roughness profile that is

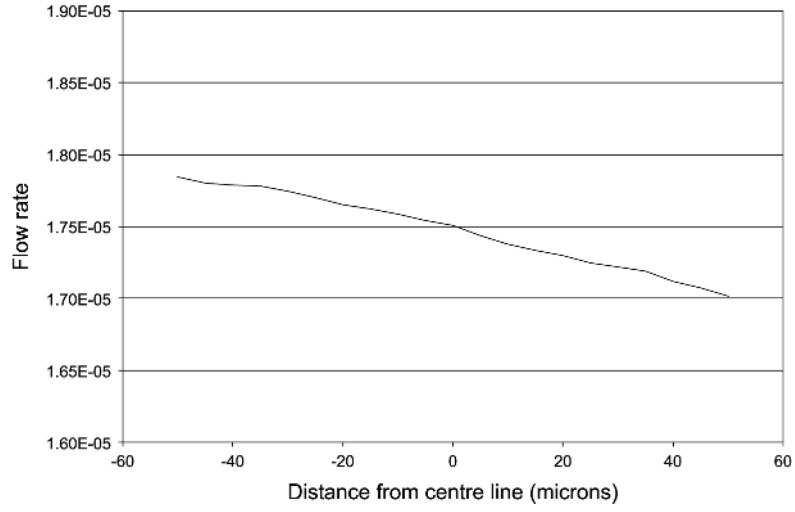

Figure 11.
Flow rate changes with varying nip gap

mainly circumferential. The result implies that achieving a fine surface finish in the circumferential direction may not be so important with respect to pumping capacity within the nip. In comparing longitudinal and circumferential roughness effects, the results indicate that there are significant differences for equal changes in roughness amplitude. Longitudinal roughness changes will affect the flow rate to a much greater extent, with more than double the reduction in pumping capacity in the nip.

Modelling actual roughness profiles

The roughness definition, equation (7), has been incorporated such that it can be replaced with an actual roughness profile recorded digitally from a roller surface. To illustrate this, the roughness of a typical surface was measured using white light interferometry, with a measurement area of 1 mm side dimension. This yields roughness data in both circumferential and longitudinal directions. According to Figure 5, the frequency of the roughness profile effectively defines the discretisation of the fluid domain. To capture the varying frequency of the local surface roughness requires a structural discretisation that adapts to the local roughness wavelength and where high frequency components are present this will lead to a very fine discretisation and consequently long computation times. In this analysis, a mask of wavelength of 50 μm was applied to the roughness profile and in accordance with Figure 5, this was divided into 36 increments, effectively dividing the trace into 1.36 μm increments. Digitising the surface trace gave the roughness profile displayed in Figure 12 and because the contact nip exceeds 1 mm, this profile group was then repeated six times over the contact width. On a local basis, the film gradients are large and these may have an impact on the flow within this

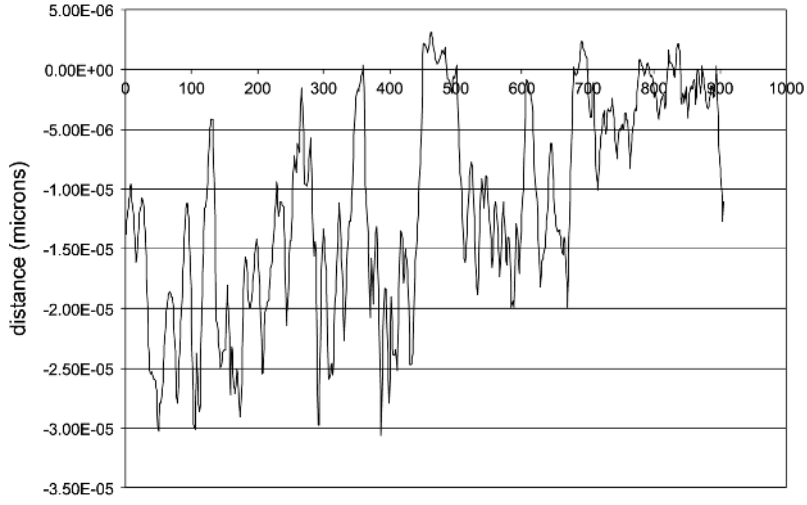

Figure 12.
An actual surface roughness profile

microscopic region (Lunde and Tønder, 1997). Strictly accurate simulation will require solution of the Navier Stokes equation within the region and it is beyond the capability of currently available computation to extend this over the contact width.

When subjected to a load of $1750\,\mathrm{Nm}^{-1}$ the consequent pressure and film thickness profiles are shown in Figure 13. In performing this analysis, no numerical stability difficulties were encountered. When compared with Figure 6 and Figure 7, the generic characteristics such as film width, pressure level and clearance profile remain closely similar. However, differences in detail are present, most specifically in the pressure profile where a smooth excursion to a maximum value is absent. The flow rate through the nip contact is reduced, by a similar amount to that calculated for the longitudinal roughness amplitude of 30 microns. This indicates that it is the total range of the roughness profile, "R_z" and not the "R_a" that is the key factor in relating the simplified sinusoidal roughness to the real roughness values.

Conclusions

A fast and computationally efficient model including roughness effects has been developed for a soft elastohydrodynamic contact lubricated using a Newtonian fluid. This is capable of assessing both axial and circumferential sinusoidal roughness profiles and it can also quantify the effects of real rough surfaces. The numerical analysis couples the solution of the Reynolds equation and those of the elastomer and incorporates the roughness profile directly within the film thickness profile in the Reynolds equation. A sensitivity study has been completed to establish the impact of roughness on the film thickness

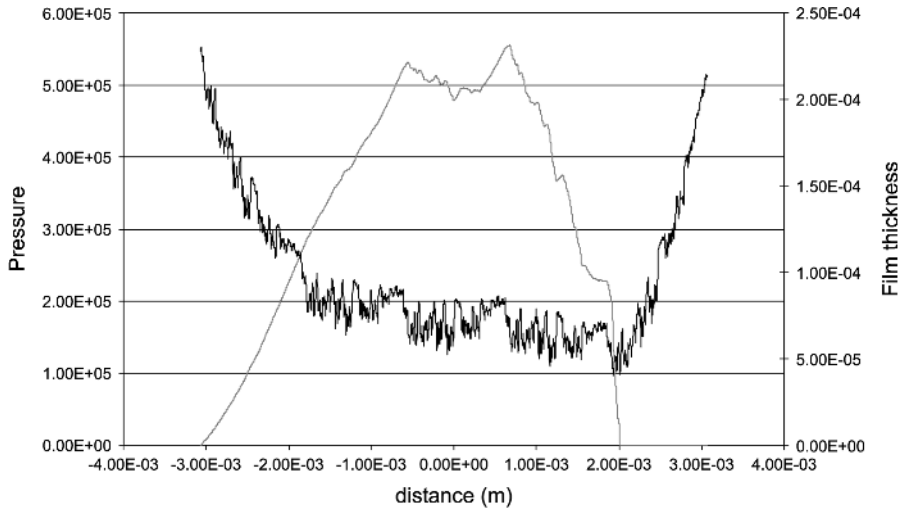

Figure 13.
Pressure and film thickness profiles for the actual roughness profile

and pumping capacity within the nip. The following conclusions can be drawn from this work.

- A multi gridding technique was found to work successfully, linking the hydrodynamic pressure to elastomer deformation and a sensitivity study confirmed that for a sinusoidal roughness profile, a minimum of 36 fluid nodes is required within each roughness wavelength.
- For longitudinal roughness and a fixed loading level, amplitude has the most significant impact on the mean film thickness. However, the flow rate through the nip is governed completely by the local minimum film thickness and not its averaged value. Therefore, increasing the roughness results in a significant decrease in the flow rate. Roughness wavelength only affects the pressure profile, with increased response at the longer wavelengths when waviness exists.
- The effect of circumferential roughness on final film thickness was found to be negligible and consequently had only a small impact on the pumping capacity within the nip.
- For a longitudinal roughness and the incorporation of real surface topography the generic form of the pressure and film thickness remain relatively unchanged, however on a local basis it has a most significant impact on the pressure that is generated within the nip.

References

Banerjee, P.K. and Butterfield, R. (1981), *Boundary element method in engineering science*, McGraw Hill, New York.

Bennett, J. and Higginson, G.R. (1970), "Hydrodynamic lubrication of soft solids", *Proc. I. Mech. E. Journal of Mechanical Engineering Sciences*, 12, pp. 218-22.

Brebbia, C.A. and Dominguez, J. (1989), *Boundary elements: An introductory course*, McGraw Hill.

Bohan, M.F.J., Lim, C.H., Korochkina, T.V., Claypole, T.C., Gethin, D.T. and Roylance, B.J. (1997), "An investigation of the hydrodynamic and mechanical behaviour of a soft nip in rolling contact", *Proc. I Mech E part J Engineering Tribology*, 211 No. J1, pp. 37-50.

Bohan, M.F.J., Claypole, T.C. and Gethin, D.T. (2001), *Roughness modelling of soft elastohydrodynamic lubrication contacts*, ECCOMAS Computational Fluid Dynamics Conference,.

Carvalho, M.S. and Scriven, L.E. (1997), "Deformable Roll Coating Flows: Steady State and Linear Perturbation Analysis", *Journal of Fluid Mechanics*, 339, pp. 143-72.

Cudworth, C.J. (1979), *Finite element solution of the elastohydrodynamic lubrication of a compliant surface in pure sliding*, 5th Leeds-Lyon Symp. on Tribology, Leeds.

Dowson, D. and Higginson, G.R. (1959), "A Numerical Solution to the Elastohydrodynamic Problem", *J. Mech. Eng. Sci.*, 1, pp. 6-15.

Dowson, D. (1962), "A Generalised Reynolds Equation for Fluid Film Lubrication", *International Journal of Mechanical Engineering Sciences*, 4, pp. 159-70.

Dowson, D. and Ehret, P. (1999), "Past, Present and Future Studies in Elastohydrodynamics", *Proc I Mech E (J)*, 213, pp. 317-33.

Greenwood, J.A. (1999), "Transverse Roughness in Elastohydrodynamic Lubrication", *Proc I Mech E (J)*, 213, pp. 383-96.

Gupta, P.K. (1976), "On the heavily loaded elastohydrodynamic contacts of layered solids", *Trans. ASME, J. Lubric. Tech.*, 98, pp. 367-74.

Hannah, M. (1951), "Contact stress and deformation in a thin elastic layer", *Quarterly Journal of Mechanics and Applied Maths*, 4, pp. 94-105.

Higgson, G.R. (1965–-1966), "The theoretical effects of elastic deformation of the bearing liner on journal bearing performance", *Proc. Instn. Mech. Engrs.*, 180, pp. 31-8.

Hooke, C.J. and O'Donoghue, J.P. (1972), "Elastohydrodynamic lubrication of soft, highly deformed contacts", *Proc. I. Mech. E., Journal of Mechanical Engineering Sciences*, 14, pp. 34-48.

Hooke, C.J. (1986), "The elastohydrodynamic lubrication of a cylinder on a elastomeric layer", *Wear*, p. 111.

Hooke, C.J. (1999), "The behaviour of low amplitude surface roughness under line contacts", *Proc. Instn Mech. Engrs, Part J, Journal of Engineering Tribology*, 213, pp. 275-86.

Jaffar, M.J. (1993), "Determination of surface deformation of a bonded elastic layer indented by a rigid cylinder using Chebyshev series method", *Wear*, 170, pp. 291-4.

Lim, C.H., Bohan, M.F.J., Claypole, T.C., Gethin, D.T. and Roylance, B.J. (1996), "A finite element investigation into a soft rolling contact supplied by a non-newtonian ink", *J. Phys. D: Appl. Phys*, 29, pp. 1894-903.

Lunde, L. and Tønder, K. (1997), "Numerical Simulation of the Effects of Three-Dimensional Roughness on Hydrodynamic Lubrication: Correlation Coefficients", *Trans ASME (F)*, 119, pp. 315-22.

MacPhee, J., Shieh, J. and Hamrock, B.J. (1992), "The Application of Elastohydrodynamic Lubrication Theory to the Prediction of Conditions Existing in Lithographic Printing Press Roller Nips", *Advances in Printing Science and Technology*, 21, pp. 242-76.

Meijer, P. (1968), "The contact problem of a rigid cylinder on an elastic layer", *Applied Scientific Research*, 18, pp. 353-83.

Miller, R.D.W. (1966), "Some effects of compressibility on the indentation of a thin elastic layer by a smooth rigid cylinder", *Applied Scientific Research*, 16, pp. 405-24.

Patir, N. and Cheng, H.S. (1978), "An Average Flow Model for Determining Effects of Three-Dimensional Roughness on Partial Hydrodynamic Lubrication", *Trans ASME (F)*, 100, pp. 12-17.

Numerical study of transient instabilities in reverse-roller coating flows

M.S. Chandio and M.F. Webster
Institute of non-Newtonian Fluid Mechanics, Department of Computer Science, University of Wales Swansea, Swansea, UK

Keywords *Numerical simulation, Finite elements, Free form surfaces*

Abstract *A semi-implicit Taylor-Galerkin/pressure-correction algorithm of a transient finite element form is applied to analyse the flow instabilities that commonly arise during reverse-roller coating. A mathematical model is derived to describe the solvent coating applied to the underside of the sheet, assuming that the lacquer is a Newtonian fluid and considering the flow between application roller and foil. Here, we have investigated the effects of temporal instabilities, caused by adjustment of nip-gap width and foil-position, extending our previous steady-state analysis. Foil shifting is found to have a significant influence upon pressure and lift on the foil, drag on the roller, and free coating profiles. This would result in process instabilities, such as chatter and flow-lines. In contrast, nip-gap adjustment has no influence on the coating finish.*

1. Introduction

This work addresses the reverse-roller coating between an application roller and a sheet-foil. The study of roller-coating with free-surfaces is an important topic that commonly arises in many industrial areas, particularly those associated with the production of tape, film and printing situations. Over the past two decades, roller-coating processes have been analysed extensively, involving experimental, analytical and computational studies. Forward roller-coating has attracted the attention of many research groups. Forward roller-coating and reverse roller-coating processes are distinguished by counter-rotating and co-rotating moving rolls, respectively. The ultimate aim of such procedures is to deposit a thin uniform layer to a continuous flexible substrate. There is little reported in the literature concerning reverse roller-coating between foil and roller, taking into account start-up behaviour and time-dependent instabilities. Hence, we briefly comment upon related studies.

Cohu and Magnin (1997) conducted experimental investigations into forward roller-coating of Newtonian fluids between deformable rolls. These authors observed that the decrease of the thickness of a rubber cover on a roller, below a critical value, tends to decrease the coating thickness significantly. Based on forward roller-coating Carvalho and Scriven (1997a) have argued in

The authors wish to express their thanks to Alcoa Manufacturing Ltd. for their financial support and practical guidance throughout this study.

International Journal of Numerical Methods for Heat & Fluid Flow, Vol. 12 No. 4, 2002, pp. 375-403.

DOI 10.1108/09615530210433314

their numerical work, that the upstream free-surface touches the top roll, and air is trapped between the roll surface and the coating liquid. Consequently, the coated film that is delivered is defective. Various flow states are described, both metered and premetered, by moving the rolls apart and bringing them together. As the rolls are pushed together, the gyre moves upstream towards the inlet plane. These authors have replaced the fixed inlet film thickness condition with a weighted kinematic residual, which guarantees that the flow is normal to the inlet boundary in some averaged sense.

Carvalho and Scriven (1997b) conducted a similar study, where the stability of the given system to transverse perturbation is analysed theoretically, numerically and experimentally. A mathematical model is presented to predict the critical *capillary* number for the onset of ribbing, concluding that roll cover deformation alters the wavelength of the ribbing pattern. Roll cover softness is related to increasing the solids elasticity number. Increasing the elasticity number of the soft roll cover, largens the wavelengths and diminishes wave numbers, and this stimulates a faster increase in instability modes. The consequence is a larger ribbing wavelength and the retardation of the levelling rate. To obtain a desired coating thickness, an appropriate criterion must be selected to pinpoint the choice of roll covers.

Fourcade *et al.* (1999) investigated a coating operation of a reverse roller-coating process between two rollers. The main attention is focused on the deformation of the elastomer on the coated roll. The pressure is reported to increase in the converging section of the gap, and reaches its peak slightly to the left of the contact point of the rollers. The largest deformation of the elastomer cover of 70 μm is observed to occur at the location where the pressure reaches a maximum. The lower the gap size, the higher the pressure peak that is observed. Chen and Scriven (1988) chose to set the inflow rate based upon the incoming liquid layer, treated as a plug flow following Benjamin (1994). According to Benjamin, in meniscus coatings, the flow is always pre-metered and, therefore, imposing a velocity profile at the inflow boundary is a satisfactory boundary condition.

One difficulty with computer modelling of such coating scenarios lies in the treatment of moving free-surface problems, accommodating kinematic and dynamic boundary conditions on the free-surface and the simultaneous calculation of its position. For the last two decades the finite element method has played an important role in simulating the flow of fluids subject to free surfaces. Literature of relevance on this topic can be found in (Keunings, 1986; Sizaire and Legat, 1997; Tanner *et al.*, 1975; Silliman and Scriven, 1980; Saito and Scriven, 1981; Ramaswamy, 1990; Hirt *et al.*, 1974; Sato and Richardson, 1994; Chandio and Webster, 2001; Regalt *et al.*, 1993). For details on this issue we refer to our previous steady analysis (Chandio and Webster, 2001), where attention is focused upon the flow patterns that result and variation in pressure, lift and drag at various roll and foil-speeds. Here, a finite element

simulation of the roller-coating process is presented, based on a semi-implicit Taylor-Galerkin/Pressure-correction algorithm (Townsend and Webster, 1987; Hawken *et al.*, 1990; Carew *et al.*, 1993). For free-surface prediction, we use kinematic boundary adjustment with a mesh-stretching algorithm.

The main purpose of the present work is to provide a description of reverse roller-coating flows, accounting for the parameters affecting the coating process, and, in particular, those of most practical significance. Major attention is focused upon flow instabilities, seeking to investigate transient effects and the influence these have upon typical processing instabilities. Various nip-flow conditions are considered, to take into account some leakage at the nip and to provide consistent local settings. The effects of such leakage upon the flow are determined. In particular, temporal variations between leakage and no-leakage states are simulated. Finally, temporal foil-shifting is investigated. Foil-shifting is invoked in two distinct forms: first, via global uniform shifting, and second, through more local adjustment. Results are interpreted through pressure, lift and drag, quantified locally, and through the influence of such temporal fluctuations upon the free-surface shape of the lacquer coating.

2. Problem specification and governing equations

The isothermal and two-dimensional coating flow of Newtonian liquid is considered. The system consists of a roller of radius r_1, rotating at speed U_{roll}, applying a coating to the underside of the alloy sheet of thickness $G(x, t)$. The sheet rests on both the roller and the thin film of fluid trapped between the roller and the sheet. The sheet moves with speed U_{foil} in the horizontal direction (negative x) and the problem is posed in a Cartesian frame of reference. A schematic diagram of the flow is illustrated in Figure 1.

The isothermal flow of Newtonian fluid is governed by equations for the conservation of mass and transport of momentum. In the absence of body forces, the system may be expressed in the form

$$\rho \frac{\partial u}{\partial t} = \nabla \cdot \tau - \rho u \cdot \nabla u - \nabla p \tag{1}$$

$$\nabla \cdot u = 0 \tag{2}$$

where ρ is the fluid density, t is the time, $u(x,t)$ is the fluid velocity and p is the isotropic pressure. For Newtonian flows, the stress τ is defined via a constant viscosity μ, and the rate of deformation tensor $\mathbf{D}$,

$$\tau = 2\mu \mathbf{D} \tag{3}$$

$$\mathbf{D} = \frac{L + L^t}{2} \quad \text{and} \quad L = \nabla u. \tag{4}$$

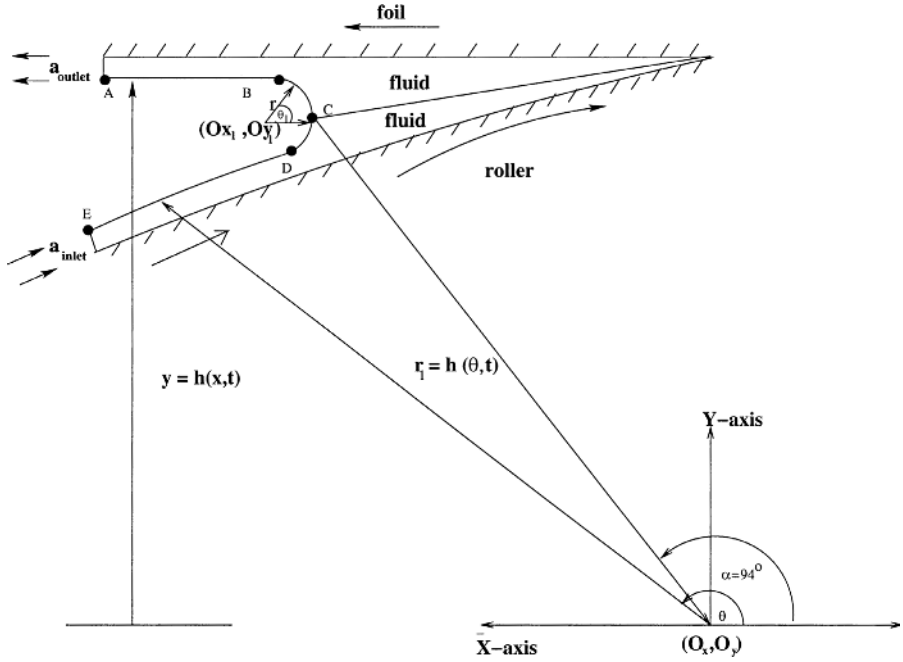

Figure 1.
Schematic flow diagram

For a Newtonian fluid, the Navier-Stokes equations can be recovered, by recourse to the continuity equation (2),

$$\rho \frac{\partial u}{\partial t} = \mu \nabla^2 u - \rho u \cdot \nabla u - \nabla p \tag{5}$$

where $\mu \nabla^2 u$ is a diffusion term.

For conciseness and convenience, adopting characteristic scales on velocity, U (standard foil speed), length, L (steady-state coating thickness, no leakage) and viscosity, μ, we may define non-dimensional variables $u = Uu^*$ and $p = [\mu U/L]p^*$. Hence, we may define an equivalent non-dimensional system of equations to (2) and (5), discarding the * notation for clarity of representation,

$$\begin{aligned} \mathrm{Re} \frac{\partial u}{\partial t} &= \nabla^2 u - \mathrm{Re}\ u \cdot \nabla u - \nabla p, \\ \nabla \cdot u &= 0, \end{aligned} \tag{6}$$

where the non-dimensional group Reynolds number is defined as $\mathrm{Re} = \rho UL/\mu$.

For the solution of the given system of governing equations, both initial and boundary conditions are required. Initial conditions can be formed by prescribing initial values for the primitive field variables at $t = 0$,

$$U(x,t) = u_0(x,0),$$
$$p(x,t) = p(x,0).$$

Conditions at the free-surface require a normal constraint,

$$p + \tau_{nn} = -p_0 + \sigma_s \beta, \tag{7}$$

whilst the absence of friction ensures the tangential constraint,

$$\tau_{nt} = 0. \tag{8}$$

Here, τ_{nn}, τ_{nt} are normal and tangential stress components, respectively, p_0 is atmospheric pressure and p local pressure, σ_s is a surface tension coefficient and β is the mean curvature of the free-surface (Saito and Scriven, 1981). Remaining boundary conditions are taken of no-slip on roller and foil, uniform flow at inlet on the roller and outlet on the foil. In a no-leakage state, there is vanishing flux across the nip. No-slip boundary conditions for the flow on solid surfaces are taken as:

$$\begin{aligned} &\text{on foil}: \quad U_x = -\overline{U}_{\text{foil}}, \quad U_y = 0; \\ &\text{on roller}: \quad U_x = U_{\text{roll}} \cos\theta, \quad U_y = U_{\text{roll}} \sin\theta; \end{aligned} \tag{9}$$

where $U_{\text{roll}} = R\omega, R$ is the radius and ω the angular rotation rate of the roller.

The evolving position of the free-surface, is unknown apriori and must therefore be computed as part of the solution. In this respect, we appeal to the kinematic boundary conditions (Keunings, 1986). On flat free-surface boundaries (lines at constant y) this leads to:

On flat free-surface boundaries (lines at constant y):

$$\frac{\partial h}{\partial t} = -U_x \frac{\partial h}{\partial x} + U_y, \tag{12}$$

On the curved meniscus boundary section (lines at fixed azimuthal angle θ setting):

$$\frac{\partial h}{\partial t} = -U_\vartheta \frac{1}{r} \frac{\partial h}{\partial \vartheta} + U_r \tag{11}$$

A combination of both equations (10) and (11) is required for the current flow problems.

3. Finite element analysis

A Taylor-Galerkin algorithm is used to solve the governing equations (6). This involves a two-step Lax-Wendroff approach, based on a Taylor series expansion up to second order in time, to compute solutions through a time

stepping procedure. A two-step pressure-correction method is applied to handle the incompressibility constraint. Employing a Crank-Nicolson treatment on diffusion terms, produces an equation system of three fractional-staged equations (Hawken *et al.*, 1990). In stage one a non-solenodal velocity field $u^{n+1/2}$ and u^* are computed via a predictor-corrector doublet. The resulting mass-matrix bound equation is solved via a Jacobi iteration. With the use of u^*, the second stage computes the pressure difference, $p^{n+1} - p^n$, via a Poisson equation, and the application of a direct Choleski solver. The third stage completes the time step loop, calculating the end-of-time-step solenoidal velocity field u^{n+1}, again by a Jacobi iterative solver. Full details upon this implementation may be found in Townsend and Webster (1987) and Hawken *et al.* (1990).

Following the notation of Cuvelier *et al.* (1986), the velocity and pressure fields are approximated by $U(x,t) = U^j(t)\ \phi_j(x)$ and $P(x,t) = P^k(t)\ \psi_k(x)$, where U and P represents the vectors of nodal values of velocity and pressure, respectively, and ϕ_j are piecewise quadratic and ψ_k linear basis functions on triangles.

The fully-discrete semi-implicit Taylor-Galerkin/pressure-correction system of equations may be expressed in matrix form:

$$\text{Stage 1a. } \left(\frac{2\text{Re}}{\Delta t}M + \frac{1}{2}S\right)\left(U^{n+\frac{1}{2}} - U^n\right) = \{ - [S + \text{Re } N(U)]U + L^T P\}^n$$

$$\text{Stage 1b. } \left(\frac{\text{Re}}{\Delta t}M + \frac{1}{2}S\right)(U^* - U^n) = (-[SU + L^T P]^n - [\text{Re } N(U)U]^{n+\frac{1}{2}} \tag{12}$$

$$\text{Stage 2 } K(P^{n+1} - P^n) = -\frac{2}{\Delta t}\text{Re } LU^*$$

$$\text{Stage 3 } \frac{\text{Re}}{\Delta t}M(U^{n+1} - U^*) = \frac{1}{2}L^T(P^{n+1} - P^n),$$

where M, S, $N(U)$, L, and K are consistent mass matrix, momentum diffusion matrix, convection matrix, pressure gradient matrix and pressure stiffness matrix, respectively. With elemental fluid area $d\Omega$, such matrix notation implies,

$$M_{ij} = \int_\Omega \phi_\iota \phi_j \, d\Omega,$$

$$N(U)_{ij} = \int_\Omega \phi_\iota \left(\phi_1 U_1 \frac{\partial \phi_j}{\partial x} + \phi_1 U_1 \frac{\partial \phi_j}{\partial y}\right) \, d\Omega,$$

$$((L_k)_{ij}) = \int_\Omega \frac{\partial \phi_j}{\partial x_k}\ d\Omega,$$

$$K_{ij} = \int_\Omega \nabla\psi_i\ \nabla\psi_j\ d\Omega,$$

$$S_{ij} = \int_\Omega \nabla\phi_i\ \nabla\phi_j\ d\Omega.$$

For the computation of the free-surface, we have used the kinematic boundary conditions (Keunings, 1986; Sizaire and Legat, 1997). These can be expressed in a general discrete variational form:

$$\text{Stage 4}\quad \begin{aligned} &\frac{1}{\Delta t}\int_\Gamma (\psi_i + (\alpha_1 + u.\nabla\psi_i))(\psi_k + (\alpha_2 + u.\nabla\psi_k))\Delta H_k^{n+1} \mathrm{d}\Gamma_F \\ &- \int_\Gamma (\psi_i + (\alpha_1 + u.\nabla\psi_i))u.\nabla\psi_k H_k^n \mathrm{d}\Gamma_F \end{aligned} \tag{13}$$

adopting notation for time-step, Δt, interpolant, $H^n(x)$, interpolating functions, $\psi_k(x)$, and nodal solution increment, ΔH_k^n,

$$H^n(x) = H_k^n \psi_k(x)\ \text{ and }\ \Delta H_k^{n+1} = (H_k^{n+1} - H_k^n). \tag{14}$$

The scheme expressed in (13) is quite flexible, where we define generalized scalar factors α_i to switch between Galerkin and Streamline-Upwind Petrov-Galerkin (SUPG) (explicit and implicit) schemes, as and when required. A free-surface boundary segment is indicated by Γ_F, over which quadrature may be established. In equation (13), the generalized form of convective term is represented, subsuming either equation (10) or (11), depending upon the particular boundary segment under consideration. We have found it most effective to use $\alpha_1 = \alpha^h$ (an SUPG parameter[3]) and $\alpha_2 = \Delta t/2$ to recover an implicit SUPG scheme. Then, both ψ_i (and ψ_k) are taken as linear functions on straight-sided boundary element sections.

4. Numerical results and discussion

A standard foil-speed setting of one unit and roller speed, 90 per cent of foil-speed, constitutes the base scenario around which solutions are sought. Results are reported in non-dimensional form for convenience of representation. The mesh used is displayed in Figure 2, with 2925 nodes, 1302 elements and 6662 degrees of freedom. A typical steady-state flow pattern is shown in Figure 2d, represented in space-filled motion blur format, based on the velocity vector field (Chandio and Webster, 2001) (colour implies speed magnitude; red-fast, green-medium, blue-slow). In this section, we are particularly interested in

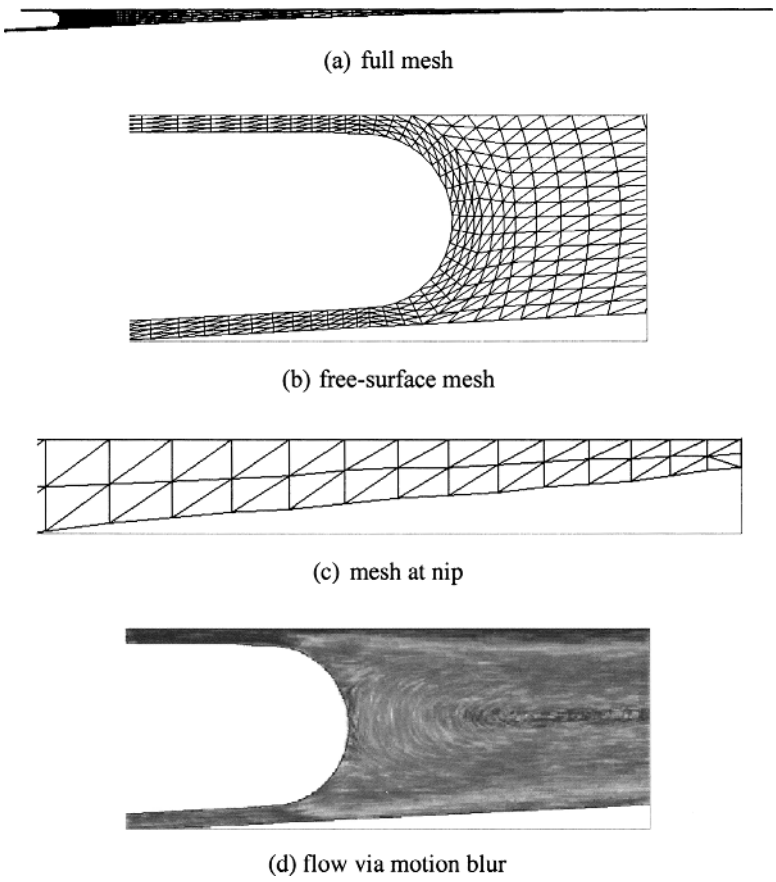

Figure 2.
Finite element mesh sections and flow representation

pressure maxima across the nip region (see Figure 2c), lift is considered along the foil surface and drag on the roller. For a Newtonian fluid, the lift (L_{foil}) and drag (D_{roller}) are given through the following expressions:

$$L_{\text{foil}} = \int_{\Gamma_{\text{foil}}} \{ -p \ \sin\theta + \tau_{xy} \ \cos\theta + \tau_{yy} \ \sin\theta \} \, \mathrm{d}\theta = \int_{\Gamma_{\text{foil}}} L_f \, \mathrm{d}\theta \qquad (14)$$

$$D_{\text{roller}} = \int_{\Gamma_{\text{roller}}} \{ -p \ \cos\theta + \tau_{xx} \ \cos\theta + \tau_{xy} \ \sin\theta \} \, \mathrm{d}\theta = \int_{\Gamma_{\text{roller}}} (-D_R) \, \mathrm{d}\theta \qquad (15)$$

where $\tau = 2\mu D$, so that L_f and D_R are distributional quantities on the respective surfaces (unassigned where possible)

Results are categorised into different sections. The first deals with the variation in nip velocity and pressure profile conditions. This is in order to choose a suitable velocity profile at the nip, prior to investigating temporal

changes. A second section is devoted to the study of temporal changes in leakage, but without foil-shifting. This allows us to interpret transient variations of pressure at the nip. Global foil-shifting at steady-state is studied in a third section. Lastly, we consider foil-shifting locally and globally in time. All settings discussed are concerned with nodal positions N_2, N_4 and N_5. No-slip boundary conditions (9) apply on nodes N_1 and N_3, see Figure 3. In the standard no-leakage setting, fluid is not permitted to traverse through the nip-gap. So fluid travels along the roller and is carried away by the foil. The parameter of importance here in the numerical algorithm, is the time-step (Δt). This is chosen for pragmatic reasons, to satisfy accuracy and stability constraints, as 0.005 units.

4.1 Variation in nip flow conditions

Prior to analysing flow instabilities, it is instructive to choose an appropriate velocity profile to allow a degree of leakage at the nip. This automatically implies flow, out through the nip, that must be counterbalanced by inflow/coatoutlet-flow. Temporal adjustments to nip boundary conditions are consigned to later sections. There is no flow (leakage) through the nip under standard settings. No-slip boundary conditions apply on the foil and roller nodes at the nip, see Figure 3a. A typical schematic diagram of plug and Couette flow is shown in Figure 4 (vanishing vertical velocity). Natural unconstrained boundary conditions are referred to as free, and strong constrained boundary conditions as fixed. In Figure 5, various examples of horizontal velocity component profiles of plug and Couette-type are displayed over a fixed nip-gap width. At nodal positions N_2, N_4, N_5 corresponding values are charted in Tables I and II. For stable numerical calculations, one has to treat the severe conditions at the nip with care. It is found necessary to constrain some solution variables. Imposing either opposing plug (setting I) or Couette flow profiles (setting II and III), provides results (pressure, lift and drag) that lie close to the standard no-leakage setting. Couette flow setting III, is held to be more physically representative, see Figure 5c and Tables I and II.

Figure 6 shows the distributional pressure (P_f), lift (L_f) along the foil and drag (D_R) along the roller. The section of the foil considered would amount to a distance of 500 units from the nip. The maximum lift around 82×10^3 units, is observed on the nip outlet with the Couette flow setting (see Figure 5c). With the standard no-leakage setting, a negligible leakage is observed through the nip-gap, inherent to the FE discretisation, and the lift value is 63×10^3 units. With a Couette flow setting, a larger degree of leakage is allowed that generates larger lift than the standard setting. Differences in total lift across the various settings are practically identical, as shown in Table II. As pressure decreases, lift and drag also decrease, see Table II. The drag on the roller is fairly small along most of the roller-length, see Figure 6. The distributional drag on the roller, D_R, is negated to imply physical meaning through magnitude, as with

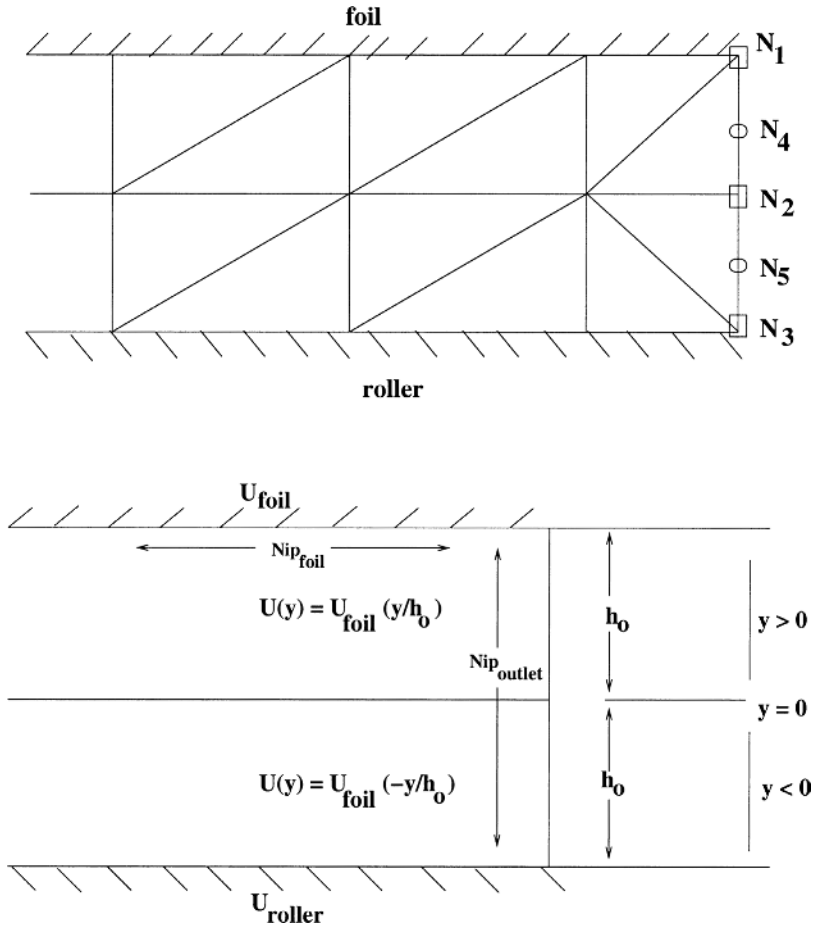

Figure 3.
Nip mesh and velocity conditions

pressure. D_R first rises along the roller travelling towards the nip, then declines around 100 units from the nip, dropping into negative values close to the nip. The sudden kinematic changes at 10 units from the nip cause a rapid rise in D_R, where large shear-rates are observed (Chandio and Webster, 2001). Such negative drag values can be attributed to the increase in cross-stream flux close to the nip (that has generated negative shear-stress) before it merges with the imposed Couette-flow profile. These sharp adjustments into negative drag values vanish as nip-gap width increases, see Figures 9–11. Since these changes are purely local and are restricted to the nip region, so the free-surface remains unaffected. Maxima of forces in Table II, are shown over Nip_{outlet} and Nip_{foil} regions, defined in Figure 3b.

4.2 Temporal adjustment of nip conditions

The main purpose here is to evaluate the effect of temporal leakage adjustment upon the pressure and lift acting on the foil, with a fixed nip-gap width. This is performed through variations in conditions across the time steps with a corresponding sensitivity analysis. The pressure variation is observed at various time step setting protocols, by switching between standard setting (no leakage) and Couette flow setting (leakage setting III, see Table I) in time. This applies to all leakage settings adopted below. Pressure, lift and drag reflect almost identical results, to those at standard settings, see Figure 7 and Table III. With temporal adjustment of nip conditions, but without foil movement, we observe in Figure 8, a trend towards a constant periodicity (regular frequency) in the temporal change of the pressure at the nip. There is only minimal pressure variation and this is local to the nip. Hence, there is hardly any influence over the coating free-surface profile on the foil.

4.3 Global foil-shifting

Thus far, we have observed that there is only minimal pressure variation and this is local to the nip. Hence, foil/meniscus pressure profiles remain unaffected. Next, the effects of foil-shifting are investigated in response to flow-instabilities. Nip-gap size is increased by shifting the foil vertically upwards,

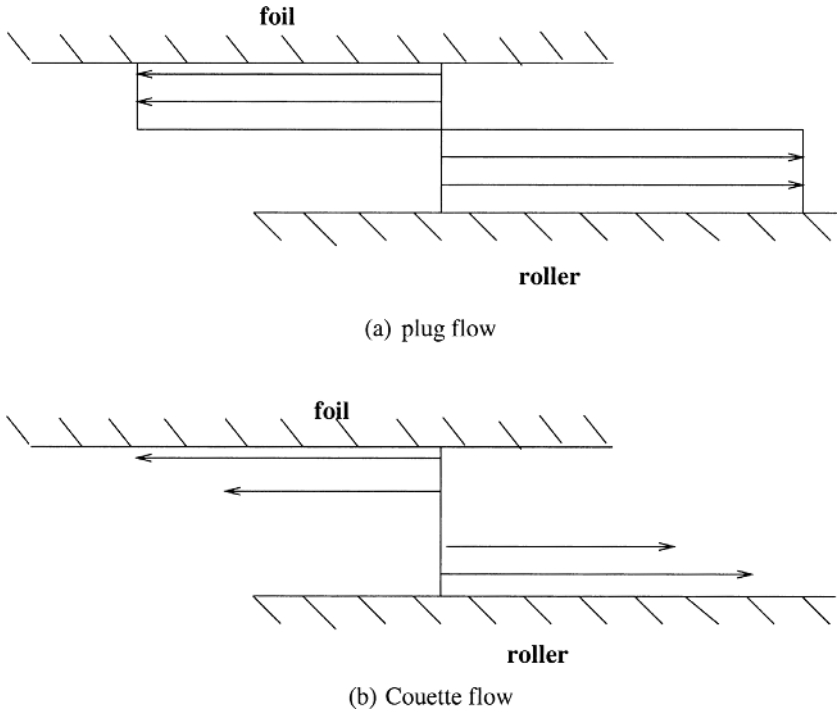

Figure 4.
Schematic diagram of (a) plug and (b) Couette flow velocity profiles at nip

(a) $U_{N4} = U_{N1}$; $U_{N5} = U_{N3}$; $U_{N2} = 0$; P_{N2} free; setting I

(b) $U_{N4} = U_{foil}\frac{1}{h_0}(y)$; $U_{N5} = U_{roller}\frac{1}{h_0}(-y)$; U_{N2} free; setting II

(c) $U_{N4} = U_{foil}\frac{1}{h_0}(y)$; $U_{N5} = U_{roller}\frac{1}{h_0}(-y)$; $U_{N2} = 0$ fixed; setting III

Figure 5.
Flow pattern with various nip velocity/pressure settings

Table I.
Nip conditions; velocity

Settings	U N_2	N_4	N_5
Standard	0	0	0
I (constrained u)	0	U_{N1}	U_{N3}
II (constrained u at N_4, N_5)	−1.8	$U_{foil}(h_o - y)$	$U_{roller}(h_o + y)$
III (constrained u)	0	$U_{foil}(h_o - y)$	$U_{roller}(h_o + y)$

Table II.
Nip conditions; maxima in P, lift (on foil) and drag (on roller), values × 10^3 units

Settings	P_{max} Nip_{outlet}	Nip_{foil}	Lift	Drag
standard	160	160	1311	1.30
I	152	150–121	1286	1.30
II	85	95–102	1286	1.30
III	156	153–123	1298	1.30

uniformly across its length, relocating at a specified new nip-width, taken as a function of time-step variation.

4.3.1 Shift and solve to steady state. The variation of leakage is considered at various nip-width settings. At 2 per cent nip-width, the pressure peak at the nip has decreased by 83 per cent to that of the standard setting result. Correspondingly, there is a decline of similar form in lift. However, these settings have no significant influence on the drag, see Table IV. It is to be noted

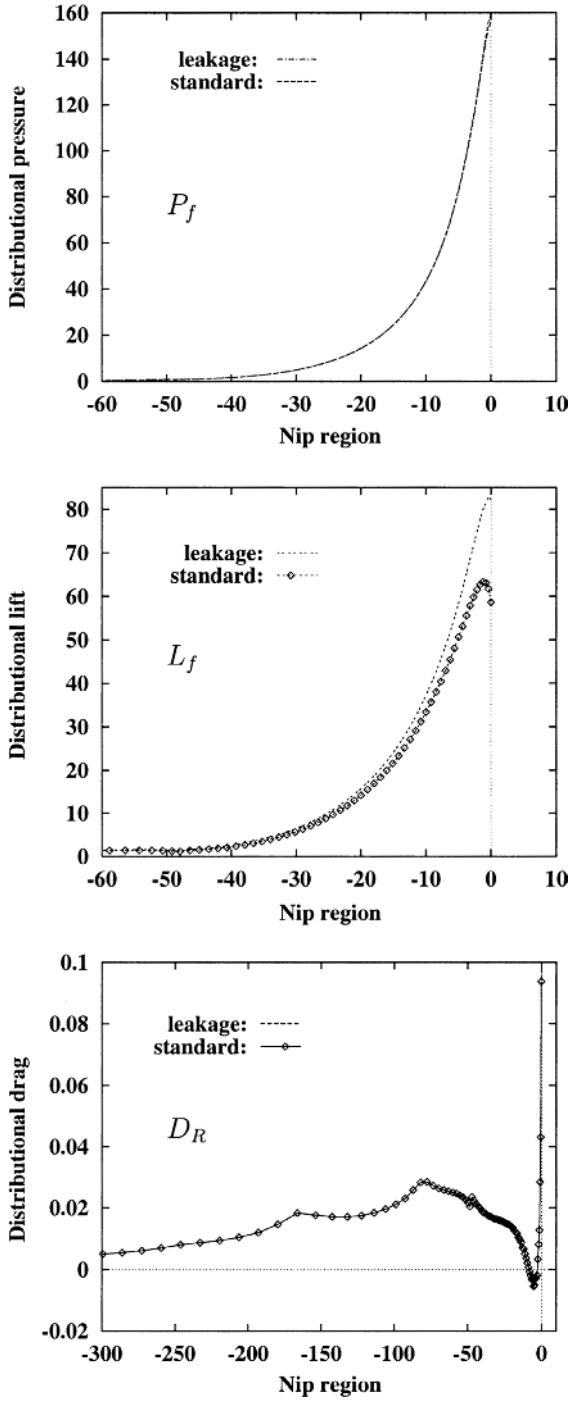

Figure 6.
Distributional pressure (P_f) and lift (L_f) along foil, and drag (D_R) on roller, (values $\times 10^3$).

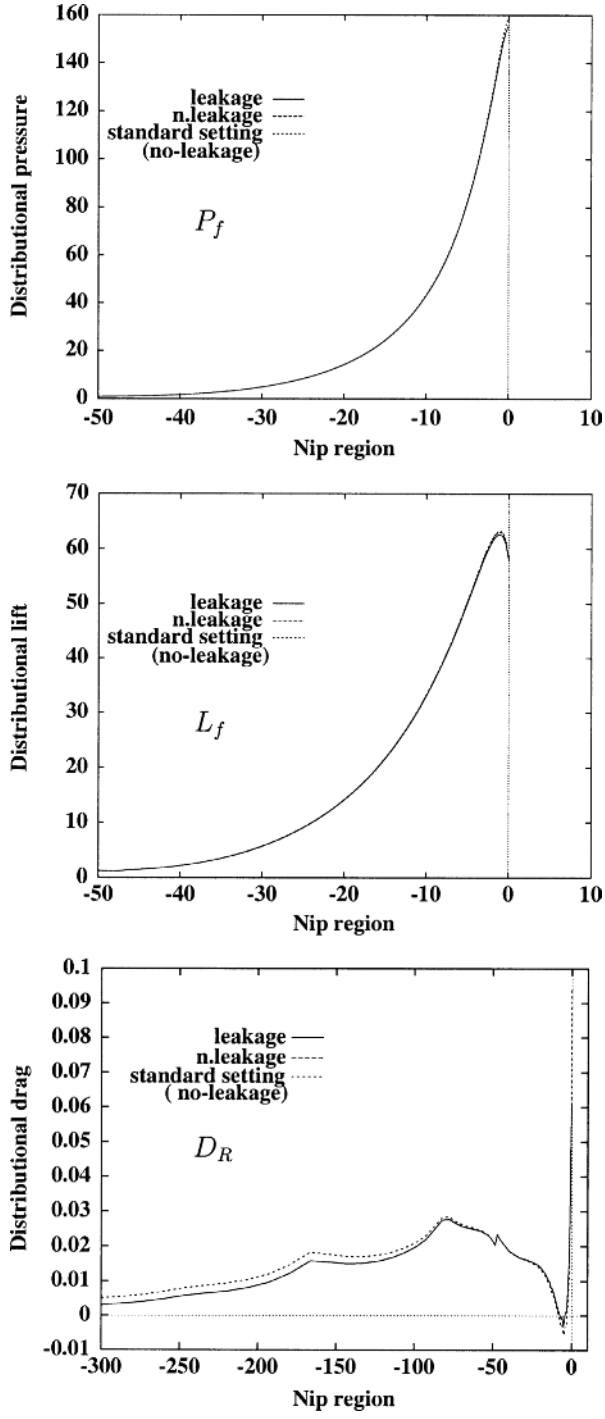

Figure 7.
Temporal leakage adjustment: settled distributional pressure (P_f) and lift (L_f) along foil, and drag (D_R) on roller, values $\times 10^3$, $10_l - 10_{nl}$, true for all protocols

that drag is a trivial quantity in the present study. Locally to the nip, lift decreases by 68 per cent and drag by 60 per cent. This is shown to be largely restricted to the nip region, see Figure 9. Similarly, at 3 per cent nip-width, pressure maxima at the nip have decreased by 90 per cent and lift by 78 per cent, see Table IV.

Such global foil shifting, considered to steady state in time, hardly affects the outlet/meniscus flow. This is entirely reasonable as the adjustment incurs such minor leakage, which hardly reduces the flow rate at the outlet, i.e. coating on the foil. We may discern the influence of nip-width adjustment, prior to transient fluctuations. That is, in contrast to the Couette flow studies of section 4.2, where an increasing degree of leakage also applied, but imposed for a 1 per cent fixed nip-gap width. The findings are broadly similar with localized force balance adjustments restricted to the nip, so that the free-surface remains unaffected. Hence, an important point to note is that changes imposed in nip-gap width have influence around the nip region only.

4.3.2 Temporal adjustment of foil position. Here, foil vibration is performed at set time-steps intervals. So, for example, the foil is allowed to move up/down by creating/removing a gap between roller and foil, after every N alternate time-steps. Effectively the foil is either rising off/laying on the roller. Nip conditions that switch between different foil positions are taken as of sub-section 4.2. The results presented below are associated with data sampled when the foil is in a shift-up mode, and are compared with the standard setting. The foil is shifted at different time-step protocols. The drop of pressure is related not only to nip-width, but also to foil shift-up time. Increment in foil shift-up time retards the pressure and lift considerably, see Table V. It is found helpful to consider integrated quantities on surfaces in their contributions per unit area (distributional), to appreciate their spread. As regards distributional

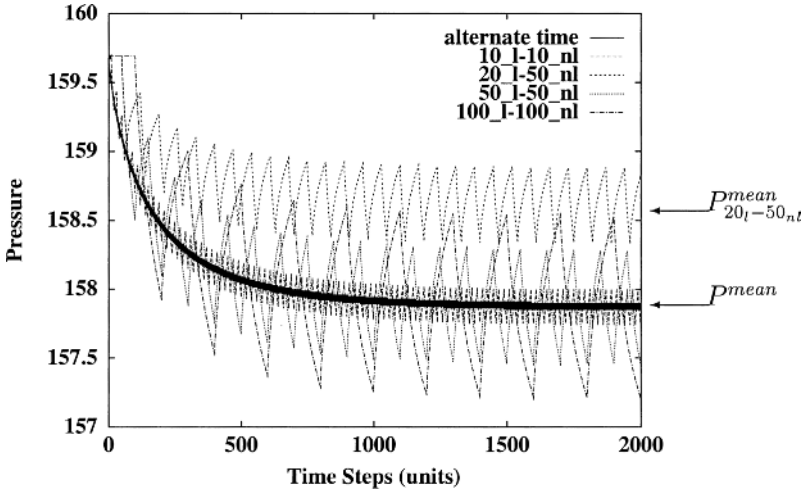

Figure 8.
Temporal leakage adjustment, pressure at nip node N_1, values $\times 10^3$

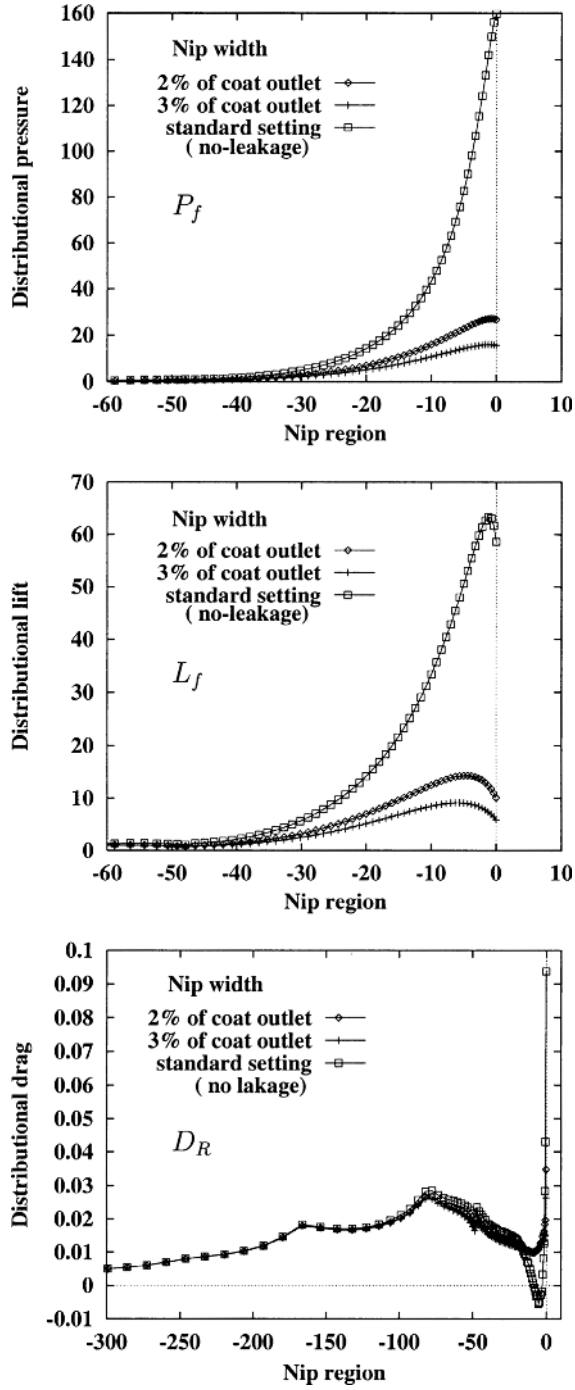

Figure 9.
Global foil shifting, steady state: distributional pressure (P_f) and lift (L_f) along foil, and drag (D_R) on roller, values $\times 10^3$.

pressure/lift on the foil and drag on the roller in a no-leakage (nl) state, it is noted that, the greater time-step variation protocol ($100_{l} - 100_{nl}$) does attain a level, close (within 10 per cent) to that of the standard nl-setting, see Figures 10 and 11. Pressure profiles, are illustrated in contrast to the standard setting. The decline and rise of pressure is clearly exhibited, at leakage (Couette velocity profile) and no-leakage (standard setting) states, across time-step variations, see Figure 11. On average, pressure and lift decrease, with increasing nip-width, see Table V.

Temporal variation in pressure is sampled at a single point, on the foil, at the nip region, see Figure 12. Pressure is observed to be a direct sensor of lift, and hence, the choice to plot this quantity. The rise and fall of pressure is clearly apparent at alternate specified time-steps. Therein, we see regular periodicity in pressure sampled at the nip. The sharpness of the profiles, over an individual period is associated with high frequency protocols. At low frequency, this sharpness is dispersed, such as with the $100_{l} - 100_{nl}$ protocol. This is so, even with increase in nip-gap width cases.

We comment that by employing an appropriate nip-width setting, one can control the threshold level of pressure. This may be used as a mechanism to constrain lift, which mitigates foil-vibration. The plots of Figure 13 for $P_{min}(t)$ in a leakage-state, for 2 per cent, 3 per cent and 5 per cent settings, at high and low frequency protocols, indicate corresponding settling times (to a steady-position). These are more rapid at larger nip-widths. Permitting a leakage/no-leakage pattern over a specified time-step variation sequence generates foil vibration, which creates oscillations at the flow-outlet free-surface region on the foil. When the roller rotates at a certain speed, the fluid exerts a potentially increasing force upwards on the foil, and the lift/pressure forces reach a maximum level. This level is sufficient to push the foil upwards, creating a larger gap between the roller and the foil at the nip region. Accordingly, a small degree of leakage may occur. The pressure/lift forces exerted by the fluid subsequently diminish in time and have the effect of resettling the foil back onto the roller. This is a transient (periodic) phenomenon. During the process of foil shifting (up/down), one may equate and balance the respective flow rates between in-flow, coat-outlet flow and nip-outlet flow. The film-layer thickness varies, in a uniform manner, along its length. When there is no-leakage, the required wet film thickness implies a flow rate balance between in-flow and coat-outlet flow. When the foil rises off the roller, a minimal degree of leakage, between 1 per cent–3 per cent of the coat-outlet, is allowed through the nip-gap. This affects the wet film-thickness, reducing its thickness by the same order as that of the leakage, so that, now the coat-outlet flow rate is decreased by the leakage flow rate at the nip.

In Figures 14 and 15, free-surface profiles are given at 2 per cent nip-width for the $100_{l} - 100_{nl}$ protocol. Identical free-surface profiles are obtained for other protocols. Wave patterns on the free-surface are apparent. The intensity of such

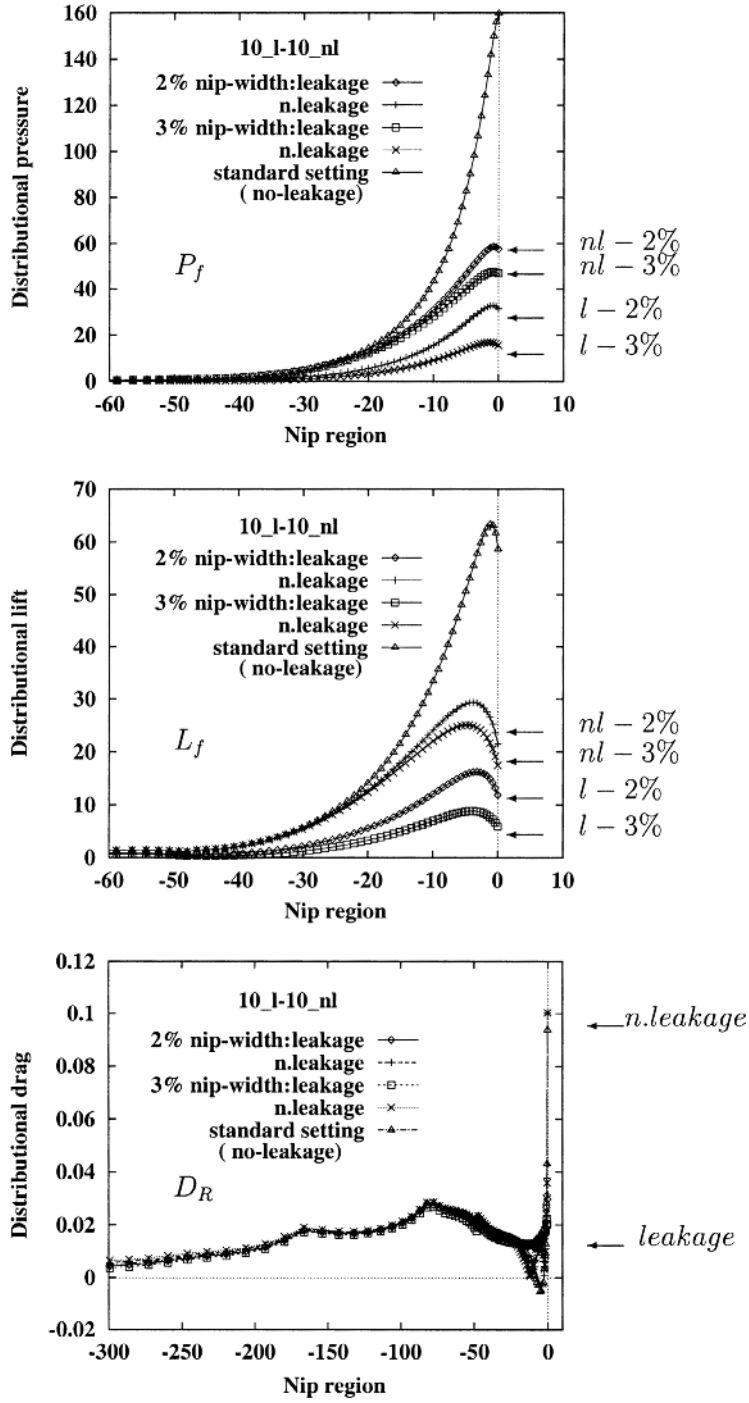

Figure 10.
Global foil shifting, temporal variations, settled distributional pressure (P_f) and lift (L_f) along foil, and drag (D_R) on roller, values $\times 10^3$ at L per cent nip-width of $coat_{outlet}$, $10_l - 10_{nl}$ protocol

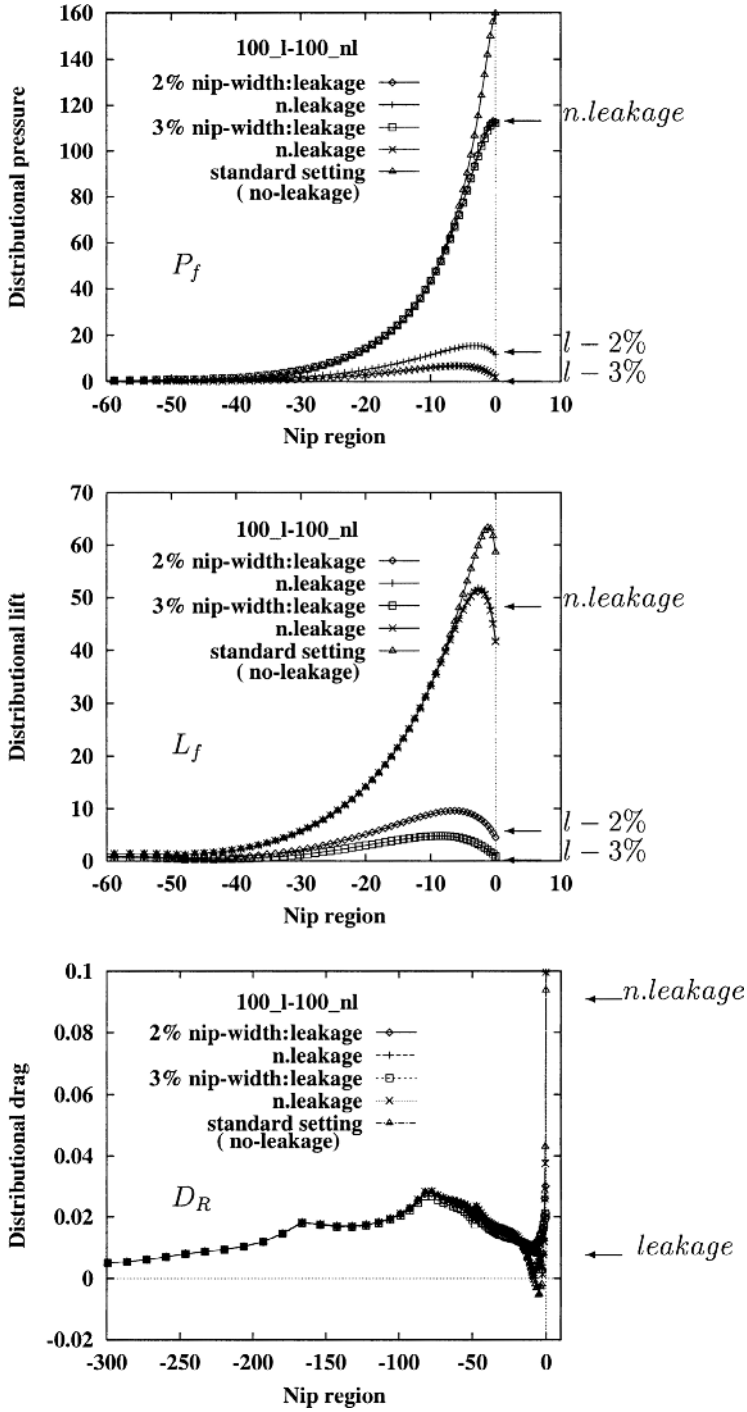

Figure 11.
Global foil shifting, temporal variations, settled distributional pressure (P_f) and lift (L_f) along foil, and drag (D_R) on roller at L per cent nip-width of $\text{coat}_{\text{outlet}}$, $100_l - 100_{nl}$ protocol

instabilities is demonstrated in Figure 15 on the coat-outlet layer and at the meniscus. These instabilities develop in time and reach a steady-state after long time periods. Such effects onset at the meniscus and propagate towards the coat-outlet region in time, see Figure 16. The amplitude of these oscillations enlarge with increasing nip-width. In Figure 15 oscillations are apparent on the free-surface. These would contribute to the final coating finish, rendering an uneven coating layer. The film-width would vary as a consequence, along the complete length of the sheet-foil. Over a leakage period, a slight decrease in the coat-outlet thickness arises to compensate and conserve flow rate. Free-surface profiles at meniscus and $\text{coat}_{\text{outlet}}$ regions for various nip-width settings are shown in Figure 16. In Figure 17, flow is presented in motion blur format at the various times of Figure 16 on the coat-outlet. At steady-state, a layer of uniform width is achieved, see Figure 17a. When the plate is allowed to move up and down in time by adjusting a nip-gap width, film-thickness varies along

Table III.
Temporal leakage adjustment; P^{mean}, lift (on foil) and drag (on roller), values $\times 10^3$ units

			Lift		Drag	
Protocol	P^{mean}	ampl.	leakage.	n.leakage.	leakage.	n.leakage
alternate Δt	157.9	0.05	1293	1296	1.279	1.305
$10_{\text{l}} - 10_{\text{nl}}$	156.8	0.25	1293	1296	1.278	1.305
$20_{\text{l}} - 50_{\text{nl}}$	157.3	0.55	1293	1299	1.278	1.305
$50_{\text{l}} - 50_{\text{nl}}$	157.8	0.75	1300	1309	1.279	1.279
$100_{\text{l}} - 100_{\text{nl}}$	157.8	1.25	1300	1309	1.279	1.280
std. Setting	159.8	–	1311		1.30	

Table IV.
Global foil shifting to steady state; maxima in P_{nip}, lift (on foil) and drag (on roller), values $\times 10^3$ units

Nip-width % of coat-outlet	Leakage	P_{nip}	Lift	Drag
1%	Nil	160	1311	1.301
2%	0.0044	27	424	1.308
3%	0.0067	16	289	1.247

Table V.
Foil shifting (globally); temporal force variations, values $\times 10^3$ units

Force	Nip-width	$10_{\text{up}} - 10_{\text{reset}}$	$20_{\text{up}} - 50_{\text{reset}}$	$100_{\text{up}} - 100_{\text{reset}}$
Max P_{nip}	2%	31.5–57.6	37.8–102	11.5–113
	3%	15.6–46.8	17.4–94.6	1.9–113
	5%	2.2–38.6	8.5–88.8	−3.2–113
Lift (on foil)	2%	407.5–805	408.3–1128	277–1186
	3%	228.2–722	216.4–1096	136–1181
	5%	49.4–649	37.5–1071	13.1–1181
Drag (on roller)	2%	1.13–1.33	1.14–1.31	1.27–1.31
	3%	1.11–1.24	1.13–1.13	1.25–1.27
	5%	1.08–1.06	1.11–1.14	1.11–1.13

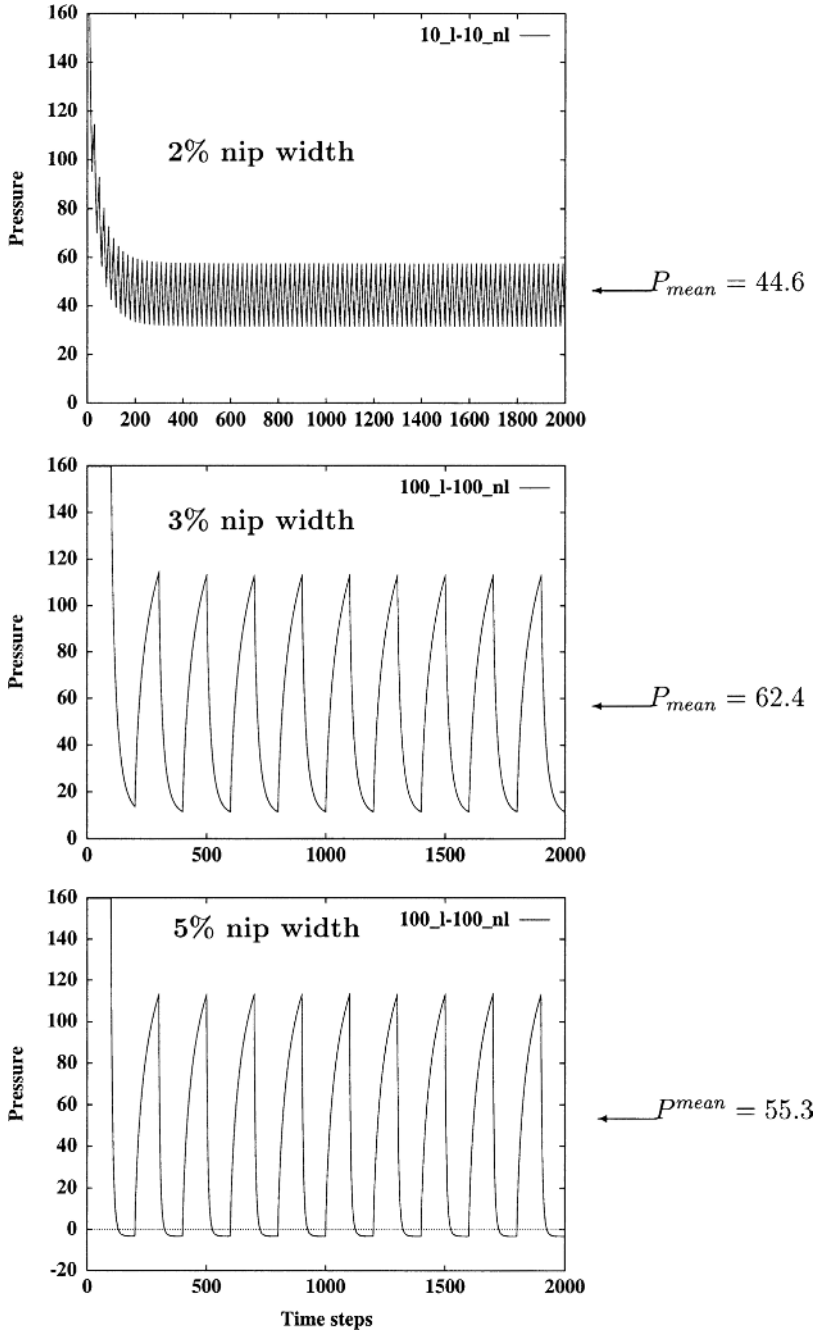

Figure 12.
Global foil shifting; pressure ($\times 10^3$) line plots at nip node N_1, L per cent nip width

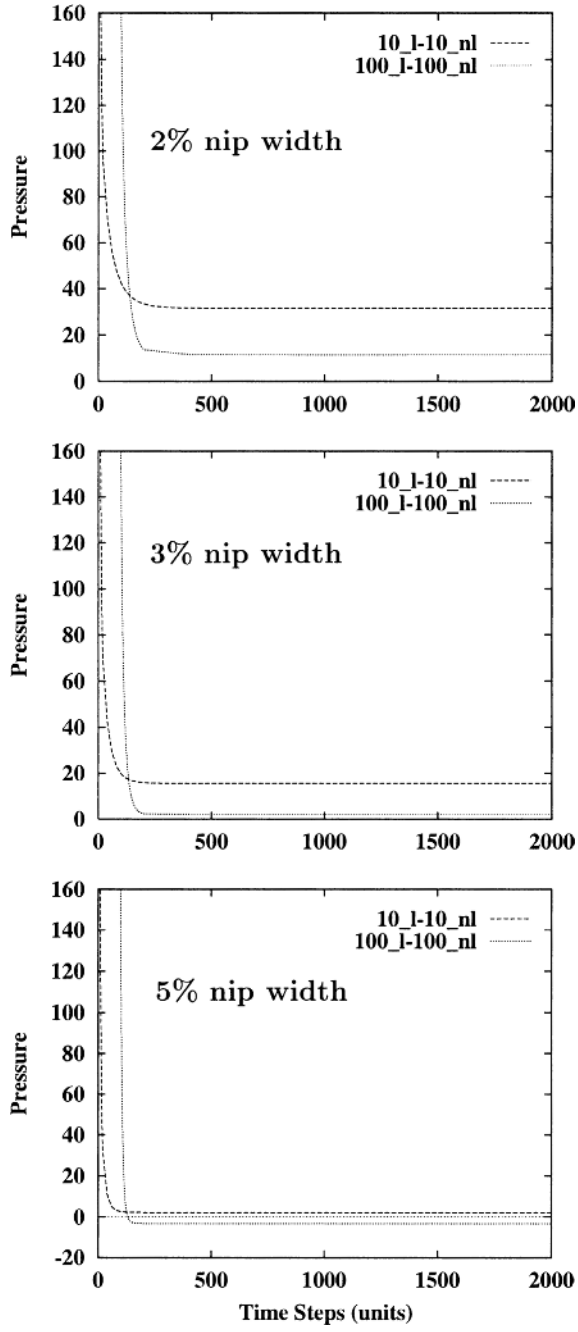

Figure 13.
Global foil shifting; pressure ($\times 10^3$) line plots at nip node N_1, leakage state $P_{\min}(t)$

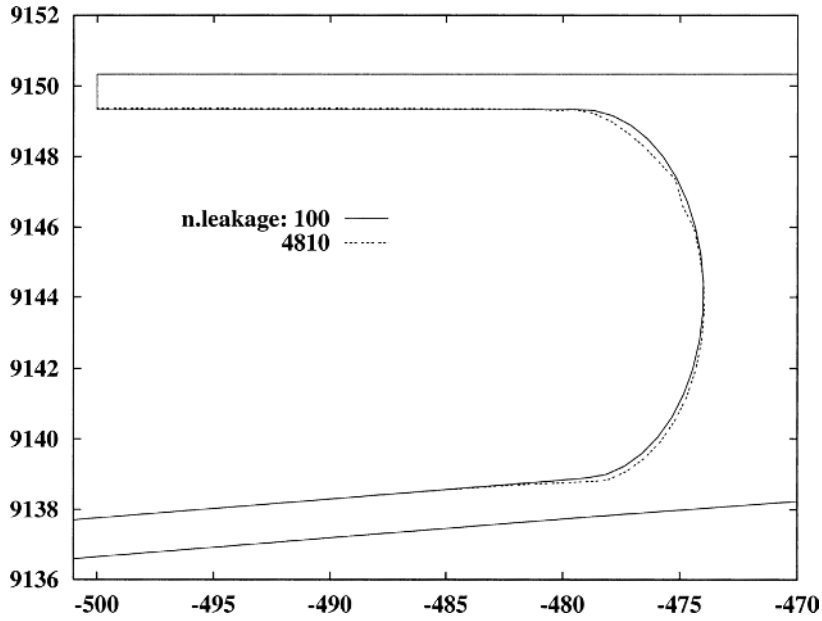

Figure 14.
Global foil shifting; free-surface profile- full view

the strip length. An appropriate criterion is required to constrain the foil vibration, so that the pressure/lift generated remains within acceptable operating levels. We speculate that this may be achieved by selecting suitable leakage/no-leakage times.

4.4 Temporal foil shifting (locally)

The motivation here is to discern whether foil vibration, local only to the nip, may have the same influence as that detected from global foil movement. Here, we are particularly concerned with lift and the adjustment of free-surface shape. The temporal solution response detected thus far, would indicate that local foil vibration may stimulate similar surface-finish fluctuations. Understanding the fundamental physical reasons behind such fluctuations is our goal.

In the preceding sections, it is observed that, the level of forces is fairly low along most of the foil/roller surfaces and rises significantly close to the nip region. Hence, the foil is shifted vertically upwards, in a local fashion, so that it takes up a linear slope of inclination within the nip region extending over a fraction of the foil length (30 per cent, 10 per cent, 4 per cent). Nip conditions are taken as of section 4.2. Maximum values of forces are charted below, and compared against those of section 4.3.1 with standard settings. We observe from Table VI and through Figures 17 and 18, that pressure and lift values,

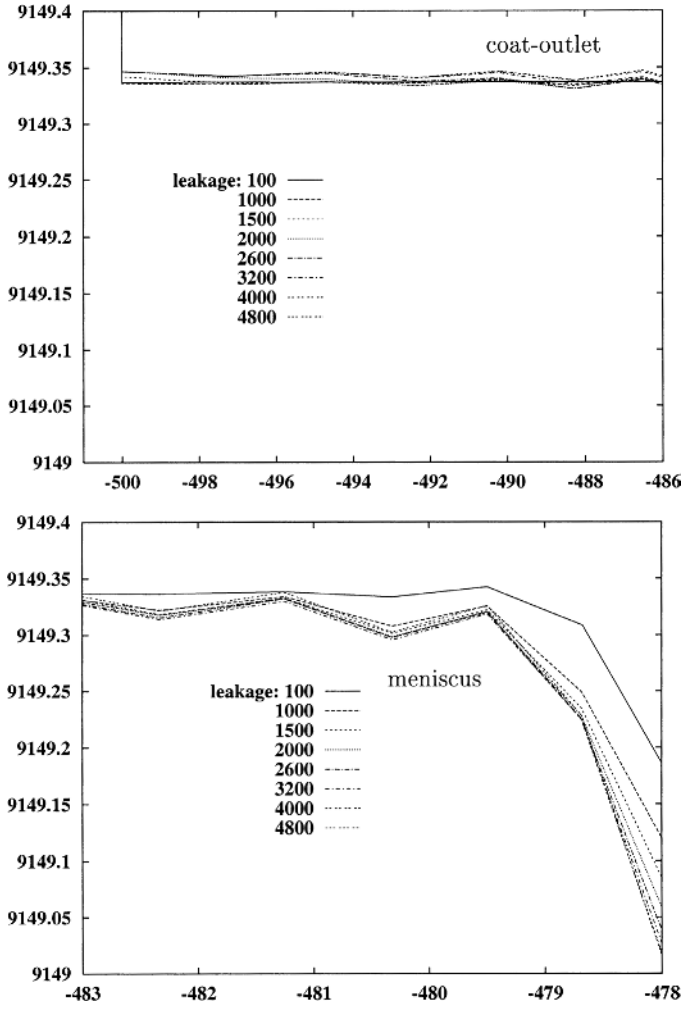

Figure 15.
Global foil shifting; free-surface profiles-meniscus and coat-outlet; 2 per cent nip-width, $100_l - 100_{nl}$ protocol, zoomed view at different time-steps

increase with decreasing length of the slope (approximating more closely to the standard setting). It is the elevation of peak values that varies between settings. The more local the foil shifting, the more elevated the peak pressures reached.

In the comparison of local versus global shifting, it is observed that the extent of disturbance from the nip coincides between global and local tests to within 10 per cent of the foil-length from the nip. This is true in all variables and for the standard no-leakage setting (i.e. time independent). Lift and drag also decrease. It is observed that, despite these differences in forces, both global

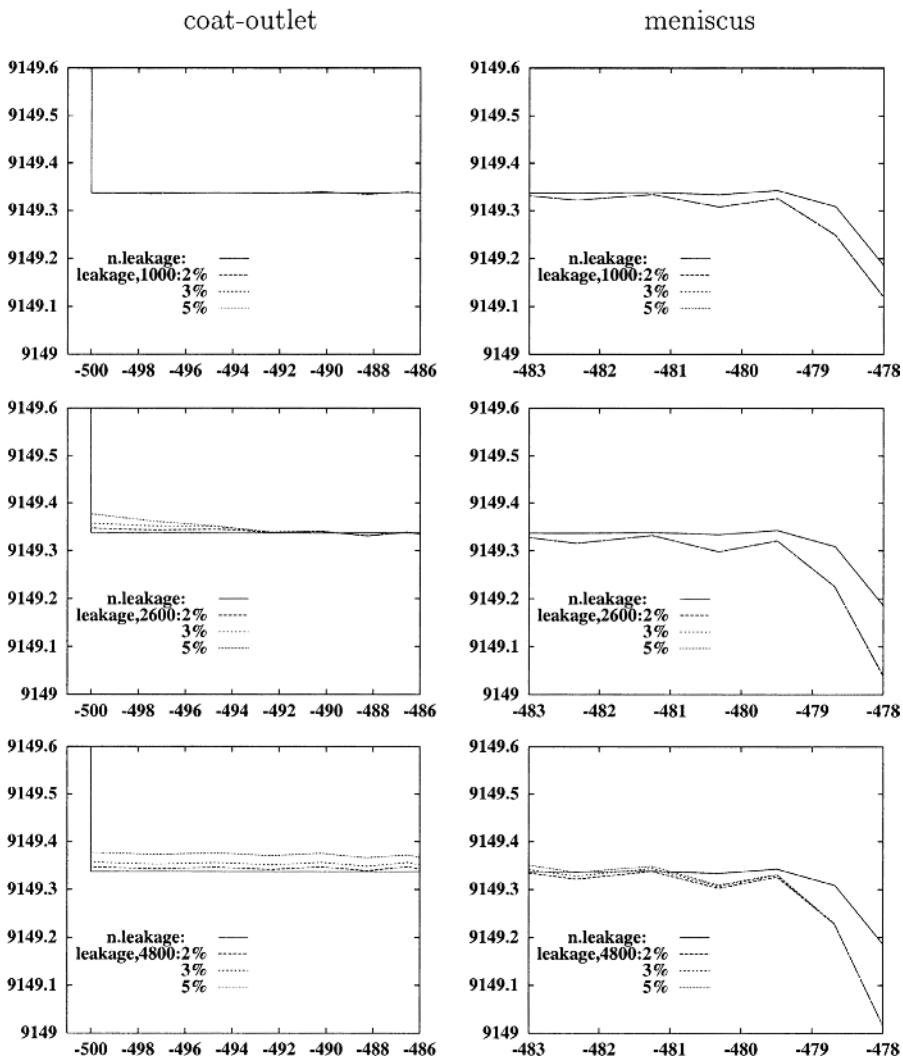

Figure 16.
Global foil shifting; free-surface profiles, meniscus and coat-outlet; comparison at 2 per cent, 3 per cent and 5 per cent nip-width, $100_{l} - 100_{nl}$, zoomed view; times 1000, 2600, 4800 (time step numbers)

and local settings have the same influence over the coat-outlet free-surface region, see Figure 19.

5. Conclusions

Generally, it is noted that when fluid travels on a coating roller, which is moving in the opposing direction to a foil, a pressure build-up will develop against whichever surface is moving with the greater differential speed. Under

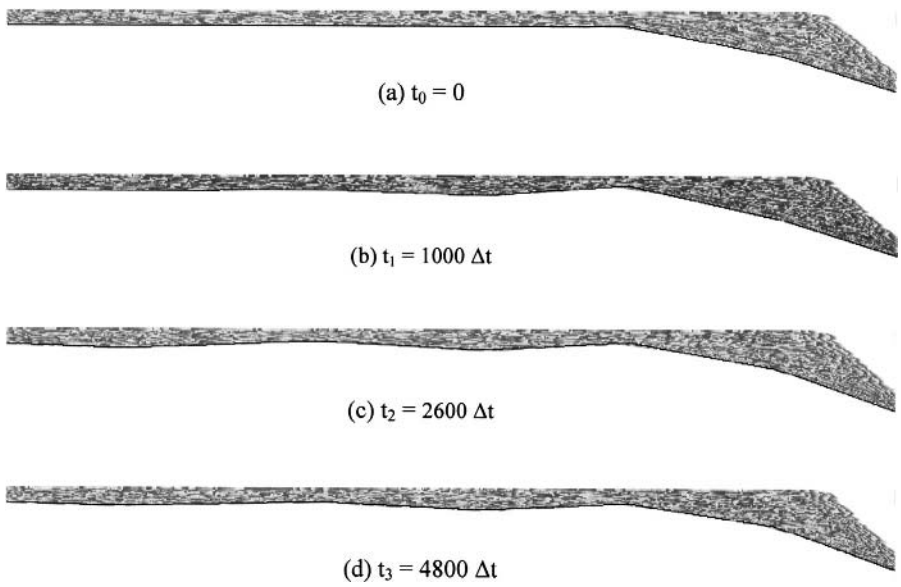

Figure 17.
Global foil shifting; coat-outlet free-surface profiles, motion blur format, different times (t_0, t_1, t_2, t_3)

Table VI.
Comparison between global and local foil-shifting, at 2 per cent nip-width, $10_l - 10_{nl}$ protocol

Force $\times 10^3$ units	Global foil-shifting	30% foil_l	10% foil_l	4% foil_l	(Standard nl)
Max P_{nip}	31.5–57.6	71.5–83	81.0–88	105–110	160
Lift (on foil)	408.– 805	833–917.5	1025–1081	1191–1458	1311
Drag (on roller)	1.13–1.33	1.21–1.36	1.24–1.36	1.11–1.35	1.301

the present circumstances, it is generally the foil that moves with greater speed. When the pressure build-up reaches a threshold, the foil will rise away from the roller. This will create a widening of the gap (nip-width) between foil and roller. As a consequence, there will be relief of pressure that will act to bring the foil back down upon the roller. This sequence of events will generate temporal foil vibration. In this regard, a major observation of the present study emerges. Disturbances on the $coat_{outlet}$ free-surface may be associated primarily with foil-vibration, either of a global or local nature. These oscillations begin at the meniscus free-surface region and propagate towards the $coat_{outlet}$ region. Vibration in the free-surface profiles has been demonstrated at different time-step protocols, under various L per cent foil shifting, and in both leakage and no-leakage states. It is observed that the disturbance ratio factor on the $coat_{outlet}$ free-surface is around 2 per cent for all leakage settings, once a settled periodic state has been established.

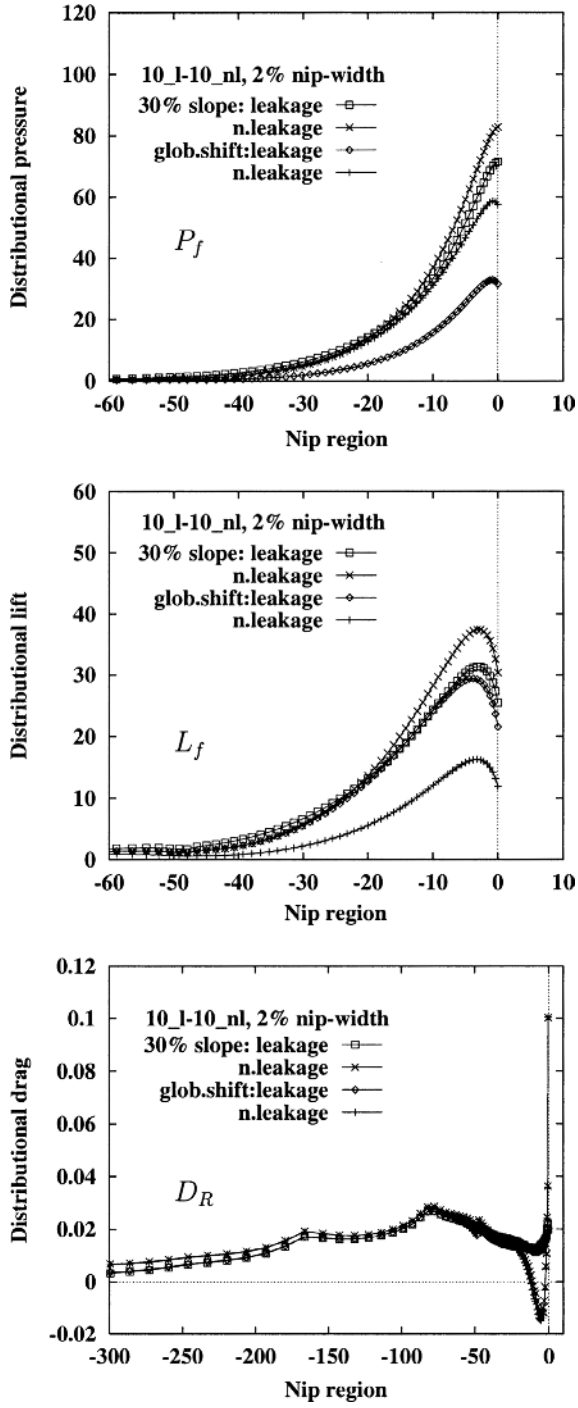

Figure 18.
Comparison of settled distributional pressure (P_f) and lift (L_f) along foil, and drag (D_R) on roller; values $\times 10^3$: global foil shifting verses local foil shifting (slope over 30 per cent of foil length)

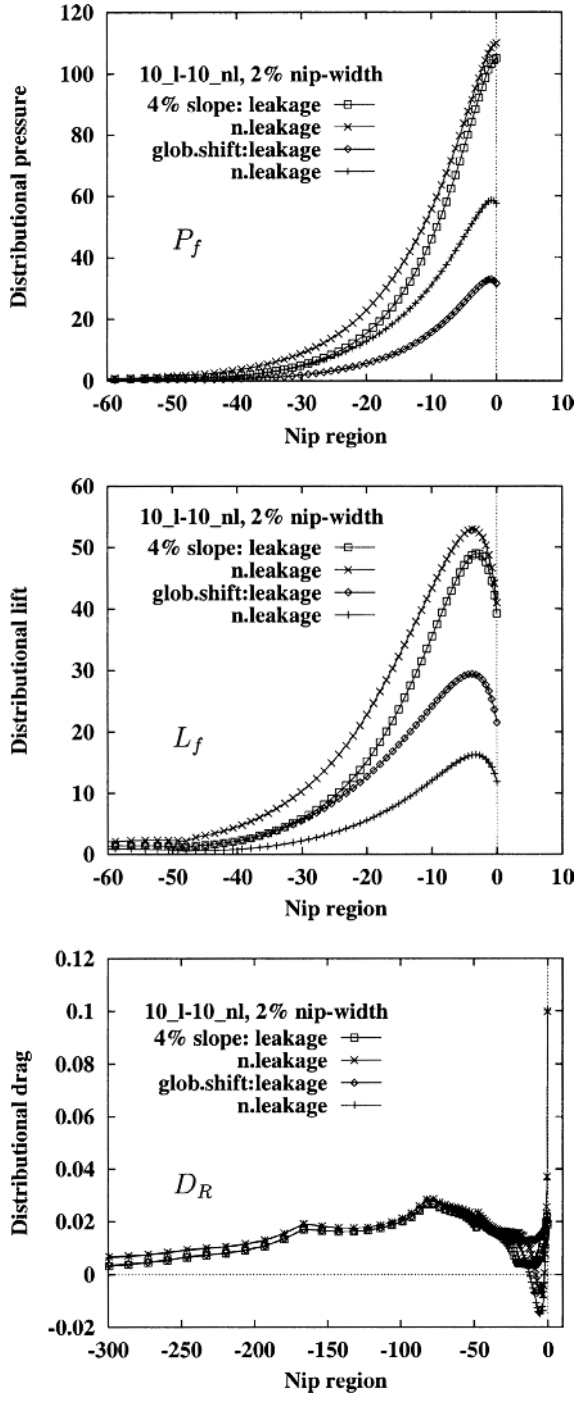

Figure 19.
Comparison of settled distributional pressure (P_f) and lift (L_f) along foil, and drag (D_R) on roller; values $\times 10^3$: global foil shifting verses local foil shifting (slope over 4 per cent of foil length)

References

Benjamin, D.F. Roll Coating Flows and Multiple Flow Systems PhD. Thesis University of Minnesota, Minneapolis, MN, University Microfilms Int., Ann. Arbor, MI.

Carvalho, M.S. and Scriven, L.E. (1997a), "Multiple States of a Viscous Free-Surface Flow: Transition from Pre-metered to a Metering Flow", *Int. J. Num. Meth. Fluids*, 24, pp. 813-31.

Carvalho, M.S. and Scriven, L.E. (1997b), "Deformable Roll Coating Flows: Steady State and Linear Perturbation Analysis", *J. Fluid Mech.*, 339, pp. 143-72.

Chandio, M. S. and Webster, M. F. *Numerical simulation of viscous free-surface flows for reverse roller-coating*, under review in Int. J. Num. Meth. Heat Fluid Flow (available as CSR 8-2001).

Chen, K. S. A. and Scriven, L. E. *Roll Coating, Forward and Reverse: Effect of Feed Condition*; AIChE Spring Nat. Meet., New Orleans, LA 1988.

Cohu, O. and Magnin, A. (1997), "Forward Roll Coating of Newtonian Fluids with Deformable Rolls: An Experimental Investigation", *Chem. Eng. Sci.*, 52 No. 8, pp. 1339-47.

Carew, E.O.A., Townsend, P. and Webster, M.F. (1993), "A Taylor-Petrov-Galerkin Algorithm for Viscoelastic Flow", *J. non-Newtonian Fluid Mech.*, 50, pp. 253-87.

Cuvelier, C., Segal, A. and Van Steenhoven, A. A., *Finite Element Methods and Navier-Stokes Equations*, D. Reidel, 1986.

Fourcade, E., Bertrand, F., Régalt, O. and Tanguy, P.A. (1999), "Finite Element Analysis of Fluid-Solid Interaction in the Metering Nip of a Metering Size Press", *Comp. Meth. Appl. Mech. Eng.*, 174, pp. 235-45.

Hawken, D.M., Tamaddon-Jahromi, H.R., Townsend, P. and Webster, M.F. (1990), "A Taylor-Galerkin Based Algorithm for Viscous Incompressible Flow", *Int. J. Num. Meth. Fluids*, 10, pp. 327-51.

Hirt, C.W., Amsden, A.A. and Cook, J.L. (1974), "An Arbitrary Lagrangian-Eulerian Computing Method for All Flow Speeds", *J. Comp. Phys.*, 14, pp. 227-53.

Keunings, R. (1986), "An Algorithm for the Simulation of Transient Visco-Elastic Flows with Free-Surfaces", *J. Comp. Phys.*, 62, pp. 199-220.

Ramaswamy, B. (1990), "Numerical Simulation of Unsteady Viscous Free-Surface Flow", *J. Comp. Phys.*, 90, pp. 396-430.

Regalt, O., Labrie, R. and Tanguy, P.A. (1993), "Free-surface Model for Dip Coating Process", *J. Comp. Phys.*, 109, pp. 238-46.

Saito, H. and Scriven, L.E. (1981), "Study of Coating Flow by the Finite Element Method", *J. Comp. Phys.*, 42, pp. 53-76.

Sato, T. and Richardson, S.M. (1994), "Numerical Simulation Method for Viscoelastic Flows with Free Surface-Fringe Element Generation Method", *Int. J. Num. Meths. Fluids*, 19, pp. 555-74.

Silliman, W.J. and Scriven, L.E. (1980), "Separating flow near a static contact line: slip at a wall and shape of a free surface", *J. Comp. Phys.*, 34, pp. 287-313.

Sizaire, R. and Legat, V. (1997), "Finite Element Simulation of a Filament Stretching Extensional Rheometer", *J. non-Newtonian Fluid Mech.*, 71, pp. 89-107.

Townsend, P. and Webster, M. F. *An Algorithm for the Three-Dimensional Transient Simulation of non-Newtonian Fluid Flows*, Proc. NUMETA 87, Martinus Nijhoff, Dordrecht, vol. 2 T12/1 (1987).

Tanner, R.I., Nickell, R.E. and Bilger, R.W. (1975), "Finite Element Method for the Solution of Some Imcompressible non-Newtonian Fluid Mechanics Problems with Free Surfaces", *Comp. Meth. App. Mech. Eng.*, 6, pp. 155-74.

Viscoelastic computations of polymeric wire-coating flows

H. Matallah, P. Townsend and M.F. Webster
Institute of Non-Newtonian Fluid Mechanics, University of Wales, Swansea, UK

Keywords *Coatings, Finite elements, Flow*

Abstract *This study considers both a single and multi-mode viscoelastic analysis for wire-coating flows. The numerical simulations utilise a finite element time-stepping technique, a Taylor-Petrov-Galerkin/pressure-correction scheme employing both coupled and decoupled procedures between stress and kinematic fields. An exponential Phan-Thein/Tanner model is used to predict pressure-drop and residual stress for this process. Rheometrical data fitting is performed for steady shear and pure extensional flows, considering both high and low density polyethylene melts. Simulations are conducted to match experimental pressure-drop/flowrate data for a contraction flow. Then, for a complex industrial wire-coating flow, stress and pressure drop are predicted numerically and quantified. The benefits are extolled of the use of a multi-mode model that can incorporate a wide-range discrete relaxation spectrum to represent flow response in complex settings. Contrast is made between LDPE and HDPE polymers, and dependency on individual relaxation modes is identified in its contribution to overall flow behaviour.*

1. Introduction

In the field of polymer coating of wires, experimental studies are extremely difficult to perform due to the small size of the dies and minute volume of polymer melt within the region of interest. This leads to the need for numerical simulation as a predictive aid to optimise the process via die design and flow modelling. This allows for the analysis of variation in certain key parameters, without having to resort to trial-and error expensive and difficult experiments. There are two basic types of cable or wire-coating die designs commonly employed. These are represented schematically in Figure 1, and are termed pressure and tube-tooling designs. In pressure-tooling, the melt is driven under pressure making contact with the wire inside the die. In contrast, for tube-tooling, the melt is drawn down by the motion of the wire and the melt is extruded beyond the die. In both instances, the geometry is annular in cross section. The setting of the flow geometry is found to be crucial in obtaining optimal coatings.

There have been a number of studies that have addressed the modelling of wire-coating flows; see for example Fenner and Williams (1967); Caswell and Tanner (1978), Mitsoulis (1986); Mitsoulis *et al.* (1988); Huang *et al.* (1994); Binding *et al.* (1996) for pressure-tooling, and Gunter *et al.* (1996); Mutlu *et al.*

International Journal of Numerical Methods for Heat & Fluid Flow, Vol. 12 No. 4, 2002, pp. 404-433.

DOI 10.1108/09615530210433279

The authors wish to gratefully acknowledge the financial support and collaboration of BICC Cables Ltd. Thanks is also due to Professor Ken Walters, FRS, Professor Russell Davies and Dr David Binding for their support work on rheological characterisation.

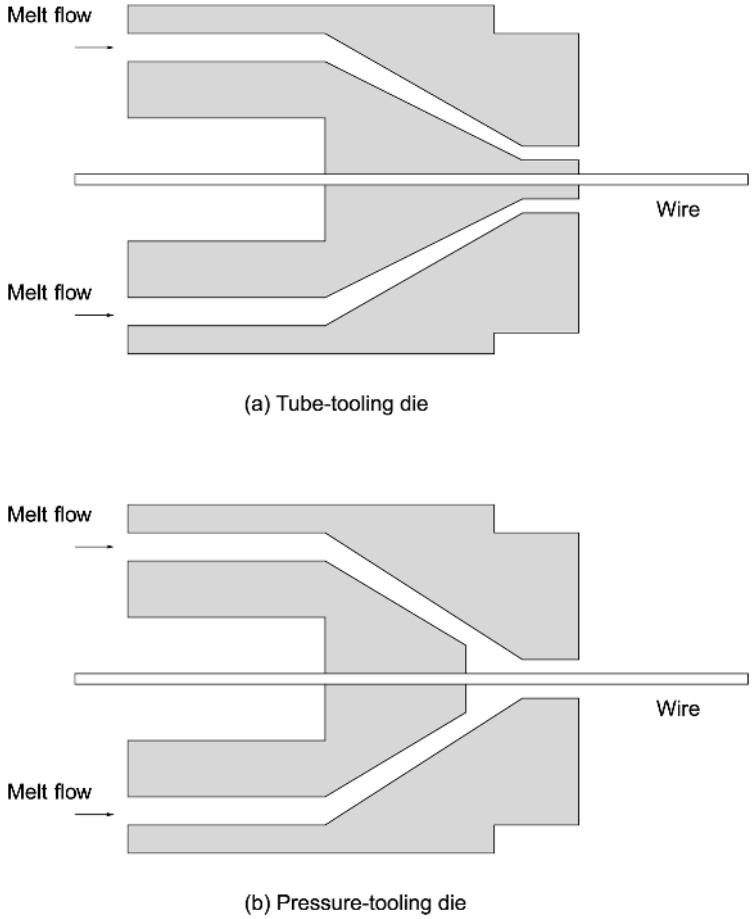

Figure 1.
Schematic diagram of wire coating dies

(1998a); Mutlu *et al.* (1998b); Mutlu *et al.* (1997) for tube-tooling. These have provided some progress within the inelastic, non-isothermal and viscoelastic regimes. In a wider flow and processing context, some recent attempts have been made to embrace differential multi-mode simulations, see for example the works of Baaijens (1994); Baaijens *et al.* (1997); Azaiez *et al.* (1996) and Gupta *et al.* (1997). Such a multi-mode approach for differential constitutive models is more costly, yet can provide a more accurate representation of the material rheology. The present study addresses the significance of employing a multi-mode, as opposed to a single-mode, differential constitutive modelling approach to predict numerically the behaviour of tube-tooling wire-coating flows for two polymer melts, low and high density polyethylene. We concentrate on the quality and significance of numerical predictions attainable from multi-mode approximations in contrast to single-mode alternatives. The modelling assumes

incompressible melt flow, isothermal conditions, no-slip within the die, and an estimated location for the free-surfaces, see Refs. Mutlu *et al.* (1998a); Mutlu *et al.*, 1998b, Practical experience from the process itself provides this location.

We are concerned with two parts of the tube-tooling wire-coating process, namely flow within the die itself and a draw-down flow beyond the die onto the wire cable. The flow is generated by a pressure head and the dragging action of the moving wire. This type of tooling design is prevalent for wide bore cables, or outer coatings of multi-cable combinations. Cable speed is taken as 0.334 m/s. The main goal of modelling such a complex industrial problem is to achieve process optimisation. This is governed typically by minimisation of the flow-induced residual stress locked into the coating, and in addition, acceptable levels of pressure-drop across the die. The flow response of the coating material and the die design (Matallah *et al.*, 2000) both have a role to play in this optimisation procedure. Pressure-drop predictions provide some means of correspondence between simulation and practice.

An exponential Phan-Thien/Tanner (PTT) differential constitutive model is selected to represent the rheometrical behaviour of low and high density polyethylene melts (LDPE and HDPE) in steady shear and uniaxial flow. Typically, such material samples display both shear thinning and strain softening properties and an exponential PTT model is capable of reproducing such behaviour in qualitative form (Phan-Thien and Tanner, 1977; Saramito and Piau, 1994). Simple shear and uniaxial flows are used to evaluate the PTT parameter set (ϵ, ξ), for which a close fit to the experimental data must be established. To calibrate pressure drops as a function of flowrate and compare experimental with predicted observations, a nineteen to one axi-symmetric contraction flow is adopted. For this flow, both single and multi-mode models are implemented. Once optimality in parameter set is established, we turn attention to tube-tooling flow and the multi-mode simulations for LDPE and HDPE polymer coatings.

The numerical implementation is a Taylor-Petrov-Galerkin/pressure-correction scheme that involves a finite element time-stepping technique (Matallah *et al.*, 1998), in conjuction with a recovery scheme to capture continuous velocity gradients. Both decoupled and coupled numerical approaches have been employed previously for a single mode analysis (Mutlu *et al.*, 1998a), where the results were found to be comparable. Here, only coupled solutions are considered for single-mode computations. For efficiency and pragmatism, multi-mode calculations are performed via a decoupled approach. This strategy is supported by the fact that in many flows the kinematics themselves do not vary significantly with variation of material (Pearson and Richardson, 1983), and hence a reasonable approximation is a linearisation of the system, adopting frozen coefficients and Picard iteration. This implies segmenting the equations of the complete system into those for stress and kinematics separately, computing each to a steady state with frozen

coefficients. We note here that the choice of initial frozen kinematic fields are taken as associated with viscoelastic and shear thinning behaviour. Such a *pragmatic* approach is adopted similarly by others (see Schoonen *et al.* (1998), but with fixed inelastic kinematics).

Single mode modelling is pragmatic, recognised as qualitative not quantitative, and yet effective in terms of relatively low computational cost. A flowrate-maximum shear rate relationship may be established for a particular material and flow, such as within a contraction flow. Once this behaviour has been determined, such knowledge may be employed to seek an acceptable rheometrical parameter fit within a neighbourhood of the maximum shear rate, referencing standard viscometric flows. This model specification may then be utilised to predict behaviour in a more general complex flow, such as in a wire-coating setting. To satisfy such criteria, single-mode modelling unfortunately leads to continually having to adjust parameter fits to suit each different flow problem (with flowrate). In this regard, preference shifts to the multi-mode scenario. In contrast, multi-mode modelling with single choice of rheological parameters provides a closer match to the shear viscosity data over a range of shear rates. This facilitates consistent and wide ranging application for complex flows without parameter adjustment. In addition it is possible in the multi-mode context, to identify the contribution of each mode to the total stress and hence determine the most dominant component.

We commence with a single-mode analysis for a Phan-Thien/Tanner (PTT) model and consider the fitting of this model to the rheometrical data of Walters *et al.* (1994), supplied for two independent case studies. The first is essentially a parameter fitting study for viscometric flows, steady simple shear and pure extension. Fitting of the various material parameters (ϵ, ξ and μ_1) is investigated for shear viscosity in shear flow. Likewise, elongational viscosity behaviour is charted under steady uniaxial extension, according to a Binding analysis for contraction flow (Binding, 1988). The second case study, involves simulations for a more complex flow, the contraction flow (Walters *et al.*, 1994). Here, selected combinations of material parameters, that represent different fluids recommended from the first case study, is employed at different flowrate settings. Of course, ideally one requires a model that for one set of parameters approximates flow over a wide range of conditions. The single mode case proves inadequate for this task. Quantitative agreement is sought on predicted pressure-drop against the available experimental pressure-drop/flowrate data.

The ultimate objective of this work is to relate the significance and sensitivity of the match for the chosen constitutive model to the flow response of the polymer melts in question, under tube-tooling processing conditions. Proceeding in a structured manner from the preliminary case studies above, a single-mode analysis is conducted for this complex industrial flow. Particular attention is paid to pressure-drop and stress build-up across the flow from entry to exit. A second aspect to this work carries over to a multi-mode

analysis, under which the three problem settings outlined above are revisited, see (Azaiez *et al.*, 1996; Quinzani *et al.*, 1990) for motivation. From a single-mode analysis it is observed that pressure-drop prediction is sensitive to the determination of the material parameters of the PTT model. These are governed by the maximum shear rate sustained in the process at any specific flowrate. Nevertheless, for the complex industrial flows of interest, that involves flow through a tube-tooling die and draw-down section, experimental data is unavailable. Hence for guidance, we turn to a comparison between single and multi-mode model simulations to provide greater insight on the underlying flow behaviour of principle significance.

2. Governing equations and constitutive model

The flow of shear and elongational thinning LDPE and HDPE fluids is modelled using a multi-mode Phan-Thien/Tanner (PTT) model, invoking both single and multi-mode approximations. The momentum and continuity equations are given as

$$\rho \frac{\partial \boldsymbol{u}}{\partial t} = \nabla \cdot \boldsymbol{\tau} - \rho \boldsymbol{u} \cdot \nabla \boldsymbol{u} - \nabla p, \tag{1}$$

$$\nabla \cdot \boldsymbol{u} = 0, \tag{2}$$

with velocity vector $\boldsymbol{u}$, fluid density ρ, pressure p, stress $\boldsymbol{\tau}$, time t and rate of deformation tensor $\boldsymbol{D} = (\nabla \boldsymbol{u} + \nabla \boldsymbol{u}^{+})/2$. Within the single mode approximation, the stress $\boldsymbol{\tau}$ is decomposed into two parts, viscous and polymeric parts viz

$$\boldsymbol{\tau} = \boldsymbol{\tau}_1 + 2\mu_2 \boldsymbol{D}, \tag{3}$$

for which μ_2 is a solvent viscosity. The extra stress tensor $\boldsymbol{\tau}_1$ is then defined by

$$f\boldsymbol{\tau}_1 + \lambda_1 \overset{\square}{\boldsymbol{\tau}}_1 = 2\mu_1 \boldsymbol{D}, \tag{4}$$

$$\overset{\square}{\boldsymbol{\tau}}_1 = \left(1 - \frac{\xi}{2}\right) \overset{\nabla}{\boldsymbol{\tau}}_1 + \frac{\xi}{2} \overset{\nabla}{\boldsymbol{\tau}}_1 = \overset{\nabla}{\boldsymbol{\tau}}_1 + \xi(\boldsymbol{D} \cdot \boldsymbol{\tau}_1 - \boldsymbol{\tau}_1 \cdot \boldsymbol{D}), \tag{5}$$

where f is given by

$$f = \exp\left[\frac{\epsilon \lambda_1}{\mu_1} \mathrm{trace}(\tau_1)\right], \tag{6}$$

see Phan-Thien and Tanner (1977); Phan-Thien, 1978. Material parameters λ_1 and μ_1, represent relaxation time and polymeric viscosity, respectively. The zero shear viscosity is then

$$\mu_0 = \mu_1 + \mu_2. \tag{7}$$

Model parameters ($\epsilon \geq 0$), ($0 \leq \xi \leq 2$) are non-dimensional parameters that can be evaluated by fitting to experimental data. ∇ and Δ are upper and

lower-convected derivatives, whose combination introduces second normal stress effects.

The PTT model has been chosen because of its shear thinning and strain softening properties, as displayed by the melts in question. Within the complex flows of interest both shear and extension are present. It is instructive, therefore, to analyse the PTT model response in pure shear and extension in isolation. With this in mind, we first present the theoretical response of this model in ideal flows, for which we are able to conduct a multi-variate sensitivity analysis in (ϵ, ξ, μ_1) against experimental values of shear viscosity μ_s and extensional viscosity μ_e given by Walters *et al.* (1994). It is found appropriate to first seek an optimal fit to the shear viscosity, prior to qualifying goodness of fit to extensional viscosity, see below.

In the multi-mode context, the equations of state are given for each mode (i) as

$$f_i \boldsymbol{\tau}_i + \lambda_1^i \overset{\square}{\boldsymbol{\tau}_i} = 2\mu_1^i \boldsymbol{D}, \tag{8}$$

where the total stress is

$$\boldsymbol{\tau} = \sum_i \boldsymbol{\tau}_i, \tag{9}$$

and f_i is defined as above, but with respect to each mode (i). Accordingly, λ_1^i represents the relaxation time of each mode. A vanishing solvent viscosity is considered in the multi-mode case i.e. $\mu_2 = 0$ appropriate for polymer melts, so that here the partial zero-shear viscosity for each mode (i) is $\mu_0^i = \mu_1^i$. In this case, ϵ is the only parameter that is varied, as ξ is chosen to be zero, see on. Hence Equations. 8 and 9 are solved with Equation 1 and 2 for momentum and continuity.

In completely general form, retaining a solvent contribution we consider a steady simple shear flow with shear rate $\dot{\gamma}$. Following (Arsac *et al.*, 1994), the representation of the total shear viscosity μ_s over all modes is the sum of the partial shear viscosities, viz.

$$\mu_s(\dot{\gamma}) = \mu_2 + \sum_i \frac{\mu_1^i f_i}{f_i^2 - (\lambda_1^i \dot{\gamma})^2 \xi(2-\xi)}, \tag{10}$$

where each f_i satisfies

$$\left\{ f_i^2 + \left(\lambda_1^i \dot{\gamma}\right)^2 \xi(2-\xi) \right\} \ln(f_i) - 2\epsilon \left(\lambda_1^i \dot{\gamma}\right)^2 (1-\xi) = 0. \tag{11}$$

Accordingly, first and second normal stress-differences, N_1 and N_2 respectively, are defined as

$$N_1(\dot{\gamma}) = \sum_i \frac{2\mu_1^i \lambda_1^i \dot{\gamma}^2}{f_i^2 + (\lambda_1^i \dot{\gamma})^2 \xi(2-\xi)}, \tag{12}$$

$$N_2(\dot{\gamma}) = -\frac{\xi}{2} N_1(\dot{\gamma}). \tag{13}$$

In contrast, for a single mode approximation, the summation collapses to a single term.

In steady uniaxial extension, the elongational viscosity μ_e is a function of extension rate $\dot{\epsilon}$, of the form

$$\mu_e(\dot{\epsilon}) = 3\mu_2 + \sum_i \frac{2\mu_1^i}{f_i^2 - 2\lambda_1^i \dot{\epsilon}(1-\xi)} + \frac{\mu_1^i}{f_i + \lambda_1^i \dot{\epsilon}(1-\xi)}, \tag{14}$$

where each f_i is now determined from

$$\left\{ f_i^2 - \lambda_1^i \dot{\epsilon}(1-\xi) - 2(\lambda_1^i \dot{\epsilon})^2 (1-\xi)^2 \right\} \ln(f_i) - 6(\lambda_1^i \dot{\epsilon})^2 \epsilon (1-\xi) = 0. \tag{15}$$

Equations (11) and (15) are solved in each case for the relevant f_i through a Newton-Raphson iteration, from which μ_s, μ_e, and N_1 may be determined. We note that via Equation 13 the second normal stress-difference, N_2, may be expressed via dependency on ξ and N_1. In this form, it may be observed that as ξ tends to zero then so does N_2. Hence, in the multi-mode context, where ξ is taken as zero for simplicity, this implies vanishing N_2, which in turn justifies the setting of $\mu_2 = 0$.

3. Numerical scheme

Single-mode solutions are generated employing a coupled procedure previously described in detail in (Matallah *et al.*, 1998). The coupled scheme involves solving for kinematics and stress simultaneously. The implementation is a fractional-stage time stepping scheme, woven around a pressure-correction method, that involves some three stages within each time step. The first stage solves for velocity and stress, in a predictor-corrector doublet. The second stage, solves for a pressure temporal increment. The third stage computes a correction to the velocity field, enforcing incompressibility at each time step to the order of the scheme. The scheme embodies implicit and explicit treatment simultaneously, and hence is of classical semi-implicit type. Diffusion terms are approximated with a Crank Nicolson discretisation over a time step, which introduces implicitness and stability for these viscous flows. A direct method of solution is employed to solve for the pressure equation step, whilst indirect Jacobi iteration is invoked for the remaining stages. Also, the benefits are realised of stability enhancing recovery-based methods and consistent streamline upwinding procedures, that are incorporated within the implementation (Zienkiewicz and Zhu, 1995; Matallah *et al.*, 1998). For these single-mode coupled calculations a continuation procedure in relaxation time parameter is employed to reach a specific value of λ_1^{spec}, chosen appropriately, (see on for discussion).

With a multi-mode decoupled procedure, a frozen kinematic field corresponding to a single-mode solution (λ_1^{spec}) is used in Equation (8) to solve for stress components and each mode (i) of the PTT model in parallel, corresponding to (λ_1^i, μ_1^i) parameters. For simplification, in the multi-mode context, the solvent part of the viscosity $\mu_2 = 0$, and hence for the polymeric part of each mode (i), μ_1^i may be replaced by the partial zero-shear rate viscosity μ_i, and the relaxation time λ_1^i by λ_i. Non-dimensional numbers are defined as follows. For each mode (i), a Weissenberg number is

$$\text{We}^i = \lambda_i \frac{U_{ch}}{L_{ch}}, \tag{16}$$

where, U_{ch}, L_{ch} are velocity and length scales, respectively. An average single mode λ_1^{spec} is estimated from the experimental data following the procedures outlined in Ref. Gunter *et al.* (1995). This value is gathered from the base material function fits to satisfy μ_s, μ_e, N_1. For the LDPE polymer, λ_1^{spec} is taken as 5s, giving a Weissenberg number of We^{spec} of 28 according to Equation 16. Similarly, λ_1^{spec} is 9s for HDPE polymer, from which We^{spec} equals 50.

The total zero-shear viscosity is given viz

$$\mu_0 = \sum_i \mu_i. \tag{17}$$

Also, the shear elastic modulus g_i for each mode (i), is defined as

$$g_i = \frac{\mu_i}{\lambda_i}. \tag{18}$$

Time steps of $O(10^{-3}–10^{-4})$ are used and convergence to a steady state is monitored via a relative temporal increment norm on the solution taken to a tolerance of $O(10^{-6})$. A summary of the steps in the numerical procedure is provided as follows:

Stage 1: calculate a Newtonian field ($\boldsymbol{u}$, p), as in Ref. Hawken *et al.* (1990).

Stage 2: Starting from the Newtonian solution and quiescent initial stress conditions a single-mode viscoelastic solution is calculated for λ_1^{spec}. The Recovery coupled scheme is used with a solvent viscosity of $\mu_2 = 0.01\mu_0$. Thus, viscoelastic kinematics are derived.

Stage 3: Commencing from such a single-mode solution, each of the three stress modes is calculated in a decoupled sense, on resetting the solvent viscosity to zero and freezing the viscoelastic kinematics. For each mode (i), the viscosity, pressure and stress are non-dimensionalised as follows

$$(\mu^i)^* = \frac{\mu^i}{\mu_0^i} = 1, \quad p = \mu_i \frac{U_{ch}}{L_{ch}} p^* \quad \text{and} \quad \boldsymbol{\tau}_i = \mu_i \frac{U_{ch}}{L_{ch}} \boldsymbol{\tau}_i^* \tag{19}$$

Stage 4: The total stress is then calculated through Equation 9. Updated velocity and pressure fields are recomputed by freezing the total stress. Here nondimensionalisation is performed according to the total zero-shear viscosity μ_0 given by Equation 17. After a single pass, this procedure is noted to correct the pressure filed, meanwhile variation in the velocity field is found to be insignificant, so that further computation is found subsequently to be unnecessary.

4. Parameter fitting for steady shear and pure extension

4.1 Single mode analysis

Under a single mode analysis, which can be taken as qualitative only, we consider the case of an LDPE polymer. The investigation into parameter sensitivity commences with the polymeric viscosity coefficient μ_1. The zero shear viscosity is estimated as 54,700 Pa.s. Employing different fits to the experimental shear data, a single mode relaxation time is evaluated as λ_1 of 5s for LDPE, as cited above (see also Gunter *et al.*, 1996; Mutlu *et al.*, 1998a; Walters *et al.*, 1994). The density ρ for both polymers considered is 760 Kg/m^3.

4.1.1 μ_1 variation. Theoretically in steady shear flow, by increasing the parameter μ_1 and keeping (ϵ, ξ) fixed, the PTT model thins at high shear rates and accordingly, will give rise to diminishing pressure-drop due to decreasing flow resistance. When $\mu_1 = 0$, there is no polymeric contribution. In Figure 2a, we indicate that the μ_1 parameter (recorded in non-dimensional form) plays an important role when the range of the shear rates is high. As the shear rates observed experimentally (Walters *et al.*, 1994) increase, it is necessary to adjust μ_1 to match the data for any isolated shear rate extrema. The inadequacy of a fixed parameter is clearly apparent here in contrast to the multi-mode model (see on). Experimental data were measured for shear viscosity at shear rates between $0.1\,s^{-1}$ to $1\,s^{-1}$ and $10\,s^{-1}$ to $10^3\,s^{-1}$. On the other hand in steady uniaxial extension, the extensional viscosity for the LDPE fluid exhibits strain-softening at high strain-rates, as illustrated in Figure 2b. Such materials may display some hardening at low strain-rates. The PTT model displays a slight increase of the extensional viscosity at extension rates less than unity, before decreasing to a high strain rate limiting plateau. The experimental measurements for elongational viscosity were taken between strain rates of $10\,s^{-1}$ and $10^3\,s^{-1}$. We comment that the Binding Analysis, used here to derive the experimental μ_e data, is an approximate theory (Binding, 1988; Cogswell, 1972; Binding, 1993; Binding *et al.*, 1998). The only difference observed in the fit for different settings of μ_1 is in the tail of the curve at high strain rates. As in Figure 2, larger values of μ_1 that asymptote to unity, tend to inherit viscosity behaviour of lesser μ_1 values over lower shear rate ranges. However, it is necessary to gradually increment values of μ_1 towards unity for reasons of numerical convergence in the continuation procedure.

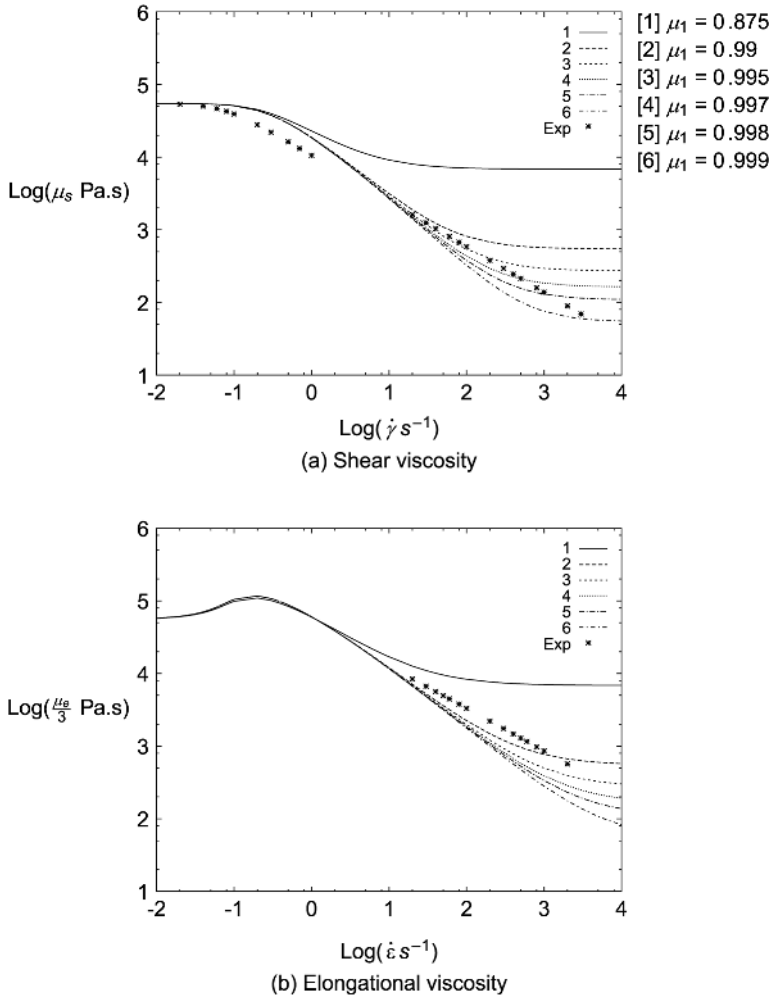

Figure 2.
Shear and elongational viscosities fits; μ_1 variation, $\epsilon = 0.15$, $\xi = 0.02$.

4.1.2 ϵ variation. We proceed to analyse the effect of increasing ϵ at fixed (ξ, μ_1). In steady shear flow, the viscosity of the PTT model decreases correspondingly, but at a lower rate than with increase of μ_1. Shear thinning behaviour of this form, with increasing ϵ, will generate a decrease in pressure-drop. In Figure 3a with $\epsilon = 0.15$, the PTT model provides a near-optimal least squares fit across the complete range of shear rates displayed, for a match to the experimental data at a maximum value of $\dot{\gamma} = 10^3\,\mathrm{s}^{-1}$. In contrast, a best fit for shear rates less than $10\,\mathrm{s}^{-1}$ is for a value of $\epsilon = 0.7$. Switching to uniaxial extension, a reduction in elongational viscosity with increase in ϵ is observed, yet without influencing the asymptotic plateau at high strain rates. Clearly,

here there is only limited experimental data available and the model can only give a qualitative representation of elongational behaviour.

4.1.3 ξ variation. Finally, adjusting the parameter ξ for constant values of μ_1 and ϵ, gives a decrease in the shear viscosity for increasing ξ. At high values of $\epsilon = 1.0$, there is barely any change in the shear viscosity for $0 \leq \xi \leq 0.1$. Some departure from the experimental values is noted at the lower value of $\epsilon = 0.15$ for $\xi = 0.1$. The elongational viscosity is unaffected by such minor adjustment in parameter ξ, that is with the exception of $\xi = 1$, for which a constant elongational viscosity is derived. The comment above regarding quality of representation also applies here.

4.2 Multi-mode analysis

Table I provides material data for LDPE and HDPE polymers at a temperature of 200°C (Davies *et al.*, 1996), in the form of relaxation times and partial zero-shear rate viscosities for a three-mode approximation. The *fits* to the shear data yield zero-shear viscosities of 105,390 and 139,184 Pa.s for LDPE and HDPE, respectively. Note, the variation to the single-mode case is due to the difference in parameters that alters the fits. Any solvent viscosity contribution is taken as minuscule for the polymer melts of interest, simply a mathematical convenience to both aid data fitting and numerical convergence. For a melt any solvent contribution is insignificant in practice; hence in the multi-mode context, μ_2 is assumed to vanish. Here, this is made practically possible from a numerical standpoint via the decoupled approach employed. Also, the second normal stress difference (N_2) is negligible compared with the first normal stress difference (N_1). Hence from Equation 13, the value of the non-dimensional parameter ξ is small, and to simplify the analysis can be taken as zero. To estimate the remaining parameter ϵ, the shear viscosity is plotted against the shear rate in Figure 3a for LDPE and Figure 4a for HDPE with various values of ϵ. For both materials, the best fit for $10^2 \leq \dot{\gamma} \leq 10^3\,\mathrm{s}^{-1}$ corresponds to a value of ϵ of unity. At such a value, we observe from both Figures 3b and 4b, the elongational viscosity (μ_e) fits provide appropriate trends in general behaviour, but gives a lower estimated value than the limited set of experimental data. This is due to the inability of the PTT model to match both shear and elongational data simultaneously.

Table I.
Material parameters

	LDPE			HDPE		
	λ_i(s)	μ_i (*Pa*.s)	$g_i = \mu_i/\lambda_i$	λ_i(s)	μ_i(*Pa*.s)	$g_i = \mu_i/\lambda_i$
Model 1	0.017	1234	72588	0.017	2792	164222
Model 2	0.87	15982	18370	0.87	19595	22523
Model 3	33.9	88174	2601	59.57	116797	1961

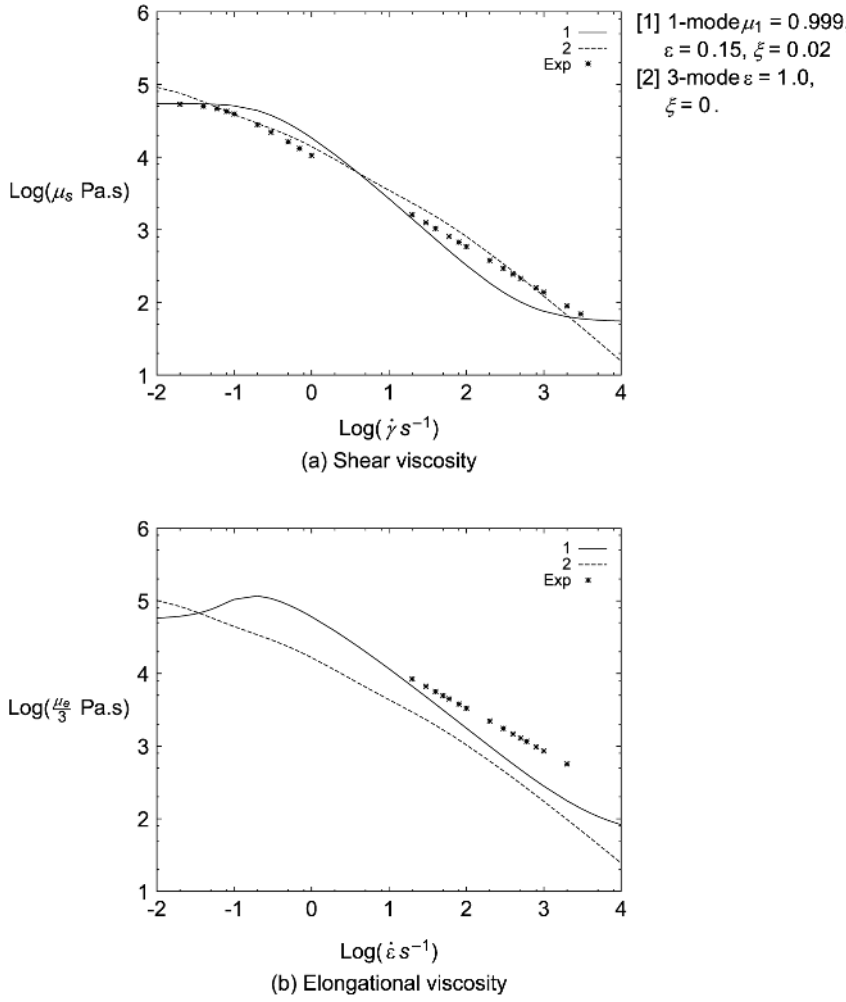

Figure 3.
Single and multi-mode fits for LDPE

From the knowledge gained through the single-mode study, we observe that the key factor to estimating the pressure-drop accurately in complex flows (see below) is the quality of fit to the shear viscosity "in situ" at the associated maxima of shear rate. Bearing this point in mind, in Figure 3 for LDPE we compare shear and elongational viscosity fits to the experimental data for both the single mode of $\lambda_1 = 5\,\mathrm{s}$ (from above) and a three-mode model. In general, and accordance with Figure 3a for shear viscosity, the multi-mode case provides the better fit to the experimental data, throughout a wide range of shear rate. The multi-mode trends of response for elongational viscosity of Figure 3b is a much better reflection of the actual fluid properties than those observed with a single-mode approximation. Nevertheless, the match here is

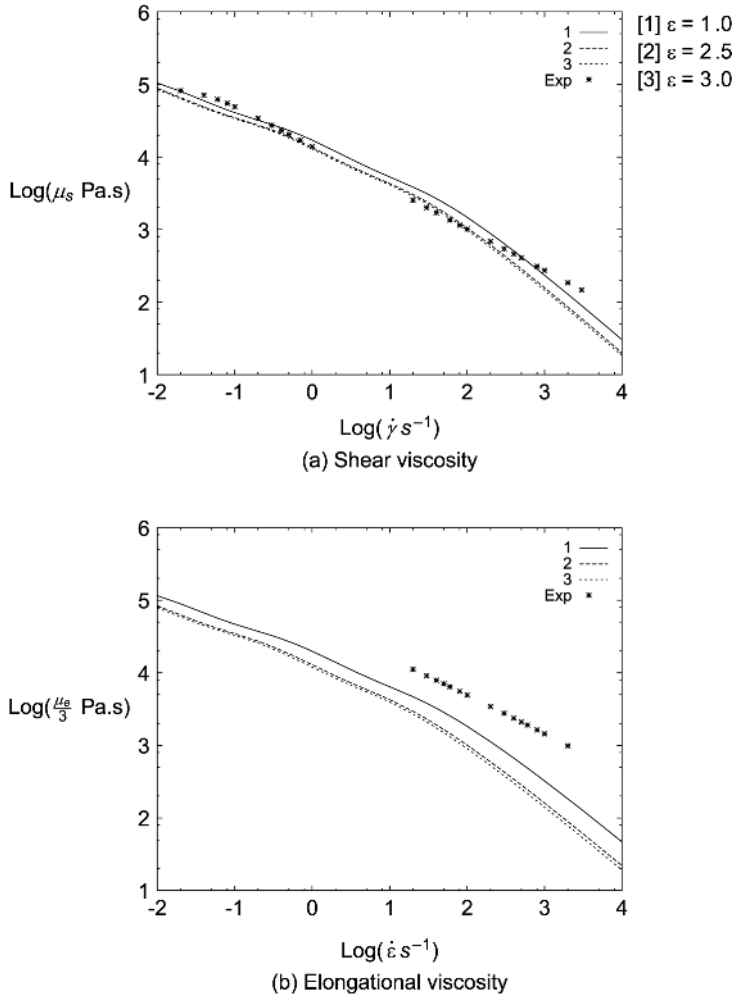

Figure 4.
Rheometrical data fits with ϵ variation for 3-mode HDPE

somewhat adrift from the experimental data values, derived from the Binding analysis. The same fitting procedure has also been carried out using a seven mode model. It is of note that no substantial improvement of fit is obtained if seven modes are employed in place of three (see Matallah *et al.* (2000)).

5. Contraction flow

Armed with the parameter fits to steady shear and pure extension, we proceed to analyse a contraction flow, testing our simulated solution pressure-drops across the domain against those observed experimentally at a series of different flowrates (Walters *et al.*, 1994).

5.1 Problem specification

A schematic flow diagram for the axi-symmetric 19:1 contraction flow with its associated finite element mesh is represented in Figure 5. The finite element discretisation is represented by 1830 elements and 3829 nodes. This problem is representative of flow in a contraction Capillary rheometer. The flow may be assumed to be symmetric about the central axis. Characteristic length and velocity scales are taken as the radius R_c of the die tube and mean exit velocity U_c, whilst the zero-shear rate viscosity μ_0 is considered as the characteristic viscosity. A non-dimensional Reynolds number is defined as

$$\mathrm{Re} = \frac{\rho U_c R_c}{\mu_0}, \tag{20}$$

and, for a single relaxation time, a Weissenberg number is taken as

$$\mathrm{We} = \lambda_1^{\mathrm{spec}} \frac{U_c}{R_c}. \tag{21}$$

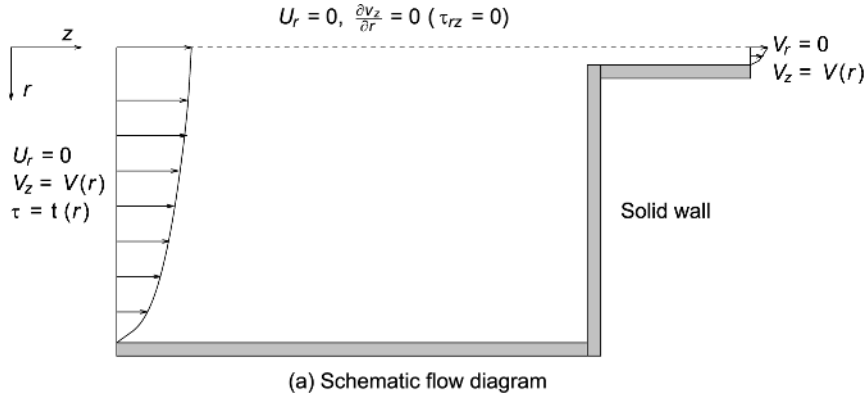

(a) Schematic flow diagram

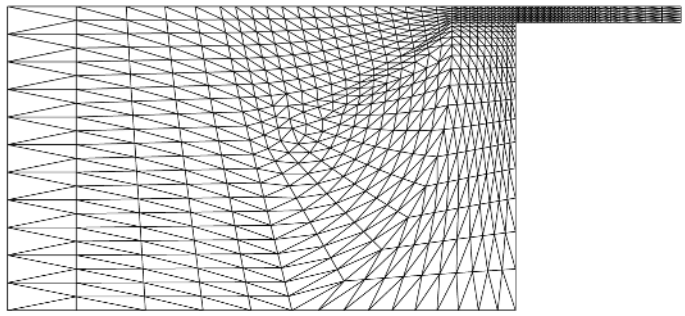

(b) Finite element mesh

Figure 5.
Schematic flow diagram and finite element mesh for 19:1 contraction geometry

For the multi-mode case, see above for comparable definitions. With respect to boundary conditions, no-slip conditions are taken on the downstream tube walls, and symmetry conditions apply on the flow centerline. The upstream length is chosen to be sufficiently large $68R_c$, to establish fully developed Poiseuille flow in the inlet region. The downstream die length is $40R_c$. At the domain exit, a fixed pressure datum is adopted for consistency and a fully developed Poiseuille flow prevails. Each individual flowrate is treated as a separate problem to which a steady state is sought. Though we are interested in steady state solutions, we note that these complex flows are transient in Lagrangian sense, so that a particle following the flow will in fact encounter different conditions at different locations (or times). For a single-mode, initial conditions are taken of a Newtonian kinematic filed, coupled to a fully relaxed stress field with appropriate inlet boundary modification. In the multi-mode case, initial kinematics are supplied from a prior single-mode computation. Then for each stress component mode, it is found suitable to impose relaxed inlet boundary conditions that rapidly adopt their appropriate levels in the entry flow region.

5.2 Results for a single mode model

In this section, we analyse our results in trends only for single-mode modeling. To establish a pressure drop versus flowrate relationship numerically and to compare this to experimental observations, three flowrates have been employed for different PTT fluid parameter sets (ϵ, ξ), in combination with μ_1. A given flowrate, Q, covers a particular shear-rate range. The shear viscosity $\mu_s(\dot{\gamma})$ may be adjusted through μ_1, ϵ and ξ parameters to fit the experimental data. Indeed, rising μ_1 tending towards μ_0, governs the second Newtonian plateau level for $\mu_s(\dot{\gamma})$. Hence, elevating μ_1, effectively extends the range of fit for the $\mu_s(\dot{\gamma})$ function over wider $\dot{\gamma}$ ranges. Thus the larger the value of Q, the more $\mu_1$must be elevated to enhance the $\mu_s(\dot{\gamma})$ fit to the data. The classification of various test fluids, with μ_1-values rising up to μ_0, highlights Fluids B-H as indicated in Table II. There, $\mu_1 = 0.875\,\mu_0$ for Fluid B, $\mu_1 = 0.99\mu_0$ for Fluid C, $\mu_1 = 0.995\mu_0$ for Fluid D, $\mu_1 = 0.999\mu_0$ for Fluid E, $\mu_1 = 0.998\mu_0$ for Fluid F and $\mu_1 = \mu_0$ for Fluids G and H. We note that, lower μ_1-values aids numerical convergence as the solvent contribution incorporates damping into the system. For the single mode approximation, a single relaxation time of $\lambda_1^{\text{spec}} = 5\,\text{s}$ is adopted to represent the relaxation time spectrum for an LDPE polymer (see Ref. Davies *et al.* (1996)). Reynolds numbers are of $O(10^{-6})$, whilst Weissenberg number values at various flowrates are summarised in Table III, and pressure-drop results in Table IV and Figure 6.

Overall, a summary of our findings reads as follows. By comparing the numerical and experimental data for these three flowrates, and investigating the parameter sensitivity of shear visocity on μ_1, ϵ and ξ at different shear

Fluid B $\mu_1 = 0.875\mu_0$	Fluid C $\mu_1 = 0.99\mu_0$	Fluid D $\mu_1 = 0.995\mu_0$
B_1: (0.1,0.01)	C_1: (0.15,0.02)	D_1: (0.15,0.02)
B_2: (0.3,0.01)	C_2: (2.0,0.02)	D_2: (0.3,0.02)
B_3: (2.0,0.01)		
Fluid E $\mu_1 = 0.999\mu_0$	Fluid F $\mu_1 = 0.998\mu_0$	Fluid G $\mu_1 = \mu_0, \ \xi = 0$
(0.3,0.02)	(0.15,0.02)	
		G_1: $\epsilon = 1.0$
		G_2: $\epsilon = 2.5$
		G_3: $\epsilon = 3.0$
		Fluid H $\mu_1 = \mu_0, \ \xi = 0$
		H_1: $\epsilon = 1.0$
		H_2: $\epsilon = 2.5$
		H_3: $\epsilon = 3.0$

Table II. Classification of fluids

		LDPE		HDPE	
	Q mm^3/s	2.37	39.9	2.37	34.0
We	Mode 1	0.10	1.73	0.10	1.47
	Mode 2	5.30	88.4	5.30	75.3
	Mode 3	204.6	3444	360.3	5156.7

Table III. We for contraction flow

Q mm^3/s	Δp^{Exp} (MPa) LDPE	Δp^{Sim} (MPa) Single mode, $\lambda_1^{spec} = 5$s	Δp^{Sim} (MPa) Multi-mode
2.37	3.27	4.09, fluid C_1	5.90, G_1, $\epsilon = 1.0$
		We = 30.18, $\epsilon = 0.15$, $\xi = 0.02$	4.00, G_2, $\epsilon = 2.5$
39.9	10.9	11.7, fluid D_2	10.3, G_1, $\epsilon = 1.0$
		We = 508.0, $\epsilon = 0.3$, $\xi = 0.02$	

Table IV. Pressure drop for contraction flow, LDPE polymer

rates, we conclude that the most influential parameter governing Δp is μ_1; the remaining parameters (ϵ, ξ) provide fine tuning of the fit. The choice of parameter μ_1 depends on the value of maximum shear rate $\dot{\gamma}_{\max}$ attained for any given flowrate. Hence with knowledge of $\dot{\gamma}_{\max}$, μ_1 may be determined by choosing a value to fit the experimental data of (Walters *et al.*, 1994). In Figure 7, maximum shear rates observed for the contraction flow are plotted against flowrate, from which a quadratic relationship emerges. From this, one may predict $\dot{\gamma}_{\max}$ for a given flowrate and hence extract a particular μ_1-fit (Figure 6).

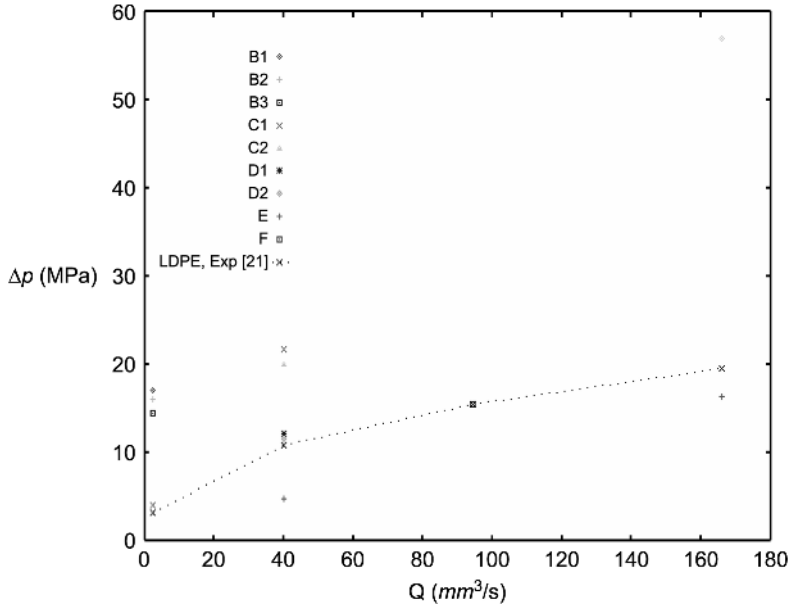

Figure 6.
Pressure drop v flowrate for contraction problem, single mode model

It is clear that with a single-mode approximation, it is necessary to continually adjust the fluid parameters at each flowrate setting, to adequately reproduce quantitative pressure-drop predictions. This keeps pace with the shear rate maxima observed, though does not provide a single fluid model representation suitable across a range of flowrates. This is a drawback to the use of a single

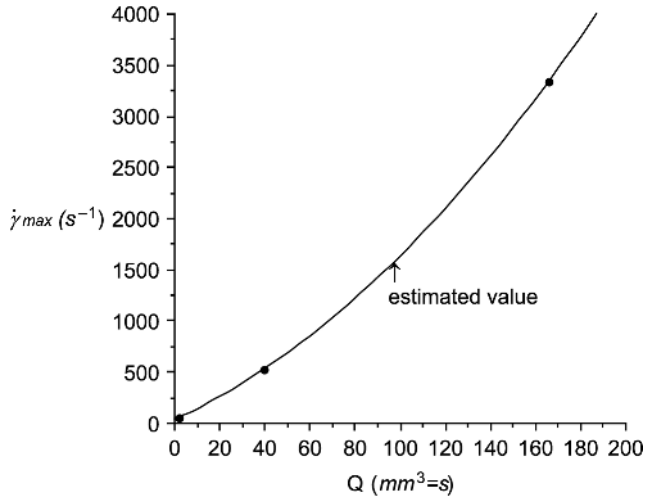

Figure 7.
Maximum shear-rate v flowrate correlation for contraction problem, LDPE

mode PTT model. Essentially, what is being achieved here is to provide a localised fit to data around the range of shear rates that dominates the process at each particular flowrate. As regards incrementation of μ_1 towards unity, this leads to more severe numerical difficulties in convergence to steady state. Thus care in continuation with this parameter is advisable purely on numerical grounds. At this juncture, it is natural to widen the study to embrace a multi-mode approximation and follow a similar line of investigation.

5.3 Results for a three-mode model

With a three-mode PTT approximation, results for both LDPE and HDPE grade polymers are presented and compared to the experimental data for the contraction flow. Comparison against the single-mode approximation is made only for the LDPE polymer, and ξ is taken as zero (see above, $N_2 \ll N_1$). Our observations are that computation times double from single to three-mode model calculations.

5.3.1 LDPE fluid. With the LDPE polymer a first flowrate of $Q_2 = 39.96\,\mathrm{mm}^3/\mathrm{s}$ is considered, for which the values of Weissenberg numbers for the corresponding three modes are given in Table III. The Reynolds number is $\mathrm{Re} = 1.8 \times 10^{-7}$ and the experimental pressure-drop is 10.9 MPa. With fluid G_1 offering a parameter combination $(\epsilon, \xi, \mu_1) = (1.0, 0.0, \mu_0)$, a simulated pressure-drop of 10.3 MPa is predicted. This contrasts to the best single mode computation of 11.7 MPa for fluid D_2 with $(\epsilon, \xi, \mu_1) = (0.3, 0.02, 0.995\mu_0)$.

In contrast, at a second lesser flowrate of $Q_1 = 2.37\,\mathrm{mm}^3/\mathrm{s}$, and the same parameter combination $(\epsilon, \xi, \mu_1) = (1.0, 0.0, \mu_0)$, i.e. fluid G_1, a simulated pressure-drop of 5.90 MPa is generated; an over-estimation compared to the experimental data of 3.27 MPa. This is in accordance with the shear viscosity fit, where for the shear rate range $10 \leq \dot{\gamma} \leq 10^2\,\mathrm{s}^{-1}$, the best fit renders a value of $\epsilon = 2.5$. For fluid G_2 of $\epsilon = 2.5$, the pressure-drop is 4.00 MPa compared to 4.09 MPa for the single mode calculation of fluid C_1. Figure 8a summarises graphically the comparison of numerical and experimental data at both flowrates, including the single mode results. The values are tabulated in a unified manner in Table IV. Conventional use of the PTT class of models, is restrictive with a constant value for the parameter ϵ. If this parameter is taken in the range $1.0 \leq \epsilon \leq 2.5$, pressure-drop will be better estimated by the multi-mode than the single mode model for the flowrate range $2.37 \leq Q \leq 40\,\mathrm{mm}^3/\mathrm{s}$. We observe in Figure 8a, that the discrepancy from the experimental value is huge for the single mode fluid C_1 – parameter set $(\epsilon, \xi, \mu_1) = (0.15, 0.02, 0.99\mu_0)$ at $Q_2 = 39.9\,\mathrm{mm}^3/\mathrm{s}$.

5.3.2 HDPE fluid. For the HDPE polymer, computations are conducted for flowrates of $Q_1 = 2.37\,\mathrm{mm}^3/\mathrm{s}$ and $Q_2 = 34.0\,\mathrm{mm}^3/\mathrm{s}$. At the former flowrate, the fitting of the PTT model to the experimental shear viscosity, as in Figure 4,

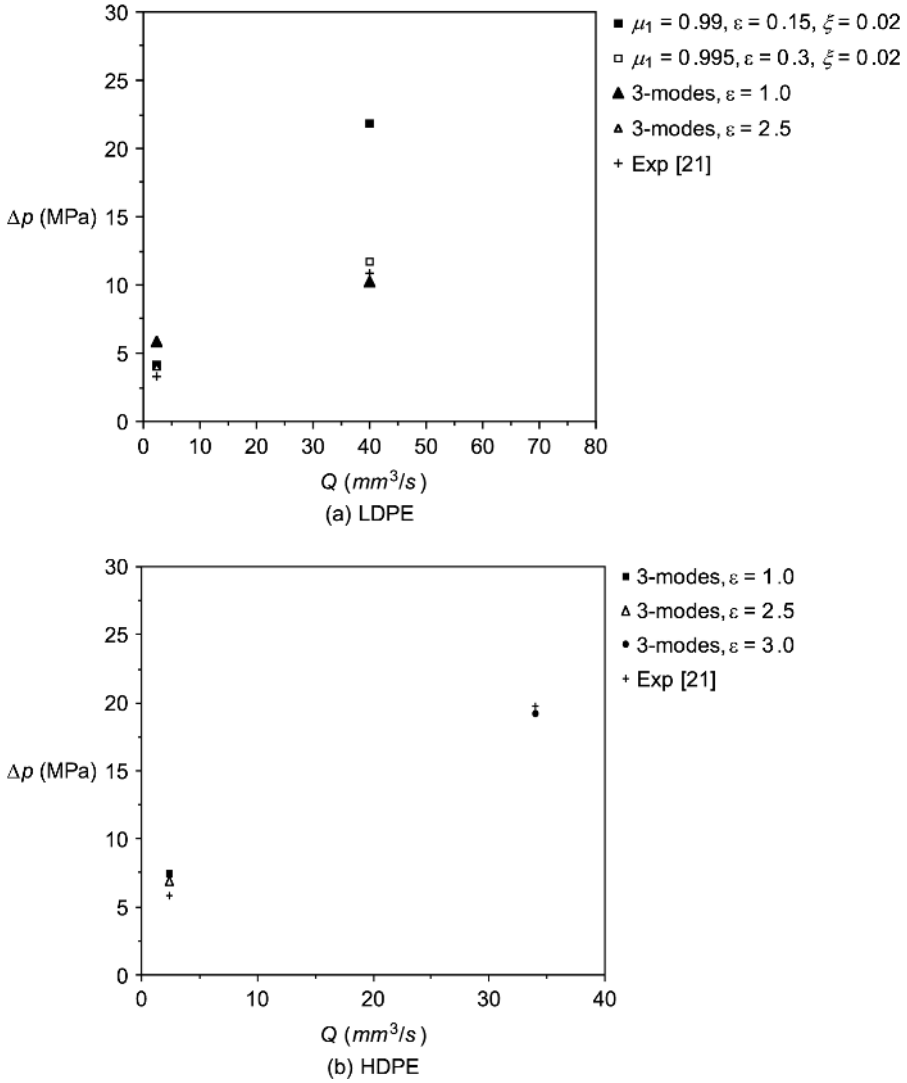

Figure 8.
Simulated and experimental pressure drops for contraction flow; (a) LDPE, (b) HDPE

provides an equally good dual set of parameters with either $(\epsilon, \xi, \mu_1) = (2.5, 0.0, \mu_0)$ or $(\epsilon, \xi, \mu_1) = (3.0, 0.0, \mu_0)$, i.e. fluid H_2 or H_3. Simulated pressure-drops are 7.40 MPa for fluid H_2 $\epsilon = 2.5$, and 6.90 MPa for fluid H_3 $\epsilon = 3.0$, that compare against an experimental value of $\Delta p = 5.83$ MPa. It is implied that additional increase in the parameter ϵ, will lead to further decrease in pressure-drop.

At a second flowrate of $Q_2 = 34.0\,\text{mm}^3/\text{s}$, and according to Figure 4, the best fit to the shear viscosity data, results in the set of parameters

$(\epsilon, \xi, \mu_1) = (1.0, 0.0, \mu_0)$ for the range $10^2 \leq \dot{\gamma} \leq 10^3\,\mathrm{s}^{-1}$, i.e. fluid H_1. The simulated pressure-drop is 19.2 MPa, whilst the experimental value is 19.9 MPa. This evidence is taken as endorsement for the choice of multi-mode representation with fluids G_1 and H_1, that is wholy acceptable across the flowrates selected. A summary of simulated and experimental pressure-drop values is provided for HDPE in Table V and Figure 8b.

6. Wire-coating flow

Having established the goodness of fit to experimental pressure-drop data for a complex contraction flow, we now proceed to the industrial flow of interest that provides the motivation for this study. The flow quantities of specific relevance are residual flow-induced stress and pressure-drop. The former is fresh information to be gathered for this problem that is important to control coating properties. These quantities have impact on the optimisation of the process design. Only fluid G_1 (i.e. one set of parameters $(\epsilon, \xi) = (1, 0)$) is adopted throughtout the study of tube-tooling wire-coating for LDPE and H_1 for HDPE polymer, since a reasonable fit is achieved in the shear-rate range under consideration ($\dot{\gamma} \leq 10^3\,\mathrm{s}^{-1}$).

6.1 Problem specification

A schematic flow diagram for the tube-tooling problem with its finite element mesh is displayed in Figure 9. The flow enters the annular tube AB, then a converging cone section BC and a land region CD, and is draw-down by the wire in a converging cone form DE, and coating part of the wire EF, as shown in Figure 9a. Due to symmetry, it is necessary to model only one half of the problem. Characteristic length and velocity scales are taken as the horizontal distance between the die exit of the tube and the contact point on the wire, i.e. the draw-down length L_{draw} and the velocity of the wire U_{wire}, respectively. The zero-shear viscosity μ_0 is considered as the characteristic viscosity. Here, the same definition for Reynolds and Weissenberg numbers is taken as for the contraction flow problem. Boundary conditions are given as follows. No-slip conditions are taken on tube walls for the die tube, ABCD and D'C'B'A'. At the entry AA' a fully developed Newtonian annular velocity profile corresponding to a specific flow rate Q is imposed, ($U_r = 0$ and $V_z = V_z(r)$). From this velocity profile, a PTT stress profile is generated analytically. This specifies inlet flow boundary conditions. Free surface boundary conditions along DE

Q mm^3/s	Δp^{Exp} (MPa) HDPE	Δp^{Sim} (MPa)
2.37	5.83	7.40, fluid H_2, $\epsilon = 2.5$ 6.90, fluid H_3, $\epsilon = 3.0$
34.0	19.9	19.2, fluid H_1, $\epsilon = 1.0$

Table V.
Pressure drop for contraction flow, HDPE polymer, multi-mode

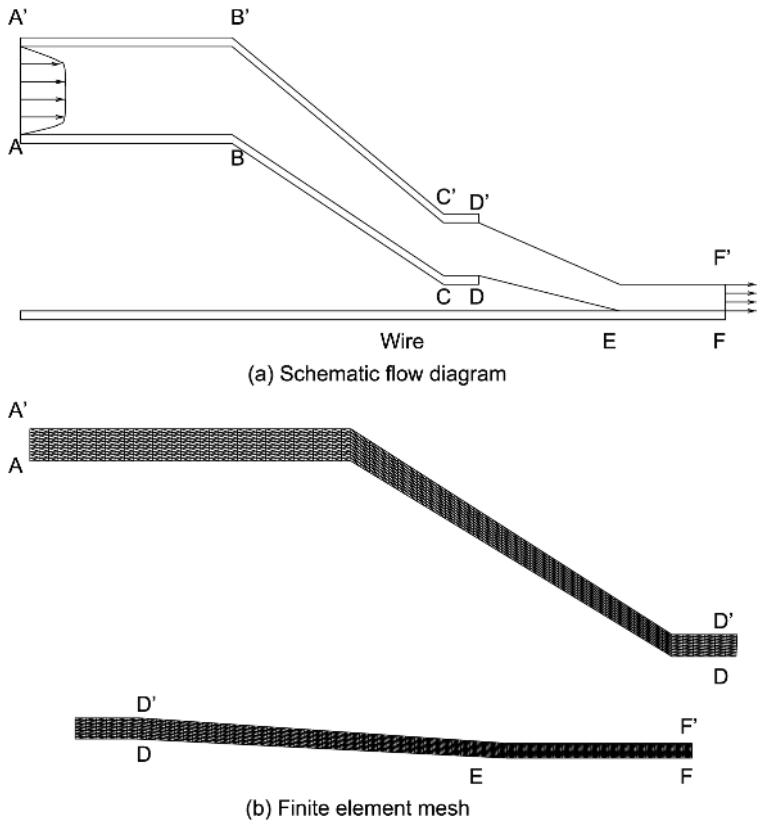

Figure 9.
Schematic diagram and finite element mesh for wire coating tube-tooling die

and F'D' are taken equivalent to the average velocity per cross sectional area, consistent with draw-down flow. On EF, the fluid is considered to be moving with the wire (no slip). A uniform structured mesh is used in the finite element discretisation, 2680 elements and 5649 nodes, (thoroughly investigated in our prior studies, see Mutlu *et al.* (1998a); Mutlu *et al.* (1998b)). To capture sharp velocity gradients near singular regions, different meshes were employed elsewhere (see Mutlu *et al.* (1998a); Mutlu *et al.*, 1996). In the present study only the finest mesh of Ref. (Mutlu *et al.*, 1998a) is employed, for which the number of elements per region is given in Table VI.

Table VI.
Number of elements per region

ABB'A'	BCC'B'	CDD'C'	DEE'D'	EFF'E'
680	680	120	800	400

6.2 LDPE fluid

Table VII provides values of Weissenberg numbers for an LDPE polymer, with material parameters given in Table I, for a standard flowrate (1Q) and double flowrate (2Q). The Reynolds numbers are $\mathrm{Re} = 1.5 \times 10^{-4}$ and $\mathrm{Re} = 3.0 \times 10^{-4}$, respectively. Figure 10 plots the pressure-drop line for both 1Q and 2Q, along a sample line tangential to the flow. The sample line for plotting lies along the inner radius of the annular settings. Cross stream variation is hardly significant. Simulated pressure-drop values are 6.90 and 8.40 MPa, respectively, and are compared to 7.49 and 11.2 MPa using fluid C_1 for the single mode approximation (as (Mutlu *et al.*, 1998a) using $\mu_1 = 0.99\mu_0$, $\epsilon = 0.15$ and $\xi = 0.02$). Pressure-drop results are tabulated in Table VIII accordingly. For the single mode, pressure-drop at 2Q is one and a half times that at 1Q, whilst for a multi-mode model, this factor reduces to 1.22. Overall, the trend in variation of pressure-drop is similar for single and multi-mode models in the tube-tooling die sections, notwithstanding the elevation of the single-mode 2Q result. In contrast in the draw-down section for the single mode, pressure-drop is almost constant for 1Q, but for 2Q, it increases around the location where the fluid meets the wire. Traveling with the wire, pressure

		LDPE		HDPE	
		1*Q*	2*Q*	1*Q*	2*Q*
We	Mode 1	0.095	0.19	0.095	0.19
	Mode 2	4.843	5.686	4.843	5.686
	Mode 3	188.7	377.4	332.3	664.6

Table VII.
We for tube-tooling flow

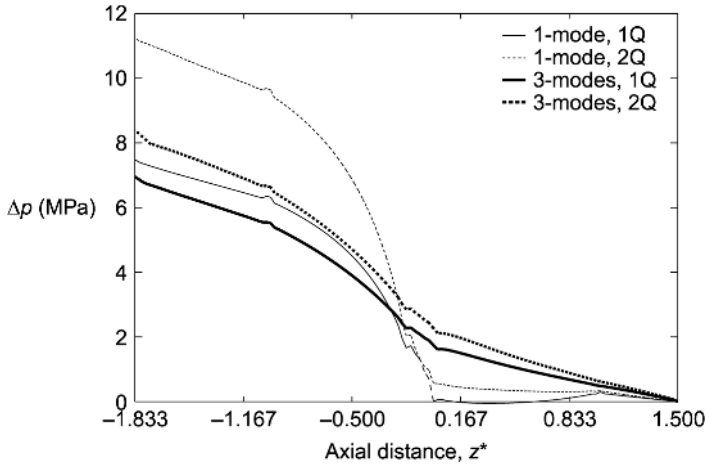

Figure 10.
Tube-tooling flow, streamwise pressure profiles, single and multi-mode models, LDPE

diminishes to zero. However for a multi-mode model, the pressure-drop decreases continuously with only a slight change in the slope on encountering the wire. These differences in response for these models, are due to the variation in radial shear stress gradients, particularly at die exit, that are about one third of the level observed in the inlet tube-tooling section.

In Figure 11, the shear stress is plotted along the inner annular radius. A constant value is observed in the inlet tube (shear flow), followed by a change of sign over the contracting flow within the tube-tooling cone. Shear stress increases in absolute value as the cone contracts. In the land section, the degree of shearing increases again, sharply at the start, flattens across the land region, and rises slightly at the end. There is then a dramatic sharp drop and oscillation in shear stress at the inlet of the draw-down cone. This is where there is a sudden adjustment from the annular shear flow to an extensional drawing flow. Thereafter, it decreases gradually but smoothly along the draw-down cone, to increase slightly when the wire is met and subsequently remains steady. This behaviour is similar for both flowrates, only differing in the absolute level of the stress.

For the normal stress component in the axial direction, τ_{zz}, a sharp oscillation is experienced at the inlet of the tube-tooling cone due to the sudden geometry changes. This is followed by a smooth increase in τ_{zz} as the shear rate increases in the cone. Over the land region, τ_{zz} suddenly decreases as the polymer enters, and remains fairly constant to the land region exit. A shock is noted in the transition from land to draw-down flow. Over the draw-down section, the stress component decreases. A smaller variation rate in τ_{zz} is observed as opposed to that in the tube-tooling cone, and there is a marginal increase when the fluid meets the wire. A relaxation of stress occurs within the coating flow on the wire, with larger slope than in the draw-down cone.

In summary, a build-up of shear and normal stress is observed in the tube-tooling cone, followed by relaxation in the draw-down and wire-coating flow sections.

For stress, the trends are identical for single to multi-mode cases, the differences lie in the stress levels, that are dictated by the inlet flow. At inlet and for the shear rates that apply there, see Figure 3, a closer match to μ_s is observed with a single mode model, yielding a lower value of shear stress (via viscosity) than with the multi-mode model. We note also that in the converging

Table VIII.
Pressure drop for tube-tooling flow

		LDPE		HDPE	
		1*Q*	2*Q*	1*Q*	2*Q*
Δp (MPa)	Single mode	7.49	11.2, fluid C_1	–	–
	Multi-mode	6.90	8.40, fluid G_1	12.4	15.4, fluid H_1

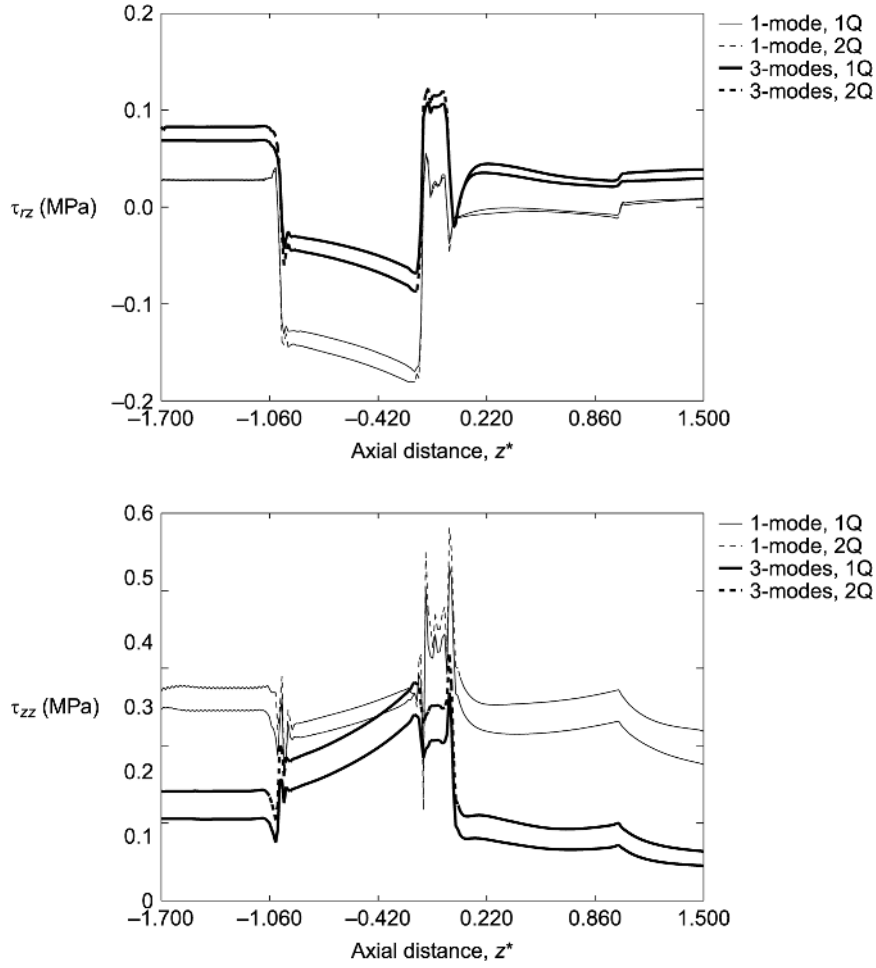

Figure 11.
Tube-tooling flow, streamwise stress profiles, single and multi-mode models, LDPE, (a) τ_{rz}, (b) τ_{zz}

tube the rate of increase of τ_{zz} in the multi-mode case is greater than that corresponding to the single mode instance. This is due to the influence of the shortest mode $\lambda_1 = 0.017$ s; see below for further comment on the contributions due to the separate modes.

6.3 HDPE fluid

Results for the HDPE polymer are also presented at the same flowrates as above for LDPE. In this case, the parameter $\epsilon = 1.0$ represents the best fit to the shear viscosity, as in Figure 4, hence fluid H_1. Predicted pressure-drops are 12.4 and 15.4 MPa for the two associated flowrates, respectively. Figure 12 shows a sample line plot for pressure-drop at both flowrates, and a similar

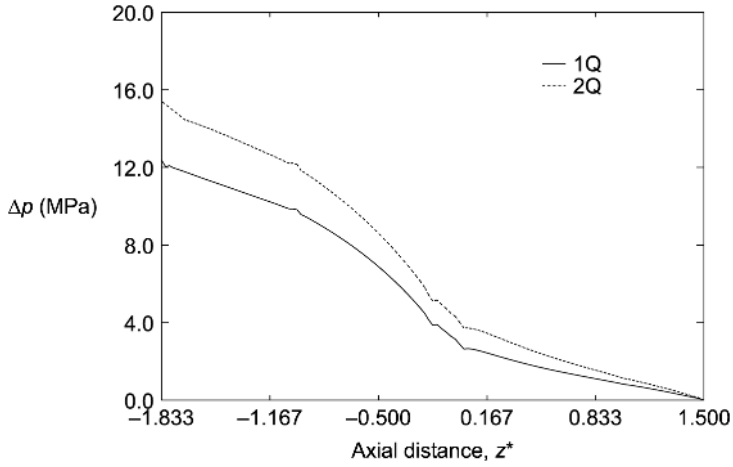

Figure 12.
Tube-tooling flow, streamwise stress profiles, standard and double flowrate, HDPE,

trend to that for the LDPE polymer is observed. We note that pressure-drop at the double flowrate is 1.24 times as great as that at the standard flowrate; the factor relating pressure-drops is similar to that found for LDPE, of 1.22. It is conspicuous that corresponding pressure-drops for HDPE polymer are almost double those for LDPE polymer. According to Figure 13, line plots for shear and normal stress components along a sample line tangential to the flow, the general behaviour of stress is similar to that for LDPE, though scales are doubled in shear stress and increase by about 20 per cent in normal stress. These findings are in keeping with general expectations for these materials and flows.

6.4 Analysis of separate modes

To understand the contribution of each mode (i) to the total stress of the multi-mode model, both τ_{rz} and τ_{zz} are plotted for the standard flowrate, LDPE polymer in Figure 14. Of the individual modal contributions, the two shorter relaxation time modes dominate. The shear stress is dominated by the shortest relaxation time. This is true for all cases studied, covering both materials and flowrates, as confirmed in Figure 14 for LDPE and Figure 15 for HDPE.

Alternatively, for the τ_{zz} component, according to Figure 14 and LDPE, the shortest relaxation time dominates in the tube-tooling cone; this made dictates the shape of the total stress in all the sections of the flow. In contrast, the second shortest relaxation time dominates in the inlet tube and draw-down sections, including the flow on the wire. For the HDPE polymer, as in Figure 15, the shortest relaxation time dominates throughout the tube-

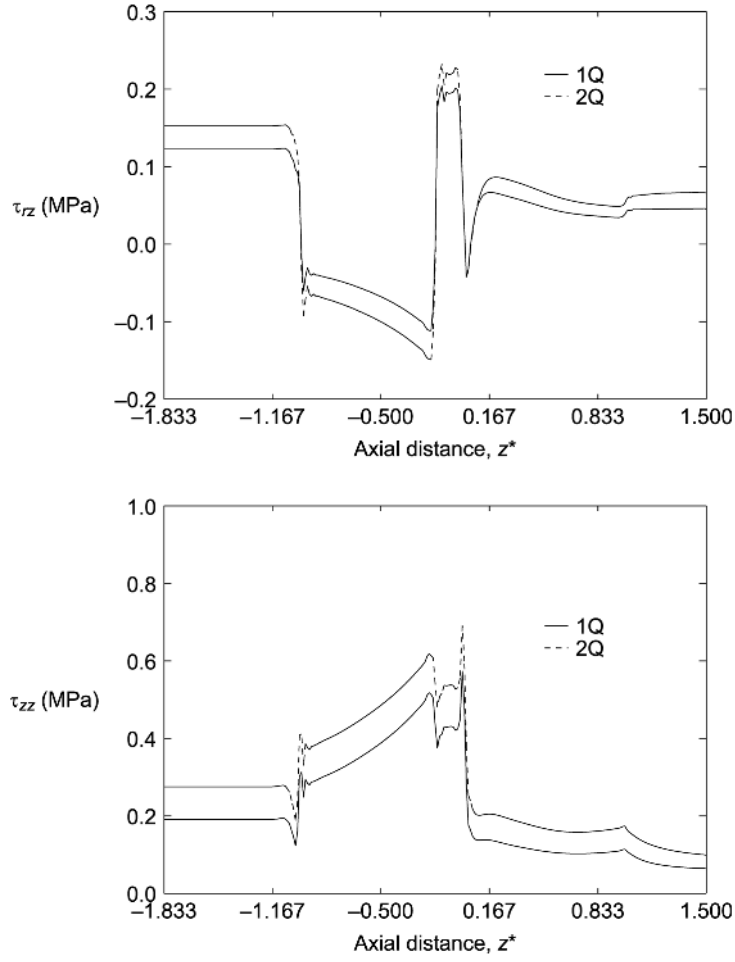

Figure 13.
Tube-tooling flow, streamwise stress profiles, multi-mode, HDPE, (a) τ_{rz}, (b) τ_{zz}

tooling die sections, whilst in the draw-down, the second shortest relaxation time dominates.

7. Conclusions

A contraction flow has been used effectively to demonstrate how single and multi-mode PTT models perform in quantitatively replicating pressure-drop/flowrate data. Essentially this is governed by the goodness of fit to the shear viscosity. In this regard, the multi-mode instance performs better across the range of shear rates of interest. In the single-mode case reasonable qualitative correspondence has been derived, presupposing a judicious choice of averaged relaxation time, which has been possible here.

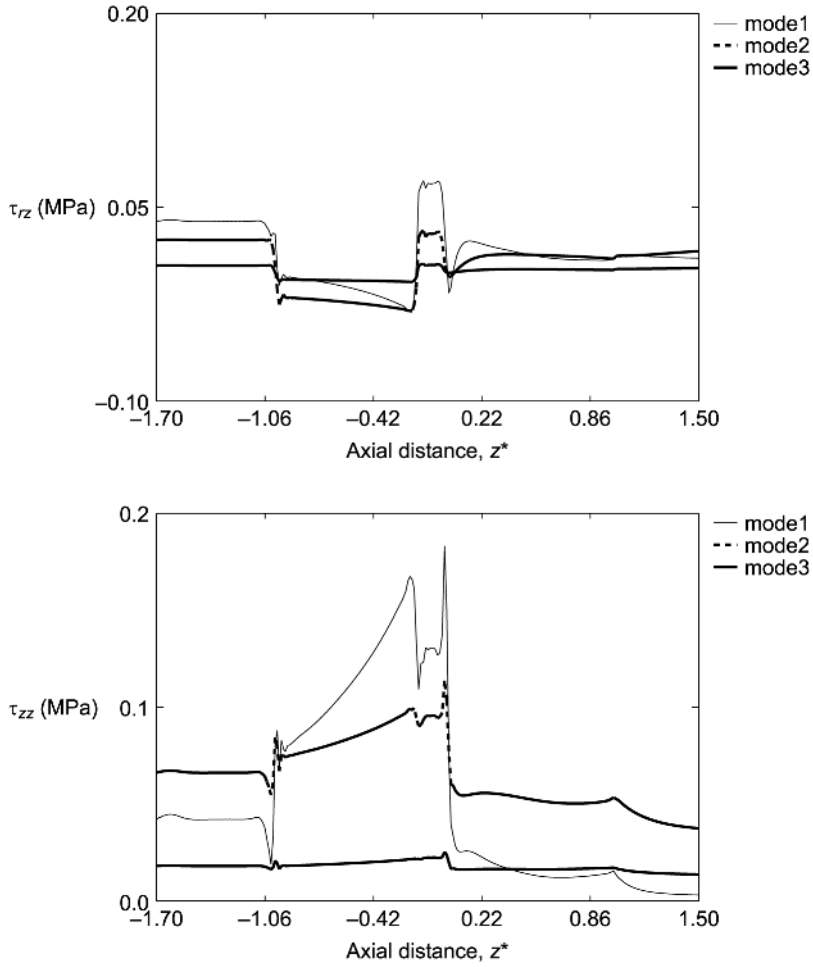

Figure 14.
Tube-tooling flow, streamwise stress profiles for individual stress mode, LDPE, (a) τ_{rz}, (b) τ_{zz}

Also, the choice of material parameter combination must vary with each flowrate (and its associated maximum shear rate) to adequately reflect the experimental data. This generates different fluid model representations and demonstrates the shortcomings of an averaged mode approximation. The multi-mode alternative, performs better in this respect with a fixed fluid parameter set.

In the more generalised context of the industrial tube-tooling wire-coating flow, the differences in results on stress distributions and pressure-drop between these modelling approaches is more stark. Here, the multi-mode approximation reveals the fine detail of stress response throughout the

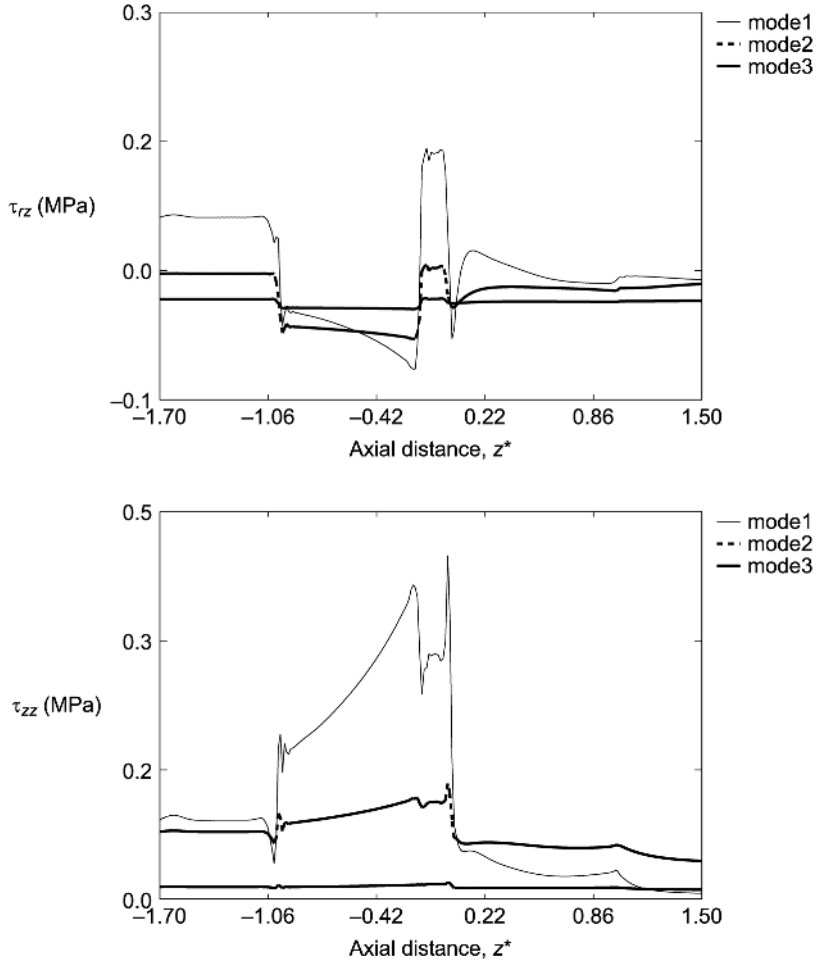

Figure 15.
Tube-tooling flow, streamwise stress profiles for individual stress mode, HDPE, (a) τ_{rz}, (b) τ_{zz}

flow, peak values attained and dominance of individual components. The key point emerges that the shorter relaxation time modes are observed to dominate within the process. These modes are of the order of less than one second, being synonymous with a representative particle residence time as it travels through the flow domain. Stress and pressure-drop levels are practically doubled for the HDPE above the LDPE polymer, which is consistent with practical industrial experience for these materials. Also pressure-drop variation with flowrate doubling is held to be more realistic with the multi-mode option. The differences from single to multi-mode total stress appear minimal in the draw-down and coating regions, taking into account the elevations in stress levels within the steady shear die entry flow as discussed above.

References

Arsac, A., Carrot, C., Guillet, J. and Revenu, P. (1994), "Problems originating from the use of the Gordon-Schowalter derivative in the Johnson-Segalman and related models in various shear-flow situations", *J. Non-Newtonian Fluid Mech.*, 55, pp. 21-36.

Azaiez, J., Guénette, R. and Ait-Kadi, A. (1996), "Entry flow calculations using multi-mode models", *J. Non-Newtonian Fluid Mech.*, 66, pp. 271-81.

Baaijens, H.P.W. Evaluation of constitutive equations for polymer melts and solutions in complex flows PhD. Thesis Eindhoven University of Technology, Netherlands.

Binding, D.M. (1993), *Techniques in Rheological Measurement*, Chap 1. Collyer, A.A., (Eds) Chapman and Hall, London, UK.

Binding, D.M. (1988), "An approximate analysis for contraction and converging flows", *J. Non-Newtonian Fluid Mech.*, 27, pp. 173-89.

Baaijens, F.P.T., Selen, S.H.A., Baaijens, H.P.W., Peters, G.W.M. and Meijer, H.E.H. (1997), "Viscoelastic flow past a confined cylinder of a LDPE melt", *J. Non-Newtonian Fluid Mech.*, 68, pp. 173-203.

Binding, D.M., Blythe, A.R., Gunter, S., Mosquera, A.A., Townsend, P. and Webster, M.F. (1996), "Modelling polymer melt flows in wirecoating processes related fields", *J. Non-Newtonian Fluid Mech.*, 64, pp. 191-206.

Binding, D.M., Couch, M.A. and Walters, K. (1998), "The pressure dependence of the shear and elongational properties of polymer melts", *J. of Non-Newtonian Fluid Mech.*, 79, pp. 137-55.

Cogswell, F.N. (1972), "Converging flow of polymer melts in extrusion dies", *Polymer Eng. Sci.*, 12, pp. 64-74.

Caswell, B. and Tanner, R.I. (1978), "Wirecoating die design using finite element methods", *Polymer Eng. Sci.*, 18 No. 5, pp. 416-21.

Davies, A. R., Walters, K. and Binding, D. M. "An analysis of the discrete relaxation spectra of 3 polyethylene samples for BICC group", private communications. Technical report, Institute of non-Newtonian Fluid Mechanics, University of Wales, Aberystwyth, June 20, 1996.

Fenner, R.T. and Williams, J.G. (1967), *Trans. J. Plastics Inst.*, pp. 701-6.

Gunter, S., Webster, M.F. and Townsend, P. (1995), "BICC internal report", in, *Computer Science Department*, University of Wales, Swansea.

Gunter, S., Townsend, P. and Webster, M.F. (1996), "Simulation of some model viscoelastic extensional flows", *Int. J. Num. Meth. Fluids*, 23, pp. 691-710.

Gupta, M., Hieber, C.A. and Wang, K.K. (1997), "Viscoelastic modelling of entrance flow using multimode Leonov model", *Int. J. Numer. Meth. Fluids*, 24, pp. 493-517.

Hawken, D.M., Tamaddon-Jahromi, H.R., Townsend, P. and Webster, M.F. (1990), "A Taylor-Galerkin based algorithm for viscous incompressible flow", *Int. J. Num. Meth. Fluids*, 10, pp. 327-51.

Huang, H.C., Townsend, P. and Webster, M.F. (1994), *Numerical Grid Generation in Computational Fluid Dynamics and Related Fields*, Weatherill, N.P., Eiseman, P.R., Hauser, J., Thompson, J.F. (Eds), Pineridge Press, Swansea.

Mitsoulis, E. (1986), "Fluid flow and heat transfer in wire coating: A review", *Advances in Polymer Technology*, 6 No. 4, pp. 467-87.

Matallah, H., Townsend, P. and Webster, M.F. (1998), "Recovery and stress-splitting schemes for viscoelastic flows", *J. Non-Newtonian Fluid Mech.*, 75, pp. 139-66.

Matallah, H., Townsend, P. and Webster, M.F. (2000), "Viscoelastic multi-mode simulations of wire-coating", *J. Non-Newtonian Fluid Mech.*, 90, pp. 217-41.

Mitsoulis, E., Wagner, R. and Heng, F.L. (1988), "Numerical simulation of wire-coating low-density polyethylene: Theory and experiments", *Polymer Eng. Sci.*, 28 No. 5, pp. 291-311.

Mutlu, I., Townsend, P. and Webster, M.F. (1996), "Adaptive solutions for viscoelastic flows", *Commun. Numer. Meth. Eng.*, 12, pp. 643-55.

Mutlu, I., Townsend, P. and Webster, M.F. (1997), *Mathematics of finite elements and applications-highlights 1996*, Whiteman, J.R., (Eds) Wiley, Chichester vol 18 pp. 299-312.

Mutlu, I., Townsend, P. and Webster, M.F. (1998a), "Simulation of cable-coating viscoelastic flows with coupled and decoubled schemes", *J. Non-Newtonian Fluid Mech.*, 74, pp. 1-23.

Mutlu, I., Townsend, P. and Webster, M.F. (1998b), "Computation of viscoelastic cable coating flows", *Int. J. Numer. Meth. Fluids*, 26, pp. 697-712.

Phan-Thien, N. (1978), "A non-linear network viscoelastic model", *J. Rheol.*, 22, pp. 259-83.

Pearson, J.R.A. and Richardson, S.M. (1983), "Computational Analysis of Polymer Processing", in Applied Science Publishers Ltd, London and New York.

Phan-Thien, N. and Tanner, R.I. (1977), "A new constitutive equation derived from network theory", *J. Non-Newtonian Fluid Mech.*, 2, pp. 353-65.

Quinzani, L.M., McKinley, G.H., Brown, R.A. and Armstrong, R.C. (1990), "Modeling the rheology of polyisobutylene solutions", *J. Rheol.*, 34, pp. 705-48.

Saramito, P. and Piau, J.M. (1994), "Flow characteristics of viscoelastic fluids in an abrupt contraction by using numerical modelling", *J. Non-Newtonian Fluid Mech.*, 52, pp. 263-88.

Schoonen, J.F.M., Swartjes, F.H.M., Peters, G.W.M., Baaijens, F.P.T. and Meijer, H.E.H. (1998), "A 3D numerical/experimental study on a stagnation flow of a polyisobutylene solution", *J. Non-Newtonian Fluid Mech.*, 79, pp. 529-61.

Walters, K., Binding, D. M. and Evans, R. E. "Modelling the rheometric behaviour of 3 polyethylene melts". Technical report, Institute of non-Newtonian Fluid Mechanics, University of Wales, Aberystwyth, May 10, 1994.

Zienkiewicz, O.C. and Zhu, J.Z. (1995), "Superconvergence and the superconvergent patch recovery", *Finite Element in Analysis and Design*, 19, pp. 11-23.

Numerical simulation for viscous free-surface flows for reverse roller-coating

M.S. Chandio and M.F. Webster
Institute of non-Newtonian Fluid Mechanics, Department of Computer Science, University of Wales, Swansea, UK

Keywords *Free form surfaces, Numerical simulation, Finite elements*

Abstract *This article is concerned with the numerical simulation of a reverse roller-coating process, which involves the computation of Newtonian viscous incompressible flows with free-surfaces. A numerical scheme is applied of a transient finite element form, a semi-implicit Taylor-Galerkin/pressurecorrection algorithm. For free-surface prediction, we use kinematic boundary adjustment with a mesh-stretching algorithm. In the present work, an alloy sheet (foil) passes over a large roller and then a smaller applicator roller, which provides the in-feed. In combination, the applicator roller, the foil and the fluid form part of the underside coating mechanism. The aim of this study is to investigate fundamental aspects of the process, to ultimately address typical coating instabilities. These may take the form of chatter and starvation. A uniform coating thickness is the desired objective. A mathematical model is derived to describe the solvent coating applied to the underside of the sheet, assuming that the lacquer is a Newtonian fluid. In particular, the work has concentrated on the flow patterns that result and a parameter sensitivity analysis covering the appropriate operating windows of applied conditions. Effects of independent variation in roll-speed and foil-speed are investigated, to find that maxima in pressure, lift and drag arise at the nip and are influenced in a linear fashion.*

1. Introduction

In this study the effectiveness of finite element modelling is investigated to predict the flow associated with the reverse roller-coating of alloy sheets using a protective film of solvent-based lacquer. A mathematical model is derived to describe the coating applied to the underside of the foil sheet, assuming that the lacquer is a Newtonian fluid. In particular, the work has concentrated on the flow patterns that result and a parameter sensitivity analysis covering appropriate operating windows of applied conditions. This covers variation in application roll-speed and foil-speed, and consideration of flow conditions in the nip region. A finite element simulation of the roller-coating process is presented, based on a semi-implicit Taylor-Galerkin/Pressure-correction algorithm (Townsend and Webster, 1987; Hawken *et al.*, 1990; Carew *et al.*, 1993).

International Journal of Numerical Methods for Heat & Fluid Flow, Vol. 12 No. 4, 2002, pp. 434-457.

DOI 10.1108/09615530210433288

Author for correspondence, Institute of Non-Newtonian Fluid Mechanics, Department of Computer Science, University of Wales Swansea, Singleton Park, Swansea SA2 8PP, UK, E-mail: M.F.Webster@swan.ac.uk

Viscous flow with free-surfaces is common and arises in many important industrial application areas, particularly in coating and printing situations. In the literature, flows between pairs of rolls have been extensively studied (Fourcade *et al.*, 1999; Cohu and Magnin, 1997; Carvalho and Scriven, 1997; Carvalho and Scriven, 1997; Chen and Scriven, 1988; Benjamin, 1994), where a substrate is pressed between a set of contra or forward rotating rollers. The general requirement is to achieve a uniform coating thickness. It is reported in The literature would indicate that, high-pressure in the nip region generates instability in the flow, that subsequently affects the coating liquid layer, see Fourcade *et al.* (1999); Cohu and Magnin (1997); Carvalho and Scriven (1997); Carvalho and Scriven (1997); Chen and Scriven (1988). Similar findings are observed in this study, where pressure has an elevated value in the nip region. There is a sparsity of work in the open literature on reverse roller-coating between foil and roller. Hence, we first review work cited on roller-coating between two rollers. Fourcade *et al.* (1999) investigated a coating operation of a reverse roller-coating process between two rollers. The main attention is focused on the deformation of the elastomer on the coated roll. It is reported that the pressure increases in the converging section of the gap, and reaches its peak slightly to the left of the contact point of the rollers. The largest deformation of the elastomer cover of 70 mm is observed to occur at the location where the pressure reaches a maximum. The lower the gap size, the higher the pressure peak that is observed.

Cohu and Magnin (1997) conducted experimental investigations into forward roller-coating of Newtonian fluids between deformable rolls. These authors observed that the decrease of the thickness of a rubber cover on a roller, below a critical value, tends to decrease the coating thickness significantly. Carvalho and Scriven (1997) have argued in their numerical work, based on forward roller-coating, that the upstream free-surface touches the top roll, and air is trapped between the roll surface and the coating liquid. Consequently the coated film that is delivered is defective. Various flow states are described, both metered and premetered, by moving the rolls apart and bringing them together. As the rolls are pushed together, the gyre moves upstream towards the inlet plane. These authors have replaced the fixed inlet film thickness condition with a weighted kinematic residual that guarantees the flow is normal to the inlet boundary in an integral sense.

Carvalho and Scriven (1997) investigated the effect of soft-roll deformation with respect to the onset of ribbing on the coated liquid layer. Their main findings showed how a deformable cover may be used to lessen the ribbing on the liquid layer to achieve a required coating thickness. They found that in forward-roller coating, deformation influenced gap geometry and this generated ribbing on the liquid layer, on each of the roll surfaces at high roller speeds. They also analysed time-dependent response to infinitesimal transverse disturbances. A mathematical model was presented to predict the

critical capillary number for the onset of ribbing. They concluded that roll cover deformation alters the wavelength of the ribbing pattern. Roll cover softness is related to increasing the solids elasticity number. Increasing the elasticity number of the soft-roll cover makes the ribbing pattern wavelengths larger and wave numbers smaller; this stimulates the fastest instability modes. The consequence is a larger ribbing wavelength and consequently an extended period to achieve a level film.

It is necessary to consider the state of inflow to provide appropriate flow conditions, stipulating flow rate and profile form. According to Benjamin (1994), in meniscus coatings, the flow is always pre-metered and therefore imposing a plug-velocity profile at the inflow boundary is a satisfactory boundary condition. Hence, we follow this thinking, as do Chen and Scriven (1988) likewise. This implies that we adopt a constant inflow rate, as delivered by the premetering. Largely, this flow rate is determined by that at outflow, based upon a known film-speed and thickness.

For the last two decades the finite element method has played an important role in simulating the flow of fluids subject to free surfaces. Literature of relevance on this topic can be found in Keunings (1986); Sizaire and Legat (1997); Tanner *et al.* (1975); Silliman and Scriven (1980); Saito and Scriven (1981); Ramaswamy (1990); Hirt *et al.* (1974); Sato and Richardson (1994); Ding *et al.* (1993); Regalt *et al.* (1993). One difficulty with computer modelling of such coating scenarios, lies in the treatment of moving free-surface problems, accommodating kinematic and dynamic boundary conditions (Keunings, 1986) on the free-surface and the simultaneous calculation of its position. Sizaire and Legat (1997) have adopted an approach similar to that of Keunings (1986) for the treatment of free-surface boundaries, within the viscoelastic regime.

Tanner *et al.* (1975), constructed a Galerkin finite element scheme for computing free surfaces with the use of the kinematic condition. Drawbacks to this approach are commented upon by Silliman and Scriven (1980) who argue that such a choice is expensive to implement and relies heavily upon the initial guess. Furthermore, such kinematic conditions alone will not provide an efficient way to update the free surface in stagnant regions. This technique is suitable only when surface tension effects dominate viscous effects.

Saito and Scriven (1981) have illustrated a particular strategy to represent the free-surface position, referencing the meniscus section with the polar arm of length $f(\theta)$ and flat sections by height $h(x)$. This introduces a new degree of freedom on each free-surface node that corresponds to the nodal position. A variant of this is advocated in the present study, as this is taken to be most suitable for the present requirements. A corresponding Petrov-Galerkin formulation is derived for free-surface location and the subsequent adjustment of the original mesh. This allows for local point wise corrections that may supplement the solution procedure and invoke remeshing locally, if required.

Generally, Eulerian techniques are used to compute the field variables at fixed nodal points of the mesh. A separate system of equations is generated for the free surface location. These schemes are suitable even with meshes that see large distortions. Lagrangian approaches localize the fluid location properties to a finite number of particles that move with the fluid. This approach fails when distortions are large. Ramaswamy (1990) has presented an arbitrary Lagrangian-Eulerian finite element technique, similar to that of Hirt *et al.* (1974). In the Lagrangian section, the mesh velocity equates to the fluid velocity, that removes the convective fluxes from the momentum transport equation. In this manner, nodal point location may be computed via a velocity-correction scheme. Subsequently, the mesh velocity is updated using these nodal point locations. In the Eulerian phase, convective fluxes are evaluated. Finally, an updated position of the free-surface is computed, using both fluid and mesh velocities. A conventional Galerkin-Bubnov finite element method is employed. This mixed Lagrangian-Eulerian method (Ramaswamy, 1990) takes advantage of these aspects and mitigates any mesh distortion difficulties that may arise during the Lagrangian phase.

Sato and Richardson (1994) proposed a fringe element generation method based upon a hybrid finite element/finite volume method. There is no global remeshing performed with this method. Instead, the fluid flows over a fixed mesh wetting new portions. New fringe elements are created in the surface neighbourhood, conforming to the original mesh structure. In contrast to local remeshing/stretching methods, such an approach avoids mesh distortion. Each element and node is assigned a dry-wet Boolean flag to identify whether it is wetted by the fluid or not. Starting from the nodal flag information, the new location of the free surface at time t^{n+1} is traced via kinematics considerations, based on an Euler scheme. A similar strategy is adopted by Ding *et al.* (1993) for the computation of moving free-surface boundaries. Regalt *et al.* (1993) used a nodal displacement scheme with a combination of remeshing of the flow domain for a dip coating process. Since the free surface position is not known apriori and if its initial guess is far from the actual solution, then it is observed in Regalt *et al.* (1993) that the use of kinematic boundary conditions directly lead to convergence difficulties. In order to force the search procedure to converge with this scheme, the kinematic boundary conditions were under-relaxed, during the first few iterations.

The present work introduces new aspects of implementation, based on the ideas of Saito and Scriven (1981) for the computation of free-surfaces. This scheme is not restricted to a particular shape. Rather it can be transformed from one coordinate system to another, locally or globally, according to the free-surface orientation and domain. The method is tested on the complex flow section, described below in Figure 1, that contains both flat and curved meniscus shapes. The flow zone comprises of the inflow on the roller, passing

to the nip between roller and foil, and the coating flow, from the meniscus to the outflow on the foil.

2. Governing equations

For an incompressible and isothermal laminar flow, the system of governing equations may be described by momentum and the continuity equations. In the absence of body forces, the system may be expressed in the form

$$\rho \frac{\partial u}{\partial t} = \nabla \cdot T - \rho u \cdot \nabla u - \nabla p \tag{1}$$

$$\nabla \cdot u = 0 \tag{2}$$

where ρ is the fluid density, t is the time, $u(x,t)$ is the fluid velocity and p is the isotropic pressure. For Newtonian flows, the stress $\boldsymbol{T}$ is defined via a Newtonian viscosity μ, and the rate of deformation tensor $\boldsymbol{D}$,

$$T = 2\mu \boldsymbol{D} \tag{3}$$

where

$$\boldsymbol{D} = \frac{L + L^t}{2} \quad \text{and} \quad L^t = \nabla u. \tag{4}$$

With a constant viscosity and using the continuity equation (2), the Navier-Stokes equation can be recovered,

$$\rho \frac{\partial u}{\partial t} = \mu \nabla^2 u - \rho u \cdot \nabla u - \nabla p \tag{5}$$

where $\mu \nabla^2 u$ is the diffusion term.

Adopting characteristic scales on velocity, U, length, L and viscosity, μ, we may define non-dimensional variables $u = Uu^*$ and $p = [\mu U/L]p^*$. Hence, we may define an equivalent non-dimensional system of equations to (5) and (2), discarding the * notation for convenience of representation,

$$\begin{aligned} \mathrm{Re} \frac{\partial u}{\partial t} &= \nabla^2 u - \mathrm{Re}\, u \cdot \nabla u - \nabla p, \\ \nabla \cdot u &= 0, \end{aligned} \tag{6}$$

where the non-dimensional group Reynolds number is defined as $\mathrm{Re} = \rho UL/\mu$.

For the solution of the given system of governing equations, both initial and boundary conditions are required. Initial conditions can be formed by prescribing initial values for the primitive field variables at $t = 0$,

$$U(x,t) = u_0(x,0),$$

$$p(x,t) = p(x,0).$$

Conditions at the free-surface require a normal constraint,

$$p + \tau_{nm} = -p_0 + \sigma\beta, \tag{7}$$

whilst the absence of friction ensures the tangential constraint,

$$\tau_{nt} = 0. \tag{8}$$

Here, τ_{nn}, τ_{nt} are normal and tangential stress components, respectively, p_0 is atmospheric and p local pressure, σ is a surface tension coefficient and β is the mean curvature of the free-surface (Chen and Scriven, 1988). The effects of surface tension are neglected in these calculations. On the free-surface boundary, the normal stress is equated to that of atmospheric pressure, which is taken as ambient ($p_0 = 0$) and the tangential stress should vanish, so the surface tension is zero. Remaining boundary conditions are taken of no-slip on roller and foil, uniform flow at inlet on the roller and outlet on the foil, with vanishing flux across the nip. This suffices to specify the problem.

3. Finite element analysis

The general procedure adopted is one of time-stepping to a steady-state solution. This approach may be used either in a true transient context or one simply to achieve steady-state. Here, we are interested primarily in steady conditions, though subsequently, we wish to consider transient instabilities. A Taylor-Galerkin algorithm is used to solve the governing equations (6). A twostep Lax-Wendroff approach, based on a Taylor series expansion up to second order in time, is used to find the solution at steady-state. A two-step pressurecorrection method is applied to handle the incompressibility constraint. Employing the Crank-Nicolson treatment on diffusive term, the resultingsolution method produces three fractional-staged (Hawken *et al.*, 1990).

In stage one non-solenoidal velocity field $u^{n+1/2}$ and u^* are computed via a predictor-corrector doublet. A Jacobi method is used to solve the resulting mass matrix equation. With the use of u^*, the second stage computes the pressure difference, $p^{n+1} - p^n$, via a Poisson equation, applying Choleski method. The third stage completes the loop, calculating the end-of-time-step solenodal velocity field u^{n+1} by Jacobi iterative solver. The details upon this implementation may be found in Townsend and Webster (1987) and Hawken *et al.* (1990).

Following the notation of Cuvelier *et al.* (1986), the velocity and pressure fields are approximated by $U(\mathbf{x}, t) = U^j(t)\phi_j(\mathbf{x})$ and $P(\mathbf{x}, t) = P^k(t)\varphi_k(\mathbf{x})$, where U and P represents the vector of nodal values of velocity and pressure respectively and ϕ_j is a piecewise quadratic and φ_k is a linear basis function.

On a specified field domain, the fully discrete semi-implicit Taylor-Galerkin/pressure-correction system of equations in matrix form is given as follows:

$$\text{Stage 1a.}\quad \left(\frac{2\mathrm{Re}}{\Delta t}M+\frac{1}{2}S\right)\left(U^{n+\frac{1}{2}}-U^{n}\right)=\{-[S+\mathrm{Re}N(U)]U+L^{T}P\}^{n}$$

$$\text{Stage 1b.}\quad \left(\frac{\mathrm{Re}}{\Delta t}M+\frac{1}{2}S\right)(U^{*}-U^{n})=(-[SU+L^{T}P]^{n}-[\mathrm{Re}N(U)U]^{n+\frac{1}{2}} \tag{9}$$

$$\text{Stage 2.}\quad K(P^{n+1}-P^{n})=-\frac{2}{\Delta t}\mathrm{Re}LU^{*}$$

$$\text{Stage 3.}\quad \frac{\mathrm{Re}}{\Delta t}M(U^{n+1}-U^{*})=\frac{1}{2}L^{T}(P^{n+1}-P^{n}),$$

where M, S, $N(U)$, L, and K are consistent mass matrix, momentum diffusion matrix, convection matrix, pressure gradient matrix and pressure stiffness matrix respectively. In matrix form, these can be expressed as follows:

$$M_{ij}=\int_{\Omega}\phi_i\phi_j\,\mathrm{d}\Omega,$$

$$N(U)_{ij}=\int_{\Omega}\phi_i\left(\phi_i U_1\frac{\partial\phi_j}{\partial x}+\phi_1 U_1\frac{\partial\phi_j}{\partial y}\right)\mathrm{d}\Omega,$$

$$((L_k)_{ij})=\int_{\Omega}\frac{\partial\phi_j}{\partial x_k}\,\mathrm{d}\Omega,$$

$$K_{ij}=\int_{\Omega}\nabla\psi_i\nabla\psi_j\,\mathrm{d}\Omega,$$

$$S_{ij}=\int_{\Omega}\nabla\phi_i\nabla\phi_j\,\mathrm{d}\Omega.$$

4. Free-surface location

Some of the difficulties, which arise in the mathematical modelling, are associated with the presence of a free-surface, whose position is unknown apriori and must therefore be computed as part of the scheme. In the first instance, the geometry of the free-surface is based on a set (estimated) initial position, see Figure 1. The coat-outlet flow on the foil is taken as uniform thickness (width of a_{outlet}, qualifies positions A and B). The same is true on the roller for inflow (gives D and E). The meniscus is specified on the basis of extremities B and D, and interconnecting arc through C. Guidance on the angle of location of meniscus from the nip, can normally be obtained by experiment. Here, the intersection of the angle bisector between foil and roller, with the polar arm to the origin is taken at an angle of 94°, establishing point C. Arcs BC

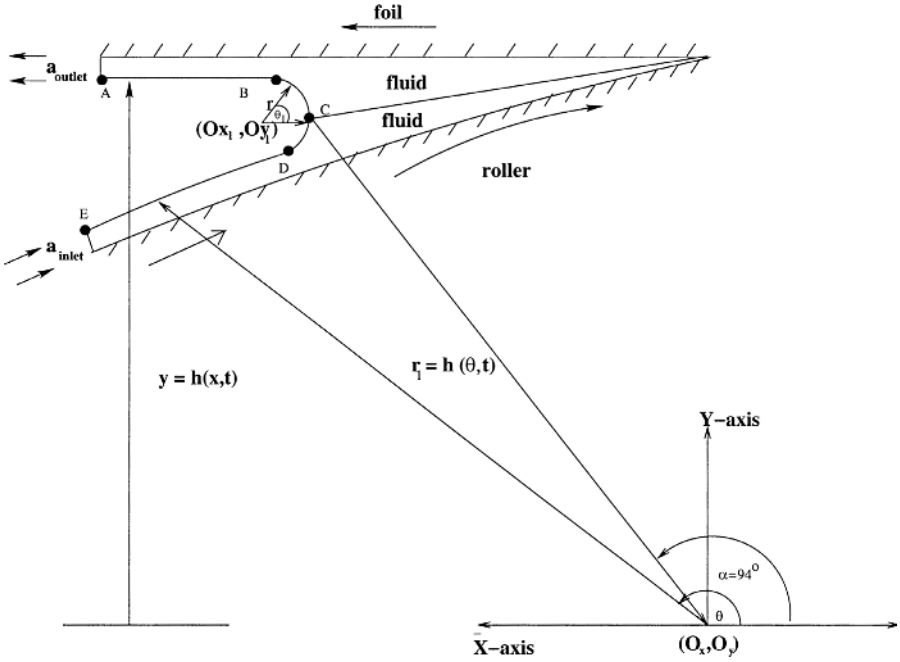

Figure 1.
Schematic flow diagram

and CD are then taken as circular arc segments, so that BC tangents the coating level and, likewise, CD tangents the roller inflow level (radius of arcs is then equally distant from B, C and D; this locates B and D precisely). A meniscus shape is sketched for illustration in Figure 1. The eventual position of the free-surface $h(x,t)$, is determined via solution of the following two equations:

On flat free-surface boundaries (lines at constant y):

$$\frac{\partial h}{\partial t} = -U_x \frac{\partial h}{\partial x} + U_y, \tag{10}$$

On the curved meniscus boundary section (lines at fixed azimuthal angle θ setting):

$$\frac{\partial h}{\partial t} = -U_\vartheta \frac{1}{r} \frac{\partial h}{\partial \vartheta} + U_r, \tag{11}$$

where the translation between Cartesian and polar coordinates is assumed.

Initial conditions for the transient algorithm are taken as quiescent upon the field, but with plug flow imposed at inflow and outflow. It is also found helpful, to enhance efficiency in convergence to a steady scenario, to first fix the free boundary as a solid surface (location as above) and compute an internal flow field from which to commence the free-surface solution. This provides a contrast to free-surface movement from a predefined position. With free-surface

movement, the new position of each node on the free-surface is computed using the above equations (10) or (11), according to the particular boundary section. Remeshing must be performed after each time-step to avoid excessive distortion of elements in the boundary zones.

In a general discrete variational form, equation (10) and (11) can be expressed in a fourth algorithmic stage to the time-step cycle:

$$\text{Stage 4} \quad \begin{aligned} &\frac{1}{\Delta t}\int_{\Gamma}(\psi_i + (\alpha_1 + u\cdot\nabla\psi_i))(\psi_k + (\alpha_2 + u\cdot\nabla\psi_k))\Delta H_{\mathrm{k}}^{n+1}\,\mathrm{d}\Gamma_F \\ &\quad - \int_{\Gamma}(\psi_i + (\alpha_1 + u\cdot\nabla\psi_i))u\cdot\nabla\psi_k H_{\mathrm{k}}^{n}\,\mathrm{d}\Gamma_F \end{aligned} \tag{12}$$

adopting notation for time-step, Δt, interpolant, $H^n(x)$, interpolating functions, $\psi_k(x)$, and nodal solution increment, ΔH_k^n,

$$H^n(x) = H_k^n\psi_k(x) \quad \text{and} \quad \Delta H_k^{n+1} = (H_k^{n+1} - H_k^n). \tag{13}$$

We utilise generalized scalar factors α_i to switch between Galerkin and SUPG (explicit and implicit) schemes, as and when required. A free-surface boundary segment is indicated by Γ_F, over which quadrature may be established. In equation (12), the generalized form of convective term is represented, subsuming either equation (10) or (11), depending upon the particular boundary segment under consideration. We have found it most effective to use $\alpha_1 = \alpha^h$ (an SUPG parameter (Carew *et al.*, 1993)) and $\alpha_2 = \Delta t/2$ to recover an implicit SUPG scheme. Then, both ψ_i (and ψ_k) are taken as linear functions on straight-sided boundary elements sections. In the present work, the free-surface location is computed by an SUPG approach. This is due to the dominant hyperbolic type of the corresponding equations (10–11), for which some form of upwinding is appropriate. This approach has accelerated solution convergence in comparison to a conventional Galerkin approach. In addition, we have the freedom of choice of free-surface time step size. Here, we have employed the same Δt for field and free-surface computations, as we are interested only in steady-state solutions. Elsewhere, when transient accuracy is important, we may take advantage of socalled pseudo-time-steps (Ding *et al.*, 1993; Nithiarasu and Zienkiewicz, 2000).

5. Problem specification

In the first instance, we confine attention to the model problem as illustrated in Figure 1. The problem is parameterised through coating thickness (characteristic length), foil speed, U_{foil}, (characteristic speed, typically $O(10^2)$), and rotation speed of the roller, U_{roll}, 90 per cent of the foil speed. A roller of radius r_1, rotates at angular rate ω (speed $U_{\mathrm{roll}} = \omega r_1$), applying a coating to the underside of the alloy sheet of thickness $h(x, t)$. The sheet rests on both the

roller and the thin film of fluid between the roller and the sheet. The sheet moves with speed U_{foil} in the horizontal direction (negative x) and the problem is posed in a Cartesian frame of reference. As a first approximation, there is no leakage assumed in the nip region and steady-state flow configurations are sought.

The system of governing equations, in conjunction with free boundary equations, in the absence of surface tension, is solved by employing a timemarching finite element semi-implicit Taylor-Galerkin/Pressure-correction algorithm (Townsend and Webster, 1987; Hawken *et al.*, 1990; Carew *et al.*, 1993), applying appropriate initial and boundary conditions. The mesh used is displayed in Figure 2 and has 2925 nodes, 1302 elements and 6662 degrees of freedom. Three distinct mesh views are displayed. Figure 2a is a full mesh view that clearly indicates the wide aspect ratios involved. Figure 2b and 2c provide zoomed sections of mesh at the meniscus region and towards the nip, accordingly.

Variation in roll speed covers settings of 90 per cent, 99 per cent, 108 per cent and 120 per cent of the standard foil speed, $\bar{U}_{\text{foil}}$, typically $O(10^2)$m/min. Similarly, variation in foil-speed is taken from $0.5^*\bar{U}_{\text{foil}}$ to $2.5^*\bar{U}_{\text{foil}}$ at increments of $0.5^*\bar{U}_{\text{foil}}$.

No-slip boundary conditions for the flow on solid surfaces are taken as:

$$\text{on the foil: } U_x = -\bar{U}_{\text{foil}}, U_y = 0;$$

$$\text{on the roller: } U_x = U_{\text{roll}} \cos\theta, U_y = U_{\text{roll}} \sin\theta;$$

where $U_{\text{roll}} = R\omega$, R is the radius and ω the angular rotation rate of the roller.

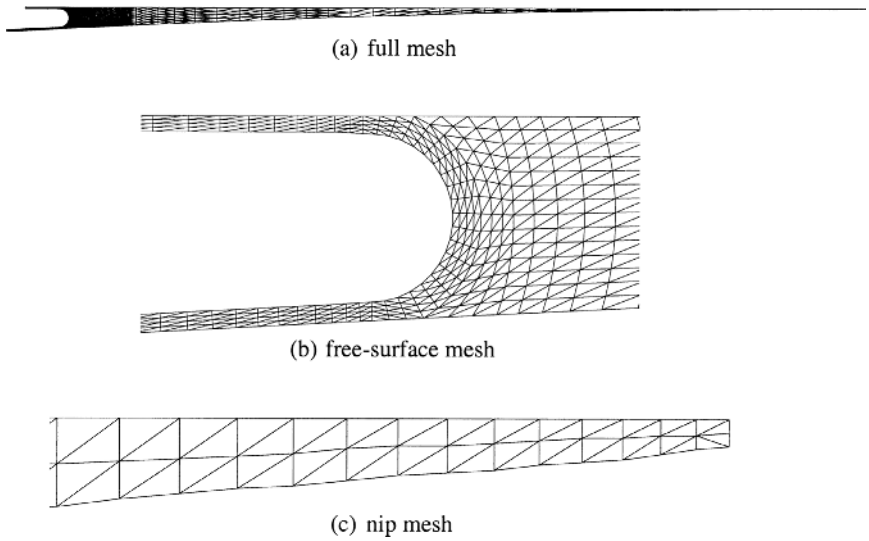

Figure 2.
Finite element mesh sections

On free-surface boundaries, conditions (7) and (8) apply, and there, pressure remains unspecified. Hence, once foil and roll-speeds have been set, there is a balance imposed between inflow and outflow, presuming there is no leakage at the nip. If we assume that the coating thickness is given (experimentally determined) and that a plug flow is generated both on the foil and roller, then the roller feed thickness is also set.

5.1 Lift and drag

Lift and drag are mechanical forces that arise between solid and liquid surfaces. Here we are concerned with the lift on the foil and the drag on the roller. For a Newtonian fluid the lift, drag and stress may be expressed through the following expressions:

$$L_{\text{foil}} = \int_{\Gamma_{\text{foil}}} \{ -p \sin\theta + \tau_{xy} \cos\theta + \tau_{yy} \sin\theta \} \, \mathrm{d}\theta = \int_{\Gamma_{\text{foil}}} L_{\text{f}} \, \mathrm{d}\theta \qquad (14)$$

$$D_{\text{roller}} = \int_{\Gamma_{\text{roller}}} \{ -p \cos\theta + \tau_{\text{xx}} \cos\theta + \tau_{xy} \sin\theta \} \, \mathrm{d}\theta = \int_{\Gamma_{\text{roller}}} (-D_{\text{R}}) \, \mathrm{d}\theta \qquad (15)$$

where $\tau = 2\mu D$; L_f and D_R are distributional lift and drag quantities.

6. Numerical results

The simulation results begin with the standard setting as discussed in section 5, that follows four sub-sections of study. The first is associated with the increment of roll-speed at fixed foil-speed. The second considers the effects upon the flow behaviour of variation in foil-speed at fixed roll-speed. Next we switch our attention to inlet flow instability on roller. Presentation of results is achieved through flow field representation of streamlines in the meniscus free-surface regions and pressure line contours in the nip region. At various flow settings, tabulations in pressure, shear-rate, and lift on the foil and drag on the roller are provided, from which we may infer certain properties of the flow. All values are reported in a non-dimensional form.

6.1 Flow patterns at standard settings

A standard foil-speed setting of 1 unit and roller speed, 90 per cent of foil-speed, constitutes the base scenario around which variations are subsequently sought. A steady-state solution is obtained, starting from rest, by imposing Dirichlet boundary conditions. Here, free boundary conditions refer to natural unconstrained forms, where boundary location is also determined. Fixed implies strong constrained boundary conditions on restrained boundary locations. When the boundaries are set as fixed, a flow reversal around the meniscus is apparent, see Figure 3a. Switching from fixed to free boundary settings, removes any flow reversal around the meniscus, see Figure 3b. So that

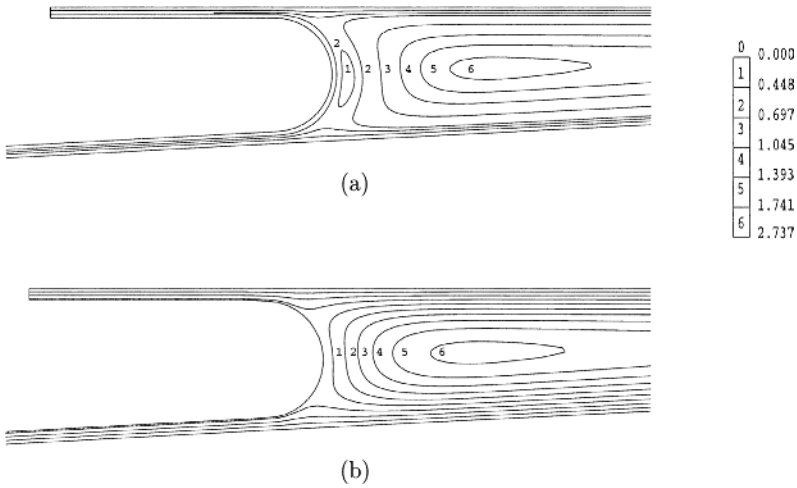

Figure 3.
Streamline patterns: a) fixed and b) free boundary conditions, $U_{\text{roll}} = 90\%\ \bar{U}_{\text{foil}}$

in the free-surface configuration, streamline patterns indicate that flow travels with the roller to the nip, before reversing and being taken up by the foil, to pass into the coating film on the sheet. A central long thin vortex is set up in the flow region between the roller and the foil, see Figure 3. Free boundary conditions apply to all calculations performed below.

6.2 Analysis with increasing roll-speeds

We study the streamline patterns that emerge in the meniscus region for speeds of 90 per cent, 99 per cent, 108 per cent and 120 per cent of foil-speed, see Figure 4, with ten contours per field plot from maximum at the vortex center to minimum at the meniscus. A slight distortion is observed of the streamline adjoining the meniscus, indicating a shift with dominance of foil over roll-speed initially at 90 per cent setting, to a balanced scenario at 99 per cent setting. The distortion is reversed for 108 per cent and 120 per cent settings. A single vortex has dominated the flow field at each speed setting, and the maximum magnitude of these streamlines increases with increasing roll-speed (Isaksson and Rigdahl, (1994) reported similar results).

Pressure maxima in the nip region are $O(10^6)$ units, and are gradually decreasing with linear trend as roll-speed increases, see Figure 5a. Foil distributional pressure (P_f) is shown in Figure 5b along the foil length. The pressure level is fairly low along most of the foil, rises significantly close to the nip and decreases with increasing roll-speed. However, the magnitude of these decreasing trends is small due to the small variation in roll-speeds. Therefore, insignificant changes in pressure line contours are observed for the different roll-speeds. Pressure line contours are included in Figure 5c for 90 per cent roll-speed of $\bar{U}_{\text{foil}}$. The region of maximum pressure broadens away from the nip as

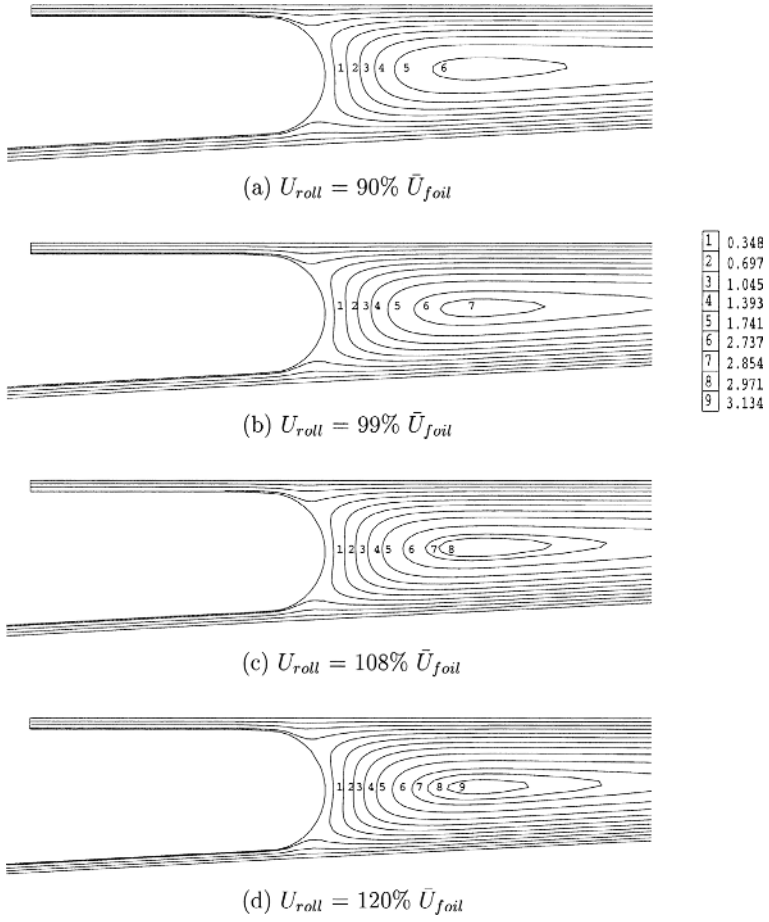

Figure 4.
Streamline patterns, increasing roll-speed

rollspeed increases. Likewise, maximum shear-rate is charted against increasing roll-speed setting in Table I, attaining values of $O(10^3)$ units in the nip region, see Figure 5a. Maxima in shear-rate shift from the foil at 90 per cent roll-speed, to a balanced pattern at 99 per cent roll-speed, and finally towards the roller at 108 per cent speed and above, see Figure 7. Since the locations of application of shear-rate maxima shift, from foil to roller with increasing roll-speed, it is no surprise that shearrates increase with roll-speed, see Table I. Inlet layer thickness a_{inlet} is taken relative to outlet, that is maintained at a constant level as speed of roller increases. Note, that due to pre-metering, a constant flow rate is assumed for all settings.

Lift (L_{foil}) on the foil and drag (D_{roller}) on the roller are charted correspondingly against roll-speed setting (see Table I, Figure 6). Lift on the foil is $O(10^7)$ units and decreases with increasing roll-speed, in contrast drag on

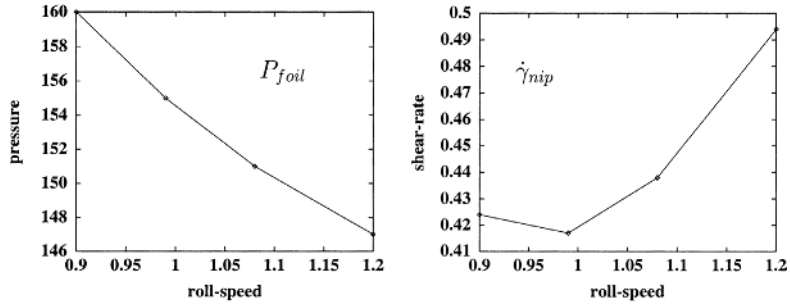

(a) Pressure and shear-rate line plots (values*10^3), increasing roll-speed

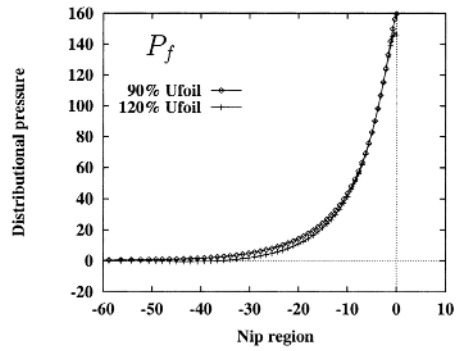

(b) Foil distributional pressure (P_f) values*10^3, towards the nip

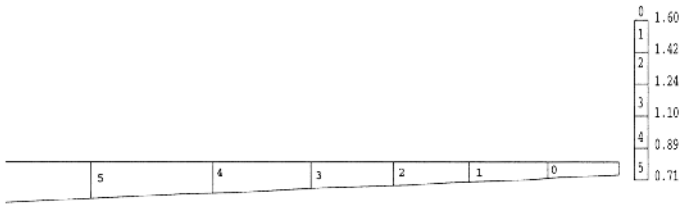

(c) Nip-region, pressure line contours (values*10^5), U_{roll} = 90% $\bar{U}_{foil}$

Figure 5.
a. Pressure and shear-rate line plots (values*10^3), increasing roll-speed b. Foil distributional pressure (P_f) values*10^3, towards the nip c. Pressure line contours (values *10^5), $U_{roll} = 90\%\ \bar{U}_{foil}$

$u_{roll}/\bar{U}_{foil}$	a_{inlet}	$\dot{\gamma}_{nip}$	P_{nip}	L_{foil}	D_{roller}
0.9	1.1	0.424E+00	0.160E+03	0.131E+04	0.131E+01
0.99	1.01	0.417E+00	0.155E+03	0.126E+04	0.136E+01
1.08	0.92	0.438E+00	0.151E+03	0.122E+04	0.142E+01
1.20	0.83	0.494E+00	0.147E+03	0.116E+04	0.149E+01

Table I.
Solution variation with roll-speed, values *10^3 units.

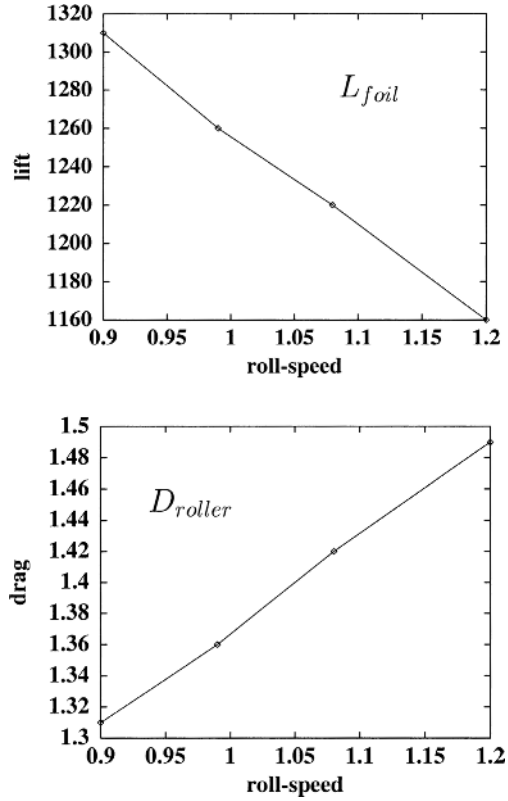

Figure 6.
Line plots, lift on foil and drag on roller (values $*10^3$), increasing roll-speed

the roller is $O(10^4)$ units and increases with increasing roll-speed, but remains three orders of magnitude lower in size than the lift. Hence, with increasing roll-speed, decreasing linear trends are observed in pressure and lift, and increasing trends in drag and shear-rate. It is not surprising that the lift on the foil decreases with increasing roller speed. As the roll-speed is increased, the foil-speed becomes smaller in comparison. Thus, the lift on the foil decreases with increasing roll-speed (or decreasing foil-speed). The variation in each quantity is noted in Table I, where a_{inlet} is the inlet layer thickness carried by the roller. We reiterate, outlet-coating thickness is maintained throughout at 1 unit.

Free-surface location and its adjustment with increasing roll-speed may be discerned from Figure 8 and is calibrated by the departure from the initial fixed location setting. These adjustments are noted to be only minor perturbations. The inflow feed decreases in thickness with increasing roll-speed, as the outlet strip-coating width is held fixed.

6.3 Analysis with increasing/decreasing foil-speeds

With the alternative series of adjustments based upon variation in foilspeeds, flow patterns in streamlines indicate a rise in vortex location with increase

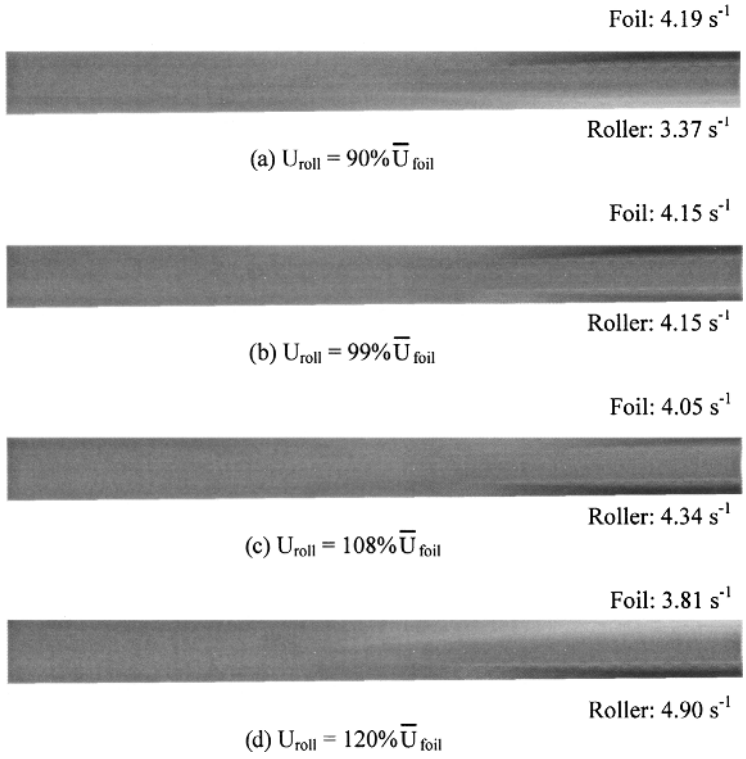

Figure 7.
Shear-rate contours (values $*10^2$), increasing roll-speed

in foil-speed, see Figure 9. Since flow rate is determined by the coat-oulet flow, increasing foil speed implies enhanced flow rate from one setting to another, presuming adjustment in pre-metering. The rising inflow rate at increasing foil-speeds, generates high pressures that push the vortex up towards the foil, see Figure 9b–e. Correspondingly, there is a drop in vortex location with decrease in foil-speed to $0.5\,\bar{U}_{\text{foil}}$, see Figure 9a. Distortion in the streamline patterns near the meniscus region is clearly apparent with increasing and decreasing foilspeeds. Meniscus shapes adjust accordingly. At fixed-strip coating width, the inflow thickness on the roller widens as foil-speed increases, see Figure 9b–e, and narrows with decreasing foil-speed, see Figure 9a.

In contrast to the scenario of increasing roll-speeds, here foil-pressures, nip shear-rates, foil-lift and roller-drag all demonstrate essentially linear increasing trends with increasing foil-speed, see Figure 10. This means that the levels of foilpressure, foil-lift and roller-drag double, with doubling of foil-speed. It is noticeable once more that lift on the foil is three orders of magnitude larger than that of drag on the roller. The corresponding results are charted in Table II. Figure 11 shows the foil-pressure distribution travelling towards the

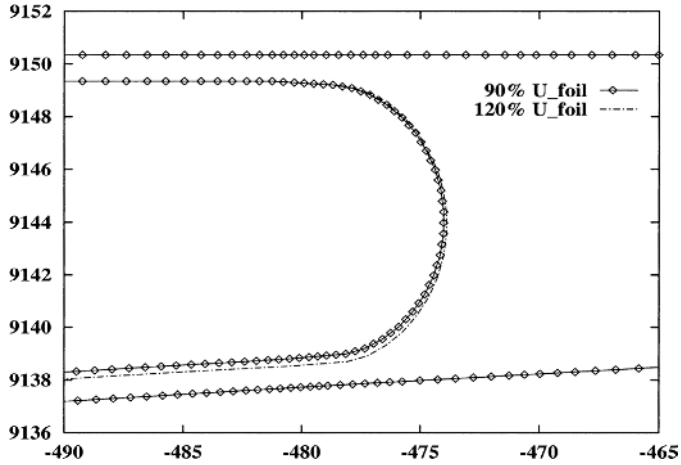

Figure 8.
Free-surface profiles, increasing roll-speed

nip-region. The level of pressure increases with increasing foil-speed raising the maximum nip-pressure level. In contrast to roller-speed variation, the region of maximum pressure is drawn towards the nip as foil-speed increases and pressure levels rise at the meniscus region, correspondingly. Limiting trends at both meniscus and nip are displayed in line contours of Figure 12, to associate the spatial distribution of pressure. The rising pressure at the nip with foil-speed is clearly evident by inspection in Figure 13. Here, the increase in foil-speed is more than twice the standard setting. For foil-speeds lower than roll-speeds, maximum shear-rates shift to the roller, see Figure 14, and pressure levels decline at the meniscus zone (Figure 12a).

6.4 Instability analysis: inlet flow on roller

Lastly, we consider flow response to variation in roller inflow. This is to identify flow sensitivity (coating outlet) to inlet flow perturbations. We note that the roller-inlet flow may inherit any flow disturbances generated, either from the pickup-metering roll or metering-applicator roll. To accomplish this a small sinusoidal wave (Carvalho and Scriven, 1997) is imposed at the free-surface inlet boundary on the roller and the full flow is solved up to the nip, meniscus and coating regions. As shown in Figure 3, no flow penetrates the flow zone internal to the meniscus free-surface region (recirculation region). Such sinusoidal disturbances die away, due to the presence of the roller-inlet and meniscus free-surfaces, see Figure 15. The crosssection velocity profiles are observed to merge into a plug flow form, similar to those in the standard setting (with absence of imposed inlet disturbances). Hence, plug flow patterns are resumed prior to the meniscus region. The freesurface setting has dissipated inlet oscillations, so that these do not influence the meniscus or

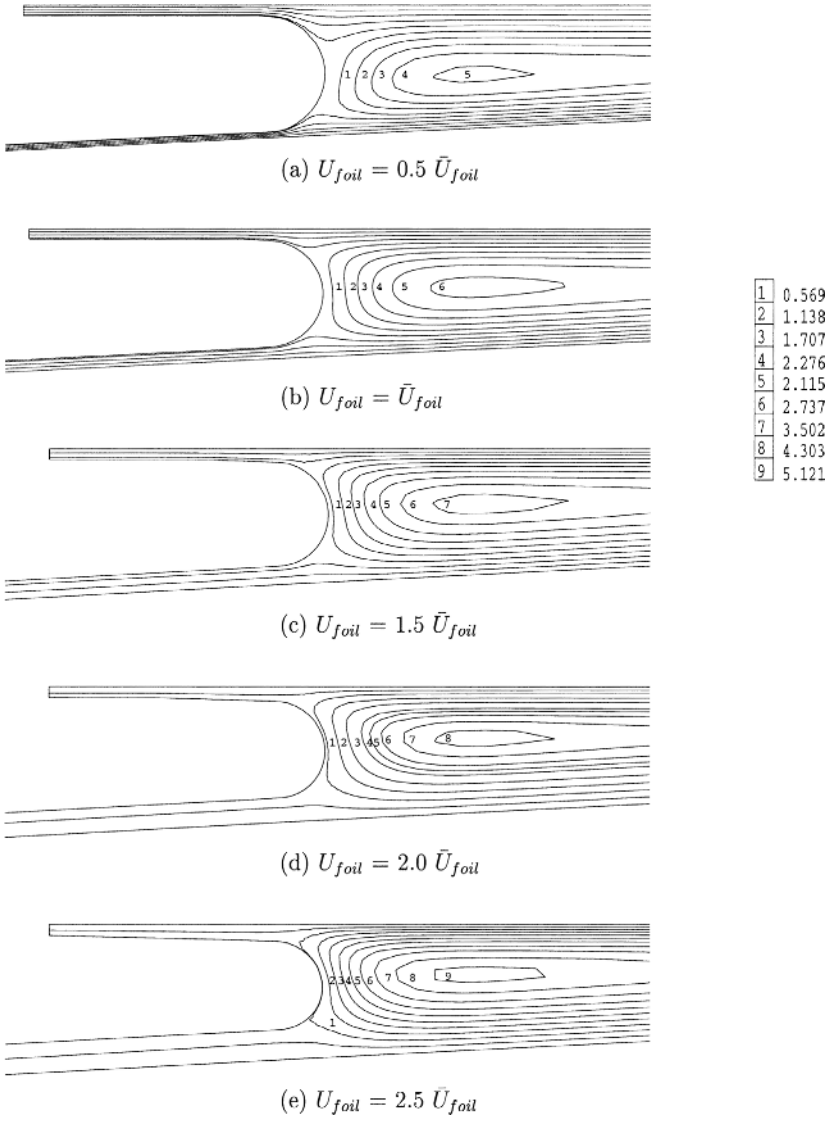

(a) $U_{foil} = 0.5\ \bar{U}_{foil}$

(b) $U_{foil} = \bar{U}_{foil}$

(c) $U_{foil} = 1.5\ \bar{U}_{foil}$

(d) $U_{foil} = 2.0\ \bar{U}_{foil}$

(e) $U_{foil} = 2.5\ \bar{U}_{foil}$

Figure 9.
Streamline patterns, increasing foil-speed

foil-coating flow structure. We illustrate these findings in Figure 15, on profiles and free-surface shapes, covering the zoomed section at the roller inlet alone. Fluid travels along the roller to the nip, the flow reverses at the nip-region and returns along the foil. We conclude that these influences do not affect the $\text{coat}_{\text{outlet}}$ flow.

On this evidence and under constant inflow due to pre-metering, it would appear reasonable to disregard roller inflow spatial instabilities, within the

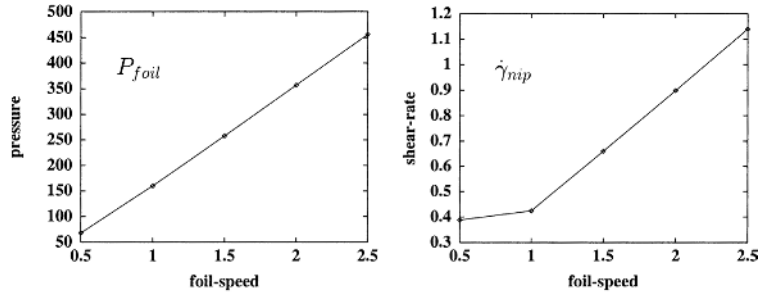

(a) Line plots, pressure and shear-rates (values*10^3), increasing foil-speed

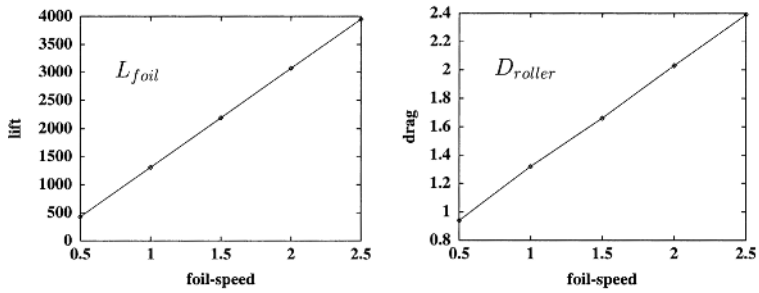

(b) Line plots, lift and drag (values*10^3), increasing foil-speed

Figure 10.
a. Line plots, pressure and shear-rates (values *10^3), increasing foilspeed, b. Line plots, lift and drag (values *10^3), increasing foil-speed

$u_{foil}/\bar{U}_{foil}$	a_{inlet}	$\dot{\gamma}_{nip}$	P_{nip}	L_{foil}	D_{roller}
0.5	0.55	0.388E+00	0.678E+02	0.427E+03	0.094E+01
1.0	1.1	0.424E+00	0.160E+03	0.131E+04	0.130E+01
1.5	1.6	0.660E+00	0.258E+03	0.219E+04	0.166E+01
2.0	2.2	0.898E+00	0.357E+03	0.307E+04	0.203E+01
2.5	2.7	0.114E+01	0.456E+03	0.395E+04	0.239E+01

Table II.
Solution variation with foil-speed, values *10^3 units.

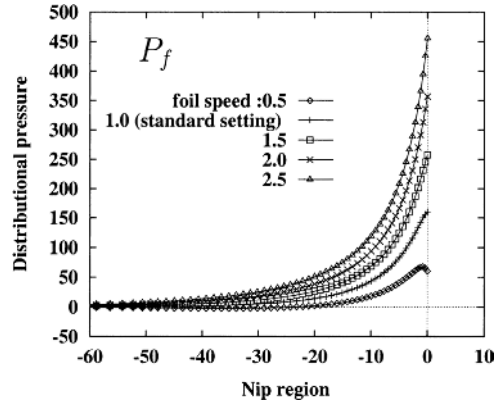

Figure 11.
Foil distributional pressure (values *10^3), towards nip, increasing foilspeeds

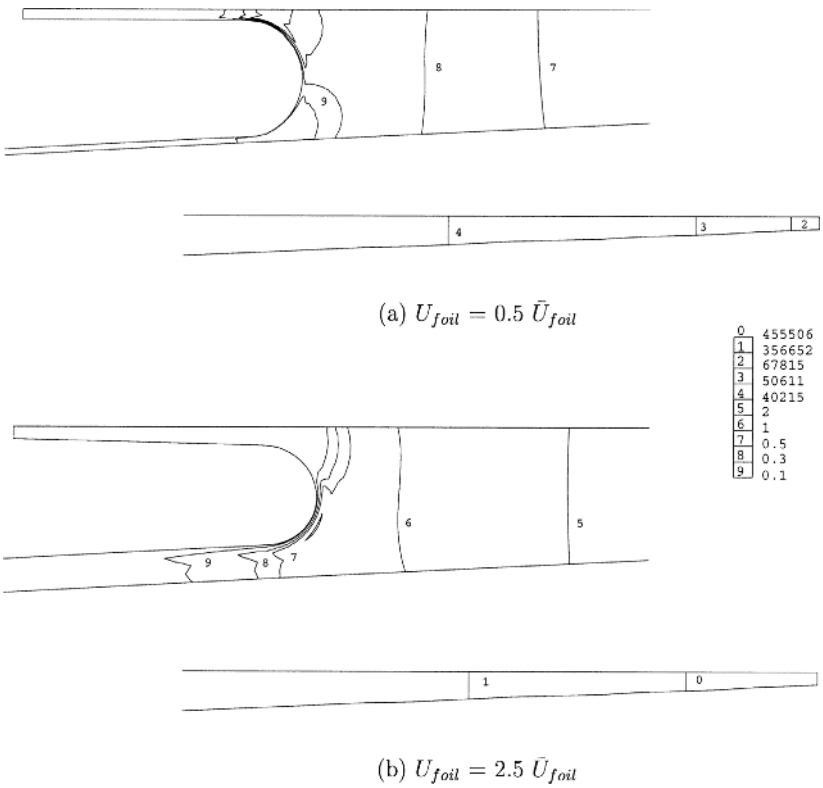

Figure 12.
Pressure line contours, meniscus-nip zones, increasing foil-speed

overall scheme of analysis. Flow adjustment at the nip and temporal instabilities remain outstanding.

7. Conclusions

A complex roller-coating problem of industrial relevance is analysed. The effects of increasing foil and roll-speeds on characteristic flow quantities such as pressure, lift, drag and shear-rate are reported. At increasing roll-speeds, pressure and lift on the foil display a linear decreasing trend, the levels of maximum field pressure broaden away from the nip and the location of maximum shear-rate shifts towards the roller. In contrast with increasing foil-speeds, a linear increasing trend is observed in foil-pressure and lift. Also the levels of maximum pressure migrate towards the nip and the location of maximum shear-rate switches towards the foil. As for drag on the roller, a linear increasing trend is observed with both increasing roller and foil speeds.

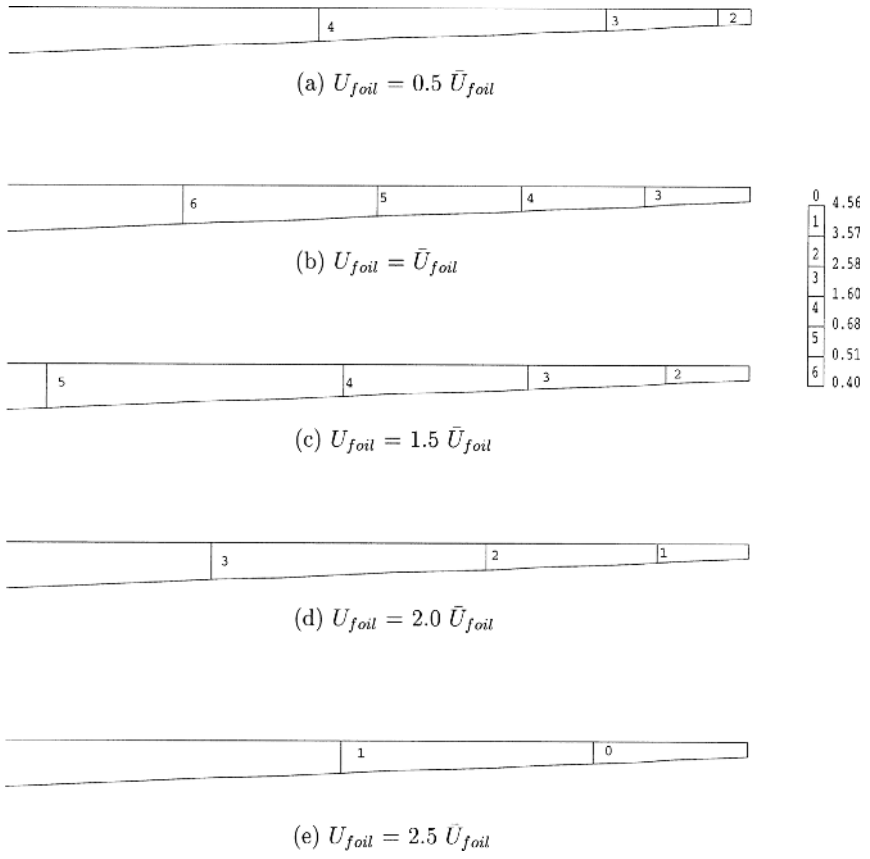

Figure 13.
Pressure line contours, nip zone; full range of foil speeds

Distorted streamline patterns are identified adjoining the meniscus upon increasing foil-speed. The higher the speed, the greater the streamline distortion in the direction of dominant flow (roller or foil speed). Vortex centres shift towards the foil at increasing foil-speed, and towards the roller at decreasing foil-speed. Any inherited flow disturbances generated, from the pickupmetering-applicator rollers, are not found to have any influence on the coatoutlet flow, due to the presence of the roller inlet and meniscus free-surfaces.

Significantly, no flow reversal is encountered around and in the vicinity of the free-surface meniscus. The lacquer coatings are essentially Newtonian in character. It is not surprising therefore that, linear trends are observed with parameter variation in the different quantities measured. As excess of lift above sheet weight may be equated unequivocally to vertical shift of foil position, hence it is conspicuous that flow instability is more likely to be

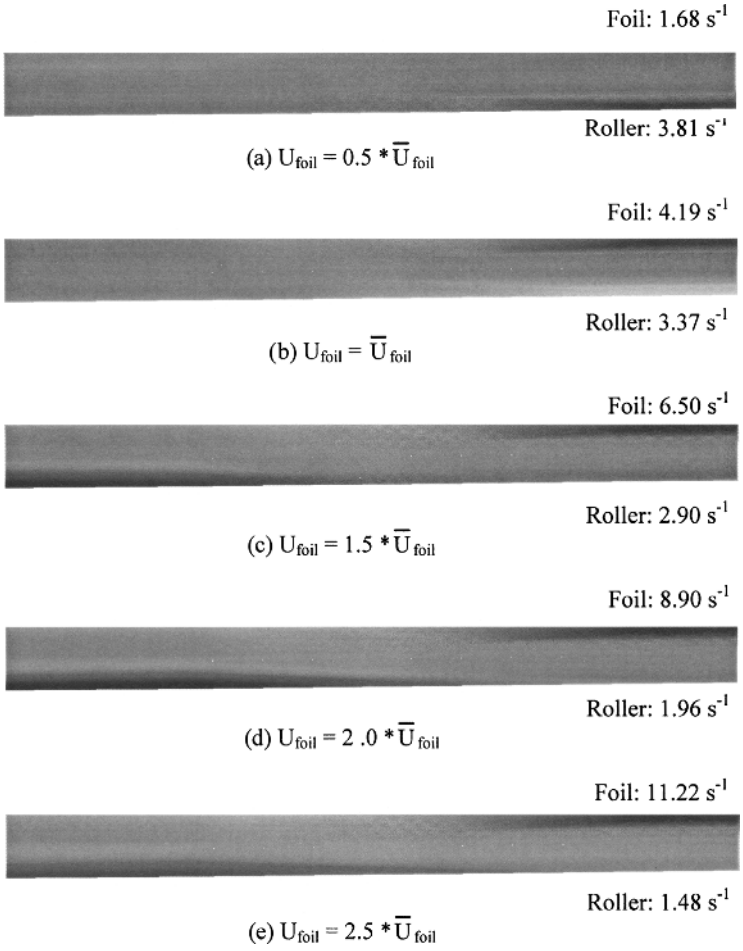

Figure 14.
Shear-rate contours (values $*10^2$), increasing foil-speed

stimulated by increase of foil-speed than that through roll-speed. The excessive build-up of pressure in the nip region (magnitude of 10^6 units), influences vortex flow structure and meniscus shapes. The elevated pressure in the nip, will force the foil to move vertically and relax the normal forces by creating a wider gap between roller and foil. This phenomenon, occurring in time, will create foil vibration and generate flow instabilities, subsequently giving rise to wavy patterns on the film coating (chatter and starvation, causing flow

Figure 15.
Interior velocity fields at roller inlet

lines). Future studies are intended to focus on these temporal processing instabilities.

References

Benjamin, D.F. (1994), *Roll Coating Flows and Multiple Flow Systems*; PhD. Thesis, University of Minnesota, Minneapolis, MN, University Microfilms Int., Ann. Arbor, MI.

Carvalho, M.S. and Scriven, L.E. (1997a), "Multiple atates of a viscous free-surface flow: transition from pre-metered to a metering flow", *Int. J. Num. Meth. Fluids*, 24, pp. 813-31.

Carvalho, M.S. and Scriven, L.E. (1997), "Deformable foll coating flows: steady state and linear perturbation analysis", *J. Fluid Mech.*, 339, pp. 143-72.

Chen, K.S.A. and Scriven, L.E. (1988), *Roll Coating, Forward and Reverse: Effect of Feed Condition*, AIChE Spring Nat. Meet., New Orleans, LA.

Cohu, O. and Magnin, A. (1997), "Forward roll coating of Newtonian fluids with deformable rolls: an experimental investigation", *Chem. Eng. Sci.*, 52 No. 8, pp. 1339-47.

Carew, E.O.A., Townsend, P. and Webster, M.F. (1993), "A Taylor-Petrov-Galerkin algorithm for viscoelastic flow", *J. non-Newtonian Fluid Mech.*, 50, pp. 253-87.

Cuvelier, C., Segal, A., Van Steenhoven, A.A. (1986), *Finite Element Methods and Navier-Stokes Equations*, D. Reidel.

Ding, D., Townsend, P., Webster, M.F. (1993), *Numerical Simulation of Filling Problems Related to Injection Moulding*, Proceedings of IUTAM symposium on Numerical Simulation of non-isothermal flow of Viscoelastic Liquids, Netherlands.

Fourcade, E., Bertrand, F., Régalt, O. and Tanguy, P.A. (1999), "Finite element analysis of fluid-solid interaction in the metering nip of a metering size press", *Comp. Meth. Appl. Mech. Eng.*, 174, pp. 235-45.

Hawken, D.M., Tamaddon-Jahromi, H.R., Townsend, P. and Webster, M.F. (1990), "A Taylor-Galerkin based algorithm for viscous incompressible flow", *Int. J. Num. Meth. Fluids*, 10, pp. 327-51.

Hirt, C.W., Amsden, A.A. and Cook, J.L. (1974), "An arbitrary Lagrangian-Eulerian computing method for all flow speeds", *J. Comp. Phys.*, 14, pp. 227-53.

Isaksson, P. and Rigdahl, M. (1994), "Numerical simulation of blade coating with short dwell and roll application coaters", *Rheo. Acta*, 33, pp. 454-67.

Keunings, R. (1986), "An algorithm for the simulation of transient visco-elastic flows with free-surfaces", *J. Comp. Phys.*, 62, pp. 199-220.

Nithiarasu, P. and Zienkiewicz, O.C. (2000), "On stabilization of the CBS algorithm: Internal and external time steps", *Int. J. Num. Meth. Eng.*, 48, pp. 875-80.

Ramaswamy, B. (1990), "Numerical simulation of unsteady viscous free-surface flow", *J. Comp. Phys.*, 90, pp. 396-430.

Regalt, O., Labrie, R. and Tanguy, P.A. (1993), "Free-surface model for dip coating process", *J. Comp. Phys.*, 109, pp. 238-46.

Saito, H. and Scriven, L.E. (1981), "Study of coating flow by the finite element method", *J. Comp. Phys.*, 42, pp. 53-76.

Sato, T. and Richardson, S.M. (1994), "Numerical simulation method for viscoelastic flows with free surface-fringe element generation method", *Int. J. Num. Meth. Fluids*, 19, pp. 555-74.

Silliman, W.J. and Scriven, L.E. (1980), "Separating flow near a static contact line: slip at a wall and shape of a free surface", *J. Comp. Phys.*, 34, pp. 287-313.

Sizaire, R. and Legat, V. (1997), "Finite element simulation of a filament stretching extensional rheometer", *J. non-Newtonian Fluid Mech.*, 71, pp. 89-107.

Tanner, R.I., Nickell, R.E. and Bilger, R.W. (1975), "Finite element method for the solution of some imcompressible non-Newtonian fluid mechanics problems with free surfaces", *Comp. Meth. App. Mech. Eng.*, 6, pp. 155-74.

Townsend, P., Webster, M.F. (1987), *An Algorithm for the Three-Dimensional Transient Simulation of non-Newtonian Fluid Flows*, Proc. NUMETA 87, Martinus Nijhoff, Dordrecht, vol. 2 T12/1.

Simulation of pressure- and tube-tooling wire-coating flows through distributed computation

A. Baloch, H. Matallah, V. Ngamaramvaranggul and M.F. Webster
Institute of Non-Newtonian Fluid Mechanics, Department of Computer Science, University of Wales, Swansea, UK

Keywords *Finite element method, Viscous flows, Parallel computing*

Abstract *This article focuses on the comparative study of annular wire-coating flows with polymer melt materials. Different process designs are considered of pressure- and tube-tooling, complementing earlier studies on individual designs. A novel mass-balance free-surface location technique is proposed. The polymeric materials are represented via shear-thinning, differential viscoelastic constitutive models, taken of exponential Phan-Thien/Tanner form. Simulations are conducted for these industrial problems through distributed parallel computation, using a semi-implicit time-stepping Taylor-Galerkin/pressure-correction algorithm. On typical field results and by comparing short-against full-die pressure-tooling solutions, shear-rates are observed to increase ten fold, while strain rates increase one hundred times. Tube-tooling shear and extension-rates are one quarter of those for pressure-tooling. These findings across design options, have considerable bearing on the appropriateness of choice for the respective process involved. Parallel finite element results are generated on a homogeneous network of Intel-chip workstations, running PVM (Parallel Vitual Machine) protocol over a Solaris operating system. Parallel timings yield practically ideal linear speed-up over the set number of processors.*

1. Introduction

A number of highly viscoelastic, complex extrusion flows are investigated, commonly associated with the coatings of glass rovings, fibre-optic cables, wire and cable manufacturing processes. Three flow problems are considered, die swell/drag flow (short-die pressure-tooling), full pressure-tooling, and tube-tooling flow. The first two cases are suitable for simulating industrial narrow-bore wire-coating processes. Tube-tooling deals with thicker (wide-bore) wire-coating processes. To provide realistic flow representation for the polymer melt materials used in practice, the specific choice is made of a viscoelastic constitutive model to support shear-thinning and strain-softening behaviour. To this end, an exponential Phan-Thien/Tanner (EPTT) model is selected, flows are computed in a two-dimensional annular coordinate system

Supported by a grant from the UK EPSRC GR/L14916.
Faculty of Science, Chulalongkorn University, Thailand *Int. J. Num. Meth. Heat & Fluid Flow, 6 March 2002.*

International Journal of Numerical Methods for Heat & Fluid Flow, Vol. 12 No. 4, 2002, pp. 458-493.

DOI 10.1108/09615530210433305

under creeping flow conditions, and a parallelised version of a semi-implicit time-marching finite element scheme is used, Taylor-Galerkin/pressure-correction (TGPC).

Wire-coating has been studied extensively in experimental and computational form over recent years, see Ngamaramvaranggul and Webster (2002) for review. Most studies concentrate on the pressure-tooling design. Modelling assumptions commonly include isothermal flow conditions, incompressibility of the coating flow (Chung, 1986), concentricity of the wire (Tadmor and Bird, 1974), and wire speeds ranging up to one meter per second (Mutlu *et al.*, 1998a). Wire-coating, in the pressure-tooling context, constitutes a process of two flow regimes: a shear dominated flow within an annular die, and an extension-dominated flow along the wire-coating region beyond the die. Injection of the molten polymer into the tooling die establishes a pressure-driven flow. Contact between the molten plastic tube and the wire is made within the die for pressure-tooling, where the travelling wire induces a drag flow, drawing out the polymer melt to form a sheath around the cable. Unique to tube-tooling design is the dependency upon the effects of draw-down beyond the die. Coating production lines for narrow-bore wire use relatively high speeds, around one meter per second, and the deposition of the fluid on a rigid moving wire is treated as a free surface problem.

Recent attention by a number of authors has focused on the simulation of pressure-tooling flow for viscous fluids, such as those of Caswell and Tanner (1978); Pittman and Rashid (1986); Mitsoulis (1986); Mitsoulis *et al.* (1988) and Wagner and Mistsoulis (1985). Their work dealt mainly with shear flow under both isothermal and non-isothermal conditions. Molten polymers have been noted to exhibit highly elastic behaviour when subject to large deformation (Matallah *et al.*, 2001). Only recently, numerical techniques have proven capable of reaching solutions for sufficiently high and relevant levels of elasticity. Many attempts involving either lubrication or inelastic approximations have been conducted to addressed these shortcomings (Caswell and Tanner, 1978; Mitsoulis *et al.*, 1988; Han and Rao, 1978). With finite elements (FE) Mitsoulis (1986) studied the wire-coating flow of power-law and Newtonian fluids. Mitsoulis concluded that the inclusion of shear-thinning reduced the levels of die-swell at the die-exit, as well as the recirculation that occurred within the die. In a subsequent article, Mitsoulis *et al.* (1988) provided a detailed investigation into high-speed industrial wire-coating. Two flow formulations were used; a planar FE analysis for non-isothermal flows, and a lubrication approximation for isothermal, power-law fluids. Results corroborated the experimental findings of Haas and Skewis (1974).

The inadequacy of inelastic modelling was made apparent by (Binding *et al.*, 1996), rediscrepancies in stress and pressure drop. To predict residual stressing within the melt coating, a viscoelastic analysis was recommended to account for the influence of short residence times of the particles within the flow. Hence,

we have adopted differential viscoelastic models, to predict stress development, using state-of-the-art FE techniques to reach the high deformation rates encountered and associated high Weissenberg numbers, $O(10^4)$. For tube-tooling flows and fixed free-surface estimation, we have conducted single-mode PTT (Phan-Thien/Tanner) simulations in Mutlu *et al.* (1998a); Mutlu *et al* (1998b) and Matallah *et al.* (2001). Tube-tooling was analysed in sections in Mutlu *et al.* (1998a), isolating draw-down flow and studying the effects of stress pre-history and various boundary conditions. This led to a further study (Mutlu *et al.*, 1998b) on coupled and decoupled solution procedures for a range of model fluids, approaching those of industrial relevance. In Matallah *et al.* (2001), single-mode calculations were compared to those of multi-mode type for LDPE and HDPE grade polymers. The multi-mode computations revealed the dominant modes of most significance to the process and gave insight as to the levels of residual stress in the resultant coatings. Further work on multi-mode modelling of Matallah *et al.* (2000), emphasised the influence of die-design on optimal process setting. Three, as opposed to seven modes, were found adequate to sufficiently describe the flow. The draw-down residence time, which dictates the dominance of certain modes within the relaxation time spectrum, was found to be a major factor to influence the decay of residual stressing in the coating.

With specific attention paid to slip for viscous flows, a semi-implicit Taylor-Galerkin/pressure-correction procedure was used by the present authors (Ngamaramvaranggul and Webster, 2000a) for pressure-tooling and tube-tooling. There, the influence of slip onset, as opposed to no-slip conditions within the die, was examined. Tracking free surfaces, our earlier work on model problems addressed stick-slip and die-swell flows, see Ngamaramvaranggul and Webster (2000b); Ngamaramvaranggul and Webster (2001). In a recent article for pressure-tooling (Ngamaramvaranggul and Webster, 2002), the influence of material rheology was investigated on free-surface flow, whilst tube-tooling was the subject in Matallah *et al* (2001). The present analysis extends upon this work, contrasting comparative designs via a distributed parallel implementation. The computational efficiency over various processor-cluster sizes is of particular interest. Distributed computations are performed over homogeneous network clusters of Intel-chip workstations, running a Solaris Operating System. In this respect, our earlier experience with parallelisation for large, yet model problems (Baloch *et al.*, 2000), is taken into the industrial processing realm. There, Parallel Virtual Machine (PVM) message passing libraries were used over heterogeneous clusters, comprising of DEC-alpha, Intel-Solaris and AMD-K7 (Athlon) Linux processors.

The outline of the current paper is as follows. First, the governing equations are described, followed by the rheological behaviour of the PTT model. In section 4, the three different problems are specified. This is followed, by an outline to the parallel TGPC numerical method employed for the simulations.

The results of the simulations are presented in section 6 and some conclusions are drawn in section 7.

2. Governing equations

Isothermal flow of incompressible viscoelastic fluid can be modelled through a system comprising of the generalised momentum transport, conservation of mass and viscoelastic stress constitutive equations. The problems in this study are modeled as annular and two-dimensional. In the absence of body forces, such a system can be represented in the form:

$$\nabla \cdot \boldsymbol{v} = 0, \tag{1}$$

$$\rho \frac{\partial \boldsymbol{v}}{\partial t} = \nabla \cdot \boldsymbol{\sigma} - \rho \boldsymbol{v} \cdot \nabla \boldsymbol{v}. \tag{2}$$

Here, $\boldsymbol{v}$ is the fluid velocity vector field, $\boldsymbol{\sigma}$ is the Cauchy stress tensor, ρ is the fluid density, t represents time, and divergence and gradient operations are implied via ∇. The Cauchy stress tensor can be expressed in the form:

$$\boldsymbol{\sigma} = -p\delta + \boldsymbol{T}_e,$$

where p is the isotropic fluid pressure, δ is the Kronecker delta tensor, and $\boldsymbol{T}_e$ is the stress tensor. For viscoelastic flows, stress $\boldsymbol{T}_e$ can be decomposed into solvent and polymeric contributions,

$$\boldsymbol{T}_e = \tau + 2\mu_2 \boldsymbol{d},$$

with tensors, τ, the elastic extra-stress and rate-of-strain $\boldsymbol{d} = 0.5[\nabla v + (\nabla v)^{\dagger}]$ (superscript $\dagger$ denotes a matrix transpose). μ_2 is a solvent and μ_1 a polymeric solute viscosity, such that $\mu = \mu_1 + \mu_2$. The particular choice of constitutive model is that of Phan-Thien and Tanner (1977); Phan-Thien (1978), in exponential form (EPPT). In contrast to models, such as constant shear viscosity Oldroyd-B, this EPPT version supports shear-thinning and finite extensional viscosity behaviour. The constitutive equations for the extra-stress of the EPTT model is expressed as:

$$\lambda_1 \frac{\partial \tau}{\partial t} = 2\mu_1 \boldsymbol{d} + f\tau - \lambda_1 \{\tau \cdot \nabla \boldsymbol{v} + (\nabla \boldsymbol{v})^{\dagger} \cdot \tau - \boldsymbol{v} \cdot \nabla \tau\}, \tag{3}$$

with an averaged relaxation time λ_1 and function f, defined in terms of trace of stress, trace (τ), as:

$$f = \exp\left[\frac{\varepsilon \lambda_1}{\mu_1} \mathrm{trace}(\tau)\right].$$

The material parameters that control shear and elongational properties of the fluid are ϵ and μ_1, respectively. These may be evaluated by fitting to the

experimental data (Matallah *et al.*, 2001; Matallah *et al.*, 2000). When ε vanishes, the Oldroyd-B model is recovered and $f = 1$.

We find it convenient to express the governing equations in non-dimensional form, by defining corresponding scales of characteristic length R, taken as coating length (Figures 2–4), and wire-speed as characteristic velocity scale, V. Then, stress and pressure are scaled by a factor of $\mu V/R$,and time by R/V. There are two non-dimensional group numbers of relevance, Weissenberg number $\mathrm{We} = V\lambda_1/R$ and Reynolds number $\mathrm{Re} = \rho VR/\mu$.

3. Shear and elongational behaviour of EPTT

Many common non-Newtonian fluids exhibit non-constant viscosity behaviour. So, for example, such materials may display shear-thinning, where the viscosity is a decreasing function of increasing shear rate as illustrated in Figures 1a in pure shear. Figure 1b reflects a similar plot, demonstrating the functional dependence of viscosity under increasing strain-rate in pure uniaxial extension. This is termed the elongational or extensional viscosity behaviour. The merits of the PTT model over the Maxwell model are highlighted by Phan-Thien and Tanner (1992), noting that, the Maxwellian elongational viscosity is singular at finite strain rates. The shear and extensional viscosity functions, μ_s and μ_e, of the PTT model variants may be expressed as a function of f itself, taken of exponential form as above, via

$$\mu_s(\dot{\gamma}) = \mu_2 + \frac{\mu_1}{f}, \tag{4}$$

and

$$\mu_e(\dot{\varepsilon}) = 3\mu_2 + \frac{2\mu_1}{f - 2\lambda_1\dot{\varepsilon}} + \frac{\mu}{f + \lambda_1\dot{\varepsilon}}. \tag{5}$$

Under general flow conditions, there is need to record generalized shear and strain-rates, that are defined via flow invariants as, respectively:

$$\dot{\gamma} = 2\sqrt{\mathrm{II}_d}, \quad \dot{\varepsilon} = 3\frac{\mathrm{III}_d}{\mathrm{II}_d}, \tag{6}$$

where II_d and III_d are the second and third invariants of the rate of strain tensor $\boldsymbol{d}$. Such quantities are represented as

$$\mathrm{II}_d = \frac{1}{2}\mathrm{trace}(\boldsymbol{d}) = \frac{1}{2}\left\{\left(\frac{\partial v_r}{\partial r}\right)^2 + \left(\frac{\partial v_z}{\partial z}\right)^2 + \left(\frac{v_r}{r}\right)^2 + \frac{1}{2}\left(\frac{\partial v_r}{\partial z} + \frac{\partial v_z}{\partial r}\right)^2\right\}, \tag{7}$$

$$\mathrm{III}_d = \det(\boldsymbol{d}) = \frac{v_r}{r}\left\{\frac{\partial v_r}{\partial r}\frac{\partial v_z}{\partial z} - \frac{1}{4}\left(\frac{\partial v_r}{\partial z} + \frac{\partial v_2}{\partial r}\right)^2\right\}. \tag{8}$$

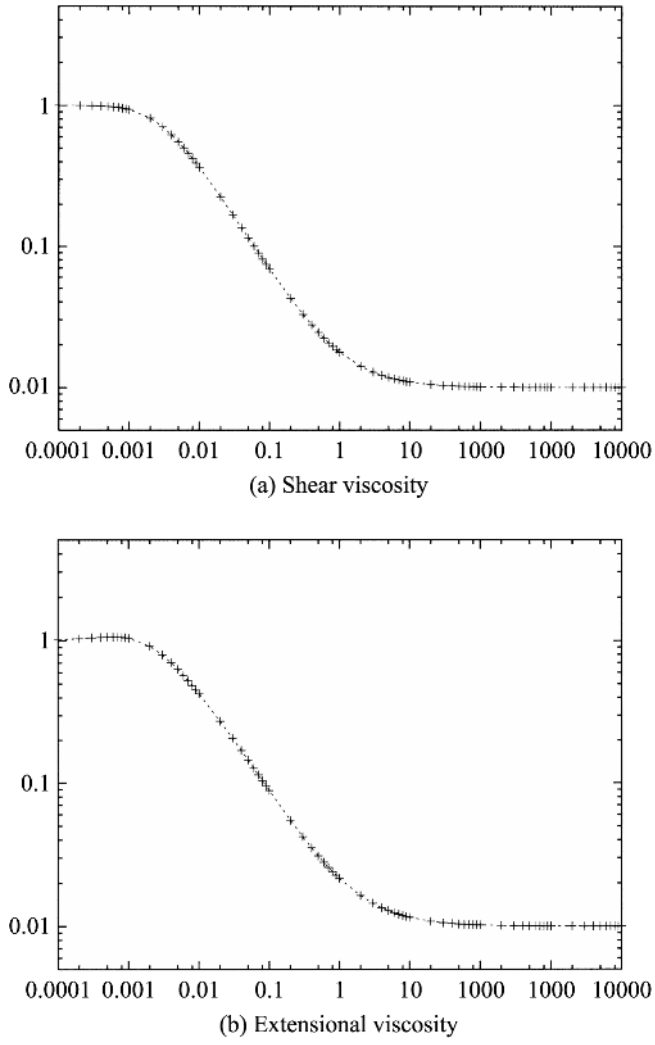

Figure 1.
EPTT model

In pure shear, μ_s varies with ϵ, μ_1, and λ_1. The effect of elevating μ_1 from levels of 0.88 to 0.99 and 0.95 reduces the second Newtonian plateau level from $0(10^{-1})$ to $0(10^{-2})$ and below. Here $\mu_1 = 0.99$ solute fraction is taken as suitable. Shifting of λ_1, (via We) from unity to 0(10) and $0(10^2)$, translates μ_s in a constant shift fashion. The larger λ_1, the earlier the departure occurs from the first Newtonian plateau. Current material and process settings suggest λ_1 of $0(1s)$ is a reasonable choice, so that We = 200. With selection of $\mu_1 = 0.99$ and We = 200, the influence of the ϵ-parameter choice is relatively minor.

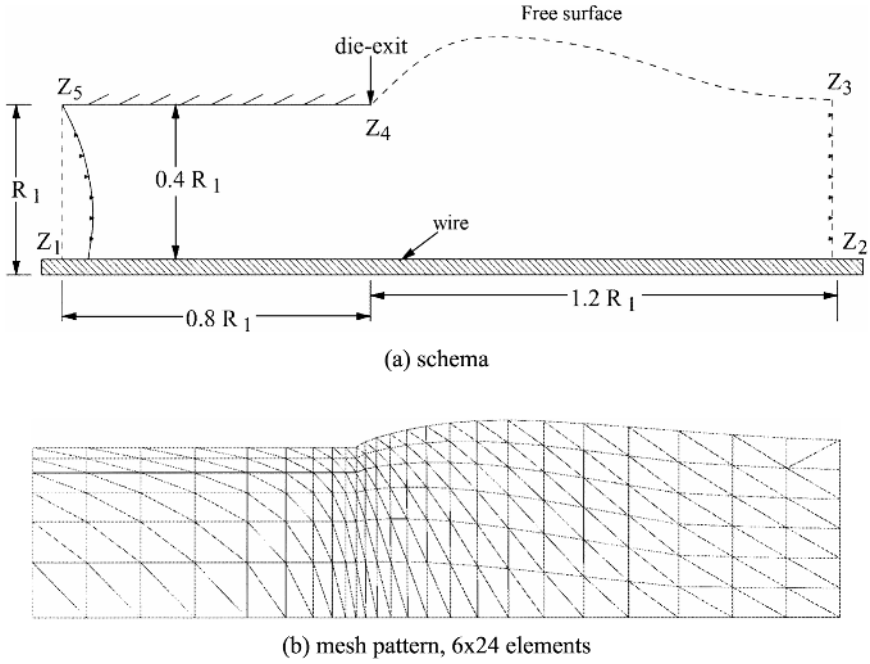

Figure 2.
Short-die pressure-tooling

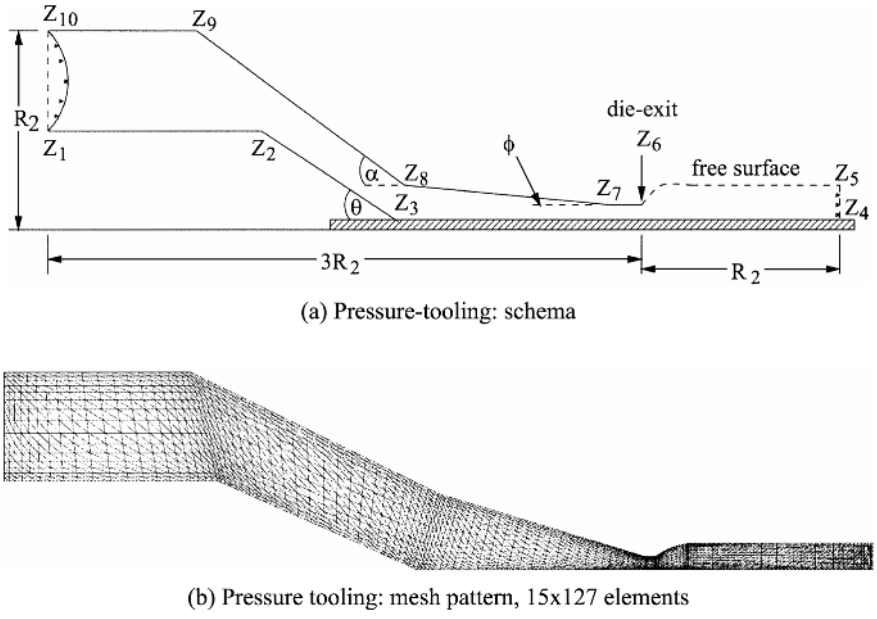

Figure 3.
Full-die pressure-tooling

Increasing ϵ from 0.1 to 0(1) slightly retards the μ_s pattern, so that earlier departure from the first Newtonian plateau occurs. Here, ϵ of unity is selected.

In steady uniaxial extension, μ_e follows the behavioural trends of μ_s for both We and μ_1 parameters. Distinction may be found via the ϵ-parameter. Taking the tuple setting $(\mu_1, \mathrm{We}) = (0.99, 200)$, for $0.1 \leq \epsilon \leq 0.5$, reflects strain-hardening at low strain rates prior to softening at rates above 10^{-2}. Only softening is apparent for $\varepsilon \sim 0(1)$. The EPTT (1,0.99,200) model demonstrates the desired viscometric functional behaviour, shear-thinning and strain-softening, within the deformation rate ranges of dominant interest for the wire-coating process, as one might typically encounter, say, for an LDPE grade polymer at 230°C. As a consequence of these viscometric functions, we observe later in the actual flows of current interest, that maximum shear-rates may rise to $O(10^2)$ units, whilst strain-rates reach $O(10^1)$. This, in turn, implies that second Newtonian plateaus will be reached *in-situ*.

4. Specification of problems

This paper deals with the study of three types of flow: die swell/drag flow (short-die tooling), full-die pressure-tooling flow, and tube-tooling flow.

4.1 Die-swell/drag flow

This annular problem illustrates the progressive effects of an imposed drag flow from the travelling wire on both the classic die swell problem (within the free jet-flow region) and stick-slip flow (see Figure 2). Mesh refinement considerations follow our previous studies (Ngamaramvaranggul and Webster, 2002; Ngamaramvaranggul and Webster, 2000b; Ngamaramvaranggul and Webster, 2001), where the fine mesh of Figure 2b is found suitable. The flowrate through the die is fixed by the fully-developed annular inlet flow profile under pressure-driven conditions. No-slip conditions are applied at the die wall boundaries. The wire and inlet channel radii comprise the characteristic length, while characteristic velocity is directly related to the constant wire-speed at the lower boundary of the domain. The rapid reduction in traction at the free jet surface gives rise to the fully-developed plug flow at the domain outflow.

4.2 Pressure-tooling

Pressure-tooling flow is an extension to the previous die-swell/drag flow study, the domain of which is specified in Figure 3a. This domain contains an initial short-die flow zone within the land region of the die (z_6, z_7), followed by a jet flow region at the die exit. The traveling wire within the die, moving at a fixed speed, first makes contact with the pressure-driven annular flow at z_3 station. The influence of the wire on the polymer melt at this boundary region is referred to in Ngamaramvaranggul and Webster (2002); Binding *et al.* (1996); Ngamaramvaranggul and Webster (2000a). Flow within the die is restrained by no-slip boundary conditions at the die walls. The swelling effects observed in

the jet flow region are caused by the sudden drop to atmospheric pressure, combined with the immediate lack of traction. This swell, in the extruded polymer, levels out to a fully-developed plug flow, by the time it reaches the end of the pressure-tooling domain. The biased fine mesh of Figure 3b is employed, for further details see our prior study (Ngamaramvaranggul and Webster, 2002).

4.3 Tube-tooling

A schematic illustration of the full-die tube-tooling domain is shown in Figure 4a. This was computed upon with the fine mesh of Figure 4b. Problem dimensions are largely in common with the full pressure-tooling specification. So, for example, the lower and upper die wall converging angles are 30° and 17°, at positions z_{10} and z_3, respectively. No-slip die-wall boundary conditions apply throughout the die. In the final draw-down region (z_4z_5 and z_8z_9), free surface conditions apply. For tube-tooling, the wire makes contact with the polymer melt at the end of the draw-down region z_5, with the coating length upon the wire being taken as the characteristic length R_2. As for pressure-tooling, the wire dimensions, inlet hydraulic radius (R_2), and total die length ($3R_2$), again apply in this example. In our previous investigations (Ngamaramvaranggul and Webster, 2002; Ngamaramvaranggul and Webster, 2001), we focused upon mesh convergence studies. Here, numerical solutions are generated on fine meshes only, the detailed statistics of which are recorded in Table I for all three problems, inclusive of degrees of freedom (DOF), for Newtonian (N) models and viscoelastic (V) models.

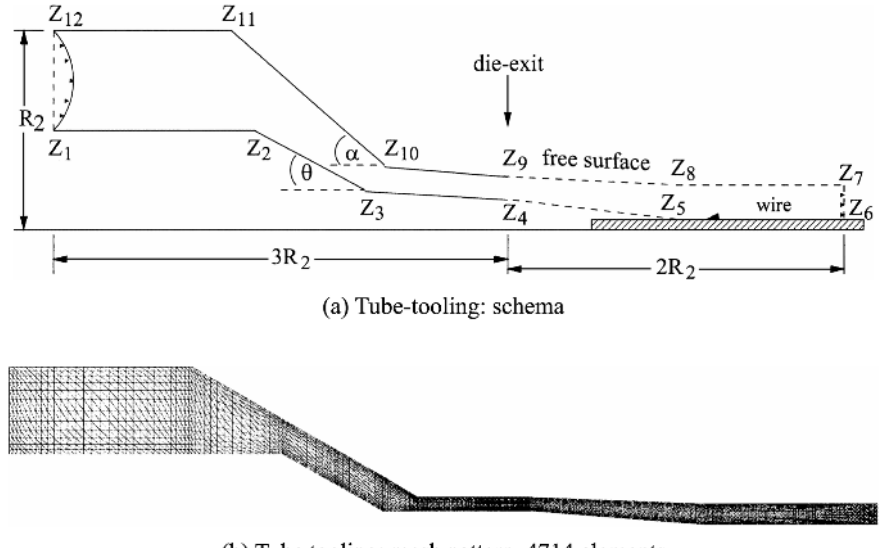

Figure 4.
Full-die tube-tooling

5. Numerical scheme

5.1 Sequential Taylor-Galerkin algorithm

A time-marching finite element algorithm is employed in this investigation to compute steady viscoelastic solution through a semi-implicit Taylor-Petrov-Galerkin/pressure-correction scheme (Townsend and Webster, 1987; Hawken *et al.*, 1990; Carew *et al.*, 1993; Baloch and Webster, 1995; Baloch *et al.*, 1998; Matallah *et al.*, 1998), based on a fractional-step formulation. This involves discretisation for equations (1–3), first in the temporal domain, adopting a Taylor series expansion in time and a pressure-correction operator-split, to build a second-order time-stepping scheme. Spatial discretisation is achieved via Galerkin approximation for momentum and Petrov-Galerkin for the constitutive equations. The finite element basis functions employed are quadratic for velocities and stress, and linear for pressure, defined over two-dimensional triangular elements. Galerkin integrals are evaluated by a seven point Gauss quadrature rule. The time-stepping scheme includes a semi-implicit treatment for the momentum equation to avoid restrictive viscous stability constraints. Solution of each fractional-staged equation is accomplished via an iterative solver. That is, with the exception of the temporal pressure-difference Poisson equation, which is solved through a direct Choleski procedure. The semi-implicit Taylor-Galerkin/pressure-correction method may be presented in semi-discrete temporal format as:

Stage 1a:

$$\frac{2Re}{\Delta t}(\boldsymbol{v}^{n+\frac{1}{2}} - \boldsymbol{v}^{n}) = [\nabla\cdot(2\mu_2\boldsymbol{d} + \tau) - Re\boldsymbol{v}\cdot\nabla\boldsymbol{v} - \nabla p]^{n} + \nabla\cdot\mu_2(d^{n+\frac{1}{2}} - \boldsymbol{d}^{n}),$$

$$\frac{2We}{\Delta t}(\tau^{n+\frac{1}{2}} - \tau^{n})^{n} = 2\mu_1\boldsymbol{d} - f\tau - We[\boldsymbol{v}\cdot\nabla\tau - \nabla\boldsymbol{v}\cdot\tau - (\nabla\boldsymbol{v}\cdot\tau)^{\dagger}]^{n}.$$

Stage 1b:

$$\frac{\mathrm{Re}}{\Delta t}(v^{*} - v^{n}) = [\nabla\cdot(2\mu_2\boldsymbol{d} - \nabla p]^{n} + [\nabla\cdot\tau - \mathrm{Re}\boldsymbol{v}\cdot\nabla\boldsymbol{v}]^{n+\frac{1}{2}} + \nabla\cdot\mu_2(\boldsymbol{d}^{*} - d^{n}),$$

$$\frac{We}{\Delta t}\left(\tau^{n+\frac{1}{2}} - \tau^{n}\right) = 2\mu_1\boldsymbol{d} - f\tau - We[\boldsymbol{v}\cdot\nabla\tau - \nabla v\cdot\tau - (\nabla v\cdot\tau)^{\dagger}]^{n+\frac{1}{2}}.$$

Meshes	Elements	Nodes	DOF(N)	DOF(V)
Short-die	288	377	929	2437
Pressure-tooling	3810	7905	17858	49478
Tube-tooling	4714	9755	22031	61051

Table I. Finite element mesh data

Stage 2:

$$\frac{\Delta t}{2}\nabla^2(p^{n+1} - p^n) = \mathrm{Re}\nabla \cdot v^*$$

Stage 3:

$$\frac{2\mathrm{Re}}{\Delta t}(\boldsymbol{v}^{n+1} - v^*) = -\nabla(p^{n+1} - p^n).$$

Here, n is the time step number and $\boldsymbol{v}^*$ is a non-solenoidal vector field. The velocity and stress components of Stage 1a are taken for a half time step (i.e., $n + 1/2$), while at Stage 1b, the $\boldsymbol{v}^*$ velocities and stresses are computed over a full time step ($n + 1$). In combination, Stage 1 constitutes a predictor-corrector doublet, performed once per time-step. This concludes derivation of stress components for a complete time step. Pressure differences over this period are calculated from the Poisson equation (Stage 2), depending upon the intermediate vector field $\boldsymbol{v}^*$. Solution of this Poisson equation yields the solenoidal velocity over a full time step, as shown in Stage 3 (see Townsend and Webster (1987); Hawken *et al.* (1990)). Free-surface reassessment is conducted at a fourth stage (see on). Recovery of velocity gradients within the constitutive equation further enhances stability of the system, along with streamline-upwind Petrov-Galerkin weighting. Determination of time step (typically $O(10^{-3})$) is made on the basis of a Courant stability constraint.

5.2 Parallel Taylor-Galerkin algorithm

The semi-implicit time-stepping TGPC algorithm is parallelised as follows. Each of the individual fractional-stage phases of the algorithm is parallelised within a single time-step loop. This implies operations of gather and scatter of data, pre- and post- each phase, respectively. In such a manner, the combined problem is split into associated sub-problems relating to each subdomain. We relate such operations with message passing between master and slave processors, achieved via PVM *send* and *receive* communication commands. This is a crucial issue to ensure correct system configuration and network communication. This slave processors solve subdomain problems, whilst the master processor resolves the interface problem and controls master-slave communication (Grant *et al.*, 1998).

Of the various fractional-stages, the pressure equation step is the only one that is conducted through a direct solution procedure (Choleski), involving the explicit parallel construction and solution of a matrix problem. Remaining stages are associated with an iterative solution procedure (Jacobi). It is upon this basis that the exceptional parallel performance characteristics are achieved. The complete detail behind the parallelisation of the TGPC and these two algebraic solution procedures is provided in Grant *et al.* (1998). Briefly, both necessitate an assembly and solution phase, involving finite element loop

construction of right-hand-side vectors and matrix components. For Choleski, the matrix components must be stored. Fortunately, this is manageable even for large problems, as the pressure variable in question is of scalar form on the field.

Solution phases radically differ between iterative and direct procedures. The iterative solution phase is nodally-based. Each sub-problem on a slave processor, first computes contributions for the boundary (interfacing) nodes, so that their result may be communicated to the master processor directly, whilst the computation for interior sub-domain nodes is completed. This enables effective masking of communication. The master processor must then process the combined domain contributions for the *interfacing nodes*, as well as performing system synchronisation and intercommunication processor control. Utilising an iteration number r, acceleration factor ω, right-hand side vector $\boldsymbol{b}$, iteration sub-domain vector $\boldsymbol{X}_{\mathrm{Pi}}$, system (mass) matrix $\boldsymbol{M}_{\mathrm{fe}}$ and diagonal matrix $\boldsymbol{M}_d$, the parallel finite element Jacobi iteration may be expressed in concise notational form, as

$$\text{par}\begin{bmatrix} X_{P_1} \\ \cdots \\ X_{P_2} \\ \cdots \\ X_{P_3} \\ \cdots \\ \vdots \\ \cdots \\ X_{P_n} \end{bmatrix}_{\text{nodes}}^{r+1} = (I - \omega M_d^{-1} M_{\mathrm{fe}}) \begin{bmatrix} X_P \\ \cdots \\ X_P \\ \cdots \\ X_{P_3} \\ \cdots \\ \vdots \\ \cdots \\ X_{P_n} \end{bmatrix}_{\text{nodes}}^{r} + \omega M_d^{-1} [\boldsymbol{b}]_{\text{nodes}}$$

The mass-matrix ($\boldsymbol{M}_{\mathrm{fe}}$) is based on quadratic finite element functions, its diagonalised form ($\boldsymbol{M}_d$) is one of absolute row-sum, and the iterative acceleration parameter ω may be selected to suit (often simply taken as unity). System matrices are referenced and evaluated at the element level only, so that a complete system is never stored. A single iteration sweep of this sort will maintain integrity levels of the data re-synchronisation. Care likewise must be taken with respect to consistent solution increment tolerance calculations, across individual slave and master processors.

The parallel direct solution phase adopts a Schur-complement approach. This introduces a herring-bone structure to the complete system matrix problem, via the associated nodal numbering on each subdomain and the

interfacing boundary nodes. The parallel herring-bone structure of the Choleski system matrix may be represented as

$$\text{par}\begin{bmatrix} [P_1] & & & & & & [MP_1] \\ & [P_2] & & & & & [MP_2] \\ & & [P_3] & & & & [MP_3] \\ & & & \cdot & & & \cdot \\ & & & & \cdot & & \\ & & & & & [P_n] & [MP_n] \\ [P_1M] & [P_2M] & [P_3M] & & & [P_nM] & [M] \end{bmatrix}$$

Herring Bone Structure (Schur-complement)

with $[P_i]$ the subdomain problem for the interior of subdomain i, $[P_iM]$, the matrix contribution of interior subdomain i to the boundary-node problem, and $[M]$ that for the boundary-nodes.

The subdomain problem, for each interior subdomain (on a single slave processor), may be solved in parallel with all others. Finally, the interfacing-node matrix problem is solved, for which all available processors may be used. To date, the size of the interfacing-node matrix problem has been such that a single processor (the master) has been employed to resolve it. In such a fashion, it is possible to render large-scale problems tractable, typically of three-dimensional or viscoelastic form (Grant *et al.*, 1998).

5.3 Free-surface procedure

The term die-swell describes the radial increase of the polymer melt in the free-jet flow on exiting the die. It is represented as the swelling ratio ($\chi = R_j/R$), where R_j is the jet radius and R is the tube radius. This phenomenon is of considerable significance to some polymer processing operations in industry. For creeping flow, without gravity, and with large surface tension, die swell was defined analytically by Richardson (1970). A number of numerical schemes can be used to calculate die swell. Comparisons in performance between free surface estimation algorithms, utilising finite differences, finite elements, and boundary element methods can be found in Crochet *et al.* (1984) and Tanner (1985). These surveys cover the varying accuracy of the above methods and asymptotic analysis for viscoelastic and Newtonian fluids in axisymmetric and planar die flows. Below we introduce two schemes for the numerical prediction of free surfaces: the streamline prediction method and the mass balance method. These are incorporated into the present algorithm at a fourth terminating stage within the time-step loop.

5.4 Stream-line prediction method

A modified iterative free surface location method was used to determine extrusion profiles. Three boundary conditions are used to describe the free surface, see Crochet *et al.* (1984),

$$v_r n_r + v_z n_z = 0, \tag{9}$$

$$t_r n_r + t_z n_z = S\left(\frac{1}{\rho_1} + \frac{1}{\rho_2}\right), \tag{10}$$

$$t_r n_z - t_z n_r = 0, \tag{11}$$

Where free surface unit normal components are (n_r, n_z), curvature radii $(\rho 1, \rho 2)$, surface tension coefficient S (vanishes here), radial and axial velocities (v_r, v_z) and surface forces normal to the free surface (t_r, t_z).

Boundary condition (10) and (11) are used when iteratively modelling the free surface. Conditions (9) is then included to define the normal velocity. The upper extruded flow surface can then be obtained for die-swell extrusion. For a tube radius R, the distance $r(z)$ of the free surface from the axis of symmetry is represented by:

$$r(z) = R + \int_{z=0}^{\infty} \frac{v_r(z)}{v_z(z)} \mathrm{d}z. \tag{12}$$

In order to accurately predict the extrusion shape, Simpsons quadrature rule is used to compute the integral of equation (12).

The procedure of solution is as follows. First, the kinematics for a converged Newtonian solution is used as initial conditions, with a relaxed stress field, and the fixed free-surface problem is solved. Subsequently, the full problem is computed, involving the free surface calculation, where the surface location itself must be determined. Continuation from one particular viscoelastic solution setting to the next is then employed. In some instances, it is stabilising to first enforce vanishing surface extra-stress (τ of equation (3)), prior to relaxing such a constraint. To satisfy the zero normal velocity free surface boundary condition and to compensate for the adjustment of the free surface, the velocity solution at the advanced time surface position must be reprojected from the previous surface position.

5.5 Mass balance method

The pressure drop/mass balance method provides an adequate means of correcting the estimation of the free surface position. Such a technique may provide improved solution accuracy and stability over the regular streamline location method. The procedure involves taking, an initial estimate of the free-surface profile for each Weissenberg number. Sampling points for We

begin from the stick-slip region. The final correction stage makes use of the streamline method, to perturb and validate the position of the die swell surface.

By examining the functional dependence of pressure drop (Δp) in swell (χ) profiles at the centreline, for each We level, the mass balance scheme relates flow characteristics between the stick-slip to die-swell phases of the problem (akin to an expression of energy balance). By taking into account known swell predictions with sampled pressure drop results, a general relationship may be established between these two scenarios:

$$\chi(z) = \frac{\Delta p(z, \mathrm{We})}{f(\mathrm{We})},$$

By fitting to prior and accepted data (say at low We levels, from the streamline method), the denominator can be represented by:

$$f(\mathrm{We}) = 10.68 - 0.133\mathrm{We} - 2.125\ \mathrm{We}^2.$$

Using this approach, it is possible to derive the approximate swell after pressure drop calculations are made. This process is then implemented within an iterative time-stepping procedure, to obtain a converged solution. Such a strategy is found to be absolutely necessary to achieve converged free-surface solutions at the extreme levels of parameters relevant to industrial processing, notably high We and low solvent contribution.

6. Numerical predictions and discussion

6.1 Short-die, pressure-tooling

The solution for short-die pressure-tooling is illustrated through field plots, in terms of pressure, extension rate and shear rate in Figure 5 and stress component contours in Figure 7. The short-die problem, taken on the 6×24 element mesh, is idealised flow. It proves useful to encapsulate the essence of pressure-tooling, devoid of the complexity of the full die. In contrast, the full-die study reveals the implications of actual processing conditions.

The pressure drop across the flow reaches 0.46 units (relative to ambient pressure), where the die length to exit gap width ratio is of the order 2:1. This drop corresponds to that across the die alone. The minimum pressure arises at the top surface die-exit. The shear rate I_2 is two orders of magnitude larger than the extension rate, peaking with 31.3 units at the top die-exit boundary. Upon entering the jet region, the shear rate rapidly decline and vanishes. The flow profile adjusts from a shear flow within the die to a plug flow in the jet. The flow profiles of Figure 6 reflect this position, with a linear decrease in pressure observed along the wire within the die. Maximum swell within the jet reaches 1.054 units. This would correspond to typical results reported in the literature Mitsoulis (1986); Mitsoulis *et al.* (1988); Wagner and Mitsoulis (1985);

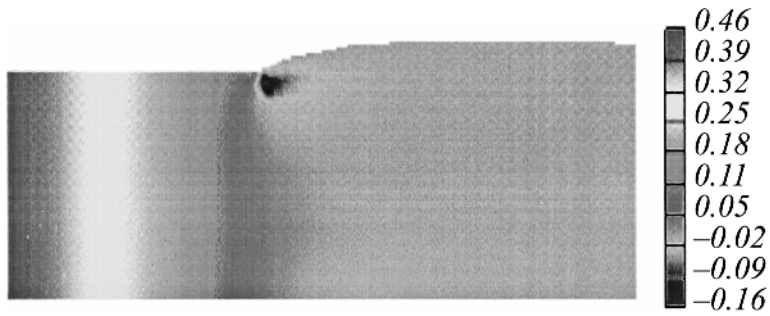

(a) pressure contours

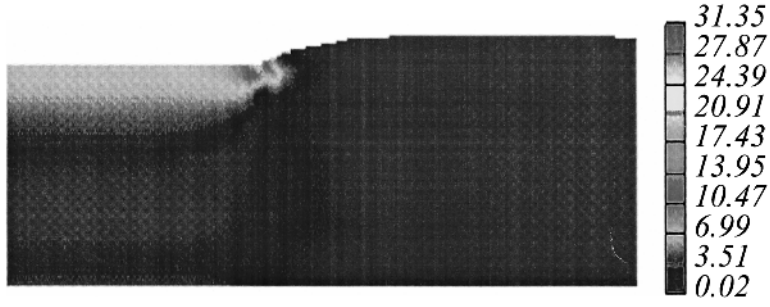

(b) I_2 contours

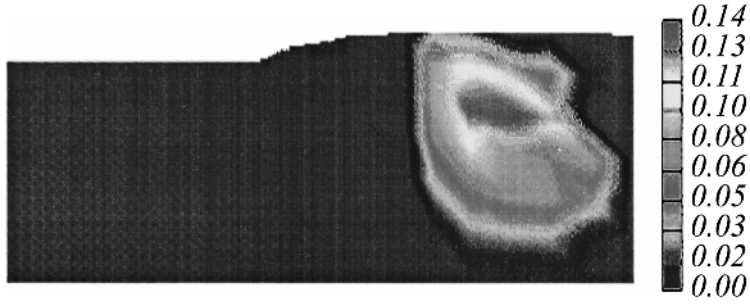

(c) $\dot{\varepsilon}$ contours

Figure 5.
Short-die

Ngamaramvaranggul and Webster (2000b); Ngamaramvaranggul and Webster (2001).

Field plots on the stress components of Figure 7, illustrate the dominance of the axial stress, that in maxima is three times larger than the shear stress and five times larger than the radial stress. The sharp adjustment is noted at die-exit on the top-surface in both shear and axial stress, T_{rz} and T_{zz}-profiles of Figure 8 and 9, respectively. Profiles on the wire are relatively smooth, in contrast. We have observed in our earlier work (Ngamaramvaranggul and Webster, 2002), that the strain-softening response of the EPTT model, stabilises

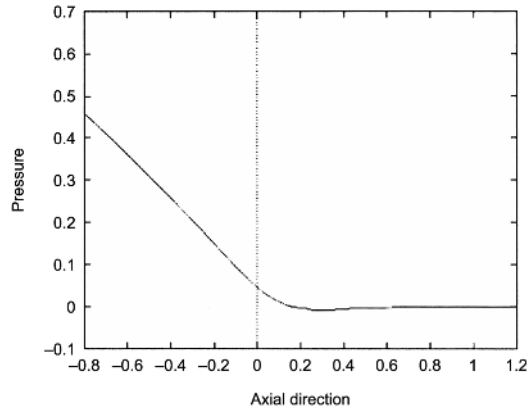

(a) pressure along the wire

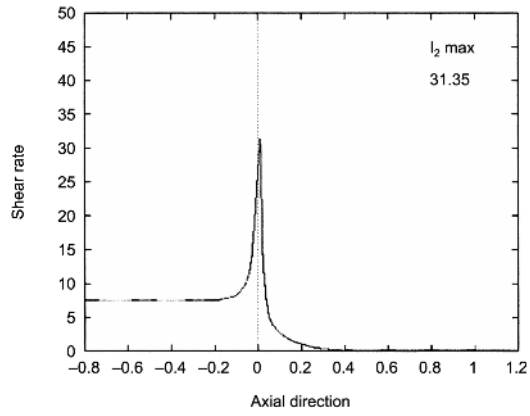

(b) I_2 on top surface

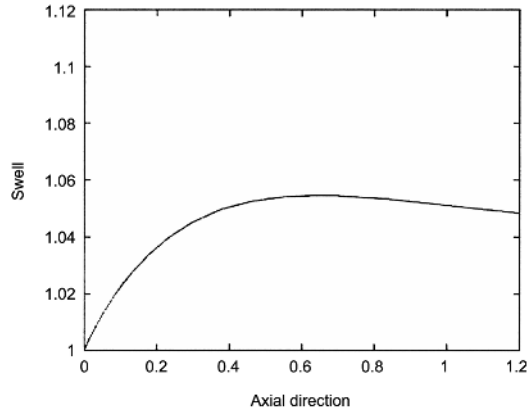

(c) die swell on top free

Figure 6.
Short-die; (a) pressure along the wire, (b) I_2 on top surface, (c) die swell on top free

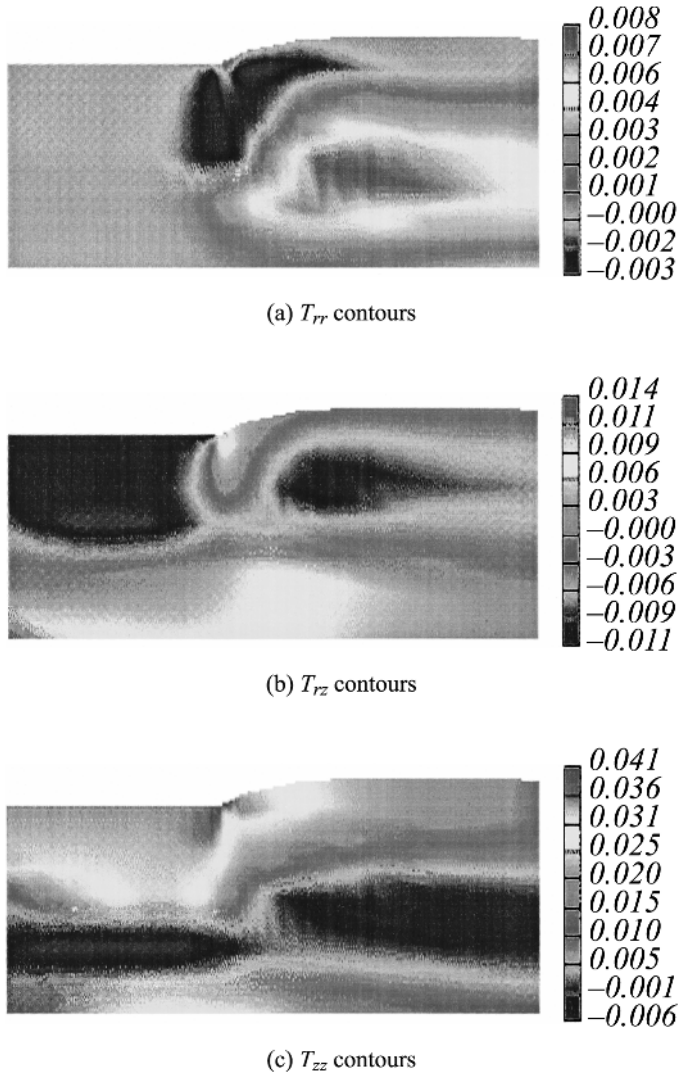

Figure 7.
Short-die: (a) T_{rr} contours, (b) T_{rz} contours, (c) T_{zz} contours

stress profiles. This stands in stark contrast to models that support strain-hardening.

6.2 Full-die, pressure-tooling

Following our earlier study on mesh convergence (Ngamaramvaranggul and Webster, 2002), for this problem our results are plotted upon the biased fine mesh of Figure 3b, with identical parameter settings as for the short-die flow. The zonal refinements are outlined in Table II, with greatest density and bias in the land and die-exit regions.

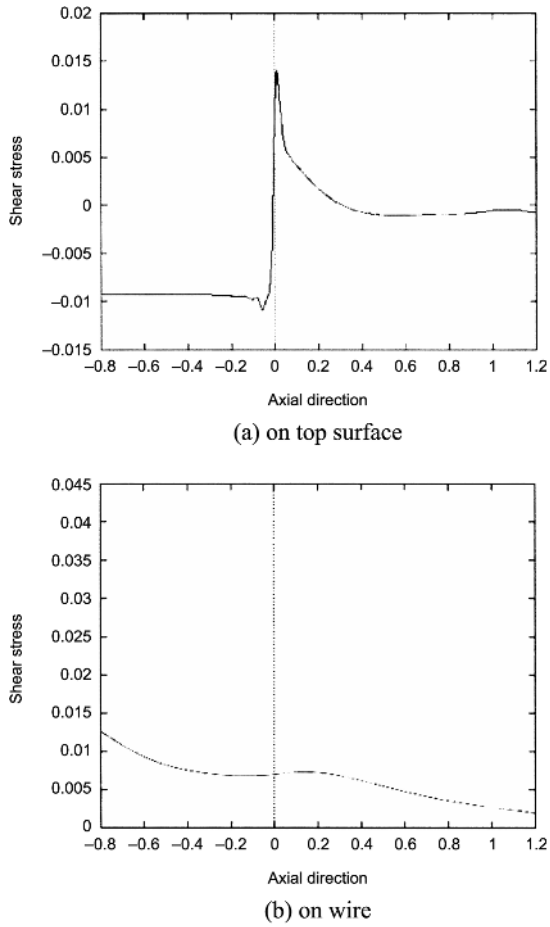

Figure 8.
Short-die: T_{rz} (a) on top surface, (b) on wire

The filed plots of Figure 10 indicate an intense drop in pressure local to the land region, reaching a maximum pressure drop of 10.1 units. Shear rate, I_2, also identifies significant shearing over the land region, reaching a peak of 461 units at the die-exit, a fifteen fold increase to that obtained for short-die tooling.

Table II.
Full-die pressure-tooling; mesh characteristics, sub-region zones

Sub-region zone	Biased fine mesh
1. inlet die	15 × 20
2. converging die	15 × 25
3. coating region	15 × 30
4. land region	15 × 5
5. jet region	15 × 47

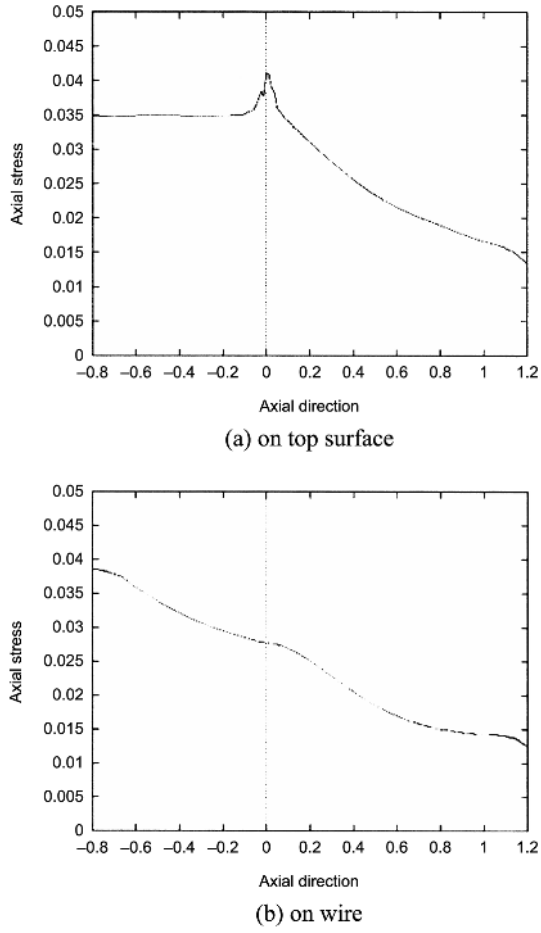

Figure 9.
Short-die T_{zz} (a) on top surface, (b) on wire

Strain rates, $\dot{\varepsilon}$, are an order of magnitude lower than shear rates, and display peaks at melt-wire contact and die-exit. At the melt-wire contact point, $\dot{\varepsilon}$ increases to 8.37 units. A rapid larger rise occurs in the wire-coating section at die-exit. The second peak in $\dot{\varepsilon}$-profile at the top boundary, characteristic for the full-die, reaches a height of 18.8 units in the post-die exit region.

The pressure along the bottom surface corresponds to the line contour plot of Figure 11a. Pressure difference is twenty two times greater for the full case, above short-die pressure-tooling (as compared with Figure 5). Note that, these drops in pressure, essentially correspond to the same flow zone, that is, over the land-region at jet-entry. The die-swell profile along the top free-surface is given in Figure 11b. The swelling ratio is fifteen percent larger than that for short-die pressure-tooling.

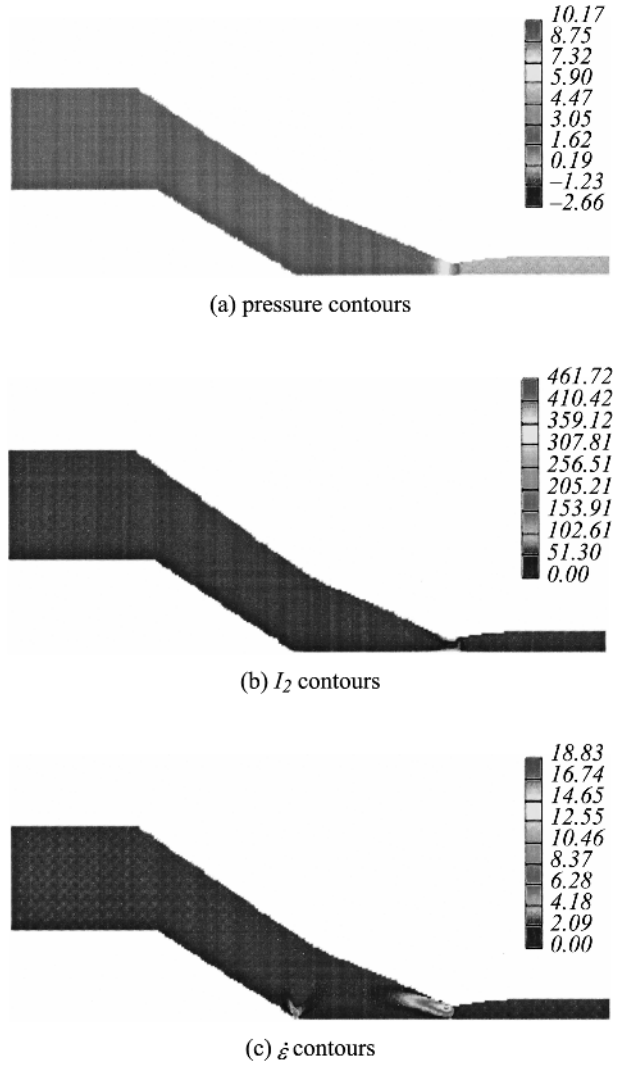

Figure 10.
Full-die pressure-tooling: (a) pressure contours, (b) I_2 contours, (c) $\dot{\varepsilon}$ contours

Shear rate profiles, along the top and bottom surfaces, are represented in Figure 12. The top surface I_2 peak of 461.7 units at the die-exit (Figure 12a), is fifteen times greater than that for short-die, pressure-tooling (see Figure 6b). Figure data on I_2 maxima may be found in Table III. Along the bottom surface, the double (sudden shock) peaks of 124 and 140 units of Figure 12b are most prominent. Such peaks do not appear in the short-die case, being a new introduction as a consequence of the full-die and melt-wire contact.

The "shock impact" as the fluid makes contact with the wire is most prominent in the radial, shear and axial stress contour plots of Figure 13.

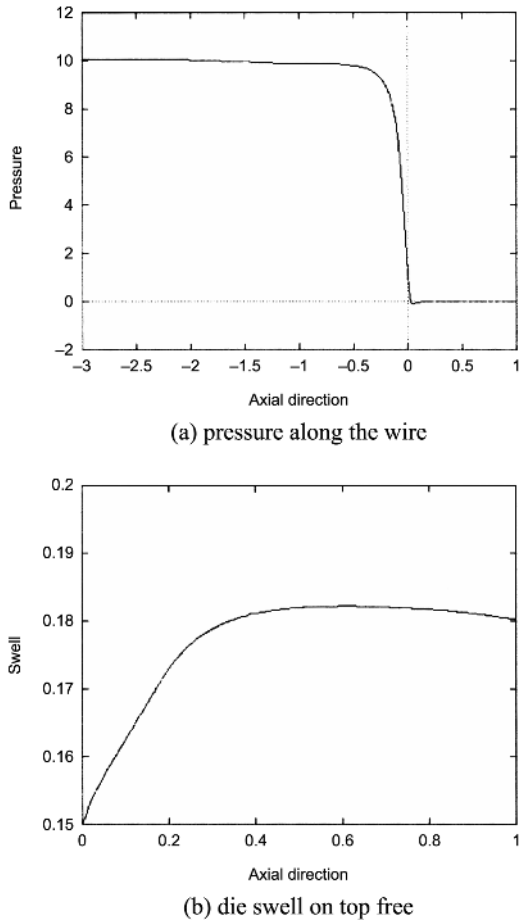

Figure 11.
Full-die pressure-tooling: (a) pressure along the wire, (b) die swell on top free

Nevertheless, stress levels within the die remain small, the greatest axial stress of 0.069 units occurs upon melt-wire contact.

Top-surface stress profiles of Figure 14a and 15a, demonstrate most clearly, the "localised effect" of die-exit point discontinuity. A violent jump in shear stress is observed over the land region. Comparison of stress between full-die and short-die pressure-tooling instances reveals factor increases of 1.8 times in T_{rz} and 1.7 times in T_{zz} (Table III). Both shear and axial stress profiles along the bottom wire-surface reveal the influence of the moving-wire on the flow at the melt-wire contact point (axial position -1.1 units). In axial stress of Figure 15, along the *bottom surface*, the characteristic "double peak" profile at the melt-wire contact point and die-exit regions is observed. The axial stress peak at the melt-wire contact point exceeds that at die-exit and is followed by a sharp relaxation on the approach to the land region, upon which a more

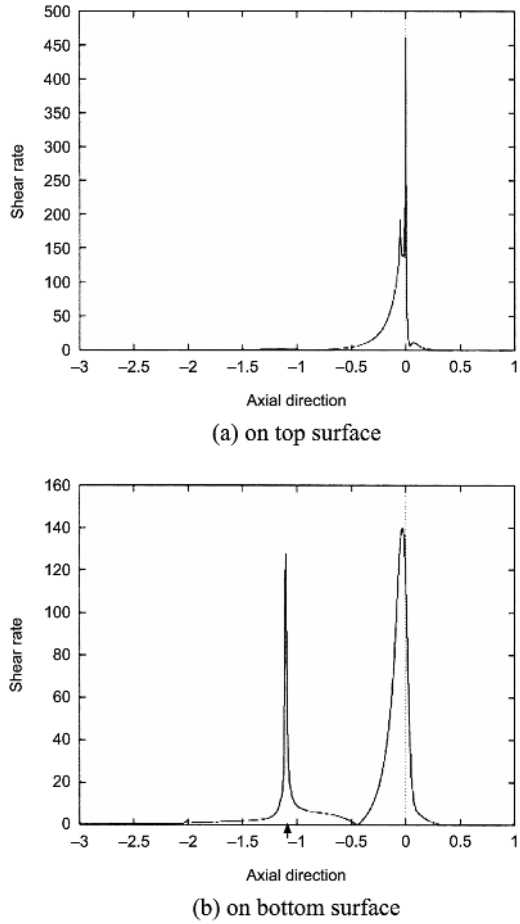

Figure 12.
Full-die pressure-tooling: I_2 (a) on top surface, (b) on bottom surface

sustained maxima forms. Notably, in the extrudate, T_{zz} remains positive, and provides some residual stressing to the coating. T_{zz}-maxima increase only slightly from case to case, with full-case pressure-tooling values being about twice for the short-die instance.

Table III.
EPTT ($\epsilon = 1$, $\mu_1 = 0.99$, We = 200), solution values

Solution variables	Short-die	Full-die	Tube-tooling
I_2 max, Top	31.35	461.7	127.7
I_2 max, Bot	–	139.7	144.2
$\dot{\varepsilon}$ max	0.144	18.83	4.43
Δp	0.462	10.18	16.09
T_{rx} max	0.014	0.025	0.024
T_{zz} max	0.041	0.069	0.050
χ	1.054	1.215	–

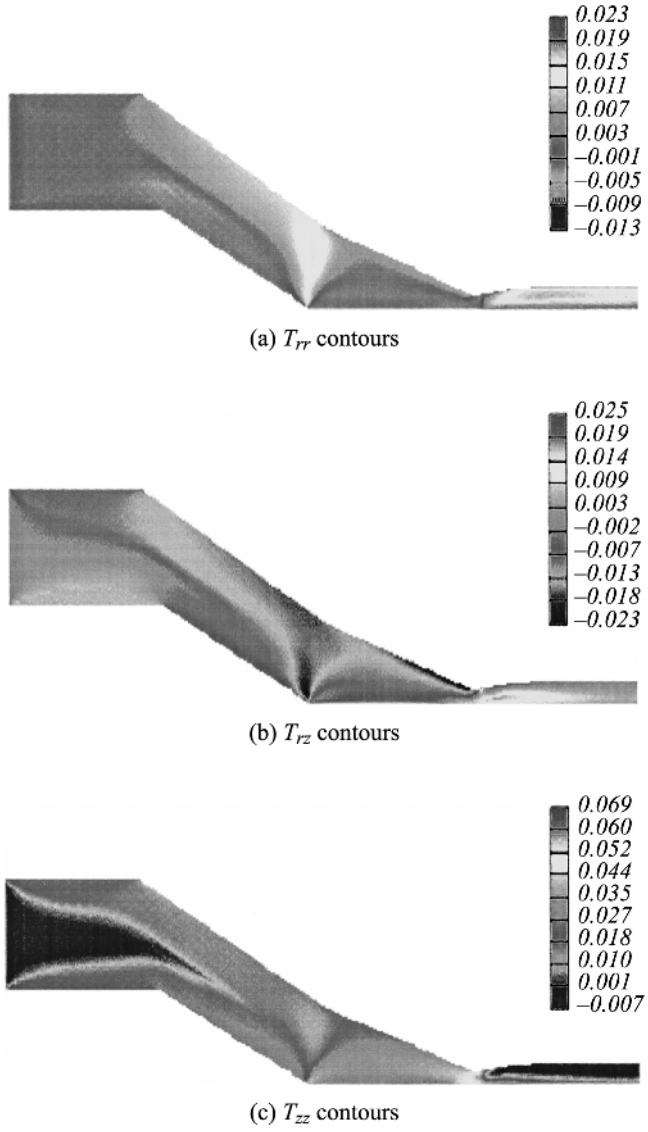

Figure 13.
Full-die pressure-tooling: (a) T_{rr} contours, (b) T_{rz} contours, (c) T_{zz} contours

6.3 Tube-tooling

Concerning the tube-tooling problem, our analyses are based on a single refined mesh as displayed in Figure 4b, see Townsend and Webster (1987). Mesh characteristics for each sub-region are provided in Table IV. As displayed in Figure 16a, the pressure-drop is most prominent across the tube-die. At the draw-down and coating regions, the pressure hold to an ambient level. The

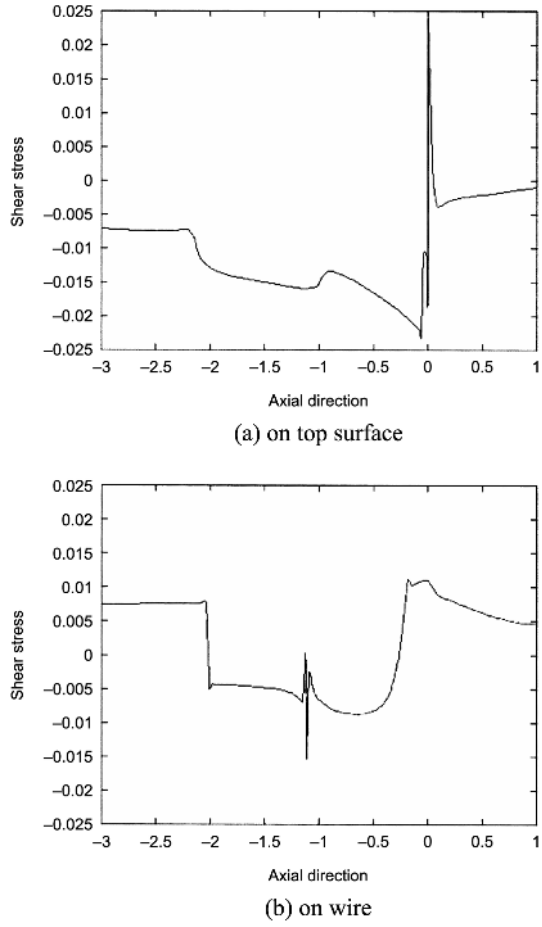

Figure 14.
Full-die pressure-tooling: T_{rz} (a) on top surface, (b) on wire

most important rate of change in pressure-drop arises across the land-region, as is true for pressure-tooling. Here, the maximum value is higher, of 16.1 units for tube-tooling compared to 10.2 units for pressure-tooling.

In contrast, shear-rate I_2, is about a quarter of that corresponding to pressure-tooling. The maximum is 144 units. Again, higher shear-rates are attained in the land-region, see Figure 16b. The remaining regions display smaller shear-rates, so that the shear-viscosity of the polymer melt will be high there. The shear-rate profiles are also displayed in Figure 17b and c, plotted along the top and bottom surfaces in the axial direction. The shear-rates increase across the converging cone, from 0.89 units at the inlet-tube and start of the converging cone to 14.6 units at its end. A sudden rise in shear-rate occurs when the polymer enters the land-region, across which a constant value is generated. Shear-rate maxima are generated at the die-exit, with values of

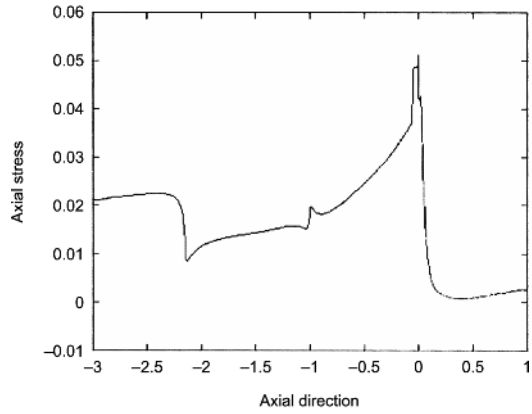

(a) on top surface

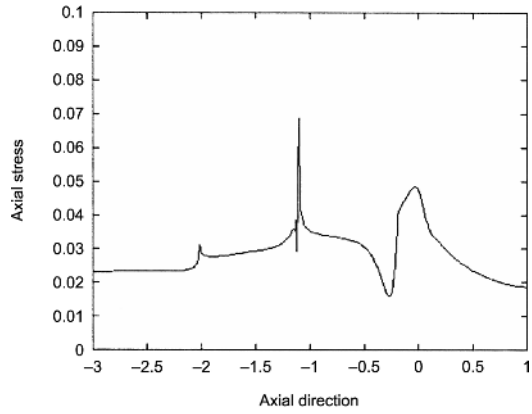

(b) on wire

Figure 15.
Full-die pressure-tooling: T_{zz} a) on top surface, (b) on wire

144.2 and 127.2 units at the bottom and top surfaces, respectively. Beyond the die-exit entering the draw-down flow, a sharp drop in shear-rate is observed. Similar behaviour is observed in both top and bottom surface shear-rate profiles. There is only a gradual decrease in shear-rate over the draw-down

Sub-region zone	Biased fine mesh
1. inlet die	12×45
2. converging die	$12 \times 18+15 \times 8$
3. land region	$15 \times 12+20 \times 12$
4. draw-down region	20×25
5. coating region	20×25

Table IV.
Tube-tooling; mesh characteristics, sub-region zones

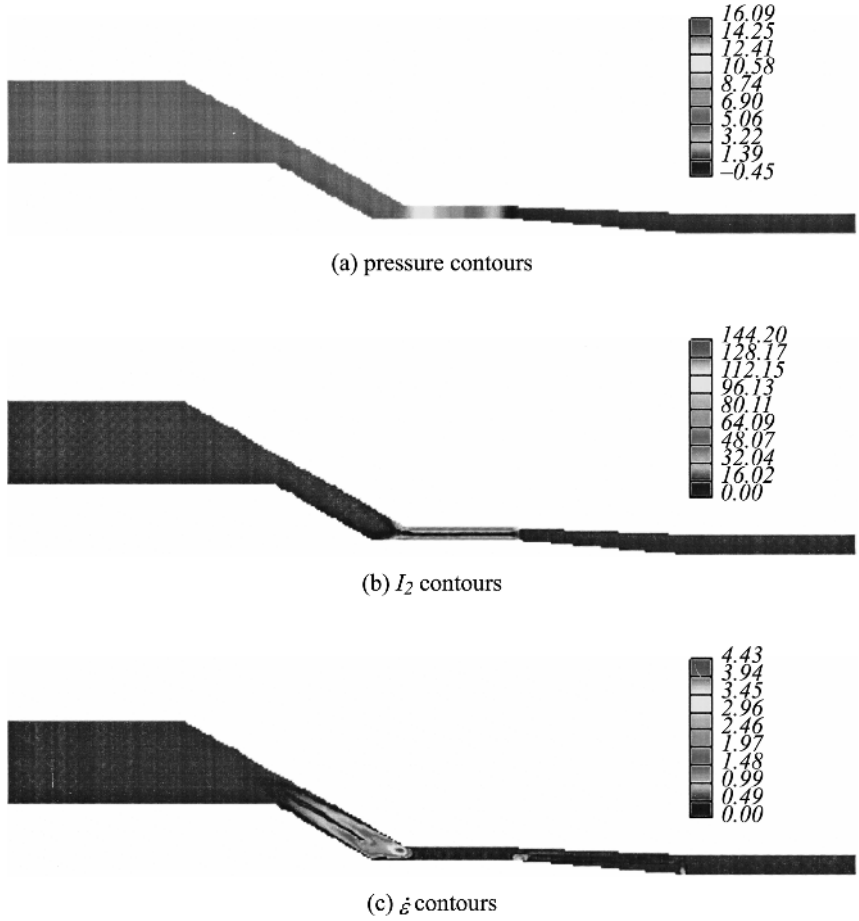

Figure 16.
Tube-tooling: (a) pressure contours, (b) I_2 contours, (c) $\dot{\varepsilon}$ contours

section, followed by a sharp decline when the polymer meets the wire. Traveling with the wire, the rate of decrease in shear-rates is minimal. The final shear-rates, taken up at the end of the coating, are about 0.26 and 1.0 units for bottom and top surfaces, respectively.

The state of strain-rate $\dot{\varepsilon}$ is illustrated in Figure 16c. This quantity is significant in the converging tube. It reaches a maximum of about 4.43 units, an order of magnitude lower than that for shear-rate maxima. This is a fifth of that corresponding to pressure-tooling maxima. Large values of strain-rate are also located, of less magnitude, at the start of the draw-down section just beyond the die-exit. The value reached is about 2.50 units, half of that observed in the converging die-cone. The profiles for $\dot{\varepsilon}$ along the axial direction, for top and bottom surfaces show similar behaviour to each other, with exceptions at the sharp adjustments in geometry. Elongation-rates are large at the land region

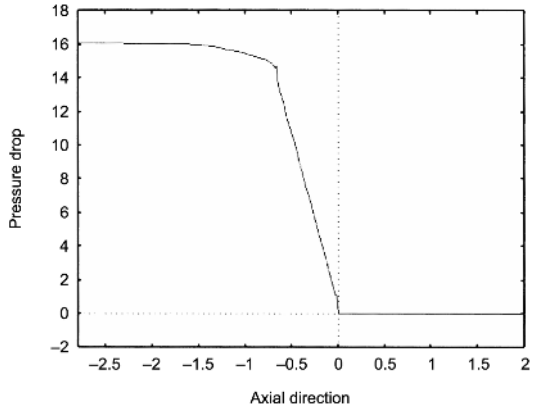

(a) pressure along the wire

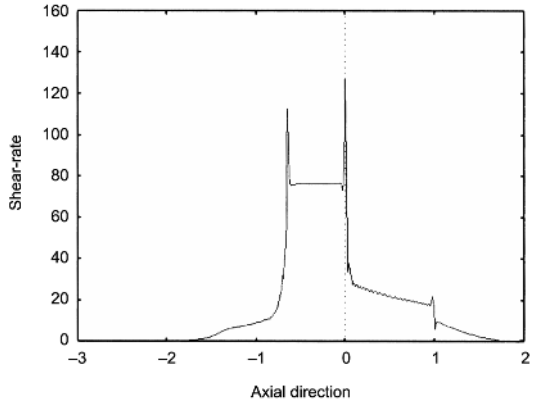

(b) I_2 on top surface

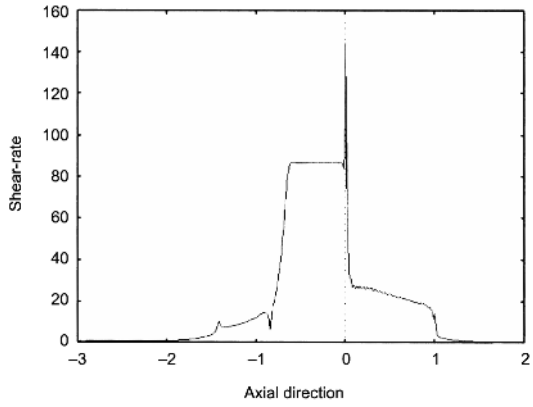

(c) I2 on wire

Figure 17.
Tube-tooling: (a) pressure along the wire, (b) I_2 on top surface, (c) I_2 on bottom surface

entrance, reaching a maximum of 4.43 units, being minimal in the remaining flow section. Shear and strain-rates are important measurable quantities that describe the state of flow and, according to the ranges encountered, may explain the polymer response to different flow scenarios.

Component stress profiles along the top surface are provided in Figure 18 a) for τ_{rz} and b) for τ_{zz}. One may observe from this, that along the inlet-tube, τ_{zz} is constant, of about 0.02 units. Sudden change occurs with each adjustment in geometry. An increase of τ_{zz} is observed within the converging cone of the die, reaching a value of 0.045 units at the entrance to the land-region. τ_{zz} is constant over the land-region, followed by a sudden increase due to singularity, where the polymer departs from the die to the draw-down section. A sharp decrease within the draw-down is generated. When the polymer makes contact with the wire, τ_{zz} increases providing a residual stress of about 0.012 units. In contrast,

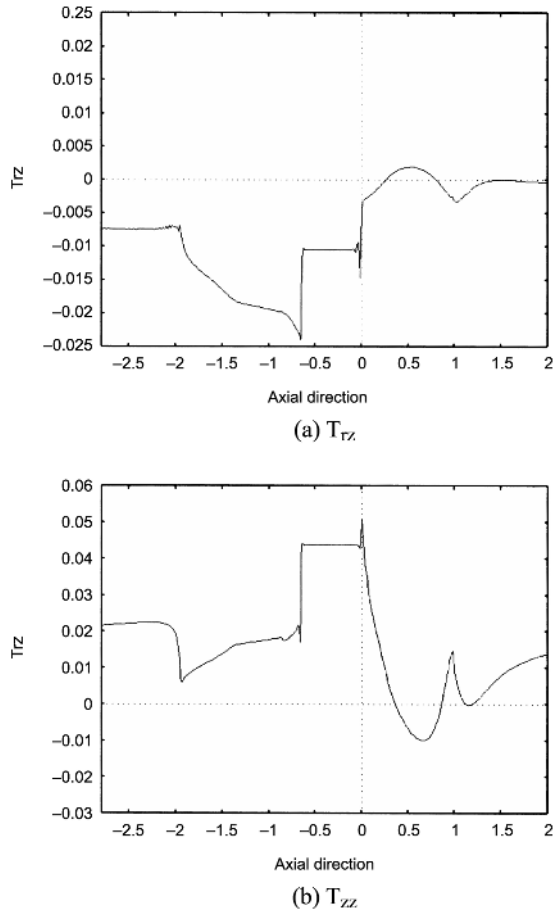

Figure 18.
Tube-tooling: on top surface (a) T_{rz} (b) T_{zz}

the shear-stress τ_{rz} is lower in value than the τ_{zz} component, as displayed in Figure 18a. τ_{rz} starts with a value of about 0.007 units at the inlet tube, increase over the converging cone to reach a constant value of 0.01 units across the land-region. Subsequently, τ_{rz} decreases in the draw-down and coating regions to a minimum value less than 0.001 units. Contours are plotted in Figure 19 to analyse the state of stress over the whole domain and in various components. τ_{rr} can be considered to be small in the inlet-tube and land-region: it is significant in the converging cone, draw-down and coating regions. A maximum of about 0.05 units is realised in the draw-down section. For τ_{rz}, we observe a peak (0.024 units) in the converging die-cone, near the entrance to the land-region. The shear-stress is also prominent in the land-region, but of less magnitude (about half) than that over the converging cone. Axial τ_{zz} stress is most significant in the land-region, as observed in Figure 19c. The maximum

(a) T_{rr} contours

(b) T_{rz} contours

(c) T_{zz} contours

Figure 19.
Tube-tooling: (a) T_{rr} contours, (b) T_{rz} contours, (c) T_{zz} contours

value, 0.051 units, is double that of the shear-stress. Hence, *residual stressing* to the coating is dominated by the axial component.

6.4 Parallel timings

Parallel computation is employed, within the simulations performed through a spatial domain decomposition method. The domain of interest is decomposed into a number of subdomains, according to available resources and total number of DOF. In this study, uniform load distribution is ensured using a Recursive Spectral Bisection method (Simon, 1991). Though the method is quite general, uniform load may be organized if domain subdivision is straightforward, otherwise loading will be approximately uniform, from which manual adjustment may be made. As the short-die domain has relatively few DOF, the domain is decomposed into instances with only two and four sub-domains. In contrast, tube-tooling and pressure-tooling domains are partitioned into as many as eight sub-domains.

In Table V, information is presented on domain decomposition, the number of elements and nodes per subdomain, the number of interfacing nodes and ratio of subdomain nodes to interfacing nodes ($C_n = N_n : I_{nn}$), With an increasing number of subdomains, interfacing nodes (I_{nn}) increase (as does communication cost), whilst the number of elements, nodes (N_n) and degrees-of-freedom per subdomain decreases.

Parallel timings are generated on a networked cluster of single processor Intel 450 MHz Solaris workstations, a distributed-memory homogeneous platform. A public domain PVM 3.4.3 version for message passing protocol has been employed to support interprocessor communication through networking with fast 100 Mbit/s EtherNet. Computed results are presented through the

Domain Short-die	Elements/ subdomain	Nodes/ subdomain	Interface nodes		C_n	
			Master	Slave	Master	Slave
1	288	377	–	–	–	–
2	144	325	13	13	4%	4%
4	72	169	39	26	23%	15.4%
Pressure-tooling						
1	3810	7905	–	–	–	–
2	1905	3968	31	31	0.78%	0.78%
4	953	1976	93	62	4.71	3.14%
8	476	988	217	62	22.0%	6.28%
Tube-tooling						
1	4714	9755	–	–	–	–
2	2357	4878	31	31	0.64%	2.75%
4	1178	2439	103	67	4.22%	2.75%
8	589	1222	272	71	22.3%	5.81%

Table V.
Domain decomposition data

parallel performance of the Taylor-Galerkin scheme, by measuring metrics of speed-up and efficiency, with increasing numbers of processors (hence, sub-tasks). The total speed-up (S_n) factor and efficiency (η_n) are defined as:

$$S_n = \frac{T_{\text{seq}}}{T_n}, \quad \eta_n = \frac{S_n}{n},$$

Where n is the number of processors, T_{seq} is the CPU time in seconds (s) for the sequential algorithm and T_n is the CPU time for the parallel algorithm. CPU time T_n of the parallel computation can be decomposed into computation time ($T_{\text{n}}^{\text{comp}}$)and communication time ($T_{\text{n}}^{\text{comm}}$). Timings correspond to total job run-time, inclusive of input-output and communication latency.

In Table VI, speed-up and efficiency factors are tabulated for our parallel implementations. Speed-up is plotted in Figure 20 for the viscoelastic simulations if short-die, tube-tooling and pressure-tooling problems, with increasing numbers of processors. As the short-die problem has fewer DOF, eight percent loss of efficiency is observed with up to four processors. For two-subdomains,

Processors	Short-die		Pressure-tooling		Tube-tooling	
	S_n	η_n	S_n	η_n	S_n	η_n
1	1.00	1.00	1.00	1.00	1.00	1.00
2	1.94	0.97	1.99	0.99	1.99	0.99
4	3.66	0.92	3.98	0.99	3.99	0.99
8	–	–	7.44	0.93	7.61	0.95

Table VI.
Parallel speed-up and efficiency

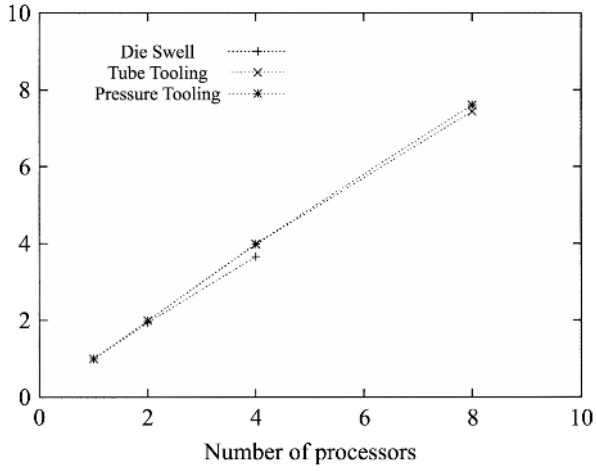

Figure 20.
Parallel speed-up

the master processor has to communicate with thirteen interfacing nodes. Moving to four-subdomains, the size of each task on a slave processor halves. For full pressure-tooling and tube-tooling, with two and four subdomains, the ratio between computation and communication remains small. At eight subdomains, this ratio is of the same order as that for the short-die problem and four processor. Under such circumstances with tube-tooling, the parallel algorithm loses five percent efficiency and seven percent for pressure-tooling problems. The consequence of this is felt within our parallel implementation via the ratio of internal to boundary nodes in each instance. This ratio will affect the proportion of cost, split between communication and sub-problem computation (hence, the masking of communication (Baloch *et al.*, 2000; Grant *et al.*, 1998)).

In Table V, we have recorded data relating to interfacing nodes and the ratio between subdomain nodes and interfacing nodes (C_n). For the short-die with two slave processors, the number of nodes is relatively few and C_n is around four percent. Therefore, we immediately lose efficiency of about three percent. The loss is even greater with four slave processors, see Table VI. Such efficiency loss diminishes as C_n decreases, as clearly demonstrated in both pressure-tooling and tube-tooling instances. To take full advantage of parallelism and gain optimal performance levels, we seek to increase problem size and select a minimal C_n ratio, through a judicious choice of domain subdivision (sub-task generation, demanding prerequisite slave processors). For both pressure-tooling and tube-tooling problems and up to four slave processors, the C_n ratio is about three percent and we lose efficiency of one percent. At eight slave processors, the parallel implementation loses seven percent efficiency for the pressure-tooling problem, and five percent for the tube-tooling problem. To achieve optimal performance levels, we must ensure a balance between the number of processors and total number of degrees-of-freedom per subdomain. This will also provide the optimal ratio between ($T_{\mathrm{n}}^{\mathrm{comm}}$) and $T_{\mathrm{n}}^{\mathrm{comp}}$ times. We recognize that communication and computation times relate to different hardware mechanisms. One may identify an acceptable threshold level on efficiency loss, of say up to five percent. For the present study, this would imply the efficient use of two slave-processors for the short-die problem, four slave-processors for pressure-tooling and eight slave-processors for tube-tooling. With the proviso of sufficient processors, larger problems may be tackled in this manner.

7. Conclusions

In the case of *short-die pressure-tooling* flow, there was no melt-wire sudden contact and smooth solutions were established on the wire at the die-exit. For the full-die study in contrast to the short-die, ranges of shear rise ten-fold and extension rate by one hundred times. For dimensional equivalents, one must scale by $O(10^3)$. For the *short-die tooling*, the major observations are: maximum

shear rates arise at die-exit, top-surface, whilst for extension rates they lie within the free-jet region. The corresponding situation for strain rates is more marked, but displaying similar trends to shear rate. Axial stress maxima occur at the top surface on die-exit. For *full-die pressure-tooling*, shear rate maxima on the top surface occur over the land-region, and in particular, peak at the die-exit. The level is some fifteen times larger than that for the short-die. Shear rate maxima on the wire are lower than that at the top surface, by a factor of three. The double (sudden shock) peaks in shear rate at the bottom surface for full-die flow, do not appear in the short-die case. These are a new feature, introduced as a consequence of the full-die and melt-wire contact. There is a double peak along the wire, with the die-exit value being marginally larger than that at melt-wire contact. Extension rate maxima are lower than shear rates by one order, but have increased one hundred fold from the short-die case. Extension rates peak at the melt-wire contact and across land/die-exit region. The maximum corresponds to the die-exit. The pressure drop across the flow is almost entirely confined to the land-region, and is magnified some twenty-two times over that for the short-die. The behaviour in stress for full-tooling reveals the "shock impact" as the fluid makes contact with the wire. The largest axial stress arises at the melt-wire contact point. The swelling ratios for the EPTT models are 15 per cent higher than that observed for short-die tooling. Hence, the influence of the die flow itself is exposed. The adequacy of the free-surface procedures is also commended.

In contrast, focusing on *tube-tooling* desing, stress and pressure build-up is realised in the land-region section, as with pressure-tooling. The principal stress component τ_{zz} is significant at the end of the coating, generating a residual stress of about 0.012 units and vanishing shear-stress. This is similar to pressure-tooling. Shear-rates are of $O(10^2)$ units, reaching a maximum of 144 units, a quarter of that corresponding to the pressure-tooling problem. This maximum is observed at the exit of the die. Tube-tooling strain-rates are an order of magnitude lower than tube-tooling shear-rates: strain-rate maxima reach 4.43 units, again one quarter of those for pressure-tooling. Largest strain-rates are generated throughout the converging did-tube, with lesser values in the draw-down section (extrudate). Such elements of variation between designs would have considerable impact upon the processes involved.

Distributed parallel processing has been shown to be an effective computational tool to simulate industrial wire-coating flows. Ideal linear speed-up in run-times has been extracted, based on the number of processors utilised. Increasing the size of the problem, would render even greater efficiency, providing a wider pool of processors were made available.

References

Baloch, A. and Webster, M.F. (1995), "A computer simulation of complex flows of fibre suspensions", *Computers Fluids*, 24 No. 2, pp. 135-51.

Baloch, A, Grant, P.W. and Webster, M.F. (2000), Homogeneous and heterogeneous distributed cluster processing for two and three-dimensional viscoelastic flows, submitted to *Int. J. Num. Meth. Fluids*, available as CSR 16.

Baloch, A., Townsend, P. and Webster, M.F. (1998), "On the highly elastic flows", *J. Non-Newtonian Fluid Mech.*, 75, pp. 139-66.

Binding, D.M., Blythe, A.R., Gunter, S., Mosquera, A.A., Townsend, P. and Webster, M.F. (1996), "Modelling Polymer Melt Flows in Wire Coating Processes", *J. non-Newtonian Fluid Mech.*, 64, pp. 191-209.

Chung, T.S. (1986), "The Effect of Melt Compressibility on a High-Speed Wire-Coating Process", *Polym. Eng. Sci.*, 26 No. 6, pp. 410-4.

Caswell, B. and Tanner, R.I. (1978), "Wire Coating Die Design Using Finite Element Methods", *J. Polym. Sci.*, 5, pp. 416-21.

Crochet, M.J., Davies, A.R. and Wlalter, K. Numerical simulation of Non-Newtonian Flow, Rheology Series, 1, Elsevier Science Publishers, (1984).

Carew, E.O.A., Townsend, P. and Webster, M.F. (1993), "A Taylor-Petrov-Galerkin Algorithm for Viscoelastic Flow", *J. Non-Newtonian Fluid Mech.*, 50, pp. 253-87.

Grant, P.W., Webster, M.F. and Zhang, X. (1998), "Coarse Grain Parallel Simulation for Incompressible Flows", *Int. J. Num. Meth. Eng.*, 41, pp. 1321-37.

Haas, K.U. and Skewis, F.H. (1974), "SPE ANTEC", *Tech. Paper*, 20, p. 8.

Han, C.D. and Rao, D (1978), "Studies of Wire Coating Extrusion. I. The Rheology of Wire Coating Extrusion", *Polym. Eng. Sci.*, 18 No. 13, pp. 1019-29.

Hawken, D.M., Tamaddon-Jahromi, H.R., Townsend, P. and Webster, M.F. (1990), "A Taylor-Galerkin-based algorithm for viscous incompressible flow", *Int. J. Num. Meth. Fluid*, 10, pp. 327-51.

Mitsoulis, E. (1986), "Finite Element Analysis of Wire Coating", *Polym. Eng. Sci.*, 26 No. 2, pp. 171-86.

Matallah, H., Townsend, P. and Webster, M.F. (1998), "Recovery and stress-splitting schemes for viscoelastic flows", *J. Non-Newtonian Fluid Mech.*, 75, pp. 139-66.

Matallah, H., Townsend, P. and Webster, M.F. (2000), Viscoelastic Computations of Polymeric Wire-Coating Flows, Int, J. Num. Meth. Heat Fluid Flow, accepted for publication 2001, available as CSR 13, University of Wales, Swansea.

Matallah, H., Townsend, P. and Webster, M.F. (2000), "Viscoelastic Multi-Mode Simulations of Wire-Coating", *J. Non-Newtonian Fluid Mech.*, 90, pp. 217-41.

Mitsoulis, E., Wagner, R. and Heng, F.L. (1988), "Numerical Simulation of Wire-Coating Low-Density Polyethylene: Theory and Experiments", *Polym. Eng. Sci.*, 28 No. 5, pp. 291-310.

Mutlu, I., Townsend, P. and Webster, M.F. (1998a), "Computation of Viscoelastic Cable Coating Flows", *Int. J. Num. Meth. Fluids*, 26, pp. 697-712.

Mutlu, I, Townsend, P. and Webster, M.F. (1998b), "Simulation of Cable-Coating Viscoelastic Flows with Coupled and Decoupled Schemes", *J. Non-Newtonian Fluid Mech.*, 74, pp. 1-23.

Ngamaramvaranggul, V. (2000), Numerical Simulation of Non-Newtonian Free Surface Flows PhD thesis University of Wales, Swansea.

Ngamaramvaranggul, V. and Webster, M.F. (2000a), "Simulation of Coatings Flows with Slip Effects", *Int. J. Num. Meth. Fluids*, 33, pp. 961-92.

Ngamaramvaranggul, V. and Webster, M.F. (2000b), "Computation of Free Surface Flows with a Taylor-Galerkin/Pressure-Correction Algorithm", *Int. J. Num. Meth. Fludis*, 33, pp. 993-1026.

Ngamaramvaranggul, V. and Webster, M.F. (2001), "Viscoelastic Simulation of Stick-Slip and Die-Swell Flows", *Int, J. Num. Meth. Fluids*, 36, pp. 539-95.

Ngamaramvaranggul, V. and Webster, M.F. (2002), "Simulation of Pressure-Tooling Wire-Coating Flow with Phan-Thien/Tanner Models", *Int. J. Num. Meth. Fluids*, 38, pp. 677-710.

Phan-Thien, N. (1978), "A Non-linear Network Viscoelastic Model", *J. Rheol.*, 22, pp. 259-83.

Phan-Thien, N. and Tanner, R.I. (1977), "A New Constitutive Equation Derived from Network Theory", *J. Non-Newtonian Fluid Mech.*, 2, pp. 353-65.

Phan-Thien, N. and Tanner, R.I. (1992), Boundary-Element Analysis of Forming Processes in 'Numerical Modelling of Material Deformation Processes: Research, Development and Application' by P. Hartley, I. Pillinger and C. Sturgess (Eds), Springer-Verlag, London.

Pittman, J.F.T. and Rashid, K. (1986), "Numerical Analysis of High-Speed Wire Coating", *Plast. Rub. Proc. Appl.*, 6, pp. 153.

Richardson, S. (1970), "A stick-slip problem relatived to the motion of a free jet at low Reynolds numbers", *Proc. Camb. Phil. Soc.*, 67, pp. 477-89.

Simon, H.D. (1991), "Partitioning of unstructured problems for parallel processing", *Computer Systems in Engineering*, 2, pp. 135-48.

Tadmor, Z. and Bird, R.B. (1974), "Rheological Analysis of Stabilizing Forces in Wire-Coating Die", *Polym. Eng. Sci.*, 14 No. 2, pp. 124-36.

Tanner, R.I. (1985), *Engineering Rheology*, Oxford University Press, London.

Townsend, P. and Webster, M.F. (1987), An algorithm for the three-dimensional transient simulation of non-Newtonian fluid flows, in G. Pamde, J. Middleton (Eds.), Proc. Int, Conf. Num. Meth. Eng.: Theory and Applications, NUMETA, Nijhoff, Dordrecht, pp. T12/1-11.

Wagner, R. and Mitsoulis, E. (1985), *Adv. Polym. Tech.*, 5, pp. 305.

Numerical modelling of elastohydrodynamic lubrication in soft contacts using non-Newtonian fluids

M.F.J. Bohan, I.J. Fox, T.C. Claypole and D.T. Gethin
Department of Mechanical Engineering, University of Wales, Swansea, UK

Keywords *Lubrication, Non-Newtonian fluids*

Abstract *The paper focuses on the solution of a numerical model to explore the sliding and non-Newtonian fluid behaviour in soft elastohydrodynamic nip contacts. The solution required the coupling of the fluid and elastomer regimes, with the non-Newtonian fluid properties being described using a power law relationship. The analysis showed that the fluid characteristics as defined by the power law relationship led to large differences in the film thickness and flow rate with a movement of the peak pressure within the nip contact. The viscosity coefficient, power law index and sliding ratio were shown to affect the nip performance in a non-linear manner in terms of flow rate and film thickness. This was found to be controlled principally by the level of viscosity defined by the power law equation. The use of a speed differential to control nip pumping capacity was also explored and this was found to be most sensitive at lower entrainment speeds.*

Introduction

Many coating processes consist of a number of rollers that form a train to meter accurately and consistently the transfer of a small amount of fluid onto a substrate to form a thin coating (Kistler and Schweizer, 1997). In such systems, alternating rubber covered and steel rollers make up the roller train, Figure 1, and the roller speeds are set to establish a significant component of sliding in the nip junction. The contacts between the rollers normally have a positive engagement that is facilitated by deformation of the elastomer surface. In addition, at each roller contact, fluid pressure will also deform the rubber surface, which in turn will affect the hydrodynamic pressure that is generated within the contact. For the purpose of simulation, this leads to the requirement for an iterative approach in solution, linking the fluid field model with the elastic deformation of the rubber cover. This is usually referred to as Soft Elasto Hydrodynamic Lubrication (SEHL) and since the rollers are long in comparison with the junction width, the geometry reflects a line contact.

The authors wish to acknowledge the financial support of EPSRC through the award of a platform grant.

International Journal of Numerical Methods for Heat & Fluid Flow, Vol. 12 No. 4, 2002, pp. 494-511.

DOI 10.1108/09615530210433297

Roller nip interaction can be classified as a contact problem. This class of problem has been reported widely in the literature, however the following will focus on studies that are relevant to this investigation.

Analysis of the behaviour of a roller pair using experimental or numerical approaches has been reported for both dry and wet contacts in which one or more surfaces is soft and therefore compliant. One of the first (Hannah, 1951), which has formed the basis of much subsequent analysis, considered the contact between narrow discs. These discs comprised one rigid surface and the second covered with a soft material and they were placed in positive engagement. The integral equations used the Hertzian theory to define the pressure distribution within the contact and calculations were carried out for roller coverings having both thin and thick compliant layers. These early results highlighted the importance of the layer thickness and contact width.

This numerical scheme was subsequently developed (Parish, 1958; Miller, 1966) from the plane stress, narrow disc model to a plane strain approach that is pertinent to roller contact analysis. The papers have assessed the influence of many parameters including layer thickness, elastic modulus, roller radius, Poisson's ratio and speed differentials. Results indicated that while the Poisson's ratio affected the deformation shape, reflecting the level of incompressibility of the covering, the thickness affected the degree of deformation.

The above work has considered dry contacts only, one of the first studies of wet contacts (Bennett and Higginson, 1970) analysed a hard roller rotating against a polythene target. This used a simple linear elastic deformation model based on the local pressure and stiffness of the polythene target, the coupling of which allowed the impact of friction to be evaluated in this simple sliding contact. Analysis of heavily loaded contacts has been reported in Hooke and O'Donoghue (1972). This used parabolic functions to express the pressure in the inlet and outlet regions, blending this with a pressure profile based on a dry Hertzian contact in the central region. The influence of the contact width to layer thickness ratio was evaluated showing that as it increased so did the peak pressure, again confirming the importance of the layer thickness.

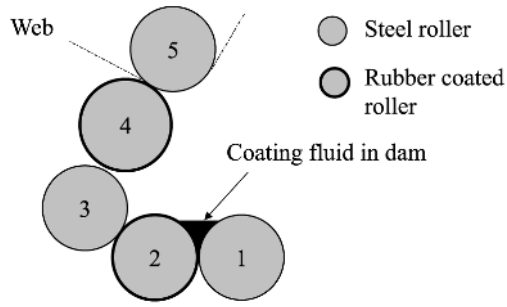

Figure 1.
Schematic of a multiple roller coating application

The requirement to iterate between the fluid and elastomer regions in the numerical solution for SEHL problems was highlighted in Cudworth (1979) in which the authors employed a finite element approach to solve the governing equations. Again this work confirmed that the film thickness and pressure profiles were influenced dominantly by layer thickness and load. This result was also confirmed in Hooke (1986) when the authors explored the effect of inlet conditions replicating the extent of flooding in the nip.

The preceding works have generally focused on tribology applications. Limited analysis has been carried out into the application of these methods to printing (MacPhee *et al.*, 1992; Bohan *et al.*, 1997). The first (MacPhee *et al.*, 1992) assessed the impact of the inlet conditions, flooded or starved, on the nip and this showed large differences in the performance when these were altered, supporting the results presented in Hooke (1986). The second (Bohan *et al.*, 1997b) adopted a more fundamental approach in which the elastomer deformation was computed from a basic elastic analysis. This effectively allowed exploration of the basic assumption that a Hertzian contact model is applicable. In terms of pressure profile, the analysis showed a favourable comparison in form with experimental data and a close match could be achieved when an appropriate Young's Modulus was chosen. This analysis also showed that the pressure in the nip departed from a Hertzian form, reflecting a hydrodynamic profile and a tapering film thickness. Calculations were also carried out to explore the impact of nip geometry and engagement conditions and this showed that increasing the contact width increased both the pressure and film thickness.

Consideration of coating applications is more recent and the work in Carvalho and Scriven (1997) includes a comprehensive review of relevant work and also details a combined modelling and experimental programme. The numerical scheme adopts a Hertzian contact model to compute deformation in the contact and this is coupled with the solution of the hydrodynamic pressure in the film, based on a Newtonian fluid. Elastomer deformation is based on a simple linear spring model. Of particular interest in this work is the application of a Landau-Levich film rupture model that incorporates a surface tension mechanism in the film splitting zone. Consequently it is capable of capturing the subambient pressure that has been measured in the nip (Bohan *et al.*, 1997b; Carvalho and Scriven, 1997). Case studies were run off for which there is no positive engagement and deformation of the elastomer is due to hydrodynamic action alone. From the steady state analysis, the most important result is that the soft elastomer layer leads to a film splitting location that is less dependent on roller position for smaller gaps. This is significant since it also makes the nip pumping capacity nearly independent of roller position for small gaps for which precise settings are difficult to achieve. The study also includes an unsteady analysis via a perturbation model to explore the conditions under which cavitation fingers are developed in the nip exit region and to establish

conditions under which they can be eliminated from the system. The results also show the importance of a soft layer in delaying the onset of ribbing instabilities.

A number of investigations have been carried out by several authors to evaluate the influence of non-Newtonian fluid behaviour in both rolling and sliding contacts. A recent review of this type of work is presented in Dowson and Ehret (1999). This showed that many of these studies have focused on transmission components where rolling action is common and in which the pressures are high and the lubricant is treated as a piezoviscous fluid. Fewer studies have been carried out focusing on the exploration of shear rate dependent behaviour. One of the most important conclusions stated in Dowson and Ehret (1999) is the need to treat "real" surface and fluid systems and that this should be a thrust of future research work.

The use of a power law to express the shear thinning behaviour of the fluid introduces numerical difficulties, since it infers an extremely high (infinite) viscosity at very low shear rates. Similarly the application of an upper shear rate may be used to prevent the fluid viscosity falling below a set level. The latter does not introduce numerical difficulties, but is driven by the process of validation against experimental measurement. An example of the use of an upper shear limit on the behaviour of the fluid is presented in Jacobson and Hamrock (1984). The limit was utilised allowing analysis using a power law expression within an operational envelope, beyond which, a Newtonian model was applied. This was demonstrated through application to a hard EHL contact for which the effect of fluid behaviour on the nip pressures and film thickness was calculated. This showed that the influence of non-dimensional speed and shear strength had only a small impact on the minimum film thickness.

An early study of SEHL in a rolling contact for a power law fluid (Lim *et al.*, 1996) was used in the exploration of a printing application in which near pure rolling takes place. Shear rate cut-off values were used to avoid numerical singularities under conditions where the shear rate approached a zero value. The importance of both the power law co-efficient and exponents on the nip performance was quantified. This showed significant impacts for both parameters, with increases in each resulting in increased film thickness and maximum pressure.

The purpose of this paper is to explore the application of numerical simulation to coating applications that involve combined sliding and rolling mechanisms. This will extend previous work (Carvalho and Scriven, 1997; Lim *et al.*, 1996) through the incorporation of actual fluid properties that exhibit shear thinning and it will also include nip configurations in which there is positive engagement. Through case studies the effect of the power law co-efficient, power law exponent and sliding on the nip performance in terms of

pressure distribution, film thickness profile, strain rate and viscosity variation through the nip section and flow rate will be investigated.

Theoretical model background

The solution of the soft elastohydrodynamic lubrication contact is obtained by coupling the solution of the fluid film equations with those describing the mechanical deformation of the surfaces. The behaviour is coupled since the film thickness determines the pressure variation in the junction and this is established in the fluid domain calculation. In turn, the pressure variation defines the rubber deformation attributed to hydrodynamic action (Cudworth, 1979) and this is computed within the structural model. This dictates the need for iteration between the fluid and structural domains within the overall solution process. The basic equations together with their solution strategy will be discussed in the following sections, including the approach for handling the non-Newtonian fluid behaviour.

Elastic deformation

Since the deformation at the roller surface is small, the displacement of the rubber layer on the roller may be assumed to be linearly elastic. The deformation of this roller may be established using a number of numerical schemes. In the present study only the deformation of the surface is of interest and this is derived economically by using a boundary element approach. For a plain strain case, the boundary element integral equation for the solution of the general problem of elasticity under steady loading is given by Brebbia and Dominguez (1989):

$$c^i_{lk} u^i_k + \int_\Gamma p^*_{lk} u_k \ \mathrm{d}\Gamma = \int_\Gamma u^*_{lk} p_k \ \mathrm{d}\Gamma + \int_\Omega u^*_{lk} b_k \ \mathrm{d}\Omega \tag{1}$$

In coating applications, the speeds are modest and so centrifugal effects are negligible. Thermal effects may also be present in the nip. Sources are localised and include the shearing of the fluid film and deformation within the elastomer structure. The film is thin and therefore the shear stresses are high. However, the narrowness of the contact (typically 6 mm) is likely to be insufficient to allow any significant temperature build up to take place. Also the thermal capacity of the fluid is high, typically an oil based coating has a density of 900 kg/m^3 and a specific heat capacity of 2000 J/kg°C and this is also likely to ensure that the heating effect of fluid shearing is small. Similarly the energy dissipation in the elastomer will be low due to small engagements and low speed. Operating experience shows that elastomer heating becomes important when multiple rigid rollers are in contact with a single rubber covered roller. This leads to catastrophic failure of the rubber roller at high running speeds (e.g 700 m/min). This suggests that local thermal influence will be small and therefore the equation can be written as:

$$c^i_{lk}u^i_k + \int_\Gamma p^*_{lk}u_k \ \mathrm{d}\Gamma = \int_\Gamma u^*_{lk}p_k \ \mathrm{d}\Gamma \tag{2}$$

The discretisation of this equation will be explained below in the solution procedure section.

Generalised pressure equation

For a non-Newtonian fluid flow the thin film equations are derived accounting for the variation of viscosity, leading to a generalised pressure equation (Dowson, 1962). Provided that the analysis plane is some distance from the roller edge then this equation can be written in a one-dimensional form as:

$$\frac{\mathrm{d}}{\mathrm{d}x}\left[G\frac{\mathrm{d}p}{\mathrm{d}x}\right] = U_2\left[\frac{\mathrm{d}h}{\mathrm{d}x}\right] + (U_1 - U_2)\left[\frac{\mathrm{d}F}{\mathrm{d}x}\right] \tag{3}$$

where

$$G = \int_0^h \frac{y}{\mu}(y - F)\mathrm{d}y \tag{4}$$

$$F_1 = \int_0^h \frac{y}{\mu}\mathrm{d}y; \ \ F_0 = \int_0^h \frac{1}{\mu}\mathrm{d}y; \ \ F = \frac{F_1}{F_0} \tag{5}$$

The integrals can be evaluated and the pressure equation (3) solved for a non-Newtonian fluid once the variation of viscosity (μ) due to the combination of Poiseuille and Couette flow is known over the film thickness. This governing equation was solved using a finite difference numerical scheme and nodal pressure convergence within 10^{-6} Pa between successive iterations was assigned.

The viscosity field can be established either via the solution of a complex set of equations (Walters, 1975) or more simply by means of a power law equation (Wilkinson, 1960), where the shear stress is related to velocity gradient via the equation

$$\tau = m\left|\frac{\mathrm{d}u}{\mathrm{d}y}\right|^{n-1}\frac{\mathrm{d}u}{\mathrm{d}y} \tag{6}$$

The term $m|\mathrm{d}u/\mathrm{d}y|^{n-1}$ effectively represents the viscosity coefficient and for a Newtonian fluid, $n = 1$ and m is the dynamic viscosity. When $n < 1$, the fluid shear thins and assumes a pseudoplastic form. The determination of viscosity through the film relies on the calculation of the local velocity gradient and these may be determined through numerical differentiation of the velocity profile. Such profiles also need to account for the cross film viscosity variation and therefore the velocity variation was derived using equation (7). This equation

embodies the velocity boundary condition that the fluid adheres to each roller surface and therefore moves at their respective surface velocities U_1 and U_2.

$$u(\alpha) = U_1 + \frac{\mathrm{d}p}{\mathrm{d}x}\int_0^\alpha \frac{y}{\mu}\mathrm{d}y + \left(\frac{U_2 - U_1}{F_0} - \frac{F_1}{F_0}\frac{\mathrm{d}p}{\mathrm{d}x}\right)\int_0^\alpha \frac{\mathrm{d}y}{\mu} \tag{7}$$

Since equation (7) includes a cross film variation of viscosity through the terms F (see Equation (5)) it needs to be solved iteratively. This was implemented within the solution algorithm with a close tolerance on viscosity at each point through the film. Typically convergence to within 10^{-4} Pas between successive iterations was satisfied. For more extreme conditions it was also necessary to introduce damping into the solution to ensure stability.

The integration of this equation into the overall solution procedure will be described in a following section.

Film thickness

Closure of the equation set requires a definition of film thickness. This was expressed using the following equation that embodies an equivalent roller radius. A negative value of h_0 indicates a roller engagement and the term $u(x)$ represents the local deformation of the elastomer layer.

$$h(x) = h_0 + \frac{x^2}{2R} + u(x) \tag{8}$$

Load

The solution strategy seeks to modify the film thickness profile to satisfy a load application constraint and completion of the solution was obtained when the computed load meets the set value, to a tolerance, T_l, of less than 0.1 per cent.

$$\left|\left[\int_{x_1}^{x_2} p.\mathrm{d}x\right] - L\right| \leq T_l * L \tag{9}$$

Solution procedure

The thin film model embodies the assumption that the elastomer may be unwrapped to give a flat surface in the locality of the contact. Previous analysis (Dowson and Higginson, 1959) has been carried out to compare results from a flat (unwrapped) model and a model that includes curvature, representing the actual roller. The latter does not use linear elements and therefore requires a numerical integration of the boundary elements. This extends the calculation duration. The work in Dowson and Higginson (1959) has shown that this has a negligible effect on the predicted deformation. The boundary of the elastomer was divided into a number of linear elements, Figure 2, from which to obtain the integrals in the elasticity equation. The use of linear elements in a finite plane model allows the element integrals to be calculated analytically. As well

as allowing a rapid solution, this allows elements to be formulated that are suited to a solution with a Poisson's ratio of 0.5 (Brebbia and Dominguez, 1989; Banerjee and Butterfield, 1981), avoiding the numerical singularity that is usually present with this material property specification. Consistent with the elastomer mesh, the fluid domain was solved over the nip contact, X_a to X_b.

Following extensive exploration of solution strategies, the following steps have been established to give an accurate and stable result.

(1) Define the mesh over the elastomer boundary and calculate the division for the fluid side calculations.

(2) Set an initial value for the engagement, h_0, from this the Hertzian pressure and the consequent deformation is calculated.

(3) Calculate the film thickness in the nip junction.

(4) Solve for the film pressure, including iteration for non-Newtonian behaviour.

(5) Recalculate the elastomer deformation.

(6) If the deformation has not met the convergence criteria, then repeat from stage (3) with the new deformation.

(7) Once the deformation criterion has been met, examine the load equilibrium. If this is not met then appoint a new value for h_0 and repeat from (2).

The convergence requirement for the analysis was 0.1 percent on the pressure and indentation. Convergence of the solutions was usually obtained in approximately 5,000 iterations.

Results and discussion

A typical industrial configuration was used in the study to illustrate the application of the model described above. It is based on a coating application where the rollers run at different surface speeds thereby introducing a sliding component as a method to control the flow rate through the nip. The roller parameters and loading condition are itemised in Table I and have been derived from process data and the elastic modulus from material property measurement. Within the calculation different roller speeds as well as different power law exponents will be explored and these will be defined accordingly.

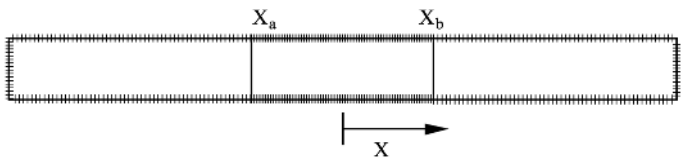

Figure 2.
Schematic discretisation of the elastomer layer

The actual fluid properties of a typical ink has been characterised using a cone and plate rheometer from which the relationship between shear stress and shear rate has been quantified (Lim *et al.*, 1996). This provides indicative values. Some coating fluids are noted to be highly viscous systems, exhibiting similar consistency. Using this information, the parameters for a power law fluid have been determined and appropriate values give a dynamic viscosity coefficient (m) of 50 and an exponent value (n) of 0.75. These have been used as a starting point for the investigation to evaluate the impact of changing from a Newtonian to non-Newtonian fluid and to explore the variations as a consequence of using different power law coefficients and exponents. As explained in the review, a lower cut-off in shear rate value needs to be used to avoid singularity in the determination of viscosity over the film thickness. An inappropriate choice can mask the shear-thinning model and therefore a range of values from 100/s to 500/s was explored. The results in terms of nip flow rate were virtually identical and therefore a cut-off of 250/s was finally chosen and this leads to a lower viscosity of limit of 12.57 Pas. This value was used in all calculations for Newtonian flow that serve as a benchmark with which to explore the effect of non-Newtonian behaviour.

Influence of non-Newtonian characteristics on nip performance

Initial calculation was carried out for a pure rolling nip in which the surface velocity was 2.5 m/s for both rollers. The results from this calculation are displayed in Figure 3 as pressure and film thickness profiles through the nip. Significant differences in the film thickness profiles and small differences in the form of the pressure profile may be noted. The latter clearly satisfies the over all load constraint of equation (9). For the non-Newtonian fluid, the pressure peak moves nearer to the nip centre and achieves a slightly higher value. At this point the fluid achieves a Newtonian level because the velocity gradients through the film are negligible (see Figure 4). In the absence of a pressure gradient, the velocity profile represents a simple plug flow when the rollers forming the nip rotate to give identical surface velocities.

The changes in minimum film thickness are much more dramatic. Over the nip contact there is significant shear thinning and this leads to a 27.4 per cent reduction in minimum film thickness. The pumping capacity is determined by the film thickness at which the pressure gradient is zero and the entraining

Table I. Roller parameter details

Parameter	Conditions
Load (Nm^{-1})	7000
Roller radius (m)	0.15
Elastic modulus (Pa)	2.0e+6
Rubber thickness (mm)	15

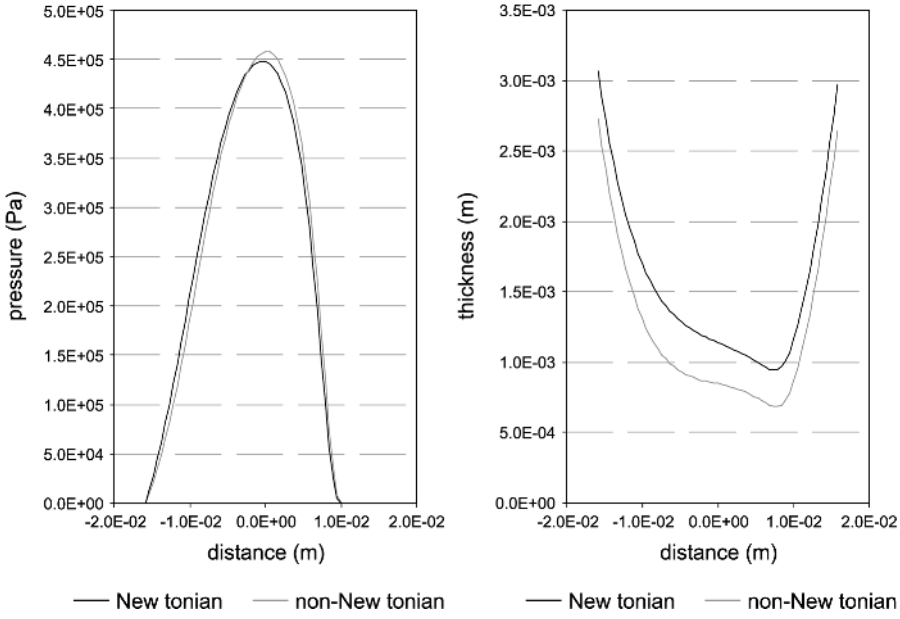

Figure 3.
Influence of non-Newtonian behaviour on the pressure profile and film thickness

velocity of the two roller surfaces. Since the point of zero pressure gradient occurs close to the point of minimum film thickness, the nip shows a commensurate reduction of 26.4 per cent in its pumping capacity. This result has an important practical implication when coating systems are set according to roller load. The shear thinning mechanism leads to a reduction in film thickness and a reduction in coating weight as a consequence.

The results in Figure 3 suggest that there are significant variations in viscosity through the film and this is confirmed by the results shown in Figure 4. The contours depict the shear rate and the corresponding viscosity variation through the nip section. High shear rates are generated in the inlet region and just downstream from the minimum film thickness point. These are a consequence of the pressure gradients that are present at these locations. The pressure gradients lead to a Poiseulle flow component and in the case of rollers having identical surface velocities, only this flow component leads to a shearing action in the film. Thus the highest shear rate occurs near to the roller surface, in this case resulting in 50 per cent change in viscosity over the film thickness. The shear rate contours also illustrate the high levels that are present through the film, even under rolling conditions. This indication is useful as a guide to the level of shear that is required in characterising fluids for these applications. The levels exhibited are within the working limits of rheometers that are commercially available, however when roller speed differentials are present, these rates will become more extreme, possibly

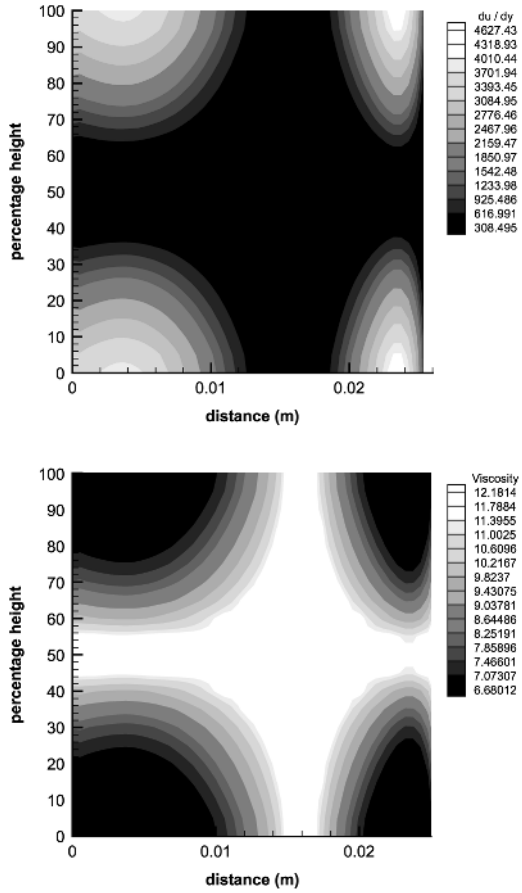

Figure 4.
Shear rate and viscosity variation through the nip section $m = 50$, $n = 0.75$, $U_1 = U_2 = 2.5\,\mathrm{m/s}$

achieving levels that are at the working limits of the most appropriate rheometer systems.

Having explored the comparison between a Newtonian and non-Newtonian model, calculation was completed to investigate the response to changing viscosity coefficient (m) and power law index (n). The viscosity coefficient (m) was varied over the range 30 to 70 Pas and the index (n) from 0.65 to 0.85. The effect of changing the viscosity coefficient is shown in Figure 5. For the prescribed load, this has the most significant impact on the film thickness profile with the more viscous fluid giving a larger film thickness. Similar behaviour has been noted for a Newtonian fluid (Bohan *et al.*, 1997a). The figure also shows that minimum film thickness decreases non-linearly with a proportionate change in viscosity coefficient. A 19 per cent reduction in film thickness occurs when the viscosity changes from 70 Pas to 50 Pas and a drop of 27 per cent in thickness occurs corresponding to a viscosity coefficient

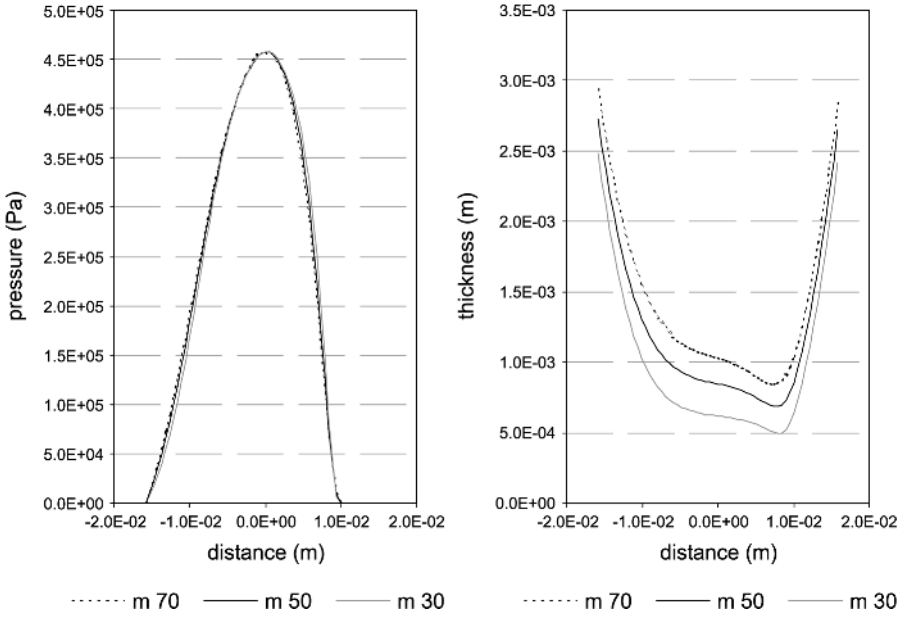

Figure 5.
The influence of viscosity coefficient on pressure and film thickness, $n = 0.75$, $U_1 = U_2 = 2.5\,\text{m/s}$

change from 50 Pas to 30 Pas. This behaviour is a consequence of employing the power law equation to represent viscosity behaviour. At the lower viscosity setting, the film thickness will be affected directly by the value of the viscosity coefficient, however, for the low viscosity, the reduction in film thickness leads to higher shear rates in the film and this exacerbates the viscosity reduction. This mechanism is more dominant at the lower viscosity level and this is reflected in the more marked reduction in film thickness.

Following on from the discussion of the previous case study concerning the direct dependence of pumping capacity on minimum film thickness, this is also reduced in near identical proportions as the viscosity coefficient is dropped from 70 Pas to 30 Pas. From a practical sense this points to a strong requirement to control viscosity closely since this will have a direct impact on the coating film thickness.

The power law exponent represents the degree of shear thinning and the impact of this parameter on nip behaviour is shown in Figure 6. The effect on the form of the pressure profile is similar to that discussed in connection with Figure 3, with the peak value moving towards the nip centre for the more shear thinning fluid. The change in minimum film thickness profile displays the expected form with the higher viscosity fluid increasing the minimum film thickness. However this increase does not depend linearly on the index. This is attributed to the non-linear change in viscosity in response to linear changes in the power law index value. Also since the pumping capacity in the nip depends

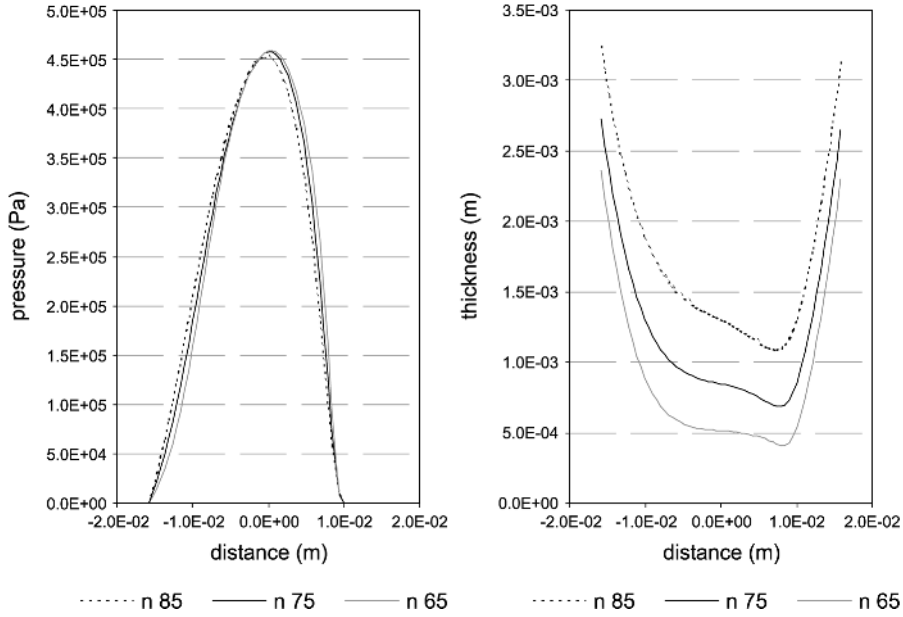

Figure 6.
Influence of power law exponent on pressure and film thickness, $m = 50\,\text{Pas}$, $U_1 = U_2 = 2.5\,\text{m/s}$

on the film thickness at the point of peak pressure, Figure 6 also suggests that the nip pumping capacity is also affected nonlinearly by identical change in power law index value.

As well as determining processing capacity, speed is one of the major control features for coating applications. Through a series of calculations, it was found that the influence of rolling speed on the flow rate per unit width of roller and minimum film thickness is significant and increases non-linearly as depicted in Figure 7. Two mechanisms are present. The first is associated with a simple increase in speed, where, for a constant load application, the film thickness is

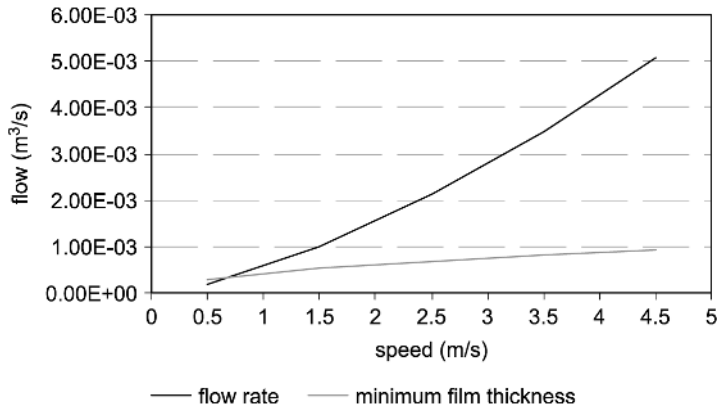

Figure 7.
Influence of speed on flow rate per unit roller width and minimum film thickness, $m = 50\,\text{Pas}$, $n = 0.75$

expected to increase in a linear manner. The second mechanism is more subtle, arising due to the increase in film thickness and the consequent small reduction in shear rate. The latter also leads to a further small increase in viscosity and this will also increase the film thickness. Their combined effect is to increase the film thickness in a nonlinear manner.

The combined effect of higher entrainment velocity together with the non-linear increase in the film thickness gives an increase in calculated flow rate that follows a similar pattern to the film thickness variation. Practically this will be reflected in higher coating weight that can be reduced most directly by increasing the load on the roller pair, or through the application of a speed differential to the rollers forming the nip. The latter will be discussed more fully in a following case study.

Influence of sliding on nip performance

As explained previously, different roller speeds are used as a means of controlling precisely the pumping capacity of the nip, particularly when thin films need to be deposited. The pumping capacity is affected by the combined influence of net entrainment and hydrodynamic action. The latter refers to the pressure field that is generated in the nip and for a given load this will determine the working film thickness in the gap. In the following case studies, the lower roller speed (U_1) is maintained constant and the upper roller speed (U_2) is varied. The consequent effect on film pressure and thickness profile is shown in Figure 8 and the associated viscosity variation through the film section is shown in Figure 9.

As shown in Figure 8, the impact of a sliding component on the shape of the pressure profile is negligible. It has a more significant effect on the minimum film thickness and this is non-linear with respect to the speed increment. As expected, decreasing the upper roller speed by 2 m/s with respect to the lower roller leads to a reduction in film thickness whereas increasing it by an equivalent amount leads to a larger film thickness. However the difference in film thickness does not vary proportionately. For a constant load application, in common with previous discussion, two mechanisms are present. Notably the lower entrainment will lead to a reduction in film thickness due to hydrodynamic action. Since the pressure profiles will be similar in each case to satisfy the load criterion, the Poiseulle flow velocity profile will also be similar. Because the basic film thickness is reduced due to the lower entrainment, this will lead to a higher shear rate through the film. Consequently there will be a further reduction in viscosity. This is confirmed on examining the viscosity contours, Figure 9, where it can be established that the overall effect was to give lower viscosity at low speed and higher viscosity at high speed.

The effect of sliding on the viscosity profiles is shown in Figure 9. These show a significant change from the rolling case, Figure 4, in which there are large zones in which the fluid viscosity is high due to the low velocity

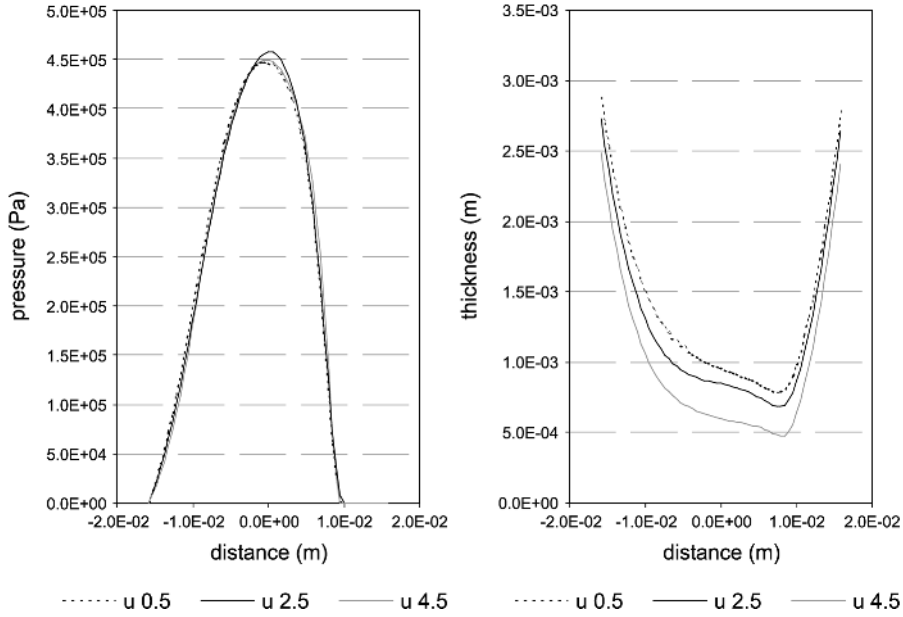

Figure 8.
Influence of sliding on pressure and film thickness, $U_1 = 2.5\,\text{m/s}$, $m = 50\,\text{Pas}$, $n = 0.75$

gradients in these regions. When different roller speeds are present, the velocity gradients are automatically increased and the viscosity field becomes asymmetric with respect to the film centreline. As shown in Figure 9, by changing the upper roller speed from 0.5 to 4.5 m/s the viscosity profile is approximately inverted. However the latter condition leads to a viscosity field that is, on average, higher in value and this affects the nip behaviour in the manner discussed above.

The application of speed differential is used as a precise control to determine the flow rate through the nip. Also the influence of roller speed and speed ratio is important since in combination they determine process through flow and coating weight. The result from a series of calculations in which their combined effect is explored is shown in Figure 10. The characteristics are similar in form with the non-linear increase in flow rate being a combination of film thickness and entrainment velocity. The governing physics has been discussed in connection with Figure 8 and Figure 9. Superimposed are different sliding ratios with the top roller speed (U_2) ranging from half to four times the speed of the bottom roller (U_1). The characteristic shows clearly the application of speed differential in controlling flow through the nip. Fortuitously this control becomes most precise as the upper roller running at speed U_2 decreases below that of the lower roller running at speed U_1 for which the ratio U_1/U_2 exceeds unity. As shown in Figure 10, large changes in relative roller speed in this operating region lead to only small changes in nip pumping capacity.

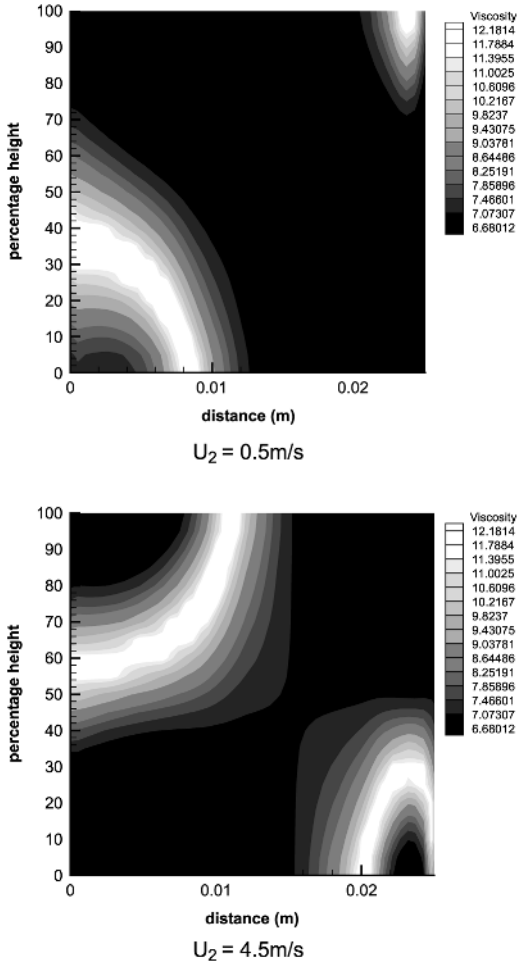

Figure 9.
Viscosity contours through the nip junction, $m = 50\,\text{Pas}$, $n = 0.75$, $U_1 = 2.5\,\text{m/s}$ $U_2 = 0.5\,\text{m/s}$ $U_2 = 4.5\,\text{m/s}$

Conclusions

A fast and computationally efficient model has been developed for a SEHL contact lubricated using a non-Newtonian fluid. This has been effected with the use of a power law fluid. The numerical analysis couples the solution of the generalised pressure equation and those of the elastomer and incorporates the non-Newtonian behaviour in the generalised pressure equation. A sensitivity study has been completed to establish the impact of rheology and speed on the film thickness and pumping capacity within the nip operating in pure rolling and under combined rolling/sliding conditions.

From this work it may be concluded that for SEHL problems, significant differences occur in the nip performance between the Newtonian and non-Newtonian fluids. For shear thinning fluids the high shear in the nip cause a

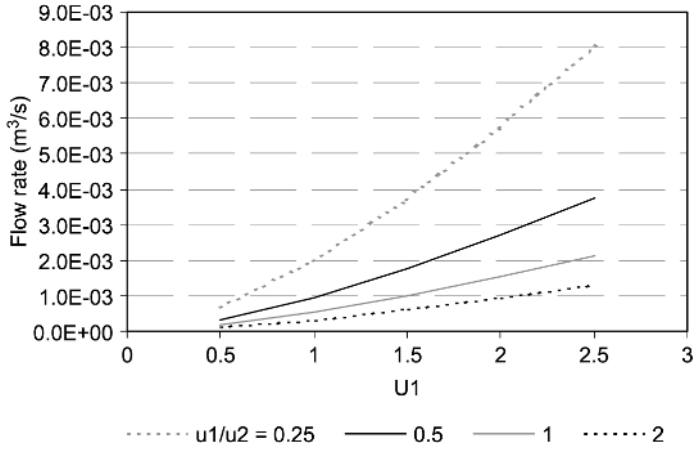

Figure 10.
Relationship between speed, sliding ratio and flow rate per unit roller width, $m = 50$ Pas, $n = 0.75$

drop in the local viscosity. This change in the fluid properties leads to a reduction in the film thickness and for the peak pressure to move closer to the centre of the nip.

With regard to fluid properties, reducing either the viscosity coefficient (m) and power law index (n) results in a reduction of the minimum film thickness with an associated reduction in the flow rate through the nip. The pressure profiles, for a constant load case, are also altered slightly with the peak pressure moving towards the centre of the nip.

In sliding, the shear rate and viscosity profiles become asymmetric. For a constant nip load, the lower entrainment leads to lower viscosity since the film thickness is reduced and the shear rates increase as a consequence. The opposite effect is observed for the higher entrainment. Roller speed has been shown to have a large impact on the flow rate and film thickness, causing increases for all roller speed ratios. For a fixed load, the increased speeds increase the film thickness and reduce the shear rate as a consequence. The combined effect is a non-linear increase in the nip pumping capacity.

For constant load, speed differential is very effective in controlling nip pumping capacity and the system response is particularly sensitive at the lower entrainment speed.

References

Banerjee, P.K. and Butterfield, R. (1981), *Boundary element method in engineering science*, McGraw Hill, New York.

Bennett, J. and Higginson, G.R. (1970), "Hydrodynamic lubrication of soft solids", *Proc. I.Mech.E. Journal of Mechanical Engineering Sciences*, 12, pp. 218-22.

Brebbia, C.A. and Dominguez, J. (1989), *Boundary elements: An introductory course*, McGraw Hill.

Bohan, M.F.J., Claypole, T.C., Gethin, D.T. Basri, S.B. (1997), "Application of boundary element modelling to soft nips in rolling contact" 49th TAGA Tech. Conf., Quebec, May.

Bohan, M.F.J., Lim, C.H., Korochkina, T.V., Claypole, T.C., Gethin, D.T. and Roylance, B.J. (1997b), "An investigation of the hydrodynamic and mechanical behaviour of a soft nip in rolling contact", *Proc. IMechE part J*, 211 No. J1, pp. 37-50.

Cudworth, C.J., "Finite Element Solution of the Elastohydrodynamic Lubrication of a Compliant Surface in Pure Sliding", 5th Leeds-Lyon Symposium on Tribology, Leeds, 1979.

Carvalho, M.S. and Scriven, L.E. (1997), "Deformable roller coating flows: steady state and linear perturbation analysis", *Journal of Fluid Mechanics*, 339, pp. 143-72.

Dowson, D. (1962), *A Generalised Reynolds Equation for Fluid Film Lubrication; International Journal of Mechanical Engineering Sciences.*, 4, pp. 159-70.

Dowson, D. and Ehret, P. (1999), "Past present and future studies in elastohydrodynamics", *Proc I Mech E (J)*, 213, pp. 317-33.

Dowson, D. and Higginson, G.R. (1959), "A numerical solution to the elastohydrodynamic Problem", *J. Mech. Eng. Sci.*, 1, pp. 6-15.

Hannah, M. (1951), "Contact stress and deformation in a thin elastic layer", *Quarterly Journal of Mechanics and Applied Maths*, 4, pp. 94-105.

Hooke, C.J. (1986), "The elastohydrodynamic lubrication of a cylinder on an elastomeric layer", *Wear*, 111, pp. 83-99.

Hooke, C.J. and O'Donoghue, J.P. (1972), "Elastohydrodynamic lubrication of soft, highly deformed contacts", *Proc. I.Mech.E., Journal of Mechanical Engineering Sciences*, 14, pp. 34-48.

Jacobson, B.O. and Hamrock, B.J. (1984), "Non-Newtonian fluid model incorporated into elastohydrodynamic lubrication of rectangular contacts", *Trans. ASME (JOLT)*, 106, pp. 275-84.

Kistler, S.F. and Schweizer, P.M. (1997), *Liquid Film Coating*, Chapman and Hall.

Lim, C.H., Bohan, M.F.J., Claypole, T.C., Gethin, D.T. and Roylance, B.J. (1996), "A finite element investigation into a soft rolling contact supplied by a non-newtonian ink", *J. Phys. D: Appl. Phys*, 29, pp. 1894-903.

Miller, R.D.W. (1966), "Some effects of compressibility on the indentation of a thin elastic layer by a smooth rigid cylinder", *Applied Scientific Research*, 16, pp. 405-24.

MacPhee, J., Shieh, J. and Hamrock, B.J. (1992), "The application of elastohydrodynamic lubrication theory to the prediction of conditions existing in lithographic printing press roller nips", *Advances in Printing Science and Technology*, 21, pp. 242-76.

Parish, D.J. (1958), "Apparent slip between metal and rubber covered pressure rollers", *Bri. J. Appl. Maths*, 9, pp. 428-33.

Walters, K. (1975), *Rheometry*, Chapman and Hall.

Wilkinson, W.L. (1960), *Non-Newtonian Fluids – Fluid Mechanics, Mixing and Heat Transfer*, Pergamon Press Ltd.